ANODIC OXIDES ON Al-Nb ALLOYS AND NIOBIUM

A thesis submitted to The University of Manchester for the degree of Doctor of Philosophy in the Faculty of Engineering and Physical Sciences

2007

ANA ISABEL T S CORREIA DE SÁ

SCHOOL OF MATERIALS
CORROSION AND PROTECTION CENTRE

CONTENTS

CONTENTS 2

LIST OF FIGURES 8

LIST OF TABLES 17

ABSTRACT 20

DECLARATION 21

COPYRIGHT STATEMENT 21

ACKNOWLEGEMENTS 22

DEDICATION 23

CHAPTER 1

INTRODUCTION AND LITERATURE REVIEW OF ANODIC FILMS ON VALVE-METALS 24

1.1 Introduction 24

1.2 Anodic oxidation of valve-metals 25

1.2.1 The fundamental equation of the high-field model 25

1.2.2 The rate-determining step and anomalous behaviour 28

1.2.3 Anodising techniques 30

1.2.4 Structure and composition of anodic oxide films 33

1.2.5 Flaws in anodic oxide films 34

1.2.6 Ionic migration and transport numbers 34

1.2.7 Incorporation of foreign species into anodic oxide films 36

1.3 Electric behaviour of anodic oxide films 40

1.3.1 Fundamentals of the electrical properties of solid materials 40

1.3.2 Dielectric behaviour of anodic oxide films 42

1.3.3 Semiconductor behaviour of anodic oxide films …………….…….. 48

1.3.4 The electrical properties of anodic oxide films of aluminium, niobium and tantalum ……………………..…………………... 51

1.4 The electrochromic effect ………………………………………… 53

CHAPTER 2

LITERATURE REVIEW OF ANODIC OXIDES ON SPUTTERED ALLOYS …………………………………………………….. 55

2.1 Introduction ……………………..…………………...….. 55

2.2 Structure of sputtered valve-metal alloys ……..……...…………. 56

2.3 Anodic oxidation of sputtered aluminium alloys ……..…..……………. 57

2.3.1 Formation of enriched alloy layers ………….………….......... 57

2.3.2 Migration rates of ionic species …………………..……..……….. 60

2.3.3 Formation of oxygen gas ...………………..……….………….. 64

2.3.4 The presence of hydrogen in anodic oxide films ..……………....… 66

2.3.5 Formation of voids and film detachment during anodising ……..… 66

2.3.6 The anodic oxidation of aluminium alloys with high concentrations of alloying elements (> 20 at.%) …………………… 67

2.4 The anodic oxidation of sputtered niobium alloys and tantalum alloys 70

2.5 Electrical properties of mixed anodic oxide films …………..………… 73

2.5.1 Anodic oxide films of niobium as a component ………....……..… 73

2.5.2 Mixed anodic oxide films of other valve-metals ………..……….. 74

2.6 Introduction to present work ……………………………………... 75

CHAPTER 3

EXPERIMENTAL TECHNIQUES ……………………...…………… 77

3.1 Introduction ……………………………..…………………. 77

3.2 Experimental procedure ..…………………..……......………………... 77

3.2.1 Materials and solutions ………………………………………………… 77

3.2.2 Electrode preparation …………………………………….…..…… 78

3.2.3 Substrate preparation for magnetron sputtering …..……….…… 79

3.2.4 Constant current anodising ………………………….……………… 80

3.2.5 Voltammetry ………………………………………….……………… 81

3.2.6 Electrochemical impedance spectroscopy (EIS) ..…..…………… 82

3.2.7 Magnetron sputter-deposition …………………..……………..... 83

3.2.8 Scanning electron microscopy (SEM) ……………………………. 85

3.2.9 Rutherford backscatering spectroscopy (RBS) ………………….. 85

3.2.10 Transmission electron microscopy (TEM) …….……….……… 85

3.2.11 X-ray photoelectron spectroscopy (XPS) and Auger electron spectroscopy (AES) ………..…………..…………….……… 86

3.3 Fundamentals of the experimental techniques ………………………….. 86

3.3.1 Voltammetry …….………………………………………………..... 86

3.3.2 Electrochemical impedance spectroscopy (EIS) …….…….……….. 88

3.3.3 Magnetron sputter-deposition …………………………..……… 92

3.3.4 Rutherford backscatering spectroscopy (RBS) …………………… 94

3.3.5 Scanning electron microscopy (SEM) ……...…………………..... 95

3.3.6 Transmission electron microscopy (TEM) ….……………………. 97

3.3.7 Energy dispersive X-ray analysis (EDX) …………...……………. 97

3.3.8 X-ray photoelectron spectroscopy (XPS) and Auger electron spectroscopy (AES) ….……………….…………………………..... 98

CHAPTER 4

ELECTROCHEMICAL BEHAVIOUR OF THE NIOBIUM/THIN OXIDE FILM/ELECTROLYTE INTERFACE ……………………………. 101

4.1 Introduction ……………………………………………...…………… 101

4.2 Electrode surface ……………………..…...……………………….… 102

4.3 Cyclic voltammetry for the niobium rod in 0.6 M Na_2SO_4 (pH 5.6) …… 102

4.3.1 Typical voltammogram …… 102

4.3.2 Effect of sweep rate …… 107

4.3.3 pH effect …… 111

4.3.4 Effect of sweep reversal …… 114

4.3.5 Effect of holding the potential at –1.5 V …… 114

4.4 Cyclic voltammetry for the niobium rod in 0.15 M H_3BO_3 + 0.075 M $Na_2B_4O_7$ (pH 8.8) …… 114

4.4.1 Effect of sweep rate …… 114

4.5 Cyclic voltammetry for the sputtered niobium in 0.6 M Na_2SO_4 (pH 5.6) …… 117

4.6 XPS and AES analyses of the electrode surface …… 117

4.7 Cyclic voltammetry of sputtered Al-Nb alloys in 0.6 M Na_2SO_4 (pH 5.6) …… 123

4.8 Discussion …… 126

4.9 Conclusions …… 129

CHAPTER 5

ANODIC OXIDATION ON Al-Nb ALLOYS AND NIOBIUM …… 130

5.1 Introduction …… 130

5.2 SEM of the metallic surfaces …… 131

5.3 Voltage-time response …… 131

5.3.1 Al-Nb alloys …… 131

5.3.2 Niobium …… 136

5.4 Oxide composition …… 140

5.5 Oxide morphology …… 145

5.6 Oxide density …… 149

5.7 Efficiency of the anodising process …… 149

5.8 Discussion …… 152

5.8.1 Al-Nb alloys (21-44 at.% Nb) …… 152

5.8.2 Al-Nb alloys (74-89 at.% Nb) ……………….……………………... 156

5.8.3 Niobium ………...……………………………………………………... 157

5.9 Conclusions ……………………………………………………………… 158

CHAPTER 6

DIELECTRIC PROPERTIES OF ANODIC OXIDES ON Al-Nb ALLOYS AND NIOBIUM 161

6.1 Introduction ……………………………………………………………... 161

6.2 Anodic oxides on Al-Nb alloys of 21 to 44 at.% Nb ……..………………… 162

6.2.1 Dielectric constant and capacitive behaviour…..………………………….. 162

6.2.2 Simulation of an EIS spectrum of a two layered oxide ……………….. 166

6.3 Anodic oxides on Al-Nb alloys of high niobium content (≥ 74 at.% Nb) and niobium 170

6.3.1 Dielectric constant and capacitive behaviour ……………….……...…. 170

6.4 Discussion ……………………………..……………………………… 175

6.5 Conclusions ……………………………………………………………… 178

CHAPTER 7

SEMICONDUCTING PROPERTIES OF ANODIC OXIDES ON NIOBIUM AND Al-Nb ALLOYS ……………………………………………….. 179

7.1 Introduction ……………………………………………………………... 179

7.2 Anodic Niobia …………………………..…...…………………………..… 180

7.3 Anodic oxides on Al-Nb alloys ……………………………………………. 187

7.3.1 Anodic oxides formed on Al-31 at.% Nb and Al-44 at.% Nb alloys 187

7.3.2 Anodic oxides on Al-Nb alloys of high niobium content (≥ 74 at.% Nb) ……………………………………………………... 191

7.4 Discussion ……...………………………………………….……….…...... 207

7.5 Conclusions …………………...………………………….…………….....… 214

GENERAL SUMMARY AND CONCLUSIONS …………………………... 216

SUGGESTIONS FOR FUTURE WORK ....………..……………………….. 219

APPENDIX 1 ……………………………………………………………………... 221

REFERENCES ……………………………………………………………………… 227

Total number of words = 48359

LIST OF FIGURES

Figure 1.1 Characteristic voltage-current response of the valve-metal/ oxide/electrolyte system [3] ……….……………………….... 26

Figure 1.2 Schematic diagram showing the displacement of a vacancy centered cluster when the vacancy moves from A to B [12] … 30

Figure 1.3 Schematic diagram of a marker experiment for anodising aluminium, showing the thickness fraction formed at each interface [24] ………………………………………………..... 35

Figure 1.4 Schematic diagram of the anodised alumina contaminated with electrolyte species with different movements: (a) immobile species; (b) outward species; (c) inward species [24] 39

Figure 1.5 Schematic diagram of the energy band for metal, semiconductor and insulator materials ……………………………... 41

Figure 1.6 Polarization of a dielectric material on a parallel-plate capacitor …………………………………………………… 43

Figure 1.7 Variation of loss factor with band gap energy in ultra-pure oxides [20] …………………………………………………… 48

Figure 1.8 Energy band diagram for an n-type semiconductor in contact with an electrolyte, illustrating the flat band condition (a) and the band bending due to the formation of a space charge region (b) …………………………………………………... 49

Figure 1.9 Energy band diagram for an n-type semiconductor in contact with an electrolyte, illustrating the formation of a complete charge depleted layer across the entire oxide layer ………….. 51

Figure 2.1 Structure of sputter-deposited aluminium alloys identified by X-ray diffraction [96] ………..……………………………. 56

Figure 2.2 Variation of enrichment of the alloying elements with Gibbs free energy per equivalent for formation of the alloying element oxide [102] ………………………………………….. 57

Figure 2.3 Schematic diagrams of oxide film growth on a dilute Al-W alloy: (a) initial alloy condition; (b) first stage growth with the formation of a tungsten-free anodic alumina film; (c) local oxidation of tungsten at the alloy/oxide interface, following achievement of sufficient enrichment of tungsten with subsequent outward migration of W^{6+} species [102] …....….. 59

Figure 2.4 Schematic diagram of oxide film growth on a dilute aluminium alloy: (a) first stage of oxide growth with formation of pure alumina ($V = V_o$); (b) final stage of oxide growth with formation of alumina contaminated with alloying element oxide ($V = V_{total}$) …………………………………… 61

Figure 2.5 Variation of cation transport number with the alloy composition for anodic films on Al-Ta alloys [123] ………… 69

Figure 3.1 Schematic diagram of the electropolishing cell [136] ………... 80

Figure 3.2 Schematic diagram of the anodising cell [136] ………………. 81

Figure 3.3 Schematic diagram of the assembling for impedance measurements with a mercury drop ………………………….. 82

Figure 3.4 Cyclic voltammogram for a reversible process; $O + ne \Leftrightarrow R$ 87

Figure 3.5 Impedance of the circuit elements when connected in parallel (a) and in series combination (b) …………………………….. 90

Figure 3.6 Randles equivalent circuit $R_s(R_{ct}$-$C_{dl})$ (a) and corresponding complex impedance diagram (b) …………………………….. 90

Figure 3.7 Schematic diagram showing momentum exchange processes on sputter-deposition [146] …………………………………... 92

Figure 3.8 Schematic representation of the sputtering system [146] ……. 93

Figure 3.9 Schematic diagram showing how the depth profile is determined by RBS analysis of a binary specimen (AB) in which $M_B > M_A$ and B is present only in the surface specimen [151]. ………………………………………………………… 94

Figure 3.10 Schematic diagram of the radiation processes induced when an energetic electron beam strikes a solid material [153]…….. 96

Figure 3.11 Energy diagram showing the photoelectron effect on which XPS analysis is based ………………………………………… 99

Figure 3.12 Energy diagram showing the electronic transitions used for Auger analysis [155] ………………………………………… 100

Figure 4.1 Scanning electron micrograph of the surface of the niobium rod after mechanical grinding ………………………………... 103

Figure 4.2 EDS analysis of the surface of the niobium rod after mechanical grinding ………………………………………… 103

Figure 4.3 Voltammograms of the niobium rod in 0.6 M Na_2SO_4, s = 0.2 V s^{-1}, -1.5 to +0.5 V_{SCE} 104

Figure 4.4 Voltammograms for the niobium rod in 0.6 M Na_2SO_4, s = 0.2 V s^{-1}, at the following potential-time profiles:
(a) -1.5 → -0.6 → -1.5 V_{SCE};
(b) -0.6 → +0.5 → -1.5 → + 0.6 V_{SCE};
(c) -0.6 → -1.5 → +0.5 → - 0.6 V_{SCE}; 106

Figure 4.5 Voltammograms showing the effect of sweep rate for the niobium rod in 0.6 M Na_2SO_4, -1.5 to +0.5 V_{SCE} ….……..… 108

Figure 4.6 Variation of log (ip) with log (s) for the niobium rod in 0.6 M Na_2SO_4, -1.5 to 0.5 V_{SCE}: (a) peak I_a; (b) zone II_{st}; (c) peak III_c 109

Figure 4.7 Variation of the peak charges (q_p) with potential sweep rate (s) for the niobium rod in 0.6 M Na_2SO_4, -1.5 to 0.5 V_{SCE}: (a) zone II_{st}; (b) peaks I_a and III_c …………………...………… 110

Figure 4.8 Voltammograms showing the effect of pH (5.6 to 2.6) for the niobium rod in 0.6 M Na_2SO_4, s = 0.2 V s^{-1}, -1.5 to 0.5 V_{SCE} .. 112

Figure 4.9 Voltammograms showing the effect of pH (5.6 to 12) for the niobium rod in 0.6 M Na_2SO_4, s = 0.2 V s^{-1}, -1.5 to 0.5 V_{SCE} .. 112

Figure 4.10 Variation of the peak current densities with pH for the niobium rod in 0.6 M Na_2SO_4, s = 0.2 V s^{-1}, -1.5 to 0.5 V_{SCE}: (a) peak I_a; (b) zone II_{st}; (c) peak III_c ………..……….…… 113

Figure 4.11 Voltammograms showing the effect of potential reversal at different values of positive potential limit for the niobium rod in 0.6 M Na_2SO_4, s = 0.2 V s^{-1}, -1.5 to 0.5 V_{SCE} …………….. 115

Figure 4.12 Voltammograms showing the effect of holding the potential at 0, 15, 100 and 200 s for the niobium rod in 0.6 M Na_2SO_4, s = 0.2 V s^{-1}, -1.5 to 0.5 V_{SCE} …………………………………… 115

Figure 4.13 Voltammograms showing the effect of sweep rate for the niobium rod in 0.15 M H_3BO_3 + 0.075 M $Na_2B_4O_7$ (pH 8.8), -1.5 to 0.5 V $_{SCE}$……………………………………………… 116

Figure 4.14 Variation of log (ip) vith log (s) for the niobium rod in 15 M H_3BO_3 + 0.075 M $Na_2B_4O_7$ (pH 8.8), -1.5 to 0.5 V_{SCE}: (a) peak I_a; (b) zone II_{st}; (c) peak III_c …………………………… 116

Figure 4.15 Voltammograms for the sputtered niobium in 0.6 M Na_2SO_4, s = 0.2 Vs^{-1}, -1.5 to +0.5 V_{SCE} showing the first sweep (a) and subsequent sweeps (b)……………………………………… 118

Figure 4.16 XPS spectra obtained for the niobium rod prepared under various experimental conditions: (a) immediately after grinding ; (b) after grinding and storing the specimen for 15 days in a desiccator; (c) after cyclic voltammetry …………… 121

Figure 4.17 Auger depth profiles for the niobium rod at the following experimental conditions: (a) immediately after grinding; (b) after cyclic voltammetry ……………………………………… 122

Figure 4.18 Voltammograms with multi-sweeps obtained at 0.2 V s^{-1}, from -1.5 V to + 2.5 V_{SCE} in 0.6 M Na_2SO_4 for the sputtered alloys: (a) Al-21 at.% Nb alloy; (b) Al-31 at.% Nb alloy; (c) Al-44 at.% Nb alloy………….………………………………. 124

Figure 4.19 Cathodic side of the voltammograms with multi-sweeps obtained at 0.2 V s^{-1}, from –1.5 V to +2.5 V in 0.6 M Na_2SO_4 for sputtered alloys: (a) Al-21 at.% Nb alloy; (b) Al-31 at.% Nb alloy; (c) Al-44 at.% Nb alloy……………………………. 125

Figure 5.1 Scanning electron micrograph of the surface of a sputtered 100 at.% niobium specimen (set of specimens sputtered at 0.2 Pa) …………………………………………………….... 132

Figure 5.2 Scanning electron micrograph of the surface of a sputtered Al-21 at.% Nb alloy specimen ……………………………….. 132

Figure 5.3 Scanning electron micrograph of the surface of a sputtered Al-31 at.% Nb alloy specimen………………………………..... 133

Figure 5.4 Voltage-time response of the Al-Nb alloys during anodising at 5 mA cm^{-2} in 0.1 M ammonium pentaborate ………………... 133

Figure 5.5 Variation of the slope of the voltage-time behaviour of the Al-Nb alloys (21 to 89 at.% Nb) and of the sputtered niobium at 5 mA cm^{-2} in 0.1 M ammonium pentaborate to 150 V with niobium content in the alloy ……... 134

Figure 5.6 Scanning electron micrograph of the surface of a sputtered Al-81 at.% Nb alloy specimen after anodising at 5 mA cm^{-2} in 0.1 M ammonium pentaborate to 150 V ……………………. 135

Figure 5.7 Voltage-time response of the sputtered niobium during anodising at 5 mA cm^{-2} in 0.1 M ammonium pentaborate to 150 V (a). Enlarged area of the previous plot (b) …………… 137

Figure 5.8 Initial 20 seconds period of the voltage-time response of the sputtered niobium (set of specimens sputtered at 0.5 Pa) after storage for different periods during anodising at 5 mA cm^{-2} in 0.1 M ammonium pentaborate ……………………………….. 137

Figure 5.9 Scanning electron micrographs of the sputtered 100 at.% niobium after anodising to 150 V at 5 mA cm^{-2} in 0.1 M ammonium pentaborate: (a) set of specimens sputtered at 0.5 Pa argon; (b) set of specimens sputtered at 0.2 Pa argon ……. 138

Figure 5.10 Voltage-time response of the niobium rod after mechanical grinding followed by chemical polishing, during anodising at 5 mA cm^{-2} in 0.1 M ammonium pentaborate to 150 V ………. 139

Figure 5.11 Scanning electron micrograph of the surface of the niobium rod surface after mechanical grinding followed by chemical polishing ……………………………………………………… 139

Figure 5.12 Experimental and simulated RBS spectra (RUMP program) for the Al-Nb alloys and the sputtered niobium after anodising to 150 V at 5 mA cm^{-2} in 0.1 M ammonium pentaborate: (a) Al-21 at.% Nb alloy; (b) Al-31 at.% Nb alloy; (c) Al-44 at.% Nb alloy; (d) 100 at.% Nb …………………………………… 141

Figure 5.13 Experimental and simulated RBS spectra (NDF program) for the Al-Nb alloys after anodising to different voltages at 5 mA cm^{-2} in 0.1 M ammonium pentaborate: (a) Al-74 at.% Nb alloy (100 V); (b) Al-81 at.% Nb alloy (150 V); (c) Al-89 at.% Nb alloy (150 V)………….……………………………. 144

Figure 5.14 Transmission electron micrograph of an ultramicrotomed section of the Al-21 at.% Nb alloy after anodising to 200 V at 5 mA cm^{-2} in 0.1 M ammonium pentaborate ……….………. 146

Figure 5.15 Transmission electron micrograph of an ultramicrotomed section of the Al-31at.% Nb alloy after anodising to 200 V at 5 mA cm^{-2} in 0.1 M ammonium pentaborate ……….………. 146

Figure 5.16 Transmission electron micrograph of an ultramicrotomed section of the Al-44 at.% Nb alloy after anodising to 200 V at 5 mA cm^{-2} in 0.1 M ammonium pentaborate……….. ………. 147

Figure 5.17 Transmission electron micrograph of an ultramicrotomed section of the sputtered niobium (set of specimens sputtered at 0.2 Pa argon) after anodising to 200 V at 5 mA cm^{-2} in 0.1 M ammonium pentaborate ………...……………..…………..… 147

Figure 5.18 Variation of anodic film parameters with niobium content in the alloy: (a) formation ratio (nm/V); (b) anodic oxide density; (c) total cation transport number ……………………. 153

Figure 5.19 Schematic diagram showing the migration rate (u_i) of the Nb^{5+} ions relative to Al^{3+} ions for the Al-21 at.% Nb and Al-31 at.% Nb alloys.……………………………….…………….. 155

Figure 5.20 Voltage-time response of the sputtered niobium and the Al-21 at.% Nb alloy during anodising at 5 mA cm^{-2} in 0.1 M ammonium pentaborate to 200 V after implanting with xenon 159

Figure 6.1 Equivalent circuit used to characterize the alloy/anodic oxide/ mercury drop system ………………………………………… 163

Figure 6.2 Experimental and simulated (line) EIS spectra obtained for the Al-21 at.% Nb alloy after anodising to different voltages at 5 mA cm^{-2} in 0.1 M ammonium pentaborate (oxide thicknesses of 44.2, 79.4 and 110.7 nm respectively) ……….. 164

Figure 6.3 Variation of reciprocal capacitance with $\delta\varepsilon_o^{-1}$ for the Al-Nb alloys with niobium content of 21 at.% to 44 at.% Nb after anodising to different voltages at 5 mA cm^{-2} in 0.1 M ammonium pentaborate ………………..…………………….. 167

Figure 6.4 Equivalent circuit model for a two layered oxide ……..…….. 167

Figure 6.5 Experimental EIS spectrum obtained for the Al-21 at.% Nb alloy after anodising to 150 V at 5 mA cm^{-2} in 0.1 M ammonium pentaborate ……………………………………… 168

Figure 6.6 Simulated EIS spectra for the equivalent circuits Rs(RC) and Rs(RC)(RC) for the oxide layers according to Table 6.2 169

Figure 6.7 Experimental and simulated (line) EIS spectra obtained for the Al-81 at.% Nb alloy after anodising to different voltages at 5 mA cm^{-2} in 0.1 M ammonium pentaborate (oxide thicknesses of 38.7, 66.4 and 194.1 nm respectively) ……….. 171

Figure 6.8 Variation of reciprocal capacitance with $\delta\varepsilon o^{-1}$ for Al-74 at.% Nb and Al-81 at.% Nb alloys after anodising to selected voltages at 5 mA cm^{-2} in 0.1 M ammonium pentaborate …..… 173

Figure 6.9 EIS spectra obtained for the Al-81 at.% Nb and Al-89 at.% Nb alloys and the sputtered niobium, after anodising to 60 V at 5 mA cm^{-2} in 0.1 M ammonium pentaborate. …………….. 173

Figure 6.10 EIS spectra obtained at different applied voltages, from +1 to –1 V for the sputtered niobium after anodising to 153 V at 5 mA cm^{-2} in 0.1 M ammonium pentaborate ………………….. 174

Figure 6.11 Variation of capacitance with voltage for the sputtered niobium after anodising to 153 V at 5 mA cm^{-2} in 0.1 M ammonium pentaborate ……………………………………... 174

Figure 6.12 Variation of relative dielectric constant (a) and deviation from pure capacitive behaviour (b) with niobium content for the Al-Nb system …………………………………………………….. 176

Figure 7.1 Bode plots obtained for the sputtered niobium after anodising to 12 V (a) and to 33 V (b) at 5 mA cm^{-2} in 0.1 M ammonium pentaborate. EIS spectra measured at different potentials in a borate buffer solution (filled circle = spectra at –0.75 V) …… 181

Figure 7.2 Bode plots obtained for the sputtered niobium after anodising to 54 V (a) and to 101 V (b) at 5 mA cm^{-2} in 0.1 M ammonium pentaborate. EIS spectra measured at different potentials in a borate buffer solution (filled circle = spectra at –0.75 V) ……………………………………………………... 182

Figure 7.3 Mott-Schottky plots obtained for the sputtered niobium after anodising to 12, 33, 54 and 101 V at 5 mA cm^{-2} in 0.1 M ammonium pentaborate (a). Enlarged plot of Figure 7.3.a (b). Capacitance was determined from EIS spectra measured in a borate buffer solution ……………………........................... 185

Figure 7.4 Complex plot obtained for the sputtered niobium specimen after anodising to 12, 54 and 101 V at 5 mA cm^{-2} in 0.1 M ammonium pentaborate. EIS spectra measured at –1.35 V in a borate buffer solution ………………………………………… 188

Figure 7.5 Bode Plots obtained for the Al-31 at.% Nb alloy after anodising anodised to 52 V (a) and for the Al-44 At.% Nb alloy after anodising to 31 V (b) at 5 mA cm^{-2} in 0.1 M ammonium pentaborate. EIS spectra measured in a borate buffer solution …………………...………………………... 189

Figure 7.6 Variation of capacitance with potential (a) and Mott-Schottky plot (b) for the Al-31 at.% Nb alloy after anodising to 52 V and for the Al-44 At.% Nb alloy after anodising to 31 V at 5 mA cm^{-2} in 0.1 M ammonium pentaborate. Capacitance was determined from EIS spectra in a borate buffer solution …….. 190

Figure 7.7 Bode plots obtained for the Al-81 at.% Nb alloy (a) and for the Al-89 at.% Nb alloy (b) after anodising to 11 V at 5 mA cm^{-2} in 0.1 M ammonium pentaborate. EIS spectra measured in a borate buffer solution (filled circle = spectra at –0.75 V) …………………………………………………… 192

Figure 7.8 Mott-Schottky plos obtained for the Al-81 at.% Nb and Al-89 at.% Nb alloys after anodising to11 V at 5 mA cm^{-2} in 0.1 M ammonium pentaborate. Capacitance was determined from EIS measured in a borate buffer solution …………………… 193

Figure 7.9 Bode plots for the Al-74 at.% Nb alloy after anodising to 51 V at 5 mA cm^{-2} in 0.1 M ammonium pentaborate. EIS spectra measured in a borate buffer solution (filled circle = spectrum at –0.75 V) …………………….……………………….…... 194

Figure 7.10 Bode plots obtained for the Al-81 at.% Nb alloy (a) and for the Al-89 at.% Nb alloy (b) after anodising to 31 V at 5 mA cm^{-2} in 0.1 M ammonium pentaborate. EIS spectra measured in a borate buffer solution (filled circle = spectra at –0.75 V) .. 195

Figure 7.11 Bode plots obtained for the Al-74 at.% Nb, Al-81 at.% Nb and Al-89 at.% Nb alloys after anodising to 51, 31 and 31 V respectively, at 5 mA cm^{-2} in 0.1 ammonium pentaborate. EIS measured in a borate buffer solution at the potentials were it was observed an inflection point in the phase angle ………… 197

Figure 7.12 Equivalent circuit adjusted to the EIS spectra obtained for Al-Nb alloys after anodising to higher voltages than 31 V when two time constants were observed …………………………… 198

Figure 7.13 Variation of capacitance and resistance with potential for the different elements of the equivalent circuits adjusted to the EIS spectra obtained for the Al-74 at.% Nb alloy after anodising to 51 V: (a) CPE and CPE1; (b) R1; (c) CPE2 …… 199

Figure 7.14 Mott-Schottky plot obtained for the Al- 74 at.% Nb alloy after anodising to 51 V at 5 mA cm^{-2} in 0.1 M ammonium pentaborate. Capacitance was determined from EIS spectra measured in a borate buffer solution ………………………… 201

Figure 7.15 Variation of capacitance and resistance with potential for the different elements of the equivalent circuits adjusted to the EIS spectra obtained for the Al-81 at.% Nb alloy after anodising to 31 V: (a) CPE and CPE1; (b) R1; (c) CPE2.…… 202

Figure 7.16 Variation of capacitance and resistance with potential for the different elements of the equivalent circuits adjusted to the EIS spectra obtained for the Al-89 at.% Nb alloy after anodising to 31 V: (a) CPE and CPE1; (b) R1; (c) CPE2.…… 203

Figure 7.17 Mott-Schottky plots obtained for the Al- 81 at.% Nb and Al-89 at.% Nb alloys after anodising to 31 V at 5 mA cm^{-2} in 0.1 M ammonium pentaborate. Capacitance was determined from EIS spectra measured in a borate buffer solution ……….…... 204

Figure 7.18 Complex plot obtained for the Al-74 at.% Nb alloy after anodising to 51 V at 5 mA cm^{-2} in 0.1 M ammonium pentaborate. EIS spectrum measured at –1.35 V in a borate buffer solution ……………………….................................... 205

Figure 7.19 Complex plots obtained for the Al-81 at.% Nb alloy (a) and for the Al-89 at.% Nb alloy (b) after anodising to different voltages at 5 mA cm^{-2} in 0.1 M ammonium pentaborate.EIS spectra measured at –1.35 V in a borate buffer solution ……... 206

Figure 7.20 Dependence of the donor concentration on the anodising voltage for the sputtered niobium and Al-Nb alloys after anodising at 5 mA cm^{-2} in 0.1 M ammonium pentaborate …... 208

Figure 7.21 Schematic diagram showing the thickness variation of the dielectric and space-charge layers in the anodic oxide film in the range of potential: $U_{FB} < U << V_f$ (V_f = final voltage of oxide formation) ……………………………………………… 210

Figure 7.22 Dependence of the donor concentration on the amount of niobium (aluminium) in the alloy for anodic oxides formed to 31/33 V 212

Figure A1.1 Equivalent circuit adjusted to the EIS spectra measured at –1.35 V for the sputtered niobium after anodising to selected voltages at 5 mA cm^{-2} in 0.1 M ammonium pentaborate …….. 222

Figure A1.2 Complex plots obtained for the sputtered niobium after anodising to selected voltages at 5 mA cm^{-2} in 0.1 M ammonium pentaborate. EIS spectra measured at –1.35 V in a borate buffer solution ………………………………………… 222

Figure A1.3 Equivalent circuit adjusted to the EIS spectra measured at –1.35 V in a borate buffer solution for the Al-Nb alloys after anodising to selected voltages at 5 mA cm^{-2} in 0.1 M ammonium pentaborate ……... 225

Figure A1.4 Complex plot obtained for the Al-74 at.% Nb alloy after anodising to 51 V at 5 mA cm^{-2} in 0.1 M ammonium pentaborate. EIS spectrum measured at –1.35 V in a borate buffer solution ………………………………………………... 225

Figure A1.5 Complex plots obtained for the Al-81 at.% Nb and Al-89 at.% Nb alloys after anodising to 31 V at 5 mA cm^{-2} in 0.1 M ammonium pentaborate. EIS spectra measured at –1.35 V in a borate buffer solution ………………………………………… 226

LIST OF TABLES

Table 1.1 Conduction mechanisms on dielectric materials [20] …………. 47

Table 2.1 Single energy-bond (M^{n+}-O) and cation migration rate for different aluminium alloys anodised in ammonium pentaborate. 63

Table 2.2 Slopes of the time-voltage curves and formation ratios, nmV^{-1}, for different sputtered aluminum alloys during anodising at 5 mA in ammonium pentaborate cm^{-2} …………………………… 68

Table 3.1 Chemical polishing solutions used on the niobium electrodes [135] ………………………………………………………….... 78

Table 3.2 Experimental parameters used for the EIS measurements……... 83

Table 3.3 Parameters used for adjusting the equivalent circuits with Zview software ………………………………………………… 83

Table 3.4 Experimental deposition conditions for magnetron sputtering .. 84

Table 3.5 Impedance of the common electrical elements used on fitting the EIS spectra [141]………………………………………….. 89

Table 4.1 Standard and experimental values of the binding energies for niobium and niobium oxides ………………………………….. 120

Table 5.1 Slopes of the voltage-time responses of the sputtered 100 at.% niobium and Al-Nb alloys during anodising at 5 mA cm^{-2} in 0.1 M ammonium pentaborate to 150 V ……………………… 134

Table 5.2 Results of RBS analyses of the Al-Nb alloys with 21 to 44 at.% Nb and the sputtered niobium after anodising at 5 mA cm^{-2} in 0.1 M ammonium pentaborate to 150 V ……………………….. 142

Table 5.3 Results of RBS analyses of the Al-74 at.% Nb alloy after anodising to 100 V and of the Al-81 and 89 at.% Nb alloys after anodising to 150 V at 5 mA cm^{-2} in 0.1 M ammonium pentaborate ………..…………………………………………...… 144

Table 5.4 Total cation transport number and formation ratios (nm/V) calculated for the Al-Nb alloys and the sputtered niobium after anodising to 200 V at 5 mA cm^{-2} in 0.1 M ammonium pentaborate. Oxide thicknesses measured from ultramicro-tomed sections ………………………………………………... 148

Table 5.5 Anodic oxide densities formed on the Al-Nb alloys obtained from the values of pure oxides by assuming an average value weighted by the oxide composition ……………………………. 150

Table 5.6 Oxide densities calculated from RBS and TEM data and from the values of pure oxides ………………………………………. 150

Table 5.7 Anodising efficiency evaluated by comparing the charge passed during anodising and number of oxidised cations determined by RBS for the Al-Nb alloys and the sputtered niobium after anodising at 5 mA cm-2 in 0.1 M ammonium pentaborate to 150 V..………………….……………………………………… 151

Table 6.1 Values obtained with the fitting $R_S(CPE_f-R_f)$ on the EIS spectra measured on Al-Nb alloys (21 to 44 at.% Nb) after anodising to different voltages at 5 mA cm^{-2} in 0.1 M ammonium pentaborate . Oxide thicknesses calculated from anodising charge ……………………………………………………….. 165

Table 6.2 Dielectric constants, oxide resistivities and corresponding time constants for pure anodic alumina and for the mixed oxide $(Al_2O_3)0.29(Nb_2O_5)$……….…………………………………… 168

Table 6.3 Values obtained with the fitting $R_S(CPE_f-R_f)$ on the EIS spectra measured on the Al-74 at.% Nb and Al-81 at.% Nb alloys after anodising to different voltages at 5 mA cm^{-2} in 0.1 M ammonium pentaborate. Oxide thicknesses calculated from anodising charge ..……………………………………………... 172

Table 7.1 Dielectric constants for the sputtered niobium after anodising to selected voltages at 5 mA cm^{-2} in 0.1 M ammonium pentaborate. Capacitances were determined from EIS spectra in a borate buffer solution and oxide thicknesses calculated from anodising charge ……………………………….................. 183

Table 7.2 Donor concentrations (N_D)and flat band potentials (U_{FB}) for the sputtered niobium after anodising to selected voltages at 5 mA cm^{-2} in 0.1 M ammonium pentaborate and analysed in a borate buffer solution ………………………….………………………… 186

Table 7.3 Capacitance (C) and exponent (n) of the CPE elements of the $R_s(CPE)$ circuit adjusted to the EIS spectra obtained for the sputtered niobium after anodising to selected voltages at 5 mA cm^{-2} in 0.1 M ammonium pentaborate ………..……… 186

Table 7.4 Donor concentrations (N_D) and flat band potentials (U_{FB}) for the Al-81 and Al-89 at.% Nb alloys after anodising to11 V at 5 mA cm^{-2} in 0.1 M ammonium pentaborate and analysed in a borate buffer solution …………………….......................... 193

Table 7.5 Values of CPE (capacitance and n parameter) obtained from the fitting of the EIS spectra ajusted to an $R_s(CPE)$ circuit for the Al-Nb alloys of high niobium content after anodising to

selected voltages at 5 mA cm^{-2} in 0.1 M ammonium pentaborate ………………………………………………………. 197

Table 7.6 Dielectric constants for the Al-74 at.% Nb, Al-81 at.% Nb and Al-89 at % Nb alloys after anodising to selected voltages at 5 mA cm^{-2} in 0.1 M ammonium pentaborate. Capacitances were determined from EIS spectra...…………………………………. 198

Table 7.7 Donor concentrations (N_D) and flat band potentials (U_{FB}) for the Al-74 at.% Nb, Al-81 at.% Nb and Al-89 at % Nb alloys after anodising to selected voltages at 5 mA cm^{-2} in 0.1 M ammonium pentaborate and analysed in a borate buffer solution 204

Table 7.8 Donor concentrations (N_D) and flat band potentials (U_{FB}) for the sputtered niobium and Al-Nb alloys of high niobium content after anodising to selected voltages at 5 mA cm^{-2} in 0.1 M ammonium pentaborate and analysed in a borate buffer solution ………………………………………………………… 208

Table A1.1 Coefficient of diffusion of H^+ in anodic niobia formed in 0.1 M ammonium pentaborate in contact with a borate buffer solution of pH 8.8 …………………………………………….. 223

Table A1.2 Coefficient of diffusion of H^+ in Al-Nb oxides formed in 0.1 M ammonium pentaborate in contact with a borate buffer solution of pH 8.8 …………………………………………….. 226

ABSTRACT

Anodic oxide films of aluminium and tantalum have been widely used as dielectric materials in the capacitor industry. Niobium is a metal that can also be anodised and it has been considered as a possible substitute for tantalum because of its similar electrochemical behaviour. However, anodic niobia (Nb_2O_5) has a higher dielectric constant than tantala (Ta_2O_5), which is advantageous for use as a dielectric because a higher capacitance can be achieved with the same oxide thickness. Furthermore, niobium is more abundant than tantalum and this usually means a reduced material price. However, niobium has some disadvantages, like semiconducting rather than dielectric properties, higher leakage current and lower potential of dielectric breakdown. The combination of aluminium with niobium may be a route to reduce these factors, and the magnetron sputtering technique is ideal for such a study since the deposited alloys can form a single solid solution over the entire concentration range.

In this study, anodising of Al-Nb alloys, containing 21 to 89 at.% niobium and niobium, prepared by magnetron sputtering, has been undertaken at a constant current density of 5 mA cm^{-2} in 0.1 M ammonium pentaborate electrolyte. The resultant anodic films were analysed by SEM, TEM and RBS to determine the film composition and thickness. Anodic oxides with a wide range of thicknesses were analysed by EIS to verify the dielectric or semiconducting properties. Xenon implantation was carried out to determine the cation and anion transport numbers and relative migration rate of incorporated species.

The results have shown that the anodic oxides are featureless, with uniform composition and of aluminium and niobium contents similar to those of the alloys. The Al-21 at.% Nb and Al-31 at.% Nb alloys, anodised to 150 V revealed a very thin alumina layer close to the oxide/electrolyte interface due to the lower migration rate of niobium cations relative to aluminium cations.

The dielectric constants of the oxides were determined by EIS using a mercury drop contact for alloys of 21 to 81 at.% niobium, and the results showed a linear trend, proportional to composition, in agreement with the dielectric constants of Al_2O_3 and Nb_2O_5. The results obtained for niobia and Al-Nb oxides with niobium content above 74 at.% Nb revealed n-type semiconductor properties when analysed in a borate buffer solution. The carrier concentration was in the range of 10^{18}-$10^{19}cm^{-3}$. Thus, the results demonstrate that anodic oxides formed on sputtered Al-Nb alloys up to 44 at.% of niobium behave as dielectric materials and represent a valid alternative for capacitors.

DECLARATION

No portion of the work referred to in the thesis has been submitted in support of an application for another degree of qualification of this or any other university or other institute of learning.

COPYRIGHT STATEMENT

The author of this thesis (including any appendices and/or schedules to this thesis owns any copyright in it (the “Copyright”) and she has given The University of Manchester the right to use such Copyright for any administrative, promotional, educational and/or teaching purposes.

Copies of this thesis, either full or in extracts, may be made only in accordance with regulations of the John Rylands University Library of Manchester. Details of these regulations may be obtained from the librarian. This page must form part of any such copies made.

The ownership of any patents, designs, trade marks and any and all other intellectual property rights except for the Copyright (the “Intellectual Property Rights”) and any reproductions of copyright works, for example graphs and tables (“Reproductions”), which may be described in this thesis, may not be owned by author and may be owned by third parties. Such Intellectual Property Rights and Reproductions cannot and must not be available for use without the prior written permission of the owners of the relevant Intellectual Properties Rights and/or Reproductions.

Further information on the conditions under which disclosure, publication and exploitation of this thesis, the Copyright and any Intellectual Property Rights and/or Reproductions described in it may take place is available from the Head of School of Materials (or the Vice-President) and the Dean of The Faculty of Life Sciences, for Faculty of Life Sciences’ candidates.

ACKNOWLEDGEMENTS

I would like to express my gratitude to:

Professor G.E. Thompson for the provision of facilities, for his supervision, suggestions and discussion of this work.

Dr Carmen Rangel for the provision of facilities, for her supervision, suggestions and discussion of this work.

Dr Peter Skeldon for his helpful suggestions and advice on this work.

Colleagues of the INETI- Electroquímica de Materiais for their general assistance, advice and support.

Colleagues of the Corrosion and Protection Centre, in particular to Loreto Iglesias-Rubianes and Sonia Mato, for their general assistance, advice and support.

Dr. Q. Lu for the preparation of specimens by TEM.

Dr. Eduardo Alves and Carlos Marques from ITN (Instituto Tecnológico e Nuclear - Sacavém - Portugal) for the analysis of RBS spectra.

Mr. D. Moore for his assistance with the technique of electron microscopy.

Finally, to INETI (Instituto Nacional de Engenharia, Tecnologia e Inovação- Lisbon) and to The University of Manchester – Corrosion and Protection Centre for the provision of facilities and financial support.

First it was a dream, then it was a thesis…

I would like to dedicate this thesis to my family

CHAPTER 1

INTRODUCTION AND LITERATURE REVIEW OF ANODIC OXIDES ON VALVE-METALS

1.1 Introduction

Anodic oxidation is the process of forming an oxide (M_xO_y) on a metal surface (M) by applying an electrical current or potential through a cell containing a suitable electrolyte. The industrial application of these oxides is various; for example, they have been used to improve corrosion resistance of metal surfaces, applied in the electronic industry as dielectric materials or used in decorative surface finishing. The process was first developed on aluminium in 1923, and it is widely at the present time [l].

The metals that can be anodised belong to the so-called valve-metals group. The name is related to the first use of these metals in electronic tubes as hot filaments [2] or due to the rectifying properties of the oxide-coated electrodes [3]. The main feature of the metals is the ability to form a high resistance protective oxide film that grows when a high electrical field is applied. Aluminium, tantalum and niobium are the most representative valve-metals, even though other metals, e.g. zirconium, hafnium, tungsten and titanium also display this behaviour [3, 4].

The oxide is formed with cations from the metal surface and oxygen ions from the electrolyte. Depending on the experimental growth conditions, the oxides show

different characteristics and are divided in two main groups. The first encompasses the barrier films: they are compact films, with high electric and ionic resistivities and are formed in neutral or slightly alkaline electrolytes. The second group embraces the porous films: they are formed generally in acid electrolytes with a porous region extending from the film/electrolyte interface to close to the metal surface. Both types are used in industrial applications; for example, the barrier films are used on the electronic industry and the porous films are used as coatings to improve corrosion or mechanical resistance. Anodising processes on aluminium and its alloys are the most studied because of the extensive practical applications of these materials in the architectural, food, electronic or transport industries [1].

This chapter provides the Literature Review on the anodic oxidation of the valve-metals, including the oxide growth mechanisms and the electrical properties of the oxides. Special emphasis is given to the aluminium and niobium since the aim of this thesis is the study of the anodic behaviour of Al-Nb metastable alloys.

1.2 Anodic oxidation of valve-metals

1.2.1 The fundamental equation of the high-field model

Anodic oxides grow when the electrical field applied is sufficiently high to promote ion migration. The field strength necessary for this process is in the range of 10^6-10^7 V cm^{-1} [5]. This field strength is very high and it normally causes dielectric breakdown on bulk oxides [3]. When a high electric field is applied to a valve-metal, the growth of the oxide shows a typical potential-current response with three distinct zones (Figure 1.1):

Zone I- growth of the oxide- the electric field applied is sufficiently high to promote ion formation and migration through the oxide and, in consequence, new oxide layers are formed on the metal surface;

Zone II- leakage current- when the electric field applied is not sufficient to promote ion formation and migration through the

oxide, other electronic processes can occur including formation of oxygen bubbles or other leakage processes related with structural defects or foreign species;

Zone III- hydrogen evolution- when a cathodic current or potential is applied, hydrogen evolution is the process usually observed and it depends on the physical and chemical characteristics of the film, electrolyte and metal purity.

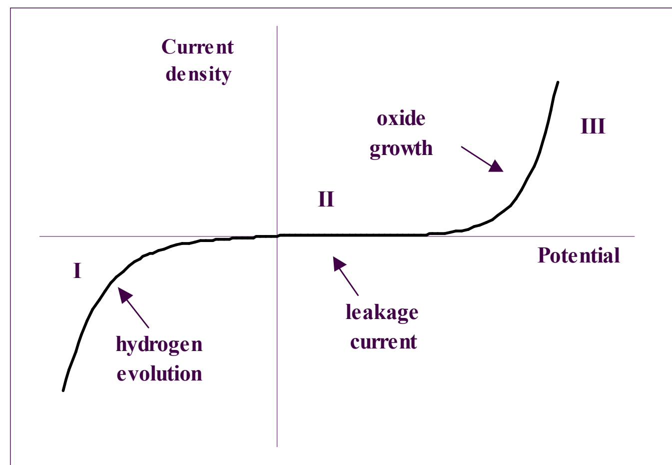

Figure 1.1 Characteristic voltage-current response of the valve-metal/ oxide/electrolyte system [3].

The oxide growth obeys to the following equation:

$$i = i_0 \exp(\beta\, E_\delta) \quad (1.1)$$

where,

i = ionic current density,

$E_\delta = \dfrac{V}{\delta}$, = electrical field strength (≈10^7 Vcm^{-1}),

V = potential across the oxide,

δ = oxide thickness,

and i_o and β are constants at a fixed temperature.

Equation 1.1 was empirically proposed by Günthershultz and Betz (1934) and is usually referred as the fundamental equation of the high-field model (HFM) [3-7]. As

already introduced, the oxide forms by ionic migration across the oxide, with cations from the metal and oxygen ions from the electrolyte. The ionic migration in crystalline oxides occurs through the movement of defects in the lattice. These defects are anion or cation vacancies and/or interstitial ions. Most of the anodic oxides formed on valve-metals are amorphous, but similar ionic movements have been considered [3]. The vacancies or interstitial ions within the oxide are related to the lack of order in the network, even though the oxides formed are stoichiometric. The movement of a vacancy, between two equilibrium positions, is related to the energy barrier (W) necessary to jump that distance and it is proportional to an exponential factor, exp(-W/kT). When an electrical field is applied, the energy barrier reduces in magnitude to an extent given by:

$$W(E_\delta) = W_o - qaE_\delta \tag{1.2}$$

where,

W_o= energy barrier in absence of the electrical field,

q = charge of the moving ion/vacancy,

a = distance between the minimum and the maximum of the energy barrier,

E_δ = electrical field strength.

When a high electrical field is applied, the ionic movement proceeds in the direction of the field; movement in the reverse direction can be neglected and, therefore, the ionic movement is related to ionic current density by:

$$i = 2\,a\,n\,\nu \exp\left[-\left(W_0 - qaE_\delta\right)/kT\right] \tag{1.3}$$

where n is the number of ions per unit volume and ν is the vibrational frequency of the ions. Comparing this equation with equation 1.1, the constants i_o and β correspond to:

$$i_0 = 2\,a\,n\,\nu \exp\left(-W_0/kT\right) \tag{1.4}$$

and

$$\beta = qa/kT. \tag{1.5}$$

The equation of the high field model is not sufficient to characterize anodic oxide growth because it does not specify the rate determining step and other features that have been observed on anodising valve-metals, including transient behaviour or anomalous Tafel behaviour. Different models have been proposed to include these features, based on the fundamental equation of the high field strength.

1.2.2 The rate-determining step and anomalous behaviour

As anodising is a complex process, where ions formed at interfaces (metal/oxide and oxide/electrolyte) migrate across the oxide, the rate-determining step could be either at the interfaces or in the bulk oxide. Verwey, as well as Güntherschulze and Betz, proposed that the rate-determining step is the ionic migration through the oxide, according to the equations presented earlier (equations 1.1 to 1.5) [3]. Mott and Cabrera proposed that the rate-determining step is located at the metal/oxide interface. In this case, the fundamental equation is the same but the parameters have a different meaning, according to:

$$i = n'\nu' \exp\left[-\left(W'_0 - qa'E_\delta\right)/kT\right] \quad (1.6)$$

where,

n' = surface density of the moving ions/vacancies at the interface metal/oxide,

ν' = vibrational frequency of an atom at the metal surface,

W'_o = energy barrier between the metal and the oxide in absence of electrical filed,

q = charge of the moving ion/vacancy,

a' = equilibrium distance between the equilibrium position in the metal and the activated position in the oxide.

Other models have been proposed that are concerned with deviations from the fundamental equation of the HFM (High Field Model). Tantalum and niobium are two metals that can show anomalous Tafel behaviour. According to the HFM equation, the slope ($\delta \ln i/\delta E_\delta$) should be inversely proportional to temperature, but this variation is not observed. Young (1963) proposed a change to the fundamental equation, according to:

$$i = i_o \exp(\beta E_\delta - \gamma E_\delta^2) \quad (1.7)$$

where β and γ are constants [4]. The explanation proposed by Young is related to variation of the jump distance, a, with the temperature. This variation should be balanced by the temperature (included in β) and, consequently, the value of $\delta \ln i / \delta E_\delta$ is constant. Later, Young and Zobel (1966) proposed a second equation:

$$W(E_\delta) = W_o - \gamma E_\delta^{1/2} \quad (1.8)$$

where γ is a constant characteristic of the system [8]. The variation proposed is based on the model of Poole-Frenkel for electronic currents. More recently, Li and Young (2000) found that niobium oxides grown at different current densities, in the range of a few mA cm^{-2}, show a non-linear dependence of ln(i) with E_δ [9]. This feature was observed on oxides grown in phosphoric electrolytes in which electrolyte species contaminate the oxide layer formed at the oxide/electrolyte interface. Therefore, the non-linear behaviour was interpreted as a consequence of the oxide composition and not a characteristic of the pure oxide. The same feature had first been observed for tantalum oxide [10, 11].

Wang and Hebert proposed a mathematical model that is also derived from the HFM equation [12]. The model is based on the movement of a defect cluster that occurs by the coupled movement of an oxygen vacancy and the metallic ions. The cluster is formed by an oxygen vacancy, where the charge is partially compensated by the inward displacement of the surrounding oxygen ions (Figure 1.2). A gap is formed between the dislocated layer of oxygen atoms and the second layer of oxygen atoms that surrounds the cluster. This allows the cations to move more freely as occurs in the liquid state. When the electric field is applied, the vacancy moves and the positive ions move with it. The fundamental equation for this model takes into account the size, the number and the jump frequency of the defect clusters and, once more, it is an exponential function of the current (i) with (E_δ). The parameters obtained with this model were used to calculate the transport number and the reciprocal field coefficient for the oxides of tantalum, niobium and tungsten. The calculated results were acceptable within an experimental error less than 10 %. This

model also explains the increase of the cation transport number with increase of field strength, which is an experimental feature observed on anodising some metals where the transport number depends on the electric field, oxide permittivity and cluster radius.

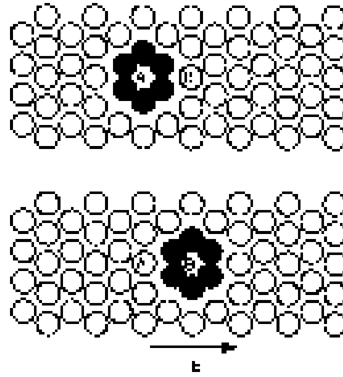

Figure 1.2 Schematic diagram showing the displacement of a vacancy centered cluster when the vacancy moves from A to B [12].

1.2.3 Anodising techniques

The most common technique for growing the oxides is by applying a constant current density, normally in the range of a few mA cm^{-2}. When the electrolytes are neutral or slightly alkaline, the growth efficiency of the anodising process is close to 100%. If the growth efficiency stays constant and the oxides form with uniform composition, a constant growth rate (nmV^{-1}) is obtained. Then Faraday's law can be used to calculate the oxide thickness, δ, if the oxide species and the oxide density are known, according to the following equations:

$$\int i\,dt = \frac{Q}{A} \qquad (1.9)$$

$$\delta = \frac{QM}{AnF\rho} \qquad (1.10)$$

$$\Leftrightarrow \frac{d\delta}{dt} = \frac{M}{nF\rho} i \qquad (1.11)$$

where i, t, Q, A, M, n, F, and ρ, are respectively, the constant current density, the anodising time, the anodising charge, the electrode area, the oxide molecular weight, the number of changed electrons, the Faraday constant and the oxide density. The relation between voltage (V) and the current density (i) is now given by:

$$\frac{dV}{dt} = \frac{dV}{d\delta}\frac{d\delta}{dt} \tag{1.12}$$

$$\frac{dV}{dt} = \frac{dV}{d\delta}\frac{M}{nF\rho}i \,. \tag{1.13}$$

The introduction of the equation for high field conduction, for a constant dV/dδ, gives the final equation:

$$\frac{dV}{dt} = \frac{1}{\beta}\ln\left(i/i_o\right)\frac{M}{nF\rho}i \,. \tag{1.14}$$

Equation 1.14 predicts the variation of dV/dt with i $\ln(i/i_o)$; however a linear increase of the slope dV/dt with current density is usually observed since $i_o << i$, and, consequently, the variation $\ln(i/i_o)$ is only a few percent of i [13].

Anodic films formed at constant voltage have a continuous variation on the growing rate. The electrical field strength is higher at the beginning of anodising and decreases with increase of the oxide thickness until the field is not sufficient to induce ionic migration, subsequently the leakage processes then dominate. Now the applied voltage (V) is constant and the current density changes with time. The current density, after conversion to thickness, is given by:

$$\frac{d\delta}{dt} = \frac{V_M}{i_o nF}\exp\beta\left(\frac{V - V_0}{\delta}\right) \tag{1.15}$$

where V_o is the initial voltage and V_M is the molar volume. This equation does not have a precise mathematical solution, but a close solution gives a linear correlation

of the reciprocal of the oxide thickness with the logarithm of the anodising time [7, 13, 14]:

$$\frac{1}{\delta} = f(\ln t) \qquad (1.16)$$

If the fractional change in thickness is too small, a linear law δ versus ln(t) is observed rather than the inverse one [13].

Both anodising processes, at constant current or constant voltage, are used in industrial applications because the anodic films produced can have the similar required properties and performance. The potentiodynamic technique is mainly used in scientific studies of the growth mechanisms of the oxides. Since galvanostatic conditions give a linear ramp voltage, the application of a voltage ramp should give a constant current density (i_{st}). The high-field equation can now be expressed as:

$$V = \beta^{-1} \ln \frac{i}{i_o} \left[\delta_o + F_c \int i_{st}\, dt\right] \qquad (1.17)$$

where F_c is the conversion factor of charge to thickness $(\frac{M}{nF\rho})$. The voltage (assuming V_o= 0) is now given by:

$$V = \frac{dV}{dt}\ t \qquad (1.18)$$

where dV/dt corresponds to the voltage sweep rate (s). The mathematical development of equations 1.17 and 1.18, assuming δ_o equal to zero, gives the final equation:

$$i_{st} \ln \frac{i_{st}}{i_o} = \frac{\beta\, nF}{V_M} s \qquad (1.19)$$

where i_{st} is the stabilized current density and s is the potential sweep rate; once more as $i_o << i_{st}$, the influence of $\ln(i_{st}/i_o)$ is negligible when compared with i_{st} [13], so the variation of $\ln(i_{st})$ with ln(s) should be linear with a slope equal to one.

1.2.4 Structure and composition of anodic oxide films

Most of the valve-metals, like aluminium, tantalum, niobium and tungsten, form amorphous oxides when anodised. The exceptions are hafnium and zirconium that are crystalline and titanium that shows a crystalline structure when anodized above 48 V [4, 15]. Amorphous structures are formed as a continuous random network with a certain short-range order due to the stoichiometry of the oxides. Amorphous alumina comprises units of AlO_4, AlO_5 and AlO_6 polyhedra with a bond length (M-O) of 0.2 nm, arranged in random orientations and sharing oxygen atoms at the vertices [15]. The distinction between amorphous and microcrystalline structure is difficult; for example, anodic Ta_2O_5 shows a structure that is not entirely amorphous, but contain microcrystalline regions of dimensions of a few nanometres [16].

Various processes can induce a crystalline structure, for example extended anodising voltages or high temperature. Shimizu et al. [17] found that when aluminium was anodised to voltages higher than 100 V, islands of crystalline alumina γ'-Al_2O_3 were formed. This crystalline structure is an intermediate form between amorphous and crystalline γ-Al_2O_3, but with more disorder on the cationic lattice [17, 18]. Shimizu et al. also found that high anodising temperature increases the amount of crystalline alumina but, on the other hand, the electrolyte concentration or pH do not affect the alumina structure significantly [17]. Freitas et al. studied the anodising process on pure niobium electrodes and found that films grown for extended periods of time (> 2000 s) show a crystalline pattern when analysed by X-ray diffraction [19].

Anodic films on valve-metals form with the metallic ions in the most stable valence state. This means that Al_2O_3, Ta_2O_5, Nb_2O_5 or ZrO_2, etc., are found on the corresponding anodised metals [15]. However, as oxides are grown in electrolytes, there are also electrolyte-derived species that contribute to the oxide composition. These incorporated species are usually present at low concentrations, but that can be

sufficient to change some oxide characteristics like the dielectric properties [20] or the ionic mobility and growth rate [4].

1.2.5 Flaws in anodic oxide films

Flaws are always present in anodic films and they are related to local sites where film material is modified compared with the adjacent film material. Differences in the structure, composition or mechanical stresses are factors that can promote the formation of flaws [21]. The flaws are termed mechanical flaws when they are the result of relief of stresses in the film grown over mechanical surface defects. They are usually associated with mechanical surface treatments and they can be healed on anodising, and reduced to an acceptable minimum [22]. This type of film is present in air-formed films and they provide preferential sites for pitting processes [22,23]. A further type of flaws is associated with impurities present in the metal composition and is termed residual flaws. The oxide formed above those impurities is different due to the micro-variation in the film structure and composition [21]. Such flaws can also be formed during anodising and usually are associated with oxygen bubbles [21]. For example, a pure alumina film of 200 nm thickness has a flaw density of the order of $10^6/cm^2$ [22]. If the flaws extend over the oxide thickness, the film will crack or detach from the surface, thereby losing its properties. Flaws are also associated with alloying elements because these elements can change the oxide structure or can promote the formation of oxygen bubbles. It is also usually observed that flaws and crystalline alumina are related because the flaws increase the resistance to ion migration, and crystalline alumina may form due to local Joule heating effects [16].

1.2.6 Ionic migration and transport numbers

In order to understand how electrolyte species are incorporated into the anodic oxide it is necessary knowledge of the ionic movement through the oxide when an electrical field applied is required. The migration process has been studied employing immobile and inert markers that do not interfere with ionic movement. It has been found that noble gases atoms (Ar, Xe, Kr) are excellent markers when implanted under appropriate experimental conditions in a thin pre-formed anodic

oxide on the metal surface. The markers establish the reference to define the interfaces from which the oxide grows and the corresponding thickness fraction formed at each interface. The total cation (t^+) and the total anion transport number (t^-) can be calculated according to:

$$t^+ = \frac{\delta'}{\delta_t}\ ;\ t^- = \frac{\delta''}{\delta_t} \tag{1.20}$$

where δ_t is the total oxide thickness, δ' is the oxide thickness formed at the oxide/electrolyte interface and δ'' is oxide thickness formed at the metal/oxide interface. The transport number is defined as the fraction of the total ionic current, (i_t), carried by a specific type of ion and the total ionic current is the sum of the cation current (i^+) and the anion current (i^-).

Amorphous anodic oxides grow with the movement of both anion and cation species across the film; on the other hand, crystalline oxides, like HfO_2 or ZrO_2, grow only through movement of the anion species from the electrolyte to the metal surface. Anodic alumina formed at an efficiency close to 100 %, reveals that 40 % of the total thickness is formed at the oxide/electrolyte interface and 60 % is formed at the metal/oxide interface. Thus the cation transport number is 0.4 and the anion transport number is 0.6 (Figure 1.3) [24, 25].

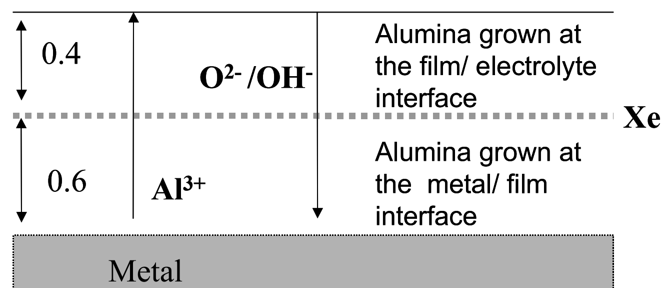

Figure 1.3 Schematic diagram of a marker experiment for anodising aluminium, showing the thickness fraction formed at each interface [24].

Pringle studied the anodising on tantalum and niobium and found that the corresponding transport numbers are similar, respectively being 0.249 for tantalum and 0.239 for niobium [26, 27]. Pringle also studied the anodising of tantalum with isotopic tracers of ^{18}O and ^{182}Ta. These experiments showed, quoting Pringle, that "*all the atoms in the oxide participate in the migration process, and that they all participate continuously, so that a thickening of the oxide film by even one atom layer requires the movement by all the atoms in the film* [28].' This means that films grow with some order; when an ion is incorporated at one of the interfaces and moves inside the oxide it takes the place of another ion that had moved inward. This perfect movement should give perfect oxides, but defects are always present due to the microscopic variations in migration related with compositional or structural variations, interfering species, interfacial effects or even mechanical effects.

The experimental conditions used to form the anodic films have also influence on the ionic transport numbers. Lu et al. found that the transport numbers of anodic tantala increase with increase of the anodising current density in the range of 0.01 to 10 mA cm^{-2}. They also decrease with increase of electrolyte temperature up to 85 ºC [29].

1.2.7 Incorporation of foreign species into anodic oxide films

During anodising, the anodic oxides can incorporate foreign species derived from the electrolyte, surface treatments or even from the anodised metal. The electrolyte species are incorporated at the oxide/electrolyte interface and they may be immobile, move inward or mobile outward, depending on their response to the electrical field. Contaminant species derived from the metal surface treatments are frequent; for example, after electropolishing, species are incorporated on the initial oxide layer that is always present on the metal surface. One common contaminant is the chloride ion, which can influence the anti-corrosion properties. The incorporated species, even at low concentrations, can have an influence on the anodic properties because, as the anodic process is a process with some order, the species can move with the electrical field and form layers of different composition within the bulk or at the surface, which can affect the global behaviour of the oxide. The composition depth profiles of these layers contribute to understanding of the migration process. For example, the depth profile of an immobile species determines the fraction of the

oxide thickness grown at the oxide/electrolyte interface, and consequently, the transport number can be calculated.

Wood *et al*. proposed a model for the incorporation of the species derived from anions of dilute electrolytes (≈ 0.1 M) in anodic alumina films [24]. The model uses the double charge density (σ), calculated from the oxide dielectric constant (ε) and the electrical field strength (E_δ), and the contaminant surface concentration ($\Gamma_{x,i}$), according to:

$$\sigma = \varepsilon_r \, \varepsilon_o \, E_\delta \tag{1.21}$$

$$\sigma = \Sigma \, \Gamma_{x,i} \, z_i \, e \tag{1.22}$$

where i is the anionic species which contain x atoms of the element X, z_i is the anion valence of i and e is the electron charge. The model assumes that one oxide monolayer (δ_m) is formed at each interface, and further, that the adsorbed species at the oxide/electrolyte interface are consumed and immediately replaced by a contaminant layer, in a way that this process does not affect the oxide growth. The model gives the following equations:

a) species moving outward,

$$\left(\frac{N_x}{N_{Al}}\right)_{out} = \left(1 - \frac{t^-}{\eta}\right) \Gamma_{x,i} \; n_{x,i} \frac{1}{\delta_m} \frac{M}{2\rho N} \tag{1.23}$$

b) species moving inward,

$$\left(\frac{N_x}{N_{Al}}\right)_{in} = \Gamma_{x,i} \; n_{x,i} \frac{1}{\delta_m} \frac{M}{2\rho N} \tag{1.24}$$

where,

N_x = number of atoms x in the total oxide thickness,

N_{Al} = number of aluminium atoms in the total oxide thickness,

η = growth efficiency (100 % = 1), where $\eta < 1$ indicates ejection of Al^{3+} ions into solution,

$\left(1-\frac{t^{-}}{\eta}\right)$ = fraction of total thickness formed at the interface oxide/electrolyte,

t^{-} = anionic transport number O_2^{-}/OH^{-} (0.6),

t^{+} = cationic transport number of Al^{3+} (0.4)

$\Gamma_{x,i}$ = concentration of the adsorbed specie i which is incorporated in the monolayer, δ_m formed at the oxide/electrolyte interface,

$n_{x,i}$ = n° of atoms x present on the absorbed specie i,

M = molecular weight Al_2O_3 ($\approx$ 102 g),

ρ = oxide density ($\approx \rho$ Al_2O_3),

N = Avogrado's number,

$\left(\frac{2\rho N}{M}\right)$ = conversion factor of the volume (area x δ_m) to aluminum atoms.

Thus, the model shows that, for contaminant electrolyte species moving outward, an amount of absorbed electrolyte species corresponding to the surface concentration, $\Gamma_{x,i}$, is incorporated at each monolayer of anodic oxide formed at the oxide/electrolyte interface. Thus, to calculate the ratio, $(N_X/N_{Al})_o$, it is only necessary to multiply by the fraction of film formed at the oxide/electrolyte interface. On the other hand, species moving inward are incorporated at the oxide/electrolyte interface, but contaminate both layers, formed at each interface, due to the inward movement. Futhermore, the model assumes that the contribution of the electrolyte species absorded is similar for both interfaces and equivalent to the surface concentration after converting to unit volume.This model was applied and compared with experimental results obtained on anodising high purity aluminium in different neutral or slighlty alkaline electrolytes. The results for the quotient between the fraction (N_X/N_{Al}) measured and predicted by the model are in the range of 0.40 to 1.57 for the most common anions, including SiO_3^{2-}, CrO_4^{2-}, HPO_4^{2-} WO_4^{2-}or $B_4O_7^{2-}$ [24].

The contaminated oxide layer thickness to the total oxide layer thickness ratio can be used to calculate the relative migration rates of the contaminant species to the

corresponding ion constituent of alumina that moves in the same direction. Species that move outward have a migration rate relative to Al^{3+}, u_{out}, given by:

$$f = 1 - \frac{1}{\eta}\left(t^- + u_o\, t^+\right). \tag{1.25}$$

Species that move inward have a relative migration rate to O^{2-}/OH^-, u_{in}, given by:

$$f = 1 - \frac{t^-}{\eta}\left(1 - u_{in}\right) \tag{1.26}$$

Figure 1.4 shows a schematic diagram of anodic oxides contaminated with different electrolyte species which are incorporated during anodising [24].

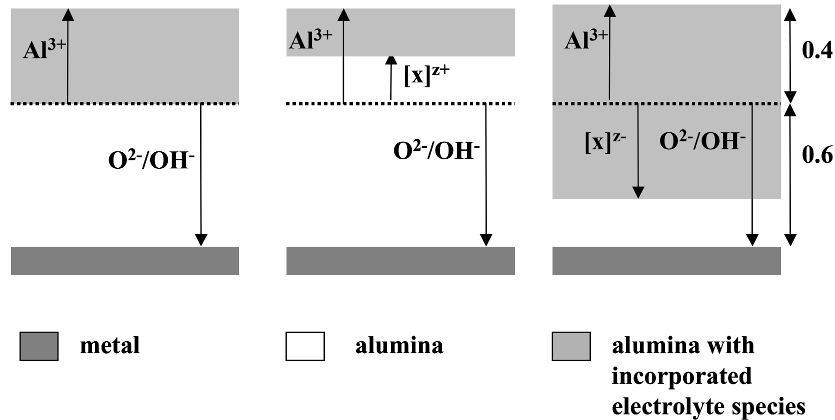

Figure 1.4 Schematic diagram of the anodised alumina contaminated with electrolyte species with different movements: (a) immobile species; (b) outward species; (c) inward species [24].

The movement of the anionic electrolyte species outward is probably related to the transformation to positively charged species [30]. In mixed electrolytes, the fraction of the contaminated thickness is equivalent to the one formed in electrolytes with only one anion species. A study of the mixed electrolyte, 0.1M molybdate + 0.1 M tungstate, showed this feature but, the amount of tungstate species was much higher (three times higher) than the molybdate species. This was interpreted by assuming

that the tungstate species are preferentially absorbed at the oxide/electrolyte interface and then incorporated into the oxide [30]. Immobile species, like borate or silicate species in aqueous electrolytes, can be used as markers to determine the oxide thickness formed at the oxide/electrolyte interface [31]. The depth profile of these incorporated species requires the use of the techniques like GDOES (Glow Discharge Optical Emission Spectrocospy) or SIMS (Secondary Ion Mass Spectroscopy) due to their low concentration [31-33].

Shimizu et al studied the contaminant effect of chloride ions in high purity Al surface, after electropolishing in an acid perchloric-ethanol mixture and then anodising in 0.1 M ammonium pentaborate. The oxide depth-profile was carried out by SIMS and a peak, correspondent to an oxide layer enriched with Cl^-, was revealed. This layer was located inside the oxide fraction formed at the metal/oxide interface, which means that Cl^- ions move inward at a lower migration rate than O^{2-}/OH^- ions The contaminated layer showed a broadening effect, when its thickness was compared with the initial contaminated thickness. At the beginning of the anodising process, the contaminated layer thickness is equivalent to the initial air-formed oxide layer that is always present on the metal surface [32]. The broadening effect was interpreted by the authors as a consequence of the degree of surface roughness together with microscopic variation in the migration rate. The same authors studied the effect of dipping the electropolished metal surfaces in a hot CrO_3-H_3PO_4 solution before anodising. The depth profiles were determined by GDOES and it was found that Cr^{3+} species move outward with a relative migration rate to Al^{3+} of 0.74 and PO_4^{3-} species move inward with a relative migration rate to O^{2-}/OH^- of 0.51 [33].

1.3 Electric behaviour of anodic oxide films

1.3.1 Fundamentals of the electrical properties of solid materials

The electrical properties of solid materials, including oxides, are divided into three main categories: conductors, semiconductors and insulators. This division is based

on the electronic conductivity (λ) of the materials, according the following categories [34]:

Material	Electronic conductivity λ / $\Omega^{-1}cm^{-1}$
conductors	10^{-1} - 10^{5}
semiconductors	10^{-5} - 10^{2}
insulators	< 10^{-12}

The electrical behaviour of materials can be explained by the band theory of solids, in which materials are analysed based on the band gap energy (E_g) [34, 35]. This energy corresponds to the difference between the lower value of the conduction band and the higher value of the valence band (Figure 1.5). The band levels (conduction and valence) are the result of individual orbitals that are very close in energy values, which are better interpreted as bands.

Metals have conduction bands and valence bands that overlap because there is a large number of atoms involved in the metallic bond, which gives very close energy levels and consequently, electrons are delocalised and move easily in both energy bands.

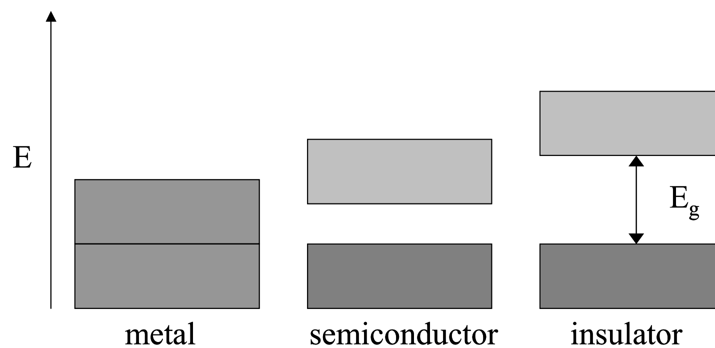

Figure 1.5 Schematic diagram of the energy band for metal, semiconductor and insulator materials.

Insulator materials have a reduced number of atoms involved in the chemical bond since electrons are trapped in covalent or ionic bonds. The conduction and valence

bands can be interpreted, respectively, as the result of the overlapping of the antibonding orbitals and of the bonding orbitals. As these two types of orbitals have different levels of energy, a gap is formed between them. This energy gap has a magnitude of 4-6 eV for typical insulators. For these materials, the electronic conductivity is very low at ambient temperature because the electrons are mainly in the valence band; the supply of energy promotes electrons to the conduction band, increasing the electronic conductivity.

Semiconductors have band gap values in the range of 1-3 eV and, if they are ultra-pure, their properties can be directly related with the band gap value (intrinsic behaviour). These materials can be doped with specific atoms to change to n or p-type semiconductor behaviour. N-type semiconductors result from doping with atoms that easily promote electron transitions to the conduction band; the electronic conductivity is the result of the movement of the electrons. The p-type semiconductors are doped with atoms that easily accept electrons of the valence band. This feature induces the formation of holes (positive charge carriers) in the valence band, which are responsible for the electronic conductivity of this type of semiconductor materials [35]. Semiconductors, as it is well known, form the basis of the microelectronic industry that has been developing since the last century. Today, one of the developing trends in the electronic industry is miniaturization of the integrated circuits in which ultra-pure and "perfect behaviour" of the materials used are even more necessary than previously.

1.3.2 Dielectric behaviour of anodic oxide films

Anodic oxides on valve-metals have low electronic conductivity, so they are globally classified as insulators. This characteristic gives one of the principal industrial applications for these oxides, as dielectric materials. The term dielectric is attributed to Faraday and means the ability to sustain the separation of charges when an electrical field is applied [36]. The materials polarize and balance the electrical field applied, thus they can be used to store charge. The electronic device that uses this feature is the capacitor and it is present in all microelectronic circuits. The stored energy is evaluated by the capacitance, measured in Faradays, and given by:

$$\text{Capacitance (F)} = \frac{\text{Charge(C)}}{\text{Voltage(V)}} \tag{1.27}$$

Capacitors can have different forms [37], but amongst them, the parallel plate capacitor can be easily adapted to the study of the dielectric behaviour of anodic oxides. This capacitor is built with two metallic surfaces (plates) separated by the dielectric material (Figure 1.6).

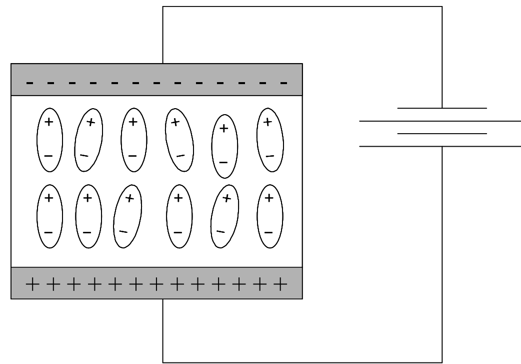

Figure 1.6 Polarization of a dielectric material on a parallel–plate capacitor.

The capacitance of a plane-plate capacitor is given by:

$$\frac{C}{A} = \frac{\varepsilon_r \varepsilon_o}{\delta} \tag{1.28}$$

$$\varepsilon_r = \frac{\varepsilon}{\varepsilon_o} \tag{1.29}$$

where, C, A, ε_r, ε_o, ε and δ, correspond respectively to the capacitance, the area of one plate, the relative dielectric constant, the vacuum dielectric constant, the dielectric constant of the material and the thickness of the dielectric material. Comparing with the metal/oxide/electrolyte system, similarity is evident. The electrolyte in contact with the oxide works as the second plate of the capacitor. This feature is used in electrochemical capacitors, sometimes referred as super-capacitors, because they are characterized by high values of capacitance as a result of a coupled

effect of the double charge layer and adsorbed species on the oxide/electrolyte interface [38].

The electrochemical system metal/dielectric-oxide/electrolyte is completely represented by three capacitors connected in series, where the total capacitance, is given by [14, 39]:

$$\frac{1}{C_{total}} = \frac{1}{C_{m/o}} + \frac{1}{C_{oxide}} + \frac{1}{C_{o/s}} \tag{1.30}$$

where $C_{m/o}$, C_{oxide} and $C_{o/s}$ correspond respectively to the capacitances of metal/oxide, oxide layer and oxide/electrolyte interfaces.

Interfaces have usually higher capacitances than the oxide bulk, so the system is simplified and the capacitance is given by [39]:

$$\frac{1}{C_{total}} = \frac{1}{C_{oxide}} \tag{1.31}$$

The dielectric behaviour can be interpreted as an electronic equivalent circuit with a capacitor connected in parallel with a resistance which corresponds to the resistance of the oxide layer. The perfect capacitive behaviour is given by a 90º shift between the applied signal (potential) and the resulting signal (current); this should correspond to an infinite resistance of the oxide layer and, in this case, the equivalent circuit is only represented by a capacitor. However, as the materials are not perfect, there is always a loss factor and the phase angle has a value lower than 90º. The difference is a small shift (ϕ) from 90º and it is used as a parameter to characterize the loss factor on a dielectric material [20]:

$$\tan(\phi) = \frac{1}{\omega R_p C_p} \tag{1.32}$$

where R_p and C_p are the resistance and the capacitance connected in parallel and representing the oxide layer.

Dielectric behaviour can be determined by EIS (Electrochemical Impedance Spectroscopy) usually by adjusting an equivalent circuit with a resistance connected in parallel with a capacitor. The replacement of a capacitor by CPE (Constant Phase Element) is useful to account for deviations from pure capacitive behaviour. The impedance of this element is given by:

$$Z_{CPE} = \frac{1}{\omega^n C} \qquad (1.33)$$

where C can be associated with a capacitance when n is close to 1. The shift, (1-n), corresponds to the deviation from pure capacitive behaviour and it is associated with surface inhomogeneities and leakage.

The dielectric constant is one of the parameters used to characterize a dielectric material because it gives information on the charge storing potential. The dielectric constant of a material has different components:

$$\varepsilon = f(\varepsilon_{ex}\varepsilon_e\varepsilon_n\varepsilon_d) \qquad (1.34)$$

The first component is an extrinsic factor, associated with impurities, interfaces, etc., and it is always present, even in the purest dielectric materials. The second one is associated with the electronic polarizability and it has an important contribution in polymer materials; ε_n is associated with the nuclei vibration, and the last, ε_d, is associated with ion deformation. This last component is the most important contribution to the dielectric constant of the oxides [20]. Valve-metals oxides are formed with metallic ions and oxygen ions; the first with ionic radii between 0.05 and 0.07 nm and the latter with ionic radii of 0.14 nm. Thus, the deformation of the ions is mainly given by oxygen ions [20].

The dielectric constant of an oxide is related to the molecular volume (V_M) and molecular polarizability (α_m) by the Clausius-Mosotti equation [40]:

$$\alpha_m = \left(\frac{3V_M}{4\pi}\right)\frac{(\varepsilon - 1)}{(\varepsilon + 2)} \qquad (1.35)$$

The same equation has been applied to mixed oxides (not anodic), where the polarizability and molecular volume are now calculated from the parameters of the oxide components maintaining the proportion of the mixed oxide composition. The equation, usually referred as oxide additivity rule, was applied to different mixed oxides, including (ZrO_2 + Yr_2O_3) and (Ta_2O_5 + Yr_2O_3) and the results have shown good accuracy [40].

The polarizability depends on the nature and strength of the oxide chemical bonds. Oxides of the valve-metals have a mixed bond character: covalent and ionic [41, 42]. On solid materials, the ionic character of a chemical bond can be determined by the energy lattice per equivalent; the covalent character can be determined by the heat of atomization per equivalent. Vigh plotted these parameters against the dielectric constant of different valve metals oxides and found that the dielectric constant increases with increase of the energy lattice and decreases with the increase of the heat of atomisation [41, 42]. The band gap energy is also related to the oxide dielectric constant; an increase of the energy gap is observed with decrease of the dielectric constant. The ionic character gives higher polarizability so it gives higher dielectric constant values, but the band gap energy is lower which usually means a higher loss factor.

The loss factor of a dielectric material is the result of various “leakage” processes. The intrinsic mechanisms include electronic and ionic conductivity, and relaxation effects. The mechanisms depend on the oxide thickness, interfaces, applied potential and frequency (Table 1.1).

Table 1.1 Conduction mechanisms on dielectric materials [20].

DC Conduction mechanisms	High field conduction (>1 MV cm^{-1})	Electrons promotion to the conduction band Tunneling effect (thin films) Space charge effects Ionic Conduction
	Low field conduction (< 0.1 MV cm^{-1})	Tunneling effect (between the two capacitor plates, $d < 3$ nm)
AC Conduction mechanisms	High and low field conduction	Interfacial Polarization Relaxation peaks Frequency independent phenomena (DC mechanisms)

The anodic oxides of the valve-metals usually have a constant loss factor in the audio frequency range (16-16000 Hz) [3]. This is the result of a distributive approach, in which the oxide behaviour is not represented by just one capacitance value and one resistance value, but it is better represented by a distribution function. High purity oxides have an inverse variation of the loss factor with band gap energy (Figure 1.7). Thus, the improvement of the dielectric behaviour on oxides appears to be limited by two contradictory factors: of higher dielectric constant giving higher capacitance but also giving a higher loss factor.

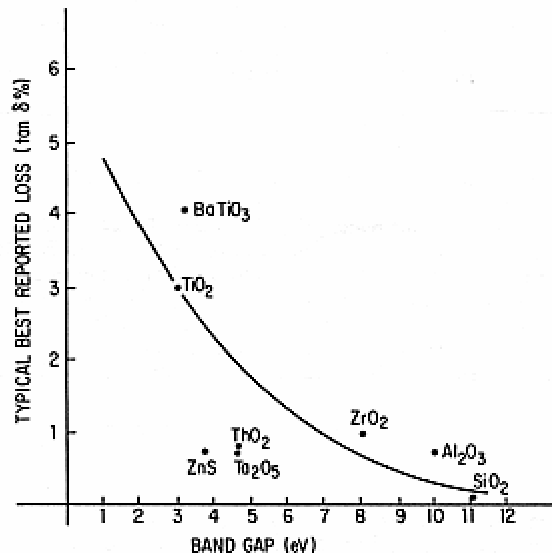

Figure 1.7 Variation of loss factor with band gap energy in ultra-pure oxides [20].

1.3.3 Semiconductor behaviour of anodic oxide films

Anodic oxides can behave as semiconductors as a result of their intrinsic behaviour or as consequence of impurities, composition or structure. The level of foreign atoms necessary to change the semiconductor properties of an oxide is very low. For example, the doping level of semiconductors of type n or p, used in the microelectronics industry, is in the range of 100 to 1000 ppm [35].

The semiconductor-oxide/electrolyte interface has a characteristic behaviour because space charge layers are formed [43-49]. Space charge layers are a consequence of the transfer of the electrons from the oxide to the electrolyte to achieve equilibrium on the interface. According to the band energy model, this effect corresponds to a band-bending phenomena related to the variation of potential at the semiconductor surface due to the charged region (Figure 1.8).

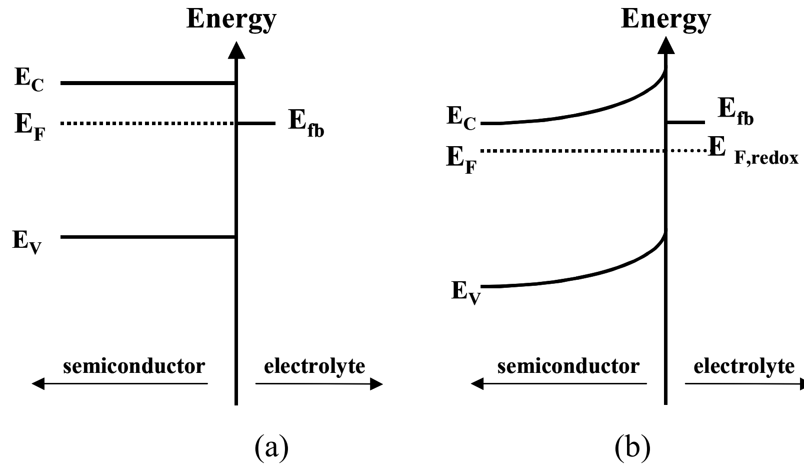

Figure 1.8 Energy band diagram for an n-type semiconductor in contact with an electrolyte, illustrating the flat band condition (a) and the band bending condition due to the formation of a space charge region (b).

The direct consequence of the existence of a space-charge layer is the dependence of the oxide capacitance on the applied potential, according the Mott-Schottky equation (for a n-type semiconductor) [43]:

-

$$\frac{1}{C_{SC}^2} = \left(\frac{2}{\varepsilon\, e N_D}\right) \left(U - U_{FB} - \frac{kT}{e}\right) \tag{1.36}$$

where,

ε = electrical permittivity of the oxide,

N_D = number of donors,

U = applied potential,

U_{FB} = flat band potential,

C_{SC} = space charge capacitance.

For a p-type semiconductor, the equation is similar, but a linear plot is obtained between (C_{SC}^{-2}) and (-U).

The flat band potential represents the position of the semiconductor Fermi level when the bands are flat. The Fermi level is the electrochemical potential of electrons in the solid. When equilibrium on the semiconductor/electrolyte interface is achieved, the electrochemical potential between both sides must be equal. As the

potential is usually measured with reference to the standard hydrogen electrode and the energy levels are related to the electron energy in the vacuum level, the conversion is given by:

$$E_F = -4.5\ \text{eV} - e\,U_{redox} \quad (1.37)$$

where,

E_F = energy of Fermi level at the semiconductor interface (eV)

U_{redox} = redox potential (V_{SHE})

e = electron charge.

The space charges depends of the delocalised electrons in the conduction band, represented by N_D, the number of donors, or holes in the valence band, represented by the number of acceptors, N_A. Typical values are in the range of 10^{16} to10^{18} cm^{-3}, which are about six orders of magnitude lower than the delocalised electrons in metals [43].

The thickness of the space charge layer is also related to the carrier concentration, with higher values allowing the equilibrium at the electrolyte interface to be achieved within a thin oxide layer. On the other hand, a low concentration needs charge carriers from deeper into the oxide. Space charge layers can extend over the range 10 to 1000 nm [43] meaning that for thin films, it is possible that the space charge layer extends across the entire oxide layer.

For an n-type semiconductor, if the capacitance is measured at a high sufficiently positive potential, the layer is completely charge depleted. In this case, the value of capacitance is directly related to the oxide polarizability and the dielectric constant can be calculated [56]. According to the band energy model, this effect corresponds to the complete bending of the energy bands (Figure 1.9)

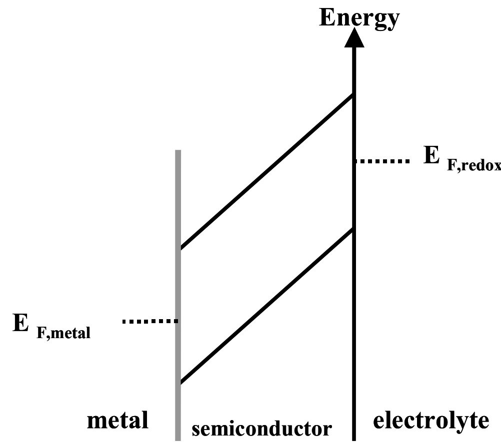

Figure 1.9 Energy band diagram for an n-type semiconductor in contact with an electrolyte, illustrating the formation of a complete charge depleted layer across the entire oxide layer.

Limitations of the Mott-Schottky plots are related to the frequency dependence of the measurements which are usually associated with surface roughness, non-uniform distribution of charge carriers, dielectric relaxation or the existence of surface states [50]. Highly doped semiconductors show high values of the space-charge capacitance and this also changes the Mott-Schottky plots. For the previous case, the capacitance of the Helmholtz layer (C_H), usually in the range of 10 to 100 μF cm^{-2}, can not be neglected, even though the number of charge carriers can still be calculated according to the following equation [6]:

$$\frac{1}{C^2} = \frac{1}{C_H^2} + \left(\frac{2}{\varepsilon\, e N_D}\right)\left(U - U_{fb} - \frac{kT}{e}\right) \qquad (1.38)$$

1.3.4 The electrical properties of anodic oxide films of aluminium, niobium and tantalum

Aluminium and tantalum oxides are dielectric materials that are widely used for commercial capacitors. The dielectric constants of these oxides are, respectively, in the range of 7-15 and 12-27. Niobium oxide has been developed recently as a possible substitute for tantalum oxide as a dielectric material in capacitors. The advantage is the increased value of the dielectric constant (41-46) [51, 52]. In scientific publications, oxides of aluminium, tantalum, hafnium and zirconium are classified as insulators, and they have a band gap energy higher than 4 eV, which

usually corresponds to a lower loss factor. Oxides of niobium, titanium, tungsten and bismute, are referred to as n-type semiconductors with donor concentrations of 10^{20}-10^{21} cm^{-3} and they have reduced band gap energies, between 3 and 4 eV [4, 14, 53]. The dielectric performance of the oxides depends strongly of the composition, structure and thickness of the oxide, as well as on the amount of impurity species, interfaces and mechanical effects. Thus, only experimental measurements of the corresponding capacitive properties of each oxide, including interfaces, can determine the behaviour of a specific oxide.

Gavliasso et al. [54] measured the dielectric constant of anodic oxides of tantalum and niobium by EIS with a measuring system comprising metal/oxide/electrolyte, in different electrolytes. The oxides were very thin, with a final anodising voltage of only 8 V_{SCE}. The results showed that the dielectric constant of the tantalum oxide was between 25 and 27, with the values being very close to those in the literature for pure Ta_2O_5. In contrast, the same authors found that the dielectric constant of Nb_2O_5 in acid electrolytes was much higher (89-119) than the literature value for the pure oxide (41). In an alkaline electrolyte (0.1 M NaOH), they found the value was 49. Kharafi and Badawy also examined the dielectric behaviour of thin anodic oxides on tantalum and niobium and found that niobium oxides show a shift from a perfect capacitive behaviour when analysed by EIS. The authors explained this effect as a result of the incorporation of electrolyte species, i.e. protons [55]. Kerrec et al. [39] reported that thin anodic oxides on tantalum electrodes, formed in acid electrolytes, show two different dielectric constants related with oxide thickness and composition:

$\varepsilon_r = 18.5$ for thin anodic films ($E_f < 15.2$ V and $\delta < 19$ nm) $\Rightarrow$ TaO,

$\varepsilon_r = 27.5$ for thick anodic films ($E_f > 15.2$ V and $\delta > 19$ nm) $\Rightarrow$ Ta_2O_5.

The results were interpreted on the existence of a "native" oxide layer of TaO, which decreased the dielectric constant of the thin oxide layer.

Modestov et al. [56] studied the electrical behaviour of the niobium oxide, formed galvanostatically to final voltages in the range 4 to 230 V in a neutral electrolyte. They measured the oxide capacitance with the applied potential and found two different regions related to the space charge layer formation. At relatively low potentials, the oxide behaved like an n-type semiconductor but when the applied

potential was extended up to oxide film formation potential, dielectric behaviour is observed.

Di Quarto et al have also studied the electrical behaviour of different anodic oxides, including niobium, by differential capacitance measurements and EIS [57, 58]. The anodic oxides were formed galvanostatically in sulphuric acid solution to film thicknesses ranging between 20 to 200 nm [57], and also, potentiodynamically to a final voltage of 5 V at 10 mV s^{-1} with a stabilization time of 2 h [58]. The results showed that some thick films ($\delta > 100$ nm) do not show variation of the capacitance with the applied potential over the range of applied frequency (3 Hz -10 KHz). On the other hand, films of reduced thickness showed a capacitance-potential dependency on frequency. At a frequency less than 100 Hz, a strong variation of the capacitance near the flat band potential, followed by a less dependent region at more positive potential, was observed. To explain this variation, the authors adjusted the EIS spectra to an equivalent circuit where the amorphous structure of the oxide was considered [58]. The lack of order in amorphous oxides modifies the band gap energy that is now substituted by a mobility gap. Consequently, the space charge depends not only on the usual charge carriers but also on the localized states within the mobility gap. According to Di Quarto et al, the contribution of localized states to the measured capacitance is localized at low frequencies due to electronic transitions through these states having a slower response to the imposed AC signal [58]. The authors adjusted the EIS spectra to a complex equivalent circuit, where the effect of surface states was included, which allowed the determination of the distribution of the electronic states within the oxide gap.

1.4 The Electrochromic effect

The electrochromic effect is an optical phenomenon characterized by a change of colour in a material when an electrical field is applied. Some oxides of the transition metals (niobium, molibdenium, vanadium, nickel, tungsten, titanium) and also doped polymers show this effect [59-73]. When an oxide is cathodically polarized, it shows a colour change that disappears when the polarization is reversed (bleaching effect). The process is very stable and can be repeated without significant changes, which is suitable for application in electro-optical displays.

Niobium oxide is one of the materials in which this effect has been studied more widely because of its high chemical stability. Many techniques have been used to prepare the oxide to examine electrochromic properties, including sol-gel [61, 64-66], thermal oxidation [62, 53, 67-69], oxide sputtering [66], anodising [59, 70, 72] and chemical vapor deposition [72]. The effect has been observed in amorphous or crystalline oxides and it has been analysed by electrochemical, optical and surface analysis techniques (XPS and XRD).

The colour change during cathodic polarization is a consequence of the injection of monovalent positive ions like H^+, Li^+ or Na^+ into the oxide, according to the reaction:

$$xA^+ + ne + Nb_2O_5 \Rightarrow A_xNb_2O_5 \qquad (1.39)$$

The monovalent ions can be inserted within the oxide because of their small size, but some authors also interpreted this insertion process based on the simultaneous reduction of Nb(V) to Nb(IV) [60, 62]. The process is usually classified as reversible and is independent of the technique used to prepare the oxides; some authors observed that the oxides lose their colour when they are left at open-circuit potential. Cabanel et al. [69] observed a change on the electrical properties of the oxide after the insertion of protons. If the insertion was sufficiently high, the oxide changed behaviour, from non-conductive into an electrical conductor with conductivity values close to those for metal. When analysed by XPS, the binding energies of the Nb_2O_5 species showed a subtle shift (0.1- 0.3 eV) when compared with the energies before insertion [62, 66, 68, 72]. It was also observed that crystalline Nb_2O_5, after the insertion of H^+, shows a small shift (≈ 1º) on the XRD (X-ray diffraction) peaks that characterize the oxide [67].

CHAPTER 2

LITERATURE REVIEW OF ANODIC OXIDES ON SPUTTERED ALLOYS

2.1 Introduction

Anodising processes on metastable aluminium alloys has been extensively studied for the last 30 years. Most other metals, as alloying elements, have been examined including niobium, zirconium, titanium and tantalum [74], tungsten [75-79], chromium [21, 80, 81], molybdenum [82], magnesium [83], zinc [84], manganese [85], cerium [86], neodymium [87], copper [88], iron [89-90], cadmium, indium and tin [91]. Firstly, the interest arises because these alloys, with a valve-metal as alloying element, show better corrosion resistance than aluminium. The observed features include increased pitting potentials in chloride solution, reduced corrosion rate in aqueous electrolytes and enhanced corrosion resistance at high temperature in sulphur or oxygen atmospheres [92-96]. Some valve-metals alloys, with other elements rather than aluminium, have also been studied, showing improved corrosion resistance than the pure components. For example, Cr-Nb alloys show a lower corrosion rate than the pure metal components in 12 M HCl solution at 30 ºC [96]. Anodising of those metal-valve alloys has also been studied, showing some features similar to aluminium alloys [16, 97-100].

This Chapter includes a Literature Review of anodic oxidation of sputtered alloys, with special emphasis on aluminium and niobium alloys. As niobium is similar to tantalum, the anodic behaviour of these alloys is also referred in this chapter.

2.2 Structure of sputtered valve-metals alloys

Sputtered materials have been studied with different metals in binary and ternary alloys or even forming composite materials. The technique is suitable to deposit alloys forming a single-phase solid solution even when the amount of the alloying element exceeds the solubility limits of the equilibrium state (metastable alloys). The structure of the alloys depends on the experimental deposition conditions; this is one of the advantages of this technique, since this dependence can be used to obtain different microstructures (Chapter 3).

Hashimoto et al. studied different sputtered aluminium alloys with titanium, zirconium, niobium, tantalum, molibdenium or tungsten as alloying elements and with a wide range of compositions [96]. The results showed that the alloys form a single-phase solid solution with amorphous or microcrystalline structure (Figure 2.1). The alloys were deposited by co-sputtering of the pure materials at about 1 x 10^{-1} Pa argon pressure, after evacuating the chamber to 1 x 10^{-5} Pa. During sputtering, the substrates were cooled to avoid heating of the deposited materials because a low temperature promotes amorphous structures [101].

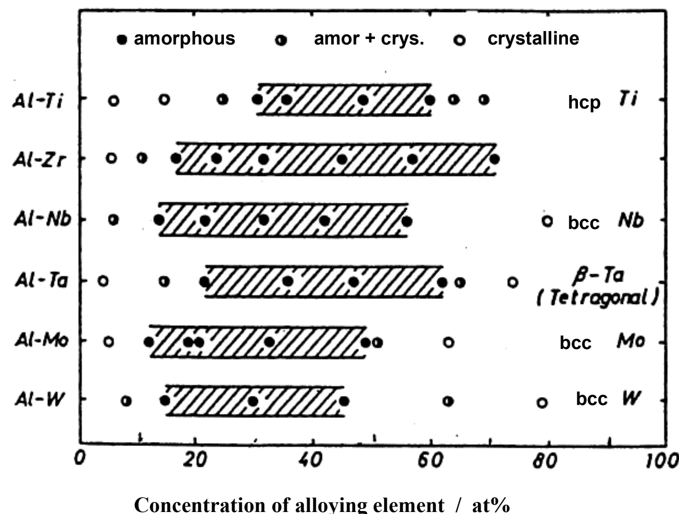

Figure 2.1 Structure of sputter-deposited aluminium alloys identified by X-ray diffraction [96].

The Al-Nb alloys show an amorphous structure in the composition range of about 15 to 55 at.% Nb. Outside this range, the structure is crystalline (or amorphous +

crystalline) and it is similar for alloys of higher concentration; the alloy concentration is face-centered cubic for high concentrations of aluminium, ranging between of 85 to 100 at.% Al, or body-centered cubic for high niobium concentrations, ranging between 80 to 100 at.% Nb. The crystalline alloys show a grain size of a few nanometres, and this usually does not imply a different behaviour on anodising at constant current. For example, the slopes of the voltage-time curves for high purity materials (99.999 %) are similar for sputtered aluminium or aluminium foil.

2.3 Anodic oxidation of sputtered aluminium alloys

2.3.1 Formation of enriched alloy layers

The anodising process on some dilute aluminium alloys promotes the formation of an enriched layer of the alloying element at the metal-oxide interface. This layer is very thin, with a thickness of 1 to 5 nm, and it is located beneath the oxide. The formation of this layer is correlated with the Gibbs free energy of the oxide formation per equivalent: only elements with energies less negative than that for alumina show this feature (Figure. 2.2) [102].

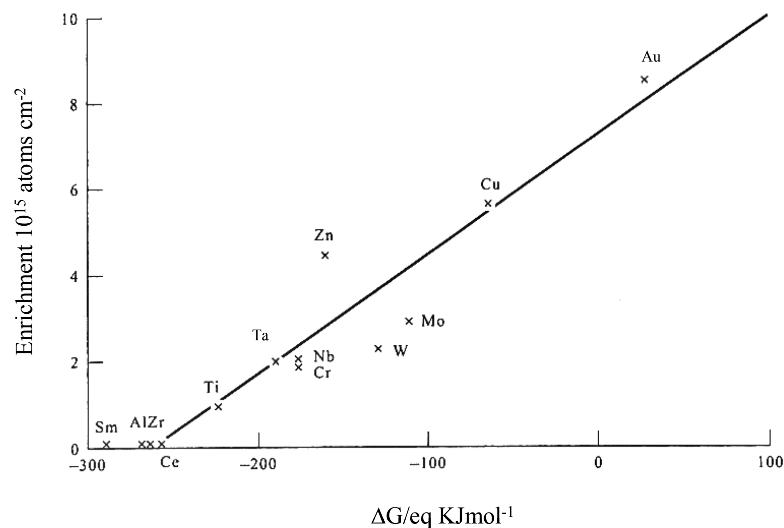

Figure 2.2 Variation of enrichment of alloying elements with Gibbs free energy per equivalent for formation of the alloying element oxide [102].

Elements like strontium or zirconium do not show this enrichment and elements like gold or copper show the highest enrichment. The layer is more easily observed after anodising to 150V or increased final voltages because of its low thickness. If there is an enrichment process on anodising, it means that the oxide is structured with layers of different composition. In the beginning of the anodising process, only aluminium ions are incorporated in the anodic oxide, so a pure anodic Al_2O_3 layer is formed. Meanwhile the concentration of the alloying element increases at the interface metal/oxide. When this concentration reaches a critical value, the alloying element starts to be incorporated into the oxide, together with the aluminium ions and with a cationic percentage close to the bulk alloy, forming a mixed oxide [102].

The enriched layer has been detected by RBS and TEM analyses. Tungsten is the alloying element that has been more extensively studied because of its higher atomic number compared with aluminium. This is an advantage for TEM observation because the heavy elements have lower transmitted electron yields, improving observation of the enriched regions under the electron beam.

Habazaki et al. [76] studied the enrichment on sputtered aluminium alloys with compositions of 0.1, 1.8 and 5 at.% W. They found that the corresponding average composition of the enriched layer was 2.5, 25 and 30 at.% W. They also proposed, based on TEM observations, that the W atoms are not distributed uniformly, but they are agglomerated in clusters. When the clusters achieved a critical concentration, tungsten ions start to be incorporated in the oxide, forming enriched tungsten oxide microzones, resembling ‘fingers’, close to the interface metal/oxide (Figure 2.3). As anodising proceeds, the fingers start to dissipate inside the oxide due to ionic variations in migration rate. The enriched layer is always observed, even at the highest anodising voltages, so it appears that the clusters grow to a critical size and reach a steady-state before the alloying element atoms start to oxidise and are incorporated in the oxide.

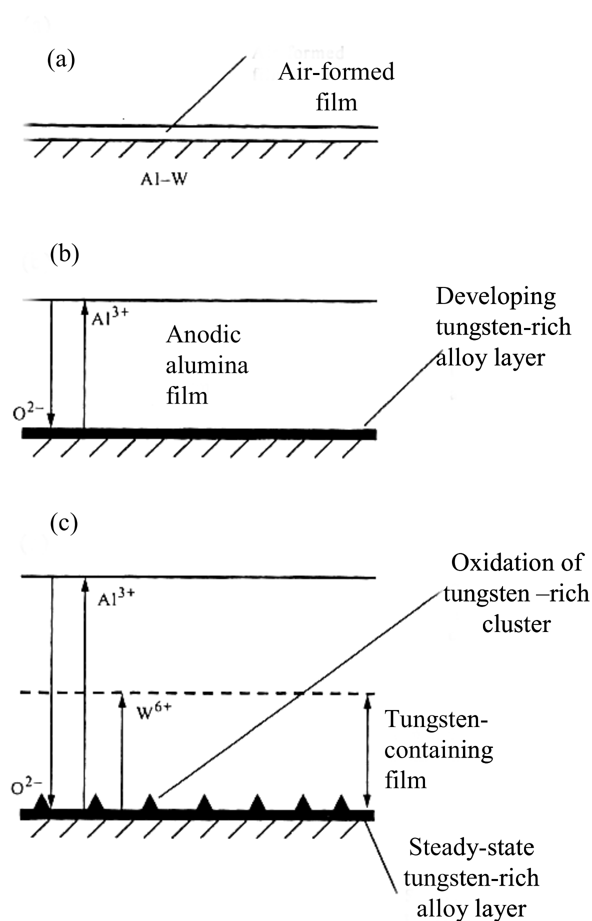

Figure 2.3 Schematic diagrams of oxide film growth on a dilute Al-W alloy: (a) initial alloy condition; (b) first stage growth with the formation of a tungsten-free anodic alumina film; (c) local oxidation of tungsten at the alloy/oxide interface, following achievement of sufficient enrichment of tungsten with subsequent outward migration of W^{6+} species [102].

Iglesias-Rubianes et al. studied the influence of the oxidation rate on the anodising of dilute Al-W alloys. The films were formed at different current densities, between 0.01 and 100 mA cm^{-2}, in sodium tungstate electrolyte. The results showed that the enriched layer was always formed for the current density range studied, but the number of tungsten atoms in the enriched layer is higher for the lower values of current [77]. Furthermore, the authors showed, that the incorporation of tungsten species into the films follows a cyclic process; firstly with local enrichment of tungsten in the alloy and alumina formation of little or no tungsten species, followed by tungsten oxidation, which forms a local enriched tungsten oxide [77, 103]. The enrichment, expressed in units of 10^{15} atoms cm^{-2} to the bulk composition of the

alloy, show a decrease of 2.5 to 0.2 in the alloys with a concentration range of 0.1-30 at.% W [104]. The transport numbers, determined by xenon implanting on Al- 5.7 at.% W alloy, and at current densities from 0.1 to 1000 mA cm^{-2}, are constant with a mean value of 0.38 and an accuracy of ≈ 10%. This suggests that the cooperative ionic movement is not disturbed for this range of electrical field strengths [105].

The Gibbs free energy correlation does not completely explain the formation of the enriched layer, but it is a good criterion for first analysis; other factors, including structural, kinetic and spatial are probably relevant, but not completely understood yet. The enriched layer is also formed on dilute conventional alloys [106-110] and other alloy systems; for example, the enriched layer is formed in dilute Mg-W alloys [97]. As a consequence of enriched layer formation, anodic oxide layers of different composition are formed; a mixed oxide layer of alumina and the alloying element oxide is present close to the metal/oxide interface, and a pure alumina oxide layer is located at the oxide/electrolyte interface.

2.3.2 Migration rates of ionic species

When an alloying element is incorporated in the oxide, the fraction of the total oxide thickness (r) contaminated with that element depends on the migration rate of the alloying cation relative to Al^{3+} ions (u_o). If the enrichment layer is not formed, the contaminated fraction is given by:

$$r = 0.6 + 0.4u_o \qquad (2.1)$$

This equation is valid for dilute aluminium alloys, in which it can be assumed that 60% of the oxide thickness is formed at the metal/oxide interface by the movement of the O^{2-}/OH^- ions and 40% is formed at the oxide/electrolyte interface by the movement of the alloy cation species. Depending on the u_o value, oxide layers with different composition are formed:

$u_o < 1$ – an alumina enriched layer is formed at the oxide/electrolyte interface;

$u_o = 1$ – just one layer of a mixed oxide of aluminium and alloying element is formed;

$u_o > 1$ – an enriched layer of alloying element oxide is formed at the oxide/electrolyte interface, if there is no cation ejection to the electrolyte.

When the enriched layer is formed at the alloy surface, beneath the oxide, there is an initial period of time corresponding to an anodising voltage (V_o) in which only alumina is formed. The fraction of the total oxide thickness corresponding to pure alumina is proportional to (V_o/V), where V is the final voltage achieved (Figure 2.4). The contaminated layer is now given by:

$$r = 0.6 + 0.4 u_o \left(\frac{V - V_o}{V}\right) \qquad (2.2)$$

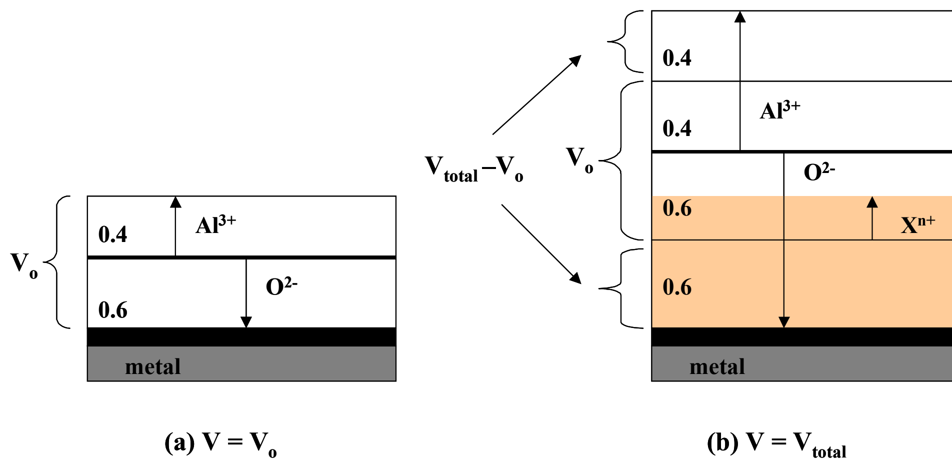

Figure 2.4 Schematic diagram of oxide film growth on a dilute aluminium alloy: (a) first stage of oxide growth with formation of pure alumina ($V = V_o$); and final stage of oxide growth with formation of alumina contaminated with alloying element oxide ($V = V_{total}$).

If different final voltages are used and r is measured experimentally by RBS or TEM, V_o and u_o can be determined by plotting r against V. Habazaki et al. examined anodised specimens of an Al-1.9 at.% W alloy to 50, 150 and 300 V in ammonium pentaborate, and found respectively that $u_o = 0.37 \pm 0.12$ and $V_o = 23 \pm 6$ V [75]. The relative migration rate can also be determined from the atomic ratio of the alloying element to aluminium in the anodic film (contaminated layer) and the same ratio in the alloy, according to:

$$\frac{(M/Al)_{film}}{(M/Al)_{alloy}} = \frac{1}{0.6 + 0.4u_0} \qquad (2.3)$$

The equation is only applicable for dilute aluminium alloys where it can be assumed that the oxide is composed of Al_2O_3 units without significant error. The equation means that when the alloying element starts to be incorporated in the oxide in a local region, the concentration in the contaminated oxide layer will be higher than the alloy concentration if the migration rate is lower that the aluminium ions and vice versa. Equation 2.3 was used to calculate the ratio $(W/Al)_{film}$, using a previously calculated value of u_o, on anodised Al-W alloys with tungsten contents of 0.1, 1.8 and 5 at.% [76]. The results were compared with the experimental values obtained from RBS spectra and showed the following agreement:

Alloy	RBS values $\left(\frac{WO_3}{Al_2O_3}\right)$	Calculated values $\left(\frac{WO_3}{Al_2O_3}\right)$
Al- 0.1 at.%	2.0×10^{-3}	2.4×10^{-3}
Al- 1.8 at.%	4.9×10^{-2}	4.9×10^{-2}
Al- 5 at.%	1.5×10^{-1}	1.4×10^{-1}

When the alloy element ions have a higher migration rate relative to aluminium ions, an enriched layer of the alloying element oxide can be formed at the interface oxide/electrolyte. These enriched layers can change the oxides properties by changing the behaviour of the oxide/electrolyte interface, i.e. for Al-Ce alloys. A study on these alloys containing up to 27 at.% of cerium revealed the formation of an enriched layer on cerium oxide at the interface metal/oxide. Due to this layer, the oxide grows with a faradaic efficiency close to 100% in alkaline electrolytes (up to pH 12), which is much higher than the usual range for anodic aluminium oxides ($4 < pH < 9$) [86].

A systematic study of diluted aluminium alloys shows a correlation between u_o and the single metal-oxygen energy bond: alloying elements with higher energy bond

than the corresponding aluminium energy bond show a relative migration to Al ions lower than 1 (Table 2.1). The single metal-oxygen energy bond, M-O, was estimated by the equation:

$$E_{M...O} = \frac{E_a}{mk} \tag{2.4}$$

where E_a is the molar atomisation energy of an oxide M_mO_n and k is the co-ordination number of the cations [16, 111]. Despite the good correlation between the M-O energy bond and the relative migration rate, there are other factors that can affect ionic migration, including ionic radius, ionic charge, local electrical field, dielectric constant and distribution of interstices within the amorphous network [16].

Table 2.1 Single energy-bond (M^{n+}-O) and cation migration rate for different aluminium alloys anodised in ammonium pentaborate.

Bond	Bond energy (kJ mol^{-1})	u_o	Al_alloy
Li^{+}-O	146	8	Al-3 at.% Li [108]
Mn^{2+}-O Mn^{3+}-O	153 189	3	Al-2.5 at.% Mn [85]
Mg^{2+}-O	166	1.5	Al-3 wt.% Mg[109] Al-5 wt.% Mg [109]
Cu^{+}-O Cu^{2+}-O	183 186	3.2	Al-0.4 at.% Cu [88]
Al^{3+}-O	281[107]	1	
Nb^{5+}-O	329[98]	--	
Ta^{5+}-O	347	0.9	Al-Ta [99]
Cr^{3+}-O	--	0.74	Al-0.8 at.% Cr [80] Al-1.7 at.% Cr [80]
W^{6+}-O	407 [103]	0.38 (mean value)	Al-0.1, 1.8, 5 at.% W [76]

2.3.3 Formation of oxygen gas

Oxygen bubbles are one of the origins of flaws in anodic films. The bubbles develop during anodising and can achieve high values of pressure within the anodic films. The equilibrium pressure corresponding to bubbles of 1, 10 and 50 nm diameter is respectively 8000, 800 and 160 MPa [21]. When the mechanical resistance of the film is exceeded, oxygen is released and flaws are formed, sometimes throughout the oxide, thereby damaging the oxide layer. The valve-metal oxides have high electronic resistivity; thus in these oxides, oxygen formation is usually associated with impurities, localised oxide imperfections or at the commencement of anodising when electron transfer can occur by tunnelling effects [21].

Anodising of different aluminium alloys shows that elements like gold, copper, nickel, cromium, iron and zinc form oxygen bubbles. All these metals, show enriched layers at the metal/oxide interface and form semiconducting oxides (except gold) [21, 112, 113].

Oxygen bubbles are also observed on conventional alloys with second phases enriched in elements such as iron or copper, or on electropolished alloys where alloying element enrichments are also produced. The same process is proposed; involving enriched alloying element oxide microzones in which oxygen formation is promoted. The bubbles are relatively immobile in the growing oxide and act as markers and they hinder the ionic migration so, consequently, when oxygen bubbles are present at a significant volume percentage, the electrical field applied to sustain the ionic migration must increase [21].

The formation of bubbles was studied by TEM after anodising an Al-1 %at Cu alloy to final voltages ranging from 20 to 100V. The results show that bubble nucleation is related to the enriched layer formed beneath the oxide. Increase of the anodising voltage promotes the growth and coalescence of the bubbles. At high voltages (70-100 V), it was observed that an approximately constant number of bubbles only grow in size. Furthermore, with increase of voltage to 100 V, the bubbles occupy a

significant volume within the oxide and a non-uniform flow of current density was observed [114].

Recent experiments (2002) have also showed that there is oxygen formation within the anodic alumina in which copper [115] or tungsten/chromium species were present without direct contact with the electrolyte [116]. This feature was interpreted, based on the species introducing impurity levels in the band gap energy which promote oxidation of the oxygen ions in local zones within the oxide, probably due to a tunnel effect [116].

The formation of oxygen bubbles was also studied on anodising an Al-1.2 at.% Ni alloy, sputtered on electropolished (99.99 %) aluminium [117]. A specimen of this alloy, of thickness 35 nm, was anodised and showed oxygen bubbles as a consequence of the nickel incorporation in the anodic alumina. After the enriched layer had been formed, the higher concentration of NiO in the oxide is a consequence of the oxidation of the nickel atoms that form the enriched layer when the alloy layer is consumed. On the other hand, dilute Al-Cr and Al-Cu alloys, of similar alloy thickness and preparation, did not show this behaviour. The authors interpreted these features as a consequence of the higher energy of the electron levels of Cr^{3+} species, and probably Cu^{2+} species, when compared with the corresponding of Ni^{2+} species. For nickel, the levels are sufficiently low to act as an impurity level, located within the bang gap energy, promoting the jump of electrons from the valence band to the conduction band of the anodic alumina and, consequently, oxygen ions are oxidized and bubbles are formed [117].

The formation of bubbles can also be associated with the formation of metal clusters of the alloying element of the enriched layer. This feature was observed on anodising Al-Au alloys in the concentration range of 0.4 to 11 at.% Au [113, 118]. In the first stage, the alloying element enriched layer is formed. Upon sufficient enrichment of gold, oxygen bubbles are produced at, or near, the alloy/film interface. If anodising is extended, gold-rich clusters and bubbles are incorporated within the oxide but remain isolated and, finally, the bubbles expand and oxygen is released, damaging the oxide layer [113].

2.3.4 The presence of hydrogen in anodic oxide films

Hydrogen, at low concentration, is revealed in anodic oxides. The presence of this element has two different sources: from electrolyte species due to the incorporation of OH^- ions into the oxide or as a consequence of the sputtering operation because hydrogen is an element usually found as an impurity in targets [119]. A study of the hydrogen distribution in the anodic oxide on an Al-6.5 at.% W alloy shows enrichment of hydrogen near the oxide/electrolyte interface, alloy/anodic film interface and anodised aluminium substrate/alloy interface. The first enrichment is associated with electrolyte species whereas the second is associated with hydrogen arising from the sputtered material, present as an impurity. Hydrogen is sputtered at the same time as the alloy elements and later, either diffuses to the metal/oxide interface or accumulates due to the growth of the anodic oxide [119].

The chemical state of hydrogen is uncertain; it can be segregated in bubbles or dissolved in solid solution. A mechanism of enrichment according to the correlation of the Gibbs free energy per equivalent to a specific level is also possible, followed by oxidation and incorporation into the oxide [119]. The presence of this element as cations in the oxide can influence the dielectric properties of the oxide layer since hydrogen ions are charge carriers with high mobility. Further studies are necessary to clarify the presence and the form of the hydrogen found on the anodic oxides, as this element can easily change, even at low concentration, the electrical properties of an oxide (Chapter 1).

2.3.5 Formation of voids and film detachment during anodising

The Pilling-Bedworth ratio (PBR) is defined as the ratio of the volume of the oxide formed to the corresponding volume of metal used to form that amount of oxide. If this ratio is less than one, the oxide formed is insufficient to cover the metal volume and voids are formed. Aluminium alloys in which the alloying element has a lower PBR than alumina may form t thus result in void formation at the metal/oxide interface during anodising. The ionic migration rate of the alloying element can also

influence void formation. It was found that alloying elements, e.g. like samarium and cerium, despite the low PBR, do not show voids at the metal/oxide interface. This was interpreted based on the higher transport number of the anion species that apparently reduces the voids formation [91].

Voids can promote oxide detachment from the metal surface. This feature was detected on anodising an Al-5 wt.% Mg alloy. It was found that the anodising curves have a significant decrease of the slope, followed by a recovery to the usual behaviour. The recovery process is a consequence of the exposure of new areas of the metal surface to the electrolyte, forming fresh oxide layers [108]. Film detachment can also induce the formation of crystalline alumina at the detached regions due to the local increase of current density and temperature [108, 112].

2.3.6 The anodic oxidation of aluminium alloys with high concentrations of alloying elements (> 20 at.%)

The enriched layer is not usually observed for anodising aluminium alloys with alloying element concentrations greater than 10-15 at.%. For example, the Al-15 at.% Ta alloy show a tantalum enriched layer of 1 nm thickness, whereas, aluminium alloys with 32 at.% and 39 at.% Ta do not show such layer [120]. Nevertheless, Liu et al. (2006) recently found an enriched copper layer on anodising an Al-20 at.% Mg-20 at.% Cu ternary alloy, i.e. similar behaviour to dilute aluminium alloys [121]. The same authors also revealed a copper enriched layer on a sputtered-deposited Al-30 at.% Cu alloy but, due to alkaline etching, it is formed priori to anodising [122].

The anodic oxidation of aluminium alloys with high concentrations of alloying elements usually results in mixed oxide of alumina and alloying element oxide in which the cation percentage is close to that of the alloy [15, 16, 74, 112]. The anodising curves (voltage versus time) of these concentrated alloys, obtained at a Faradaic efficiency close to 100 %, usually have a lower slope than for aluminium (Table 2.2) and an increased value of the formation ratio (nmV^{-1}): This means that the electrical field during anodic oxide growth is lower than the value necessary for alumina growth, i.e the oxide forms with a lower resistivity to ionic migration than for alumina.

Habazaki *et al.* studied the anodic behaviour of aluminium alloys with different valve metal additions, e.g. titanium, zirconium, niobium and tantalum, in a concentration range of 25 to 44 at.%. The alloys were anodised under the usual experimental conditions (5mA cm^{-2}, 0.01 M ammonium pentaborate) and the anodic oxide thickness was measured by TEM [74]. The formation ratio, nmV^{-1}, was calculated based on the experimental values and it was used to estimate the slopes of the time-voltage curves. The calculated and the experimental values agreed to within 10 %. The values were obtained assuming an oxide growth at 100% Faradaic efficiency and the formation of a mixed oxide with a cationic percentage equivalent to the alloy.

Table 2.2 Slopes of the time-voltage curves and formation ratios, nmV^{-1}, for different sputtered aluminium alloys during anodising at 5 mA cm^{-2} in ammonium pentaborate.

Al- alloy	Slope dV/dt	nmV^{-1}
Al-27 at.% Ce[86]	1.88	1.64
Al-25 at.% Ti[74]	1.9 ± 0.1	1.48 ± 0.005
Al-32 at.% Zr[74]	1.9 ± 0.1	1.39 ± 0.005
Al-29 at.% Nb[74]	1.9 ± 0.1	1.47 ± 0.005
Al-44 at.% Ta[74]	2.1 ± 0.1	1.33 ± 0.005
Al[5]	2.3 ± 0.1	1.2

The oxide densities were assumed to be in the proportion to the mixed oxides in the anodic films and values for the pure oxides were brought from the literature [74]. The authors also found that these oxides, when observed at a fine scale by TEM, showed a layered structure near the metal/oxide interface as a consequence of the experimental deposition conditions. Sputtering used two different targets in which the sample rotation induces a fine layer metal structure. These fine metal layers have a thickness of 1 nm, and the oxide formed reflects a similar layered structure. The oxide layers are only observed near the metal/oxide interface; it was suggested that ionic movement removes this influence and the oxide appears relatively uniform at distances of about 30 nm from the alloy/film interface [74].

The migration rate of the alloying element cation relative to aluminium ion can promote the formation of oxide layers at the oxide/electrolyte interface. These layers, in spite of their low thickness, can influence the interfacial properties and change the anodic oxide behaviour. It was found that Al-32 at.% Zr, Al-19 at.% Ti and Al-25 at.% Ti alloys, after anodising to 150 V, show an alumina layer close to the oxide/electrolyte interface, with a thickness of 2 nm. The oxides formed on these alloys were amorphous, whereas anodic oxides of titanium and zirconium are usually crystalline. The Al-44 at.% Ta alloy shows a 10 nm thick alumina film close to the oxide/electrolyte interface, implying a lower migration rate of Ta^{5+} ions relative to Al^{3+} ions [15]. The same behaviour is expected for Al-Nb alloys since tantalum and niobium usually show similar behaviour.

The oxide growth on these concentrated alloys is also associated with a cooperative mechanism, with the inward movement of O^{2-}/OH^{-} ions and the outward movement of the alloy cations. The total cation transport numbers were calculated for the entire composition range of the Al-Ta alloys after anodising and after being implanted with argon atoms. The results (Figure 2.5) show that the transport numbers of the cations vary between those for film growth on the pure metals and are proportional to the alloy composition [112, 123].

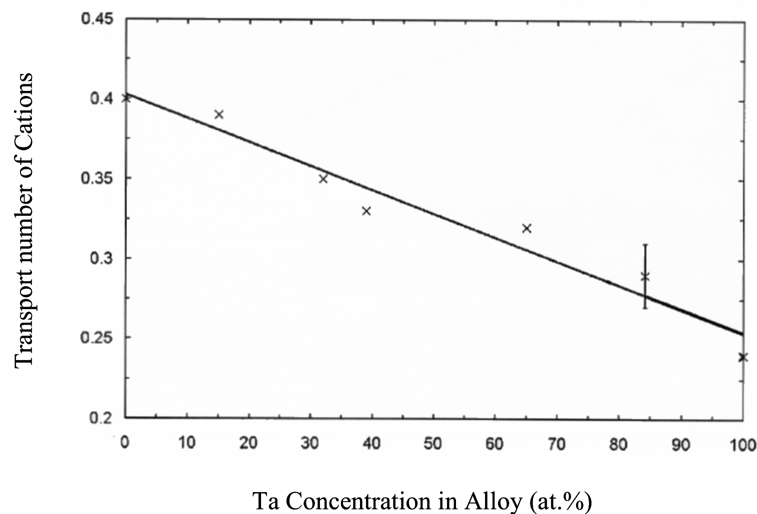

Figure 2.5 Variation of cation transport number with the alloy composition for anodic films on Al-Ta alloys [123].

2.4 The anodic oxidation of sputtered niobium alloys and tantalum alloys

The alloys in which niobium is the main element have not been studied as widely as the aluminium alloys. Mato et al. examined the anodic behaviour of Nb-3 at.% Cu and Nb-30 at.% Cu alloys under the usual experimental conditions [16, 98]. The former alloy did not form an enriched layer of alloying elements near the metal/oxide interface despite the less negative value of the Gibbs free energy per equivalent of copper oxide relative to anodic Nb_2O_5.

Further study of the anodic behaviour of dilute Ta-Cu and Ta-Fe alloys showed that the enriched layer was not present after anodising these alloys [16, 99, 124]. These features reinforce the view that other factors, probably related with kinetics parameters may also be involved [16, 98, 99]. A reason presented by the authors is the high value of the transport number of the anionic species O^{2-} in these alloys (≈0.75). This high value can hinder void formation in alloy when anodising occurs, and clusters formation is consequently hindered. The Pilling-Bedworth is also higher than alumina and can also contribute to the low capacity for void formation.

Examination of the Ta-1.5 at.% Cu alloy and it film composition by GDOES also revealed hydrogen enrichment close to the interface metal/oxide. Hydrogen is co-sputtered with other atoms from the target because it is present as an impurity species. Subsequently, it can form an enriched layer at the metal/oxide interface as observed with elements of less negative Gibbs free energy of oxide formation than alumina [99].

The Nb-30 at.% Cu alloy was studied under similar anodising conditions, but the final anodising voltage was only 5V, since oxygen bubbles were observed at increased voltages. The oxygen bubbles induce non-uniform film growth and flaws were observed throughout the film. The copper concentration is sufficiently high to form enriched copper oxide zones, probably forming a subnet across the oxide layer. The copper oxides are semiconductors and, in these oxides, the band gap energy is low allowing electrons to jump to the conduction band. The electrons in this band can move freely and oxygen can be easily formed [98].

The study of the Nb-Cu alloys also revealed a mobility of the Cu^{2+} ions relative to Nb^{5+} ions of 3.3. This value is much lower than the corresponding value of Cu^{2+} ions relative to Ta^{5+} ions of 11 ± 2. Thus, in these mixed oxides, the copper concentration is much lower than the corresponding values in the alloys. The copper ions are ejected to the electrolyte at the oxide/electrolyte interface, without formation of a copper oxide at the same interface [98].

Borate species were not detected in the anodic layer formed on Nb-Cu alloys due to the high outward migration rate of these species or to the possibility of these species are not incorporated [98]. The anodic oxide on Ta-Cu alloys only revealed borate species close to the oxide/electrolyte interface [99]. Borate species are immobile in anodic alumina, but move outward under the field in Ta_2O_5, TiO_2 and Nb_2O_5. The relative migration rate of boron species to Ta^{5+}ions is 0.55 [120]. Boron species are immobile when present as B_2O_3 units (neutral species), whereas they move outward when they are converted to B^{3+} or other cation forms under the field [120]. The formation of B^{3+} ions occurs through the dissociation of the bond B-O. This dissociation is observed on oxides where the electrical field strength necessary for oxide formation is lower than the corresponding value of Al-O bond. This can be related to the apparent field and the effective field strengths by:

$$E_{eff} = \frac{\varepsilon + 2}{3} E_{app} \qquad (2.5)$$

where E_{eff} is the effective (Maxwell field) and E_{app} is the apparent field (Lorentz field) [120].

A further feature is related to the ionic migration rate of cations present in the oxide and with the resistivity of the oxide layers formed. The anodic oxide on the Ta-40 at.% Mg alloy showed an enriched layer of MgO oxide at the oxide/electrolyte interface due to the higher migration rate of the Mg^{2+} ions relative to the Ta^{5+} ions [125]. After the formation of this layer and when the voltage was increased, fingers of tantalum oxide were developed through the MgO layer due to the lower ionic resistivity of the tantalum oxide layer. [125,126], A similar effect was also observed

on anodising Al-Ta alloys (15-45 at.% Ta) [123]. The effect is similar to the one observed by Pringle when he analysed the anodic oxides formed on superimposed metal layers: here, when the metal with an oxide of lower resistivity is anodised first, the oxides layers continue the metal order. However, when the metal with the oxide with higher resistivity is formed first, oxide fingers are developed through the outer oxide layer that has higher resistivity to ionic movement [26].

Niobia has a reduced resistance to field crystallization than alumina or tantala. Habazaki et al. studied this effect on sputtered specimens of the Nb-29 at.% W and Nb-10 at.% N alloys and compared the behaviour with pure niobium. The specimens were anodised at 5 mA cm^{-2}, with and without current decay, in 0.1 M ammonium pentaborate and in 0.1 M phosphoric acid and at 333 K. The results show that tunsgten as well as nitrogen or phosphorus species hindered field crystallisation. The authors also found that the initial air-formed oxide after thermal treatment accelerated the development of crystalline oxide and, after anodising, crystallization extended to the oxide fraction grown at the metal/oxide interface due to the predominant ionic transport by oxygen ions. On the other hand, a vacuum thermal treatment hindered crystallization. Thus, according to the authors, species able to hinder crystallization are required to be present at potential sites of crystal growth. In this case, the sites were located at about 30 % of the depth from the oxide/electrolyte interface, where the air-formed film, which acts as nuclei for crystallization, should be located. The authors also considered that the air-formed film is immobile, similar to a xenon marker, but showed short and medium ionic rearrangements that form nuclei for the oxide crystallization [127].

A further study has shown that oxygen also hinders field crystallization after anodising. The results were obtained on sputtered niobium with 20 and 50 at.% oxygen. The XRD (X-ray diffraction) results showed that crystallization was hindered in Nb-20 at.% O alloy and it was not observed when the amount of oxygen was 50 at.%, even with thermal treatment of the air-formed film [128].

2.5 Electrical properties of mixed anodic oxide films

2.5.1 Anodic oxide films of niobium as a component

Beside the Al-Nb alloy system studied in this work, other alloying elements have been examined in order to improve the dielectric properties of niobium oxide [129, 130]. Sputtered Nb–Si alloys, containing 5 and 17 at.% Si were anodised in 0.1 M ammonium pentaborate and analysed by EIS (electrochemical impedance spectroscopy). The results showed that silica species incorporated in the oxide improve the dielectric behaviour of niobium oxide, by lowering the leakage current and decreasing the dependence of the capacitance on the potential. The authors also found that, even after annealing, the oxides showed better dielectric behaviour than niobium oxide [129].

A further study has shown that the anodic oxides on Nb-N alloys containing 10 and 17 at.% N, also showed better dielectric behaviour than the niobium oxide, Nb_2O_5. The effects observed were low leakage current and no dependence of the capacitance on the potential, even after annealing [130]. In this case, nitrogen is present as N_2O bubbles with typical sizes of 10 nm [131]. It was suggested that the improved dielectric performance of the oxides was due to improvement of the mechanical properties, including increase of mechanical strength and toughness, as well as hindering the initiation of microcracks in the film.

For alloys with silicon or nitrogen, it was also shown that when specimens were annealed and then re-anodised, the leakage current and the capacitance recovered to the previous values, as before heat treatment. The GDOES depth profiles, before and after treatment, showed no difference in composition, suggesting that there is no diffusion of oxygen atoms to the metal surface as a consequence of the heat treatment. This feature has been reported to be the main cause of the high values of leakage current observed on niobium oxide (Nb_2O_5) when compared with other oxides [129, 130].

Tungsten is another element that has been considered to improve the dielectric behaviour of niobium oxide. The results showed that the tungsten oxide suppresses the increase in the leakage current on annealing [129].

2.5.2 Mixed anodic oxide films of other valve-metals

Other valve-metal binary systems have been studied in order to determine the electrical properties of the anodic oxides. For example, the dielectric constants of anodic oxides formed on sputtered Ta-Ti alloys, with titanium content from 0.6 to 40 at.%, were calculated from the capacitance measurements by EIS. The oxides were formed to 150 V in 0.1 M ammonium pentaborate at a constant current density of 5 mA cm^{-2}. The impedance spectra were measured in 0.1 M H_2SO_4 and 3.5 % NaCl. The results showed a constant dielectric, independent of the titanium concentration, and close to the value usually reported for pure Ta_2O_5 [132].

The electrical behaviour of anodic films grown potentiodynamically up to 8 V on sputtered Mo-Ta alloys of 9 to 79 at.% tantalum has also been reported by Di Quarto and co-workers. The results obtained by photocurrent spectroscopy showed that films of 21 at.% Mo behaved as insulating, but the increase of Mo content to 31 at.% was sufficient to achieve n-type semiconductor behaviour. The films were formed and tested in different electrolytes and the results also showed that the optical band gap was related to the Ta^{5+}/Mo^{6+} ratio in the film and also that the Mo species shift anodically the flat band potential [133].

Anodic films formed on sputtered W-Hf alloys, in the composition range of 17 to 80 at.% Hf, have also been studied by photocurrent spectroscopy by Di Quarto et al. The films were formed in 0.1 M ammonium pentaborate at a constant current density of 1 mA cm^{-2} to a final voltage of 10 V. The results showed semiconductor behaviour for the oxides formed on the alloys of Hf content ≤ 27 at.%, but with higher band gap values than WO_3. The results obtained for the anodic films of Hf ≥ 68 at.%, revealed insulating behaviour. The oxides formed on the W-48 at.% Hf alloy to a voltage of 10 V displayed semiconductive behaviour but, when the anodising voltage was extended to 20 V, the oxide layer behaved as an insulator. This change was attributed to enrichment of Hf species at the film surface [134].

2.6 Introduction to present work

Anodic films on valve-metals have numerous practical applications due to the formation of uniform oxide layers of high chemical and mechanical resistance. Anodising of the valve-metals has been widely examined and the oxide growth equation under high electrical field is well known. The films are formed as a result of transport of ions across the metal/oxide and oxide/electrolyte interfaces, and, under appropriate experimental conditions, a Faradaic efficiency close to 100 % is achieved during anodising.

The physical vapour depositions techniques (PVD), including sputtering, by allowing the preparation of metastable alloys, is opening a new perspective for anodic oxide applications. The anodic oxidation on different sputtered valve-metals binary alloys has been examined and some consistent behaviour has been determined. For instance, the formation of the an enriched alloying element layer close to the metal/oxide interface on dilute aluminium alloys, or an outer alumina layer at the oxide/electrolyte interface due to different migration rates of the alloy cations, are features related to the intrinsic thermodynamic properties of the oxide species present.

The aim of the present work is to study the anodising process and the electrical properties of the anodic oxides of the Al-Nb alloys prepared by sputtering in the range of concentration of 21 to 89 at.% Nb. This system, Al-Nb, formed by two valve-metals is interesting because, after anodising, a mixed oxide, containing Nb_2O_5 and Al_2O_3 units is anticipated. The electrical properties should reflect the oxide composition, since anodic niobia is usually referred to as an n-type semiconductor material and alumina is a dielectric material; i.e., the system appears attractive for future electronic applications.

It has been reported that the semiconducting properties of anodic niobia are sometimes associated with inhomogeneous and non-stoichiometric oxides formed at the metal/oxide interface or other electrochemical processes, as proton insertion in the film, interferes with dielectric behaviour. In the present work a preliminary study

by voltametry of a niobium rod electrode has been performed to examine the electrochemical processes associated with the metal/thin oxide/ electrolyte system.

Al-Nb alloys were then anodised at constant current in 0.1 M ammonium pentaborate solution since barrier-type oxides, at an anodising efficiency close to 100 %, were expected. The oxide compositions were determined by RBS and observation by TEM was undertaken to determine oxide thicknesses and particular features associated with the ionic migration process. The same experiments were performed on sputtered niobium to compare the behaviour. The electrical behaviour of the anodic oxides formed on Al-Nb alloys, including the determination of dielectric constants, was performed by EIS.

CHAPTER 3

EXPERIMENTAL TECHNIQUES

3.1 Introduction

This Chapter provides a description of the experimental techniques and associated procedures used in this work as well as a brief description of the fundamentals of the techniques.

3.2 Experimental procedure

3.2.1 Materials and solutions

The voltammetric studies of niobium were accomplished with pure niobium rod (99.9 %, Goodfellow) of 10 nm diameter. The major impurities are tantalum (< 250 ppm), tungsten (< 100 ppm) and oxygen (< 230 ppm).

The sputtered specimens were produced with an aluminium target of high purity (99.999 %, Goodfellow) and with a niobium target also from Goodfellow (99.9 %). The major impurities are Cu (< 0.3 ppm), Fe (< 0.3 ppm), Mg (< 1.2 ppm) and Si (< 0.8 ppm) for the aluminium target, and Fe (< 30 ppm), Si (< 100 ppm), W (< 100 ppm) and Ta (< 500 ppm) for the niobium target.

Electrolyte solutions were prepared with pro-analysis reagents and distilled water. For examination of the effect of pH, this was adjusted in the acid range by adding an acid solution with an anion concentration equivalent to the working solution. In the alkaline range, the pH was adjusted by adding small volumes of concentrated sodium hydroxide solution.

3.2.2 Electrode preparation

Niobium electrodes employed in the voltametric experiments were made with sections of the niobium rod, mounted in epoxy resin. Electrical contact was made with a copper ring with a soldered copper wire, adjusted to the diameter of the niobium rod. The ohmic resistance between the electrode surface and the end of the wire was less than 1 ohm. The electrodes that were chemical polished were covered with bee-wax and contact was made with a crocodile clip.

The niobium electrodes (rod) were mechanically polished with SiC paper of 1200 grit size. For chemical polishing, the niobium electrodes were first mechanically polished with SiC and then with diamond powder down to 1 μm finish (Table 3.1).

Table 3.1 Chemical polishing solutions used on the niobium electrodes [135].

Solution	Time	Surface effect
50 ml H_2SO_4 (96 %) + 20 ml HNO_3 (63 %) + 20 ml HF (40 %)	30 s	Surface dissolution
200 ml HF (40 %) + 80 g NH_4F	2 min	Remove any residual film
Boiling water	5 min	Minimize the contamination with fluoride ions

3.2.3 Substrate preparation for magnetron sputtering

The substrates were obtained by cutting high purity aluminium (99.99%) sheet of 0.3 mm thickness to dimensions of 1.5 x 3 cm. The aluminium substrates were first electropolished and then anodised to obtain flat surfaces for sputtering of selected metals and alloys for subsequent anodising.

The electropolishing bath was a solution of ethanol- perchloric acid (4:1 by volume) cooled to ≤ 283 K. This mixture produces a highly exotermic reaction with the risk of explosion when the temperature rises above 293 K; therefore, during mixing, the temperature was maintained lower than 283 K. This was normally done on ice bath surrounding the solution, added acid in small volumes and with vigorous stirring of the solution to aid heat dissipation.

The substrates were degreased with ethanol, immersed in the electropolishing bath, which was cooled to less than 283 K, and a voltage of 20 V was applied for 3 minutes. After this time, the substrates were removed from the bath, rinsed with ethanol, then with distilled water and finally dried with a cool air stream. The electropolishing cell is shown schematically in Figure 3.1. The substrate was connected to the positive terminal of the d.c. power supply, thereby acting as the anode. A cylindrical sheet of aluminium foil, covering most of the wall of the beaker, was used as a cathode. A beaker of 1000 ml was filled with 800 ml of electrolyte to assist heat dissipation.

After electropolishing, the substrates had a mirror surface; however to improve the surface for subsequent sputtering deposition, the substrates were anodized to 150 V at 5 mA cm^{-2} in 0.1 M ammonium pentaborate electrolyte at room temperature. The time-voltage response for each specimen was monitored in order to control the anodic oxide formed. Under the selected conditions, the oxide layer has a thickness of ≈180 nm (1.2 nm/V x 150 V).

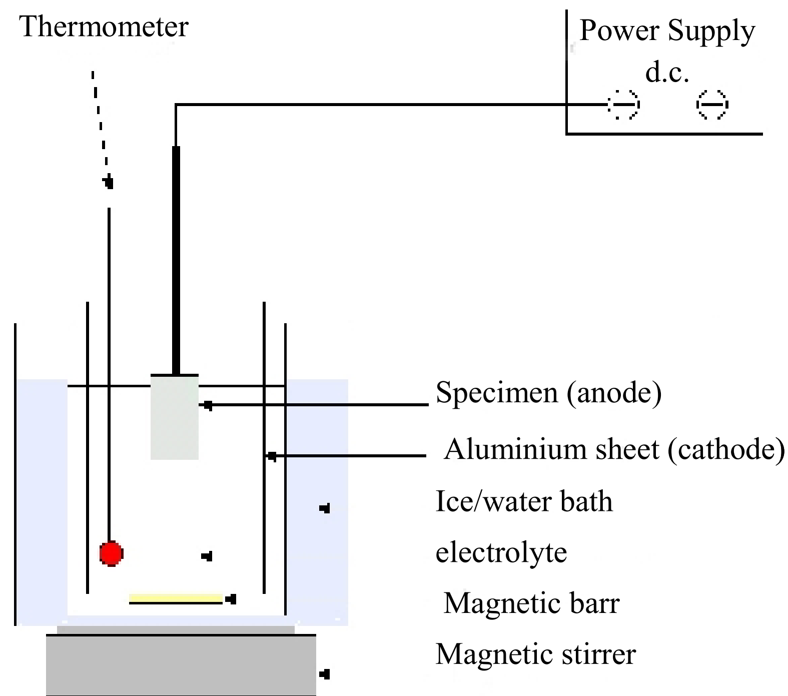

Figure 3.1 Schematic diagram of the electropolishing cell [136].

3.2.4 Constant current anodising

Anodising at constant current density was performed on the sputtered alloys and niobium, generating anodic oxides with different thicknesses with the purpose of characterising the electrical properties and the oxide growth mechanism.

The specimens were anodized at 5 mA cm^{-2} in 0.1 M ammonium pentaborate at room temperature. The final voltage was 150 V or 200 V for RBS and TEM analysis. For the EIS experiments, different final voltages were used to obtain specimens with different oxide thicknesses in order to determine the electrical properties. The anodising cell is shown in the schematic diagram of Figure 3.2 [136]. The specimens were connected as anode of the d.c. power supply and an aluminium sheet was used as cathode. The electrolyte was stirred to eliminate any rise of temperature at the surface of the specimen to be anodised. The voltage-time response was recorded on a PC and saved on file. Two forms of power supply were used for this purpose; a power supply (METRONIX 6911 DC) coupled with a PC using the software

PICOLOG for WINDOWS, or a potentiostat (EG&G Par, Model 173) coupled to an acquisition data system (HYDRA, model 2615A, Fluke Corporation) controlled by a PC.

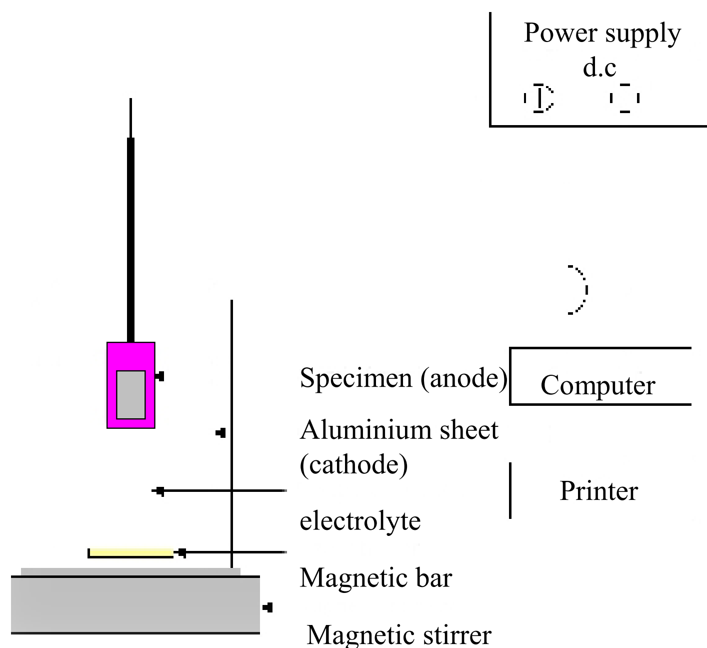

Figure 3.2 Schematic diagram of the anodising cell [136].

3.2.5 Voltammetry

The voltammetric experiments were run in a Greene cell. The working electrode was mechanically polished for study of the electrochemical behavior of niobium. The auxiliary electrode was a platinum sheet of high area (≈ 10 cm^2) comparing with the working electrode. The reference electrode was a commercial calomel electrode (SCE) or an Ag/AgCl electrode, placed in a separate compartment, connected to the electrochemical cell by a salt bridge. The potential sweeps were carried out with a PAR waveform generator, model 273 controlled by a PC using the software "Corrview" or "ECHEM".

3.2.6 Electrochemical impedance spectroscopy (EIS)

The electrochemical impedance spectra were measured with a mercury drop [137], following the experimental assembly shown in Figure 3.3. The electrode area (0.123 cm^{-2}) was defined with an O-ring placed on the surface of the anodized specimen. This O-ring was filled with mercury. A copper wire, used as electrical contact, was immersed in the mercury drop with special care not to touch the specimen surface. Previously, the wire was dipped in pure mercury for a few minutes to form an amalgam and to improve electrical contact. The other electrode was sputtered alloy beneath the oxide. With this system, a two-electrode configuration (metal/oxide/mercury drop) was obtained.

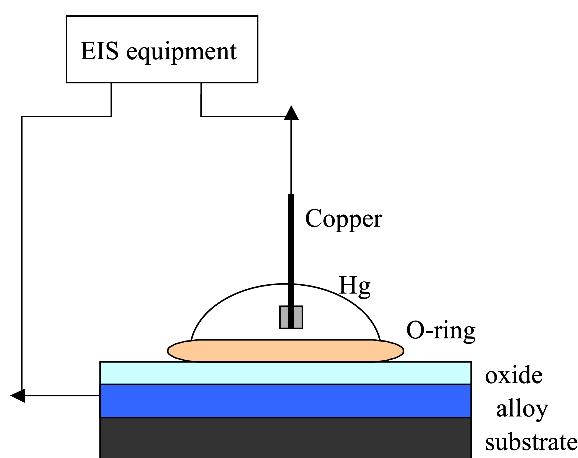

Figure 3.3 Schematic diagram of the assembling for impedance measurements with a mercury drop.

EIS spectra were also measured in a Greene cell with the usual three-electrode configuration in a borate buffer solution (0.15 M H_3BO_3 + 0.075 M $Na_2B_4O_7$, pH 8.8) to determine the semiconductive behaviour.

The spectra were obtained with a frequency response analyzer (SOLARTON, model 1250) coupled to an electrochemical interface (SOLARTON, model 1287), controlled by a PC using the “Zview” software. The experimental parameters are

given in Table 3.2. The fitting of the electrical equivalent circuit was also achieved with "Zview" software, selecting the adjusting parameters given in Table 3.3.

Table 3.2 Experimental parameters used for the EIS measurements.

Frequency Analyser System	Generator: Amplitude =10 mV Attenuation factor: auto Analyser: Integration factor = 10s Step time =1s Frequency sweep: Maximum Frequency = 65000 Hz Minimum Frequency = 1-10Hz Increment step = 10 / decade
Electrochemical Interface	Mode: potentiostatic Resistance : automatic Others settings: (default)

Table 3.3 Parameters used for adjusting the equivalent circuits with Zview software.

Maximum iterations	100
Optimization interations	10
Type of fitting	complex
Type of data weighting	Calc-Modulus

3.2.7 Magnetron sputter-deposition

The magnetron sputtering system, Atom Tech DC, was employed to deposit aluminum-niobium alloys and pure niobium metal. The layers were deposited on the surface of the aluminium substrates (3.2.3) using the experimental settings presented

in Table 3.4. In order to obtain the desired alloy concentrations of aluminium and alloying element, the current applied to each target was changed. The chamber was evacuated to 5 x 10^{-5} Pa and deposition was then carried out in argon (99.998 %) atmosphere at 0.5 Pa.

Table 3.4 Experimental deposition conditions for magnetron sputtering.

Alloy/metal Composition (%at)	Sputtering Time (min)	Current on target (mA)	
		Al	Nb
Al-21 %at Nb	30	270	180
Al-31 %at Nb	30	230	230
Al-44 %at Nb	30	200	300
Al-74 %at Nb	30	350	120
Al-81 at % Nb	50	320	100
Al-89 at % Nb	50	320	50
100 %at Nb (RBS) 1st set	45	---	320
100 %at Nb (RBS) 2nd set*	50		320
* argon pressure 0.2 Pa			

3.2.8 Scanning electron microscopy (SEM)

The deposited specimens were analysed using an Amray 1810 instrument, equipped with an EDX analysis facility or JEOL JSM 35 CF microscope with EDX analysis facility.

3.2.9 Rutherford backscattering spectroscopy (RBS)

Oxides and alloys compositions were determined by Rutherford backscattering spectroscopy, using a 2 MeV α-particles beam provided by the 2.5 MeV Van der Graaff accelerator. Particles were detected at 165º to the incident beam direction, which was normal to the surface of the specimen. The data were interpreted by comparing measured and simulated spectra using the RUMP program [138] or NDF program [139].

3.2.10 Transmission electron microscopy (TEM)

Ultramicrotomed sections were examined in a JEOL 2000FX II transmission electron microscope, equipped with energy dispersive X-ray analysis. The specimens analysed by TEM were cut with Reichert-Jung Ultracut E ultramicrotome. For cross-sections, a portion of the specimen, of dimensions of 6 x 15 mm, was mounted in a pyramidal capsule, positioned parallel to the axis of the capsule. Resin, consisting of Epon 812, DDSA and DMP30 in the ratio 20:30:1, was then injected to fill the capsule and cured at 60 ºC for 48 h. Prior to the final cutting with a diamond knife, the resin block was trimmed using a glass knife to provide a rectangular tip of dimensions < 0.5 x 1 mm comprising approximately one-half metal and one-half resin. The diamond knife employed was a Micro Star, Type SU, with an edge length of 2.4 mm. During sectioning, the trough at the rear of the diamond knife was filled with distilled water, with the meniscus almost level with the diamond knife-edge. Sections were collected from the water on appropriate grids, dried on filter paper and stored in a desiccator for later examination.

Ion implantation of xenon was employed to investigate the transport of niobium, oxygen and aluminium ions during anodic film growth. Implantation was carried out

using a ULVAC Multi-ion Vapor Deposition System BB4559, at an energy of 20 keV and a dose of 1 x 10^{15} ions cm^{-2} on the alloy that had been pre-anodised to 10 V at 1 mA cm^{-2} in 0.1 M ammonium pentaborate at 293 K.

3.2.11 X-ray photoelectron spectroscopy (XPS) and Auger electron spectroscopy (AES)

XPS spectra and Auger depth profiles were determined using a 310 F Microlab (VG Scientific) instrument, equipped with a field emission electron gun, a concentric hemispherical analyzer and a differential pumping ion gun. XPS analyses were performed using a non-monochromated magnesium anode (K_{α}. = 1253.6 eV) in ultra-high vacuum (UHV), at a pressure between 2 x 10^{-8} and 5 x 10^{-7} Pa. To prevent surface damage of the samples, Ar-ion etching was not performed prior to XPS measurements. The Auger depth profiles were obtained by removing layers from the surface by sputtering with an argon beam and performing the AES analysis on the exposed surface. The energy of the ion beam was 2 keV.

3.3 Fundamentals of the experimental techniques

3.3.1 Voltammetry

Voltammetry is the most suitable technique to be used as a first approach to characterize the electrochemical processes occurring in the electrode/solution system [140]. The method is based on sweeping the applied potential (E) and measuring the resultant current response. The potential variation is limited by the potential of hydrogen and oxygen evolution reactions in aqueous solutions. For these measurements, an electrochemical cell with a three-electrode configuration is usually used. The potential variation is applied between the working and the reference electrode, and the current is measured between the former and the auxiliary electrode. The potential sweep range used can be extended from mVs^{-1} to a few hundred Vs^{-1}, depending on the system [140]. The results are analysed by plotting the potential against the current density and the plot obtained is called a voltammogram. Different diagnostic tests can be applied to analyse the results, with processes such as

like electron transfer, mass transport, chemical or adsorption reactions as well as passivation, deposition or corrosion processes easily identified [140].

For a reversible reaction:

$$O + ne \Leftrightarrow R, \tag{3.1}$$

in which O and R are soluble species and initially only R is present in the solution, the anodic sweep of the potential shows a peak shape on the voltammogram, characterized by specific potential and current values (Figure 3.4). The peak is initiated when the redox potential is reached, according the Nernst equation:

$$E = E^{o} + \frac{RT}{nF} \ln \frac{C_O(o,t)}{C_R(o,t)} \tag{3.2}$$

As the potential is swept to anodic values, the concentration gradient increases and, consequently, the current also increases until the concentration of the species R at the electrode surface is zero. At the same time, R species diffuse from the bulk solution to the surface and, consequently, a peak is generated as the final result of both processes of charge transfer and diffusion of the reactive species.

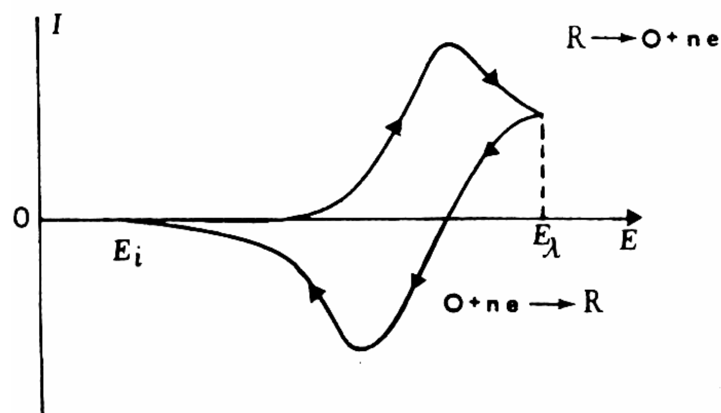

Figure 3.4 Cyclic voltammogram for a reversible process; O + ne ⇔ R.

3.3.2 Electrochemical impedance spectroscopy (EIS)

The EIS technique is based on applying an AC electrical signal and measuring the corresponding response. The amplitude of the applied signal is low (1-25 mV) and the frequency range is usually 10^{-2}-10^{5} Hz to detect the different processes at an electrode surface. When an AC potential wave of low amplitude, $\Delta V\sin(\omega t)$, is applied to an electrochemical system, the resultant current is given by $\Delta I\sin(\omega t + \theta)$. Thus the frequency response is a similar wave, but has a different phase and amplitude [140-142]. The impedance of the system, which is equivalent to a DC resistance, is now calculated by:

$$Z(\omega t) = \frac{\Delta V \sin(\omega t)}{\Delta I \sin(\omega t + \theta)} \tag{3.3}$$

The impedance value is characterized by two values; namely the modulus and the phase angle, both being related to the physical processes that can occur on a metal surface**.** Impedance is usually represented by complex numbers**,** according to the following equations:

$$Z = Z_{real} + Z_{imag} \tag{3.4}$$

$$|Z| = \sqrt{Z_{real}^2 + Z_{imag}^2} \tag{3.5}$$

$$\tan\theta = \frac{Z_{imag}}{Z_{real}} \tag{3.6}$$

The EIS spectra are usually analysed by assuming an equivalent behaviour between the electrochemical processes and the basic elements of electronic circuits including resistors, capacitors or inductors. The common electrical elements used and the corresponding impedance functions are shown in Table 3.5. The impedance of a resistor is independent of frequency and it is directly proportional to the applied potential; thus the current response has the same phase as the input potential signal. The resistance to a charge transfer reaction and the resistance of an oxide or electrolyte layer can be determined by this element. The capacitor is an element that

stores charge and is formed by two conducting plates separated by a non-conducting media. The charge is stored because the non-conducting media is able to polarize and sustain the charge. This behaviour is given by the equation:

$$C\,(\text{capacitance}) = \frac{Q\,(\text{charge})}{V\,(\text{voltage})} \tag{3.7}$$

The impedance of a capacitor is derived according to the following steps:

$$i = \frac{dq}{dt} = C\frac{dV}{dt} \tag{3.8}$$

$$Z(\omega t) = \frac{V(\omega t)}{i(\omega t)} = \frac{\Delta V \sin(\omega t)}{C\Delta V \omega \sin(\omega t + \frac{\pi}{2})} \tag{3.9}$$

$$\theta = (\omega t) - (\omega t + \frac{\pi}{2}) \tag{3.10}$$

The current through a capacitor is phase shifted by -90º with respect to the voltage and the impedance is equal to $(\omega C)^{-1}$; thus, it is represented by the imaginary component of a complex number. This angle is a theoretical value, since it is observed that even the most perfect capacitor has always a small shift from 90º. Dielectric oxides, coatings or double layer effects are represented by this element.

Table 3.5 Impedance of the common electrical elements used on fitting the EIS spectra [141].

Electrical Elements	f(V;i)	Impedance	
		Z_{real}	Z_{imag}
Resistor	V = i R	R	0
Capacitor	i = C (dV/dt)	0	$(j\text{w}C)^{-1}$
Inductor	V= L (di/dt)	0	jwL

The total behaviour of an electrochemical system is represented by the total equivalent circuit, in which the different elements are associated in parallel or in series or in combinations (Figure 3.5).

a) Impedances in parallel combination

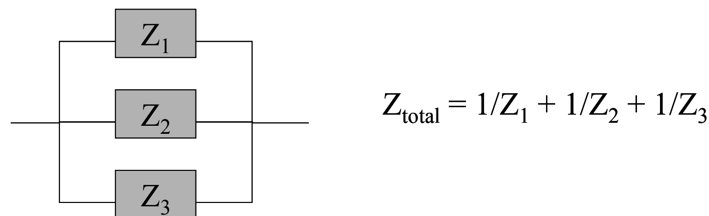

b) Impedances in series combination

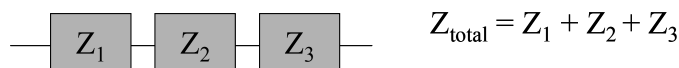

Figure 3.5 Impedance of the circuit elements when connected in parallel (a) and in series combination (b).

Electrochemical systems are often represented by the Randles circuit (Figure 3.6.a), which includes the solution resistance (R_s), the double layer capacitance (C_{dl}) and the charge transfer resistance (R_{ct}).

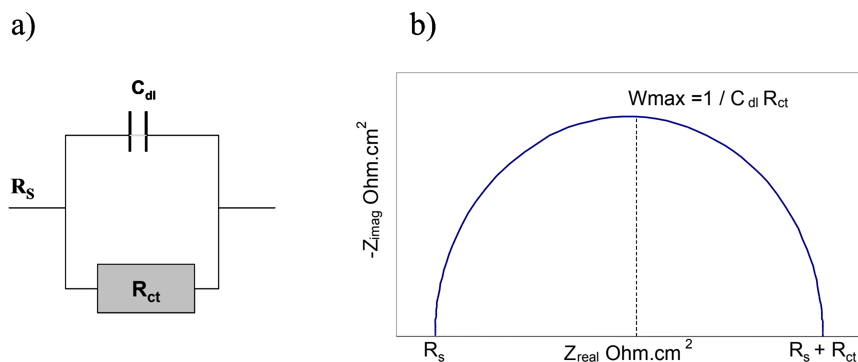

Figure 3.6 Randles equivalent circuit $R_s(R_{ct}\text{-}C_{dl})$ (a) and corresponding complex impedance diagram (b).

The same circuit can be used to determine the behaviour of a dielectric oxide, as R_s represents the measuring system resistance, C_{ox} is the oxide capacitance and R_{ox} is the resistance of the oxide layer. The complex impedance diagram (Figure 3.6b) and the Bode plot (|Z| and θ versus log f) are used in EIS analysis. The model parameters are found using computer programs with NLLS (non-linear least squares) algorithms [143, 144].

Capacitors do not have a perfect dielectric behaviour and this is evident from a small shift from –90º in the phase angle. The shifted angle is also an important characteristic of dielectric behaviour, and is related to the leakage current and represents the charge loss by a capacitor. This loss can be analysed, by transforming the impedance of a capacitive element to a new element, the constant phase element (CPE). The impedance of this element is given by:

$$Z = A(j\omega)^{-\alpha} \tag{3.11}$$

in which A is a constant. The CPE element is used for analysing different electrochemical systems and depending on the value of the exponent (α), different physical processes can be considered. For example, diffusion processes do not have an electrical element to represent them, and their behaviour is considered by a CPE element with an exponent value close to 0.5 [142].

The concept of the CPE element was effected in the study of the dielectric behaviour of pure solid materials, where the dielectric constant was measured and plotted in the complex form ($\varepsilon = \varepsilon_r + j\varepsilon_i$) [145]. The plot obtained is equivalent to a Randles circuit impedance spectrum in which the circle has an angle slightly shifted to values lower than 90º. The real part of the complex number corresponds to the usual value of the dielectric constant and the imaginary part is related to the energy loss and is related to the leakage current.

3.3.3 Magnetron sputter-deposition

Magnetron sputtering is a physical vapour deposition (PVD) technique undertaken under soft vacuum conditions in which positive ions from an ionised atmosphere strike the surface of a material. By a momentum transfer process (Figure 3.7), atoms of the material are ejected and collected on a substrate to form the deposit [101, 146-149].

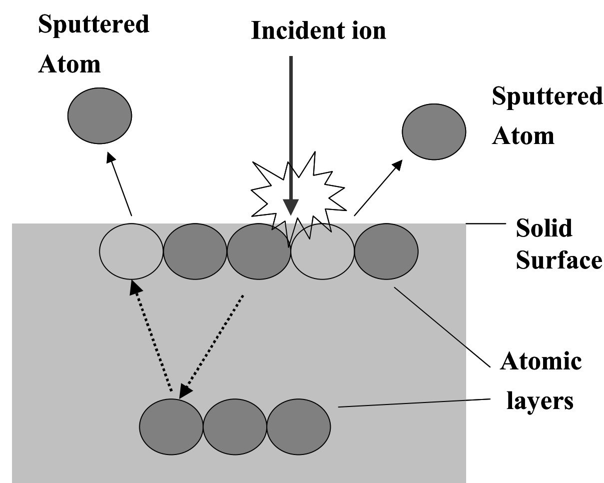

Figure 3.7 Schematic diagram showing momentum exchange processes on sputter-deposition [146].

Basically, the sputtering operation includes three steps: firstly, a vacuum of 10^{-5}-10^{-3} Pa is produced inside the sputtering chamber; then an argon or other inert gas is introduced to a pressure close to 0.1/0.5 Pa, and, finally, a potential or current is applied to the target which initiates the sputtering process (Figure 3.8). The applied electrical signal promotes the ionisation in the argon atmosphere due to the collision between free electrons, argon atoms and target surface atoms. This collision process increases until the number of electrons generated is sufficient to produce a number of ions that generates the same number of electrons. In this situation, the process is self-sustained and the gas begins to glow; this mode is called normal glow. When more power is supplied to the system, a region called abnormal discharge is achieved, which is the region used for sputtering [147].

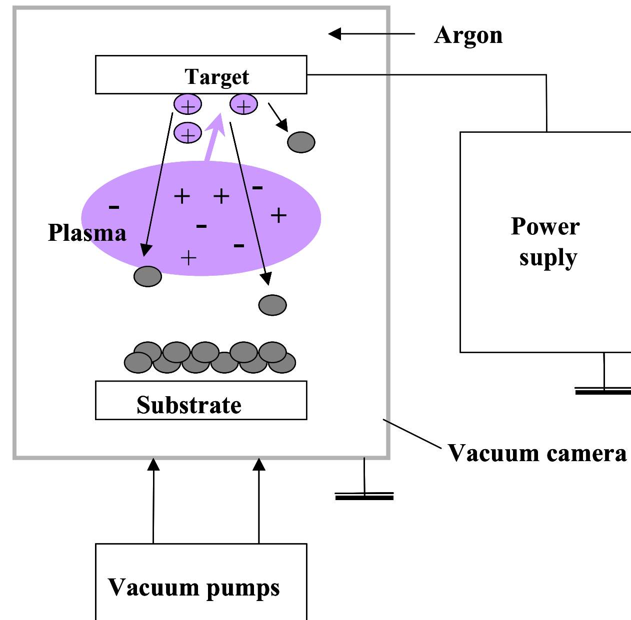

Figure 3.8 Schematic representation of the sputtering system [146].

During magnetron sputtering deposition, the plasma electrons are confined by a magnetic field, which traps the electrons near the target, thereby promoting further collisions and ionisation before drifting away. The yield of the process is increased and the same deposition is obtained at reduced potential/current values [146]. The magnetic field applied is low (0.02-0.05 T) and does not affect the positive ions; thus the yield of the sputtering process is maintained. As electrons are confined to an area above the target, defined by the magnetic field, the sputtering process is also more intense below that zone and consequently an erosion profile is formed. The magnetic field also limits the thickness of the target, as the field lines have to cross it. The target thickness usually used in laboratory sputtering machines is between 2 and 10 mm but, in industrial applications, the targets can have a thickness in the range 10-30 mm.

The sputtering process is controlled by the applied magnetic field, power supply, plasma and sputtering system configuration. The temperature of the substrates is a further parameter that has to be controlled. The structure of the sputtered metals and alloys is highly dependent of the temperature achieved during the process, affecting crystallinity, grain size and phase formation. Lower temperatures favour non-

equilibrium amorphous and/or microcrystalline structures, while high temperature of the substrates favours structures similar to materials fabricated by conventional techniques [147].

3.3.4 Rutherford backscattering spectroscopy (RBS)

RBS is a non-destructive analysis technique that measures the kinetic energy of a beam of light ions after being scattered from the surface under analysis [150-152]. The incident beam interacts with the sample and some ions are immediately scattered from the surface, while others that penetrate deeper into the sample, are also scattered, but with a lower energy that is proportional to the depth penetration (Figure 3.9). This is an important feature of this technique since the depth profile composition can be determined. Usually the incident beam is formed with He^{4+} or H^{+} ions of a few MeV energy.

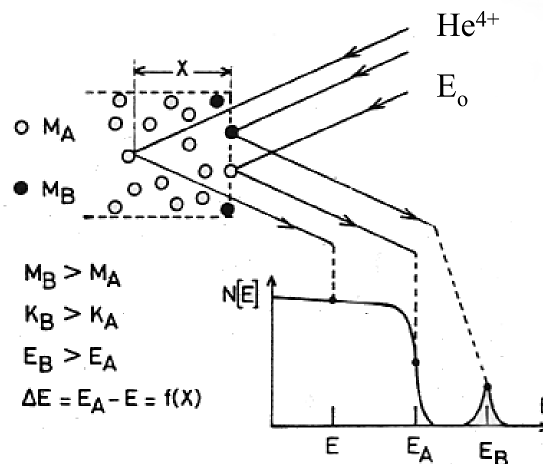

Figure 3.9 Schematic diagram showing how the depth profile is determined by RBS analysis of a binary specimen (AB) in which $M_B > M_A$ and B is present only in the surface specimen [151].

The ratio of the kinetic energy of the elastic collisions, after and before the impact, is given by the kinematic factor (K), which depends on the projectile (m) and target

(M) masses, and on the scattering angle θ (for elastic collisions). When the scattering angle is 180º, the correlation is simplified and K corresponds to:

$$K = \frac{E_1}{E_0} = \frac{(M - m)^2}{(M + m)^2} \qquad (3.12)$$

in which E_o is the incident energy and E_1 is the backscattered energy. The equation shows how the energy is translated to the atomic masses of the elements of the analysed specimen. When an ion beam strikes a surface, there are always other effects like inelastic collisions, ion implantation, etc, which means that the detected particles are only a fraction of the incident beam. The number of detected particles (P_d) is given by the equation:

$$P_d = \sigma \; \Omega \; P_i \; (Nt) \qquad (3.13)$$

in which σ is the scattering cross section, Ω is the solid detection angle, P_i represents the incident particles and Nt is the number of target atoms.

The scattering cross section is a parameter that depends on the energy of the incident beam, detection angle and on the atomic number of the target atoms. A quantitative analysis in a RBS spectrum depends on knowledge of these parameters but, if it is not possible to calculate all the parameters, the use of standard references or close composition samples is an alternative route.

3.3.5 Scanning electron microscopy (SEM)

Scanning electron microscopy (SEM) refers to an electron microscope that images the electrons that are backscattered from the analysed samples. When an electron beam strikes a sample, different interactions occur (Figure 3.10) and with the correct analysing system for each radiation or re-emitted electrons, specific information about composition, structure and thickness is obtained [153].

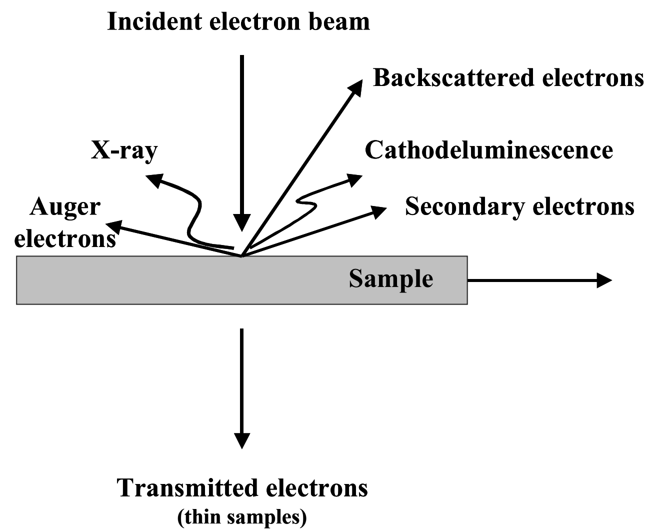

Figure 3.10 Schematic diagram of the radiation processes induced when an energetic electron beam strikes a solid material [153].

The main parts of an electron microscope are the electron source, the beam focusing system and the detector system. The most common source of electrons is a heated tungsten filament. The electrons are then accelerated in a constant stream down a column. The specimen to be examined is located near the bottom of this column. The electrons are accelerated under a DC voltage between 500 and 50000 V. During acceleration, the electron stream passes through two or more electromagnetic lenses that focus the electrons into a very fine beam, which is now ready to strike the specimen surface. The specimen is then scanned by this collimated beam and the electrons emitted from the surface move to the collector, where they are transformed into an electrical signal, then amplified and finally the image of the surface is constructed on a screen. The image magnification results from the ratio of the area scanned on the specimen to the area of the image screen; thus, when magnification is increased, this means that the electron beam is scanned over a finer area of the specimen.

Essentially there are two kinds of images used in SEM; one is formed from the secondary electrons and the other from backscattered electrons. The former type of electrons has a lower energy range (< 50 eV) as a result of inelastic interactions close to the surface. The emission of these electrons depends in an irregular way with the atomic number, but it is very sensitive to topographic effects; thus fissures, grain boundaries, precipitates or inclusions can be very easily detected. Backscattered

electrons have energies close to the incident beam, as they result from elastic collisions or with low energy loss. These electrons vary directly with the atomic number of the specimen and the image formed is brighter for heavy elements, allowing the differentiation of areas of the specimen of different composition [153].

3.3.6 Transmission electron microscopy (TEM)

Transmission electron microscopy (TEM) refers to an electron microscope that images the electrons that are transmitted through thin specimens. The specimens have to be “electron transparent” to allow the electron beam to be collected after passing through the specimen. Differences of structure and composition at a very high resolution, which can be of the order of only a few nanometres, are obtained through the image produced by the transmitted electrons [150].

Basically, the main parts of an electronic microscope are an electron source, formed by a heated filament (usually W) under high vacuum, a system of electromagnetic lenses to focus the electron beam and a collecting system. The last may be being a fluorescent screen where the sample image is produced. The energy of the electron beam depends on the analysed specimens but, for metals and oxides, is of the order of 100 - 200 kV [103].

The transmitted electrons strike a phosphor screen and light is generated: the dark areas represent areas of the specimen where fewer electrons are transmitted, corresponding to thicker or denser areas, whereas light areas correspond to thinner or less dense areas. Finally the image is also recorded on photographic film.

The sample preparation requires skill in order to achieve reliable results. For metal samples, the thickness required is in the range 150-200 nm, with ultramicrotomy representing one approach for specimen preparation.

3.3.7 Energy dispersive X-ray analysis (EDX)

EDX analysis is a technique to identify the elemental composition of the examined specimen and, nowadays, it is always an integrated feature of a scanning electron

microscope (SEM). The technique is based on analysing the X-rays emitted from the specimen surface layers after irradiation by an electron beam. The electron beam promotes electron transitions to higher energy levels in the core levels of the specimen atoms, generating inner electron vacancies. These states are unstable and tend to return to the ground state by emitting X-ray radiation. The X-ray radiation has a component, characterized by specific electron transitions, that is unique to each element, thereby allowing its identification. The emitted radiation, as usual for techniques based on energetic beams, depends on the atomic number of the target; thus, to obtain a quantitative analysis it is necessary to use standards or other methods to correct for differences in sensitivity to different elements. One such method, "ZAF" method, is used for metallic samples, where the concentration of each element (C_i) is given by:

$$C_i = Z_i A_i F_i K_i \tag{3.14}$$

where Z, A and F are factors related respectively to the atomic number, absorption of the X-ray irradiation and fluorescence effects, K_i is the ratio of the concentrations between the specimen and a standard measured under the same experimental conditions [153].

3.3.8 X-ray photoelectron spectroscopy (XPS) and Auger electron spectroscopy (AES)

XPS and AES are surface analysis techniques, both based on the photoelectron effect:

$$KE = h\nu - BE \tag{3.15}$$

where, KE is kinetic energy of the emitted core photoelectron, hν is the energy of the exciting X-ray photon and BE is the binding energy of the emitted electron (Figure 3.11) [150, 154, 155]. In XPS analysis, the energy of these ejected photoelectrons is measured precisely, which allow calculation of the binding energy of the core levels.

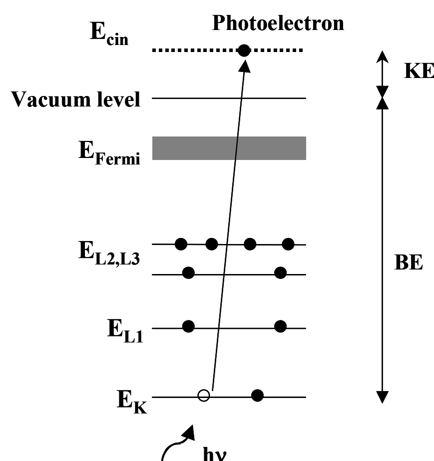

Figure 3.11 Energy diagram showing the photoelectron effect on which XPS analysis is based.

After a core hole is produced, an electron transition from an outer level occurs to fill that inner level and a photon is emitted which, in turn, promotes the ejection of an electron from an outer level. Such electrons are used in the Auger analysis (Figure 3.12).

Auger electrons and XPS photoelectrons are in a relatively low energy range, between 50 to 2000 eV. This energy range and, because other interactions may occur before the electrons leave the surface, decreases the depth penetration of these techniques, meaning that only the outermost atomic layers, in the range of a few nanometres, of the surface are analysed [154]. When a depth profile is required, the outer layers can be sputtered with an inert gas and then a new analysis is performed on the exposed surface. Sputtering and analysis are alternated until the desired depth is reached. The depth profile is then obtained as a function of the etching time. The absolute thickness of the specimen analysed can be determined by comparing the sputtering rate obtained for an equivalent specimen in which thickness is known. The sputtering process can also have an influence on the results due to changes of the valence state of the surface species, or by introducing increased roughness due to variations in the sputtering rates of the surface species. A further way to obtain depth profiles, which has the advantage of being a non-destructive method, is by changing the detection angle [150].

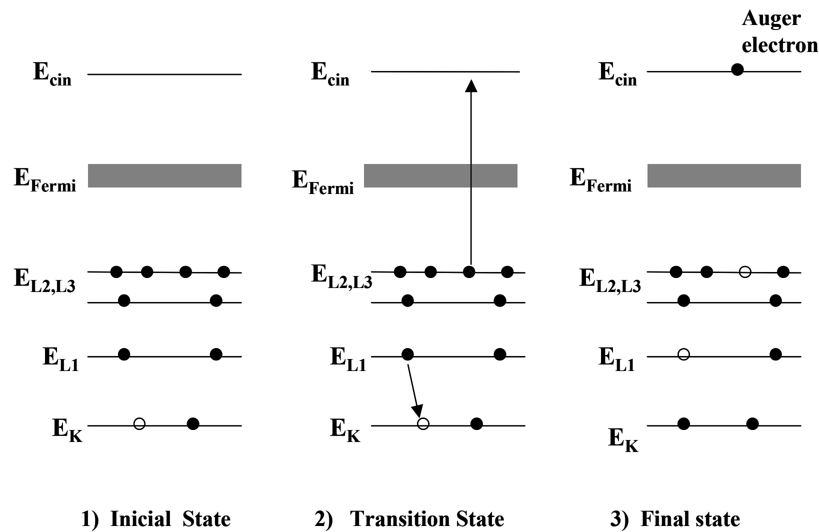

Figure 3.12 Energy diagram showing the electronic transitions used for Auger analysis [155].

One advantage of XPS analysis is the information obtained about the valence state of the elements as the energy of the core electrons is affected by the state of the outer shells as well as by the chemical environment. This feature gives rise to small shifts in the peak positions when compared with the corresponding positions in the fundamental state. Spectra usually show a great number of peaks, sometimes overlapped, and it is necessary to deconvolute the spectra of the elemental peaks to extract all information available; care should be taken with this procedure in order to avoid erroneous interpretations.

AES and XPS are usually coupled together as the equipment is similar for both techniques as well as the information obtained. AES has better lateral resolution and is able to identify fine features on the surface. XPS has the capability of determining surface chemical structure and bonding through the use of chemical shifts, whereas the same interpretation is more difficult for AES. Depth profiles are more readily obtained with AES than with XPS, which makes AES more attractive, particularly when the information desired is only related to elemental compositions.

CHAPTER 4

ELECTROCHEMICAL BEHAVIOUR OF THE NIOBIUM/THIN OXIDE FILM/ ELECTROLYTE INTERFACE

4.1 Introduction

This Chapter reports on the characterisation of the anodic processes at the metal/thin oxide film/electrolyte interface generated cyclic voltammetry. The measurements were carried out at room temperature in normally aerated and unstirred solutions of 0.6 M Na_2SO_4 (pH 5.6) and 0.15 M H_3BO_3 + 0.075 M $Na_2B_4O_7$ (pH 8.8).

It has been reported that close to the metal/oxide interface, there is an non-stoichiometric niobium oxide region, usually represented by NbO_x [156]. The presence of this oxide on the surface of the electrodes, has been associated with transient behaviour evident at the beginning of anodising. The previous behaviour corresponds to the anodic oxidation of the native oxide to the more stable Nb_2O_5 [7] species. After cathodic polarisation, the process usually observed is the insertion of hydrogen ions (protons) in the niobium oxide. This process is referred to as the electrochromic effect due to a change in oxide colour. The electrical properties of the oxide change after insertion of these ions and it has been considered to be one of the possible causes of the defecting dielectric behaviour observed on niobium oxides [54].

In order to examine the electrochemical processes of niobium electrodes, a series of voltammograms were performed. The results are also compared with data obtained with electrodes of sputtered Al-Nb alloys, with a niobium contents of 21 to 44 at.% Nb.

4.2 Electrode surface

The experiments were performed on niobium rod electrodes with a purity of 99.9 %. The electrodes were prepared by mechanical grinding as described in Chapter 3. Scanning electron micrographs show a relatively rough, mechanically prepared surface where the scratches from the grinding treatment are evident (Figure 4.1). A qualitative EDX spectrum, performed after the surface treatment, only identified niobium (Figure 4.2).

4.3 Cyclic voltammetry for the niobium rod in 0.6 M Na_2SO_4 (pH 5.6)

4.3.1 Typical voltammogram

The voltammogram obtained after mechanical grinding (wet SiC paper down to 1200 grit), performed at a potential sweep rate of 0.2 V s^{-1} between –1.5 and 0.5 V, with a step of 15 s at –1.5 V_{SCE}, shows three different zones (Figure 4.3). The values of potential and current density at the different zones or are given below:

Peak/zone identification	Potential (V_{SCE})	Current density (A cm^{-2})
peak I_a	-0.75	4×10^{-4}
zone II_{st}	-0.18 / 0.50	1.5×10^{-3}
peak III_c	-1.17	6×10^{-4}

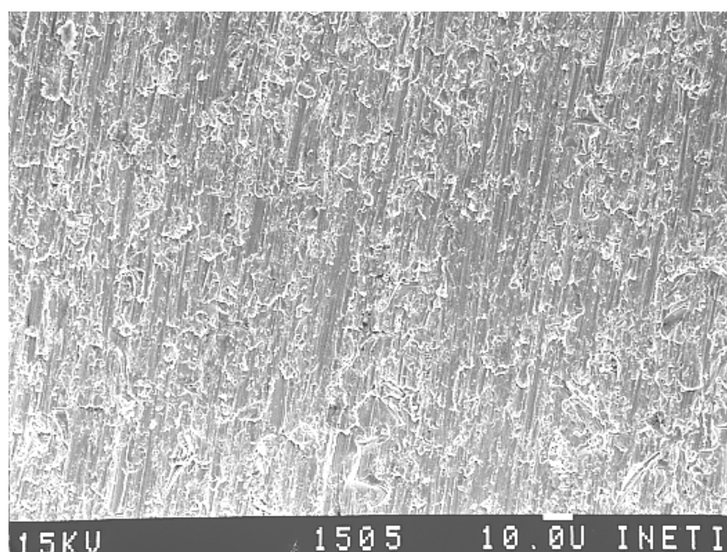

Figure 4.1 Scanning electron micrograph of the surface of the niobium rod after mechanical grinding.

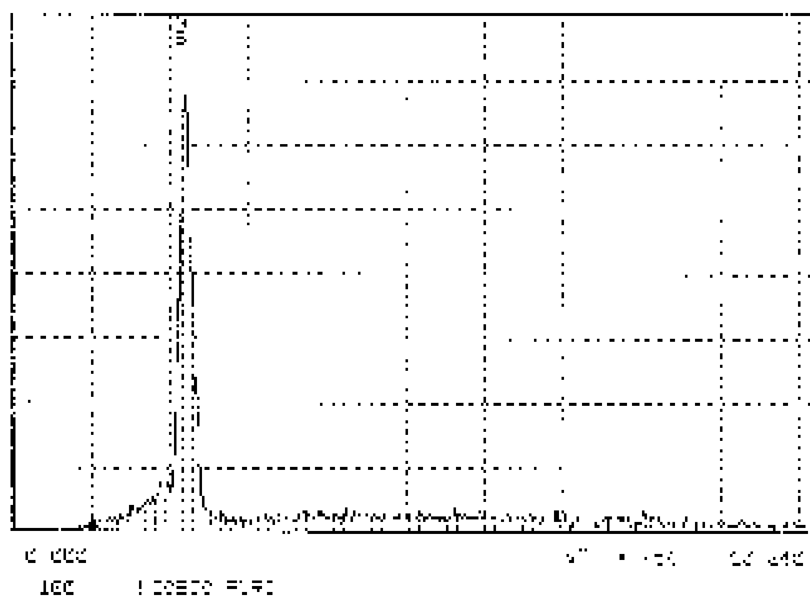

Figure 4.2 EDX spectrum of the surface of the niobium rod after mechanical grinding.

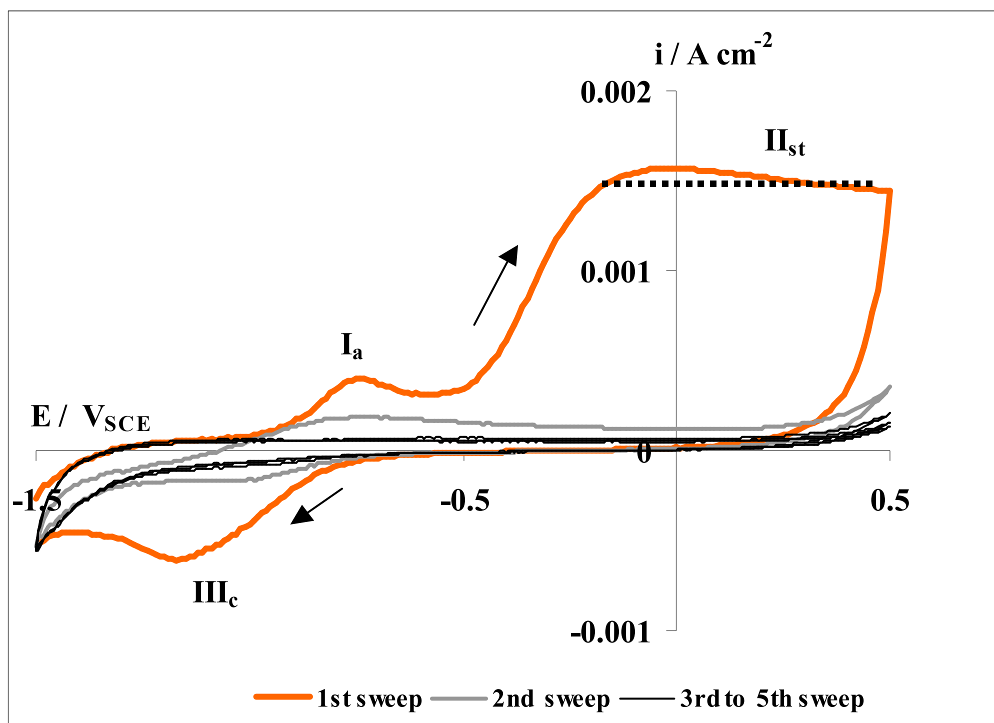

Figure 4.3 Voltammograms of the niobium rod in 0.6 M Na_2SO_4, s = 0.2 V s^{-1}, -1.5 to + 0.5 V_{SCE}.

The anodic peak (I_a) and the cathodic peak (III_c) are well defined, whereas between the potentials of –0.18 to 0.5 V, zone II_{st}, the current density is almost constant. The voltammogram also shows the differences between the first and subsequent cycles (multi-sweep effect), revealing that the zone II_{st} only appears on the first sweep. After the third sweep, no distinctive features were evident in the voltammogram.

Initial analysis suggests the following electrochemical processes are associated with peaks:

Peak I_a – associated with the surface condition of the electrode,
Zone II_{est} – formation of Nb_2O_5,
Peak III_c – insertion of hydrogen ions.

In order to further define the peak positions, different potential-time profiles were carried out, by varying the initial potential, the sweep direction (negative or positive) and the reverse potential. The following correlations were obtained:

Potential-time profile (s = 0.2 V s^{-1})	Peak Correlation
(a) -1.5 → -0.6 → -1.5 V_{SCE}	I_a
(b) -0.6 → +0.5 → -1.5 → + 0.6 V_{SCE}	$II_{st} \rightarrow III_c \rightarrow IV_a$
(c) -0.6 → -1.5 → +0.5 → - 0.6 V_{SCE}	$II_{st} \rightarrow III_c \rightarrow IV_a$

Figure 4.4.a shows that no cathodic peak is formed if the potential is reversed before reaching the zone II_{st}. The voltammogram of the second profile (Figure 4.4.b) shows that after zone II_{st}, associated with the formation of Nb_2O_5, the cathodic peak III_c is observed, which is associated with hydrogen insertion into the previously formed Nb_2O_5. Furthermore, this voltammogram shows that a new peak, not well defined, identified as IV_a, is revealed in the second sweep, after the formation of the cathodic peak III_c (Figure 4.4.b). The last profile, which corresponds to the voltammogram of Figure 4.4.c, shows that both peaks, III_c and IV_a, are only observed after the formation of Nb_2O_5.

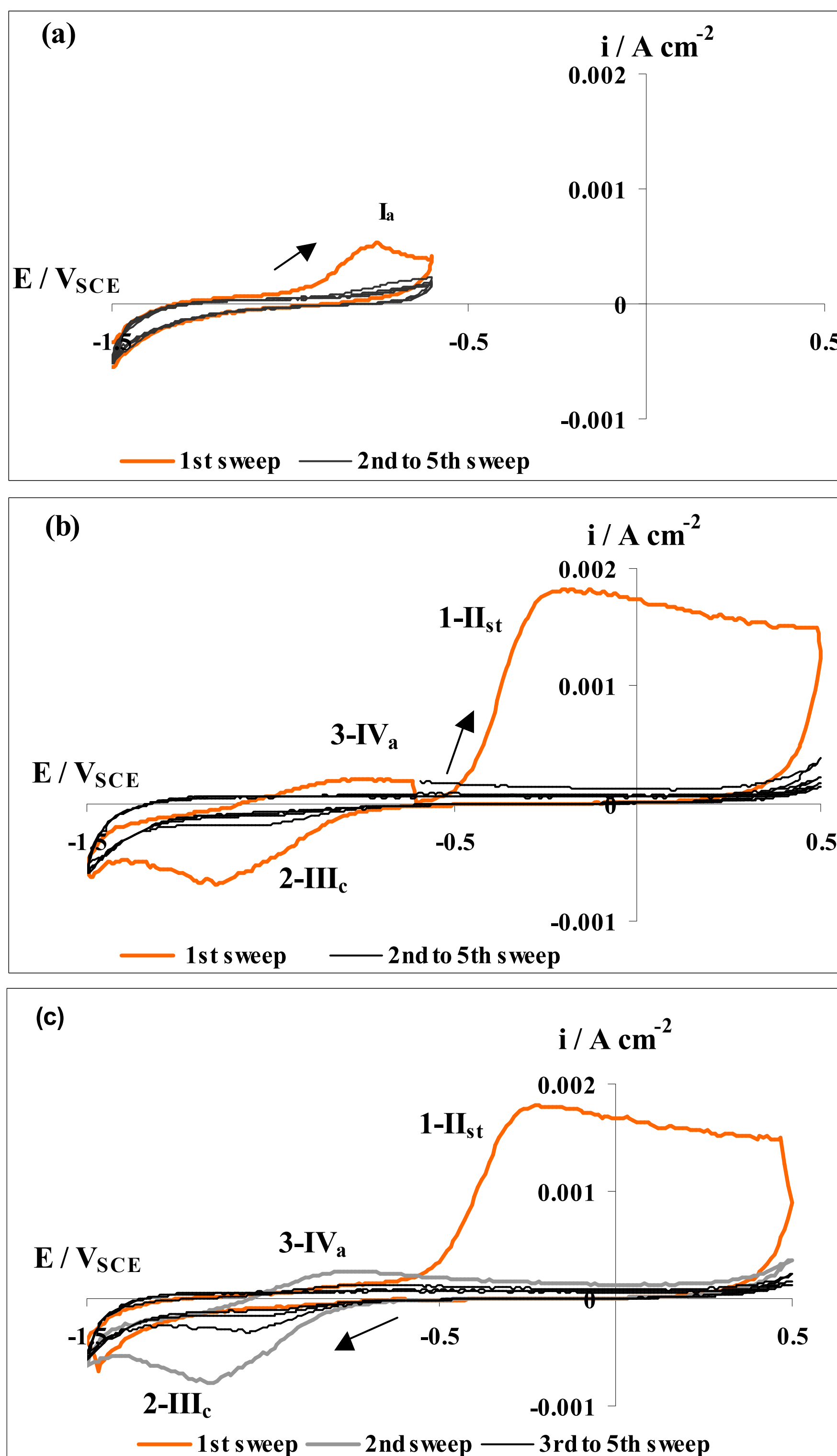

Figure 4.4 Voltammograms for the niobium rod in 0.6 M Na_2SO_4, s = 0.2 V s^{-1}, at the following potential-time profiles:
(a) -1.5 → -0.6 → -1.5 V_{SCE};
(b) -0.6 → +0.5 → -1.5 → + 0.6 V_{SCE};
(c) -0.6 → -1.5 → +0.5 → - 0.6 V_{SCE}.

4.3.2 Effect of sweep rate

The effect of sweep rate variation, from 0.65 to 0.005V s^{-1} is shown in Figure. 4.5. Voltammograms were carried out from –1.5 to 0.5 V_{SCE} for each sweep rate and the electrode was mechanically ground after each voltammogram. The results showed that the current at peaks I_a and III_c, and zone II_{st}, increase with increasing sweep rate.

The variation of log(ip) with log(s), in which ip is the peak current density and s is the potential sweep rate, displays a linear relationship (Figure 4.6). For peaks I_a and III_c, the linear relation was only fitted for a potential sweep rate above 0.1 V s^{-1} (Figures 4.6.a and 4.6.c) because these peaks are not well defined at lower rates. For the zone II_{est} the plotted values of the current density are the values measured at +0.2 V. This value was selected because it is out of the "overshoot" observed at the highest potential sweep rates. This zone, associated with the formation of Nb_2O_5, shows a linear plot over the entire range of the potential sweep rate variation (Figure 4.6.b). The slopes obtained are respectively 0.91, 0.96 and 1.3 for peaks I_a, II_{st} and III_c.

The charge per unit surface area (q_p) associated with peaks (I_a and III_c) and zone II_{st} were also calculated and plotted against the corresponding potential sweep rate (Figure 4.7). It is found that the charge associated with zone II_{st} is almost constant, in the range of 0.0075 ± 0.0002 C cm^{-2} for a sweep rate higher than 0.05 V s^{-1} (Figure 4.7.a). The charge associated with peak I_a is also constant at potential sweep rates of 0.1 to 0.65 V s^{-1}; conversely the charge associated with the cathodic peak, III_c, shows an increase from 0.15 to 0.4 V s^{-1} before reaching a plateau value (Figure 4.7.b).

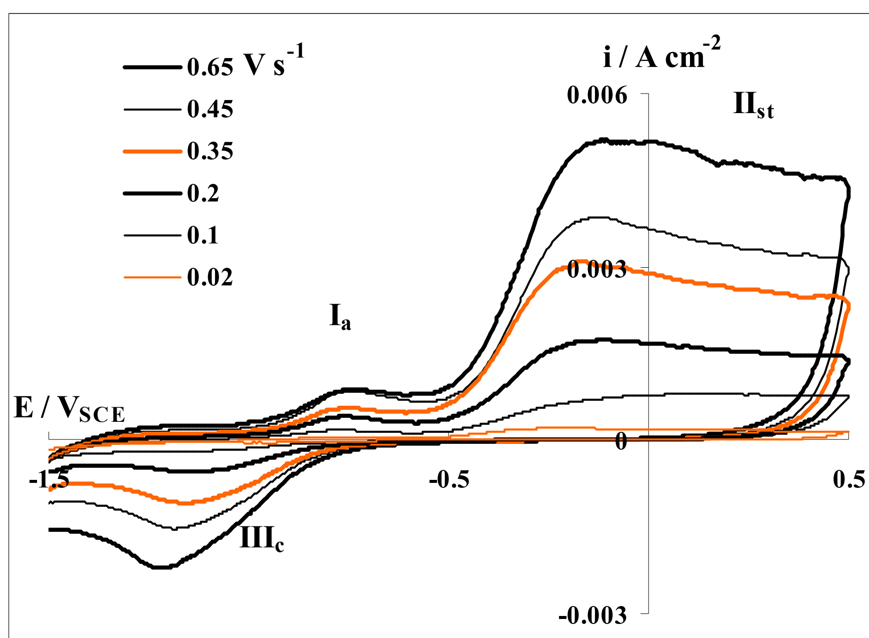

Figure 4.5 Voltammograms showing the effect of sweep rate for the niobium rod in 0.6 M Na_2SO_4, -1.5 to + 0.5 V_{SCE}.

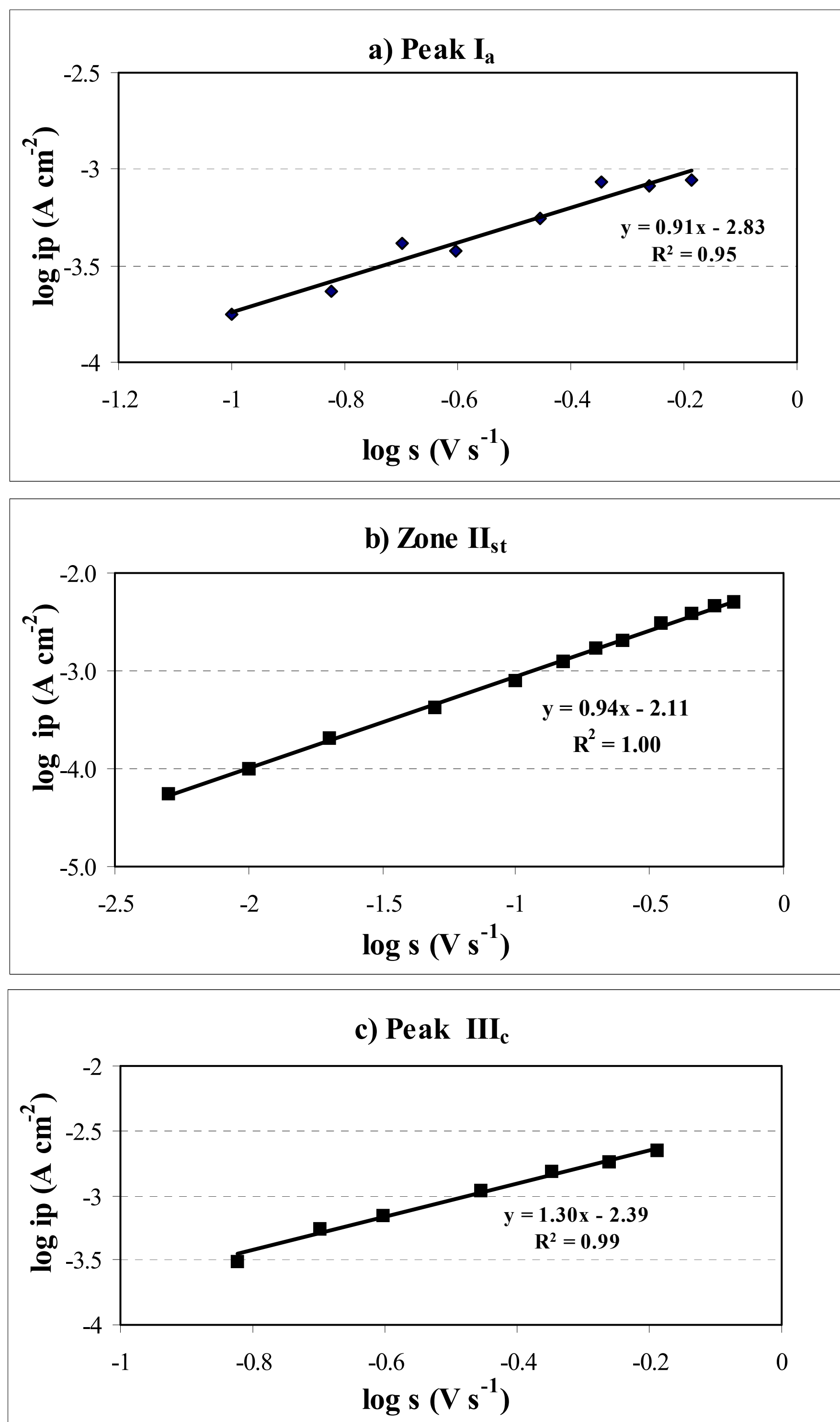

Figura 4.6 Variation of log (ip) with log (s) for the niobium rod in 0.6 M Na_2SO_4, -1.5 to 0.5 V_{SCE}: (a) peak I_a; (b) zone II_{st}; (c) peak III_c.

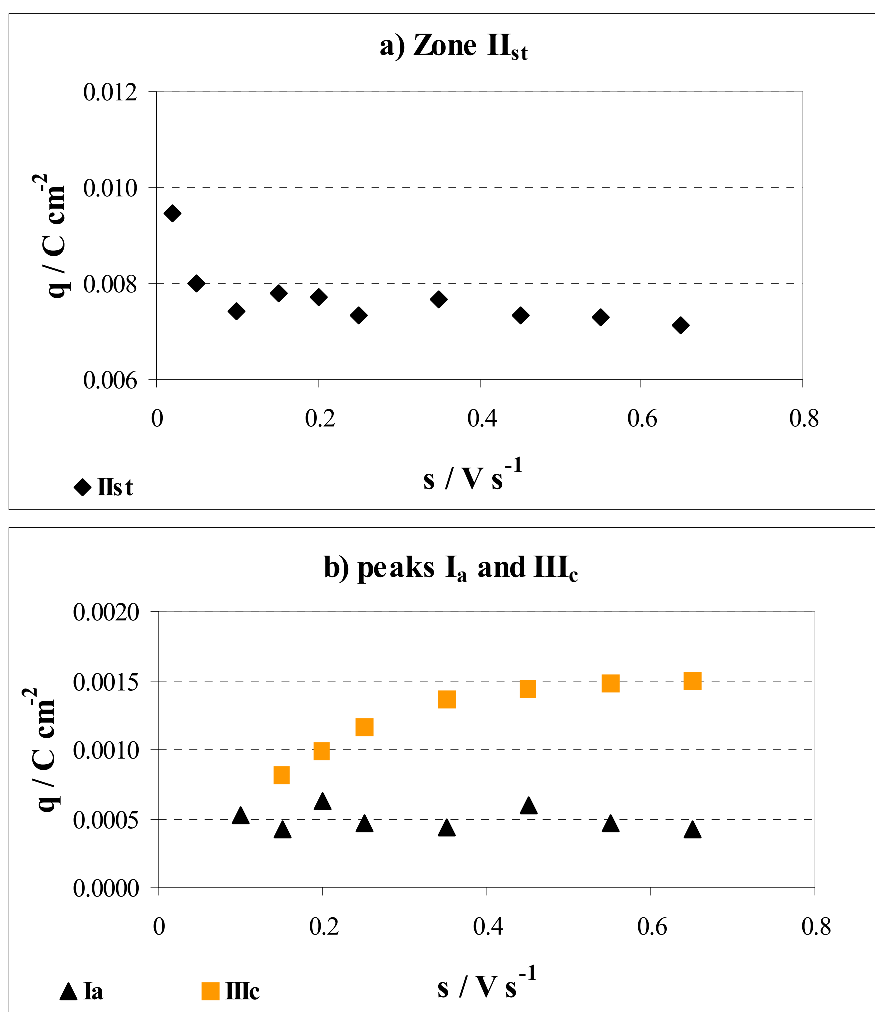

Figure 4.7 Variation of the peak charges (q_p) with potential sweep rate (s) for the niobium rod in 0.6 M Na_2SO_4,-1.5 a 0.5 V_{SCE}: (a) zone II_{st}; (b) peaks I_a and III_c.

4.3.3 pH effect

The pH variation in the acid range of 5.6 to 2.6 was examined on the behaviour. The pH adjustment was made by adding 0.6 M H_2SO_4 solution to the working solution to maintain the concentration of sulphate ions. For pH in the alkaline range (> 7 to 12), the adjustments were made by adding aliquots of 0.1 M NaOH solution.

The results obtained in the acid range show that the peak I_a is not observed and the zone II_{st} is slightly increased at pH of 2.6. The cathodic peak, III_c increases with reduction in pH and shows a marked rise at pH of 2.6 (Figure 4.8). At this pH value, a strong hydrogen evolution was observed.

In the alkaline range, the results show an increase of peak I_a to pH 11; whereas at pH 12, peaks I_a and II_a overlap. Peak III_c is not readily observed at pH ≥ 11 (Figure 4.9).

The variation of i_p with pH shows that the most significant influence is observed for peak I_a in the alkaline range (Figure 4.10). This suggests a direct correlation with the hydroxyl concentration, probably associated with an adsorption process. The current density of the zone II_{st}, associated with the formation of Nb_2O_5, shows little variation in the range of 0.0015 to 0.002 A cm^{-2}, revealing the electrochemical stability of niobium oxide over the entire pH range. Peak III_c increases with pH decrease in the acid range, but this effect is not clear because hydrogen evolution, observed at these values of pH and potentials, hinders other processes.

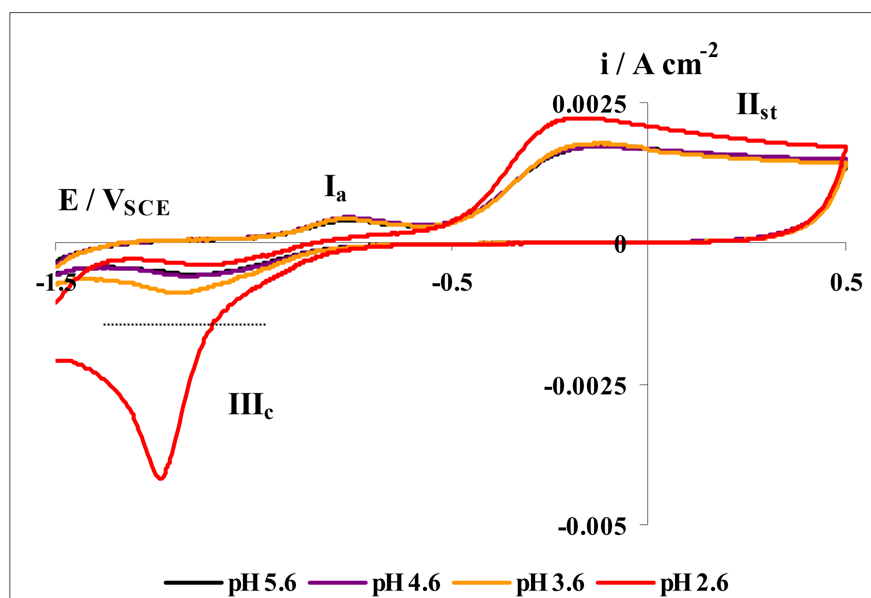

Figure 4.8 Voltammograms showing the effect of pH (5.6 to 2.6) for the niobium rod in 0.6 M Na_2SO_4, s = 0.2 V s^{-1}, -1.5 to 0.5 V_{SCE}.

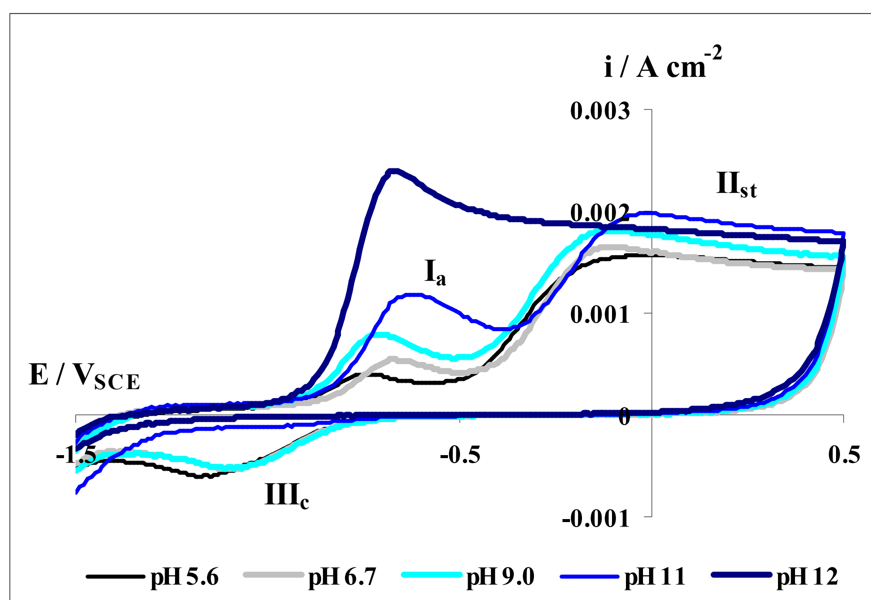

Figura 4.9 Voltammgrams showing the effect of pH (5.6 to 12) for the niobium rod in 0.6 M Na_2SO_4, s = 0.2 V s^{-1}, -1.5 to 0.5 V_{SCE}.

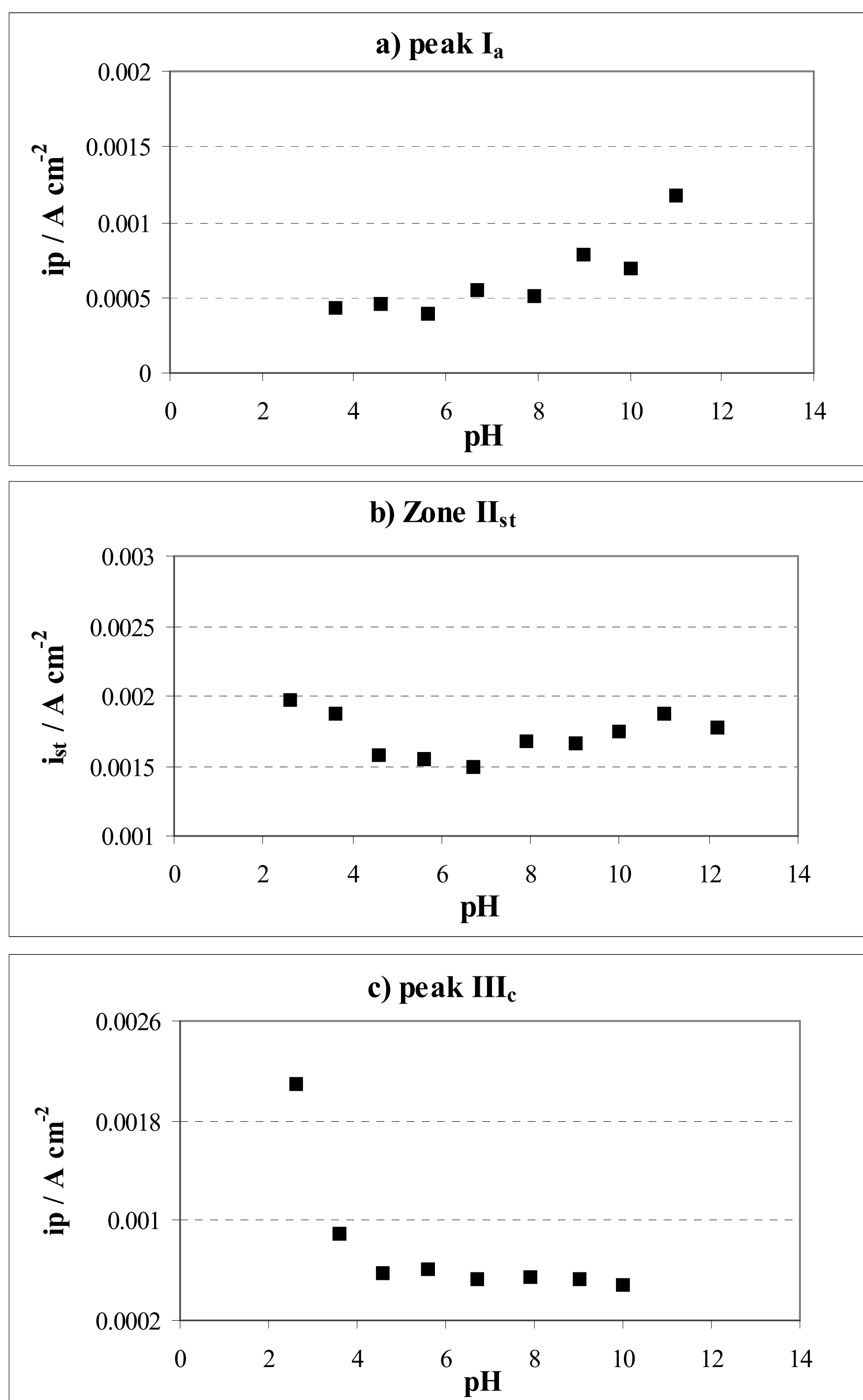

Figura 4.10 Variation of the peak current densities with pH for the niobium rod in 0.6 M Na_2SO_4, s = 0.2 V s^{-1}, -1.5 to 0.5 V_{SCE}: (a) peak I_a; (b) zone II_{st}; (c) peak III_c.

4.3.4 Effect of sweep reversal

The effect of reversing the potential at different values of anodic potential, from 0.5 to 2.5 V_{SCE}, reveals that current density of peak III_c increases with increase of the potential at which the sweep was reversed (Figure 4.11). The results show that the cathodic process associated with peak III_c is dependent on the thickness of the anodic Nb_2O_5 film formed at the electrode surface. Further, as it is also dependent on pH, it can be associated with hydrogen insertion in the formed oxide previously.

4.3.5 Effect of holding the potential at –1.5 V

The potential of –1.5 V was held for various intervals of time (0 to 200 s) before commencing the potential sweep. The voltammograms show a significant increase of the current density of the first anodic peak, I_a (Figure 4.12). This effect is interpreted as a consequence of a pH variation at the electrode surface. Thus, at –1.5 V, hydrogen evolution proceeds at the electrode surface and holding the potential influences the pH at the surface; thus, an increase of OH^- ions is generated at the surface, which increases the adsorption of these ions at local sites at the oxide/electrolyte interface. Therefore, the effect is similar to the variation of the current density of peak I_a observed with pH variation in the alkaline range.

4.4 Cyclic voltammetry of the niobium rod in 0.15 M H_3BO_3 + 0.075 M $Na_2B_4O_7$ (pH 8.8)

4.4.1 Effect of sweep rate

The effect of sweep rate was also performed in a borate buffer solution (0.15 M H_3BO_3 + 0.075 M $Na_2B_4O_7$) of pH 8.8. The voltammograms show that only the anodic peak I_a and zone II_{st} are revealed (Figure 4.13), with a linear dependence of log (i_p) with sweep rate also evident. The values of the slopes are respectively 1.29 and 0.96 (Figure 4.14).

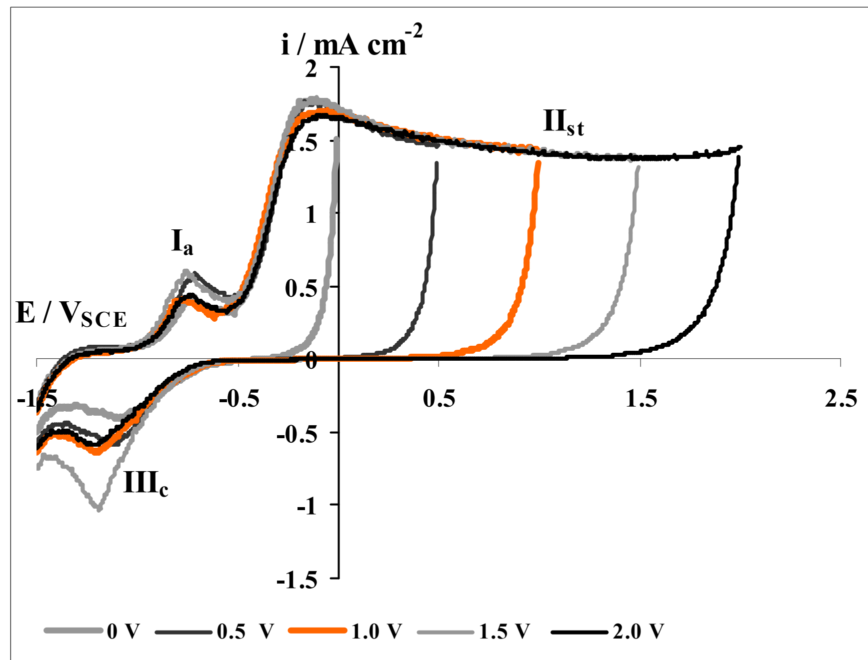

Figure 4.11 Voltammograms showing the effect of potential reversal at different values of positive potential limit for the niobium rod in 0.6 M Na_2SO_4, s = 0.2 V s^{-1}, -1.5 to 0.5 V_{SCE}.

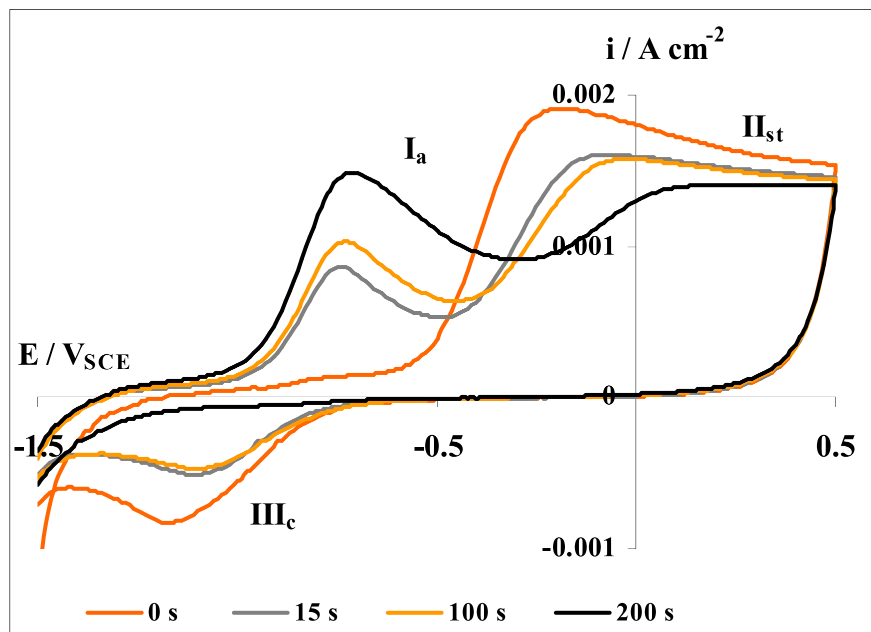

Figure 4.12 Voltammograms showing the effect of holding the potential at 0, 15, 100 and 200 s for the niobium rod in 0.6 M Na_2SO_4, s = 0.2 V s^{-1}, -1.5 to 0.5 V_{SCE}.

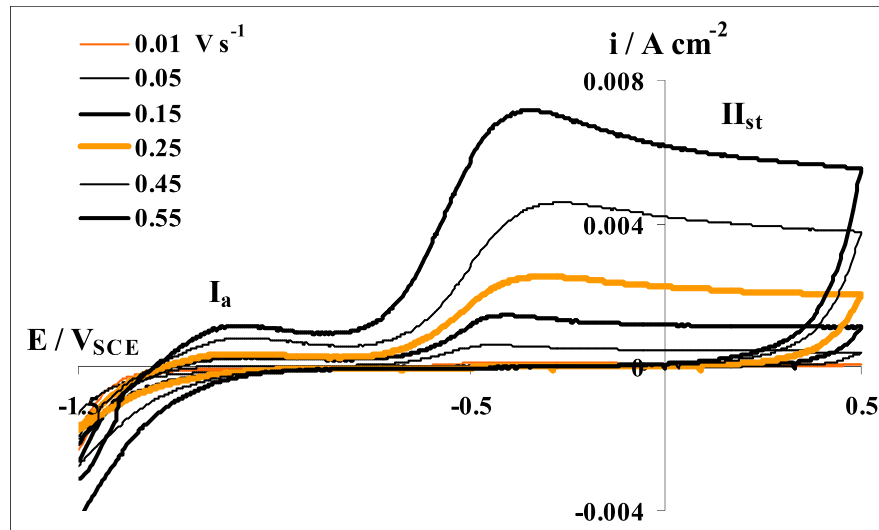

Figure 4.13 Voltammograms showing the effect of sweep rate for the niobium rod in 0.15 M H_3BO_3 + 0.075 M $Na_2B_4O_7$ (pH 8.8), -1.5 to 0.5 V_{SCE}.

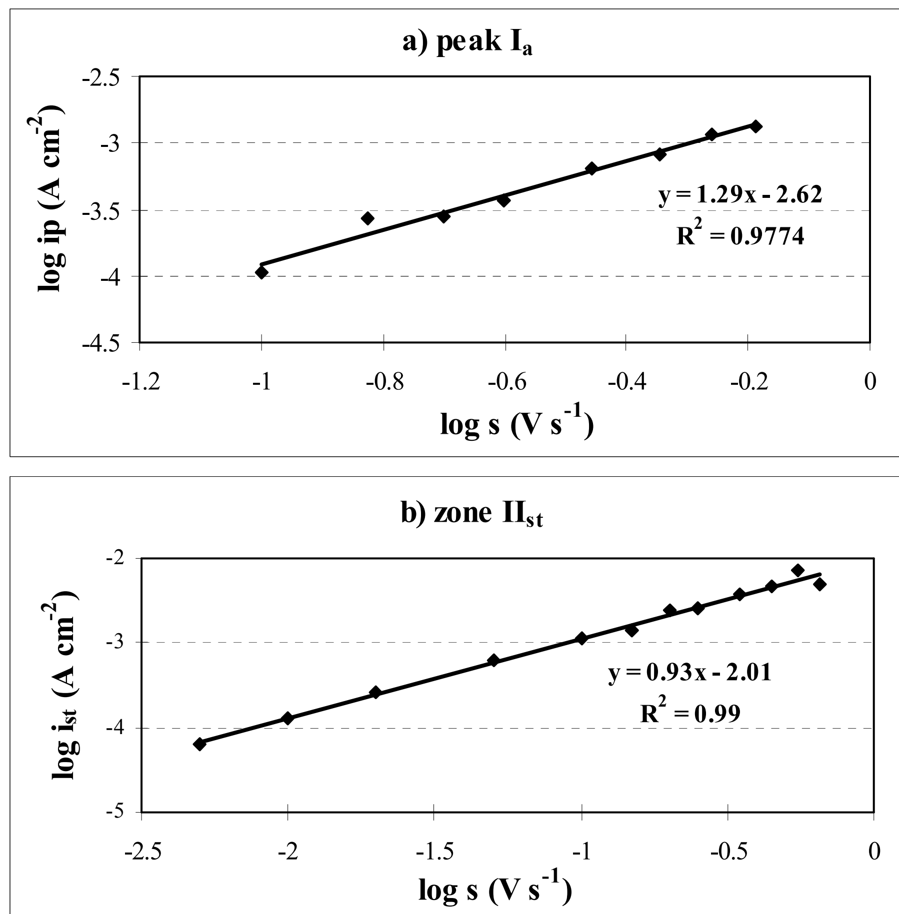

Figura 4.14 Variation of log (ip) with log (s) for the niobium rod in 0.15 M H_3BO_3 + 0.075 M $Na_2B_4O_7$ (pH 8.8), -1.5 to 0.5 V_{SCE}: (a) peak I_a; (b) zone II_{st}; (c) peak III_c.

4.5 Cyclic voltammetry for the sputtered niobium in 0.6 M Na_2SO_4 (pH 5.6)

The voltammograms for a sputtered niobium specimen, employing several sweeps, were also carried out in 0.6 M Na_2SO_4 at pH 5.6, at a potential sweep rate of 0.2 Vs^{-1} between –1.5 and 0.5 V (Figure 4.15). The voltammograms show that peak I_a is not clearly evident, whereas II_{st} is located at increased anodic potential. These voltamograms were obtained on a sputtered niobium specimen that had been stored for at least one month in a desiccator. This suggests that the oxide has thickened during storage, and, consequently, the anodic oxide is only able to form at higher values of potential. The multi-sweep effect shows the correlation between III_c and IV_a. These peaks are better defined than the corresponding ones obtained for the surface after grinding treatment. This feature is certainly associated with clean surface obtained by sputtering and to the relatively flat surface due to substrate preparation The peak IV_a is associated with the reverse hydrogen intercalation process at the Nb(V) oxide/electrolyte interface, represented by:

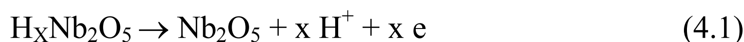

$$H_XNb_2O_5 \rightarrow Nb_2O_5 + x\ H^+ + x\ e \qquad (4.1)$$

4.6 XPS and AUGER analyses of the electrode surface

X-ray photoelectron spectra of specimens were measured for the following experimental conditions:

- immediately after surface grinding (1),
- after storage for 15 days in a desiccator (2),
- after cyclic voltammetry (50 cycles) at a potential sweep rate of 0.2 V s^{-1} between –0.5 to 2.5 V_{SCE} (3).

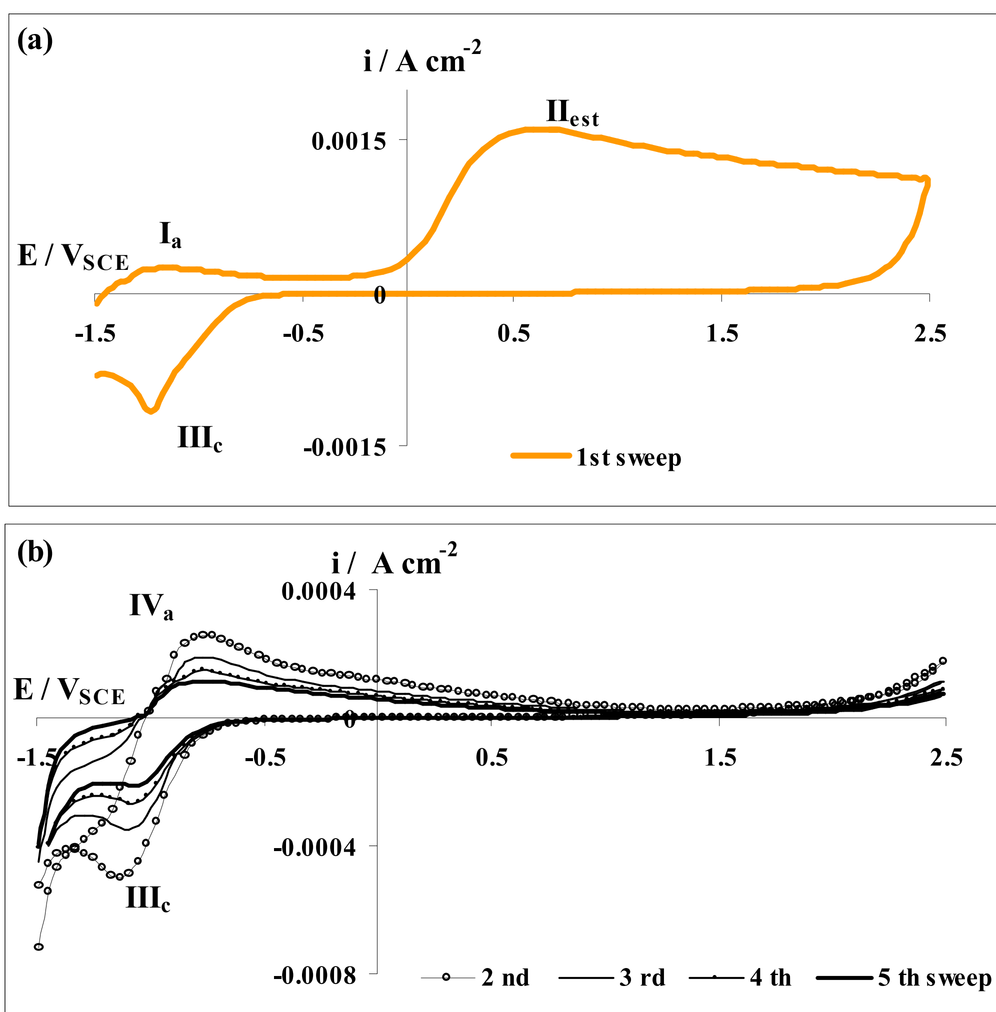

Figure 4.15 Voltammograms for the sputtered niobium in 0.6 M Na_2SO_4, s = 0.2 V s^{-1} from -1.5 to +0.5 V_{SCE} showing the first sweep (a) and subsequent sweeps (b).

The spectrum (1) for a surface that had just been ground shows the peaks Nb(V) $3d_{3/2}$ and $3d_{5/2}$ corresponding to Nb_2O_5, and the peaks Nb(0) $3d_{3/2}$ and $3d_{5/2}$ corresponding to niobium metal. Peaks are also observed with binding energies between the identified species, associated with oxides of lower valence than five (Table 4.1 and Figure 4.16). The peaks were identified after deconvolution into the component bands using VG specific software. X-ray radiation does not change the stoichiometry of the niobium species [156]; thus the results show that Nb_2O_5 is immediatly formed on air contact. The results are similar to those obtained by Grundner and Halbritter [156], as previously considered, in which a non-uniform layer of niobium oxide species of different valence states is formed on the niobium surfaces.

The second spectrum (2), measured after storage in a desiccator, show essentially the peaks corresponding to Nb(V) and Nb(IV) species, suggesting that the lower valence oxides are converted to Nb_2O_5, or that the initial oxide layer is now thicker due the increased of thickness of Nb_2O_5, since the metal peaks Nb(0) are no longer detected. The spectrum obtained after cyclic voltammetry between -0.5 to 2.5 V_{SCE} only reveals Nb_2O_5, as expected.

AUGER spectra were also obtained for the experimental conditions 1 and 3. The depth profiles were generated in function of the etching time, from the main ionisations for each element detected, niobium and oxygen, after background subtraction (Figure 4.17). The results suggests that the oxide layer is not uniform. However, the information obtained was not conclusive, since niobium species change the stoichiometry and concentration under argon ion sputter etching [156].

Table 4.1 Standard and experimental values of the binding energies for niobium and niobium oxides.

Standard energies and experimental conditions	**Binding energies (eV)**			
	Nb(V) **3d3/2** **3d5/2**	**Nb(IV)** **3d3/2** **3d5/2**	**Nb(II)** **3d3/2** **3d5/2**	**Nb(0)** **3d3/2** **3d5/2**
Standard Energies	**210.2** **207.4**	**208.7** **205.9**	**207.5** **204.5**	**205.0** **202.4**
(1) Immediately after grinding	210.2 207.7	206.8* * not identified	204.4* * not identified	205.3 202.6
(2) After storing the specimen for 15 days	210.5 207.7	208.3 205.5	----- -----	----- -----
(3) After cyclic voltammetry (-0.5 to 2.5V) 50 cycles	210.3 207.6	----- -----	----- -----	----- -----

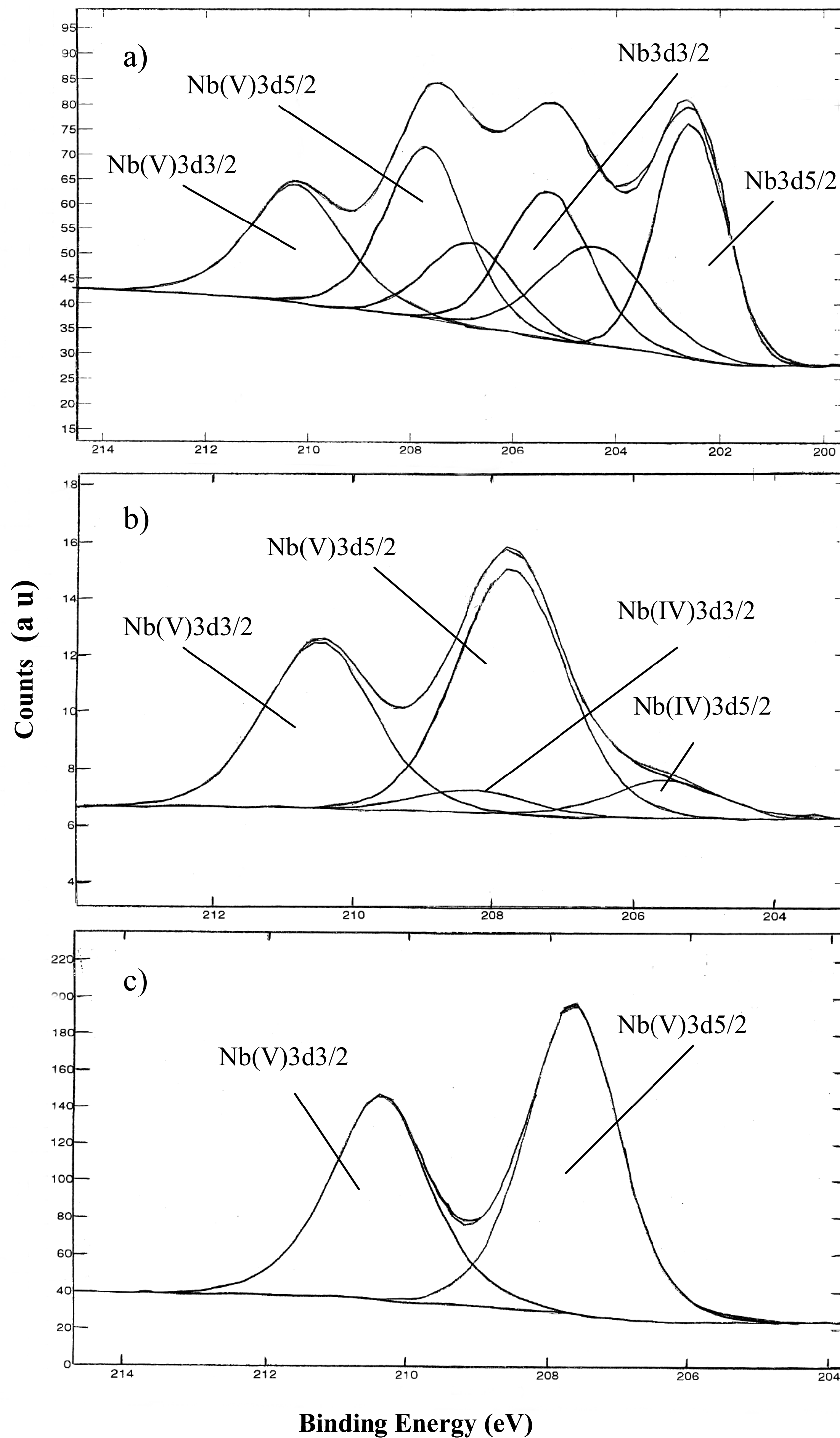

Figure 4.16 XPS spectra obtained for the niobium rod prepared under various experimental conditions: (a) immediately after grinding; (b) after grinding and storing the specimen for 15 days in a desiccator; (c) after cyclic voltammetry.

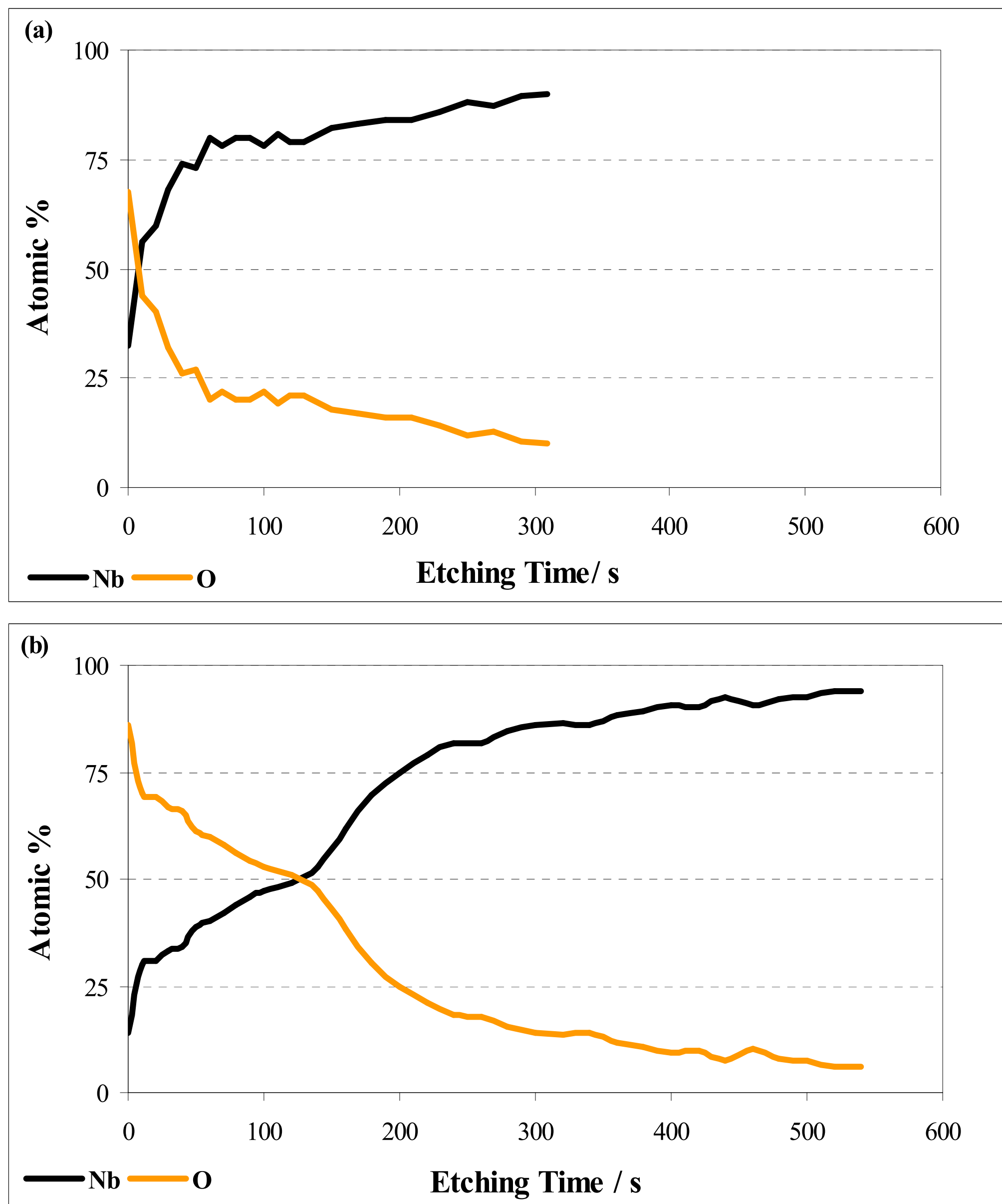

Figure 4.17 Auger depth profiles for the niobium rod prepared under various experimental conditions: (a) immediately after grinding; (b) after cyclic voltammetry.

4.7 Cyclic voltammetry of sputtered Al-Nb alloys in 0.6 M Na_2SO_4 (pH 5.6)

Voltammograms were also carried out using multi-sweeps for sputtered specimens of the alloys Al-Nb with niobium contents of 21 to 44 at.% (Figure 4.18).

The specimens were sputtered directly onto glass substrates to avoid effects from the underlying aluminium substrate. Before use, the specimens were stored for at least one month in a desiccator. The voltammograms show only one anodic peak at the potential of +0.5 V_{SCE}. This peak is associated with the formation of a mixed oxide of Al_2O_3 and Nb_2O_5. These alloys have high niobium contents; thus, a enriched alloying element layer, formed at the metal/oxide interface is not anticipated (Chapter 1), even though, 20 at.% of alloying element is close to the limits of concentration at which the layer may be observed. The voltammograms of the alloys with niobium contents of 31 and 44 at.% showed the peak associated with hydrogen ion insertion, III_c (Figure 4.19).

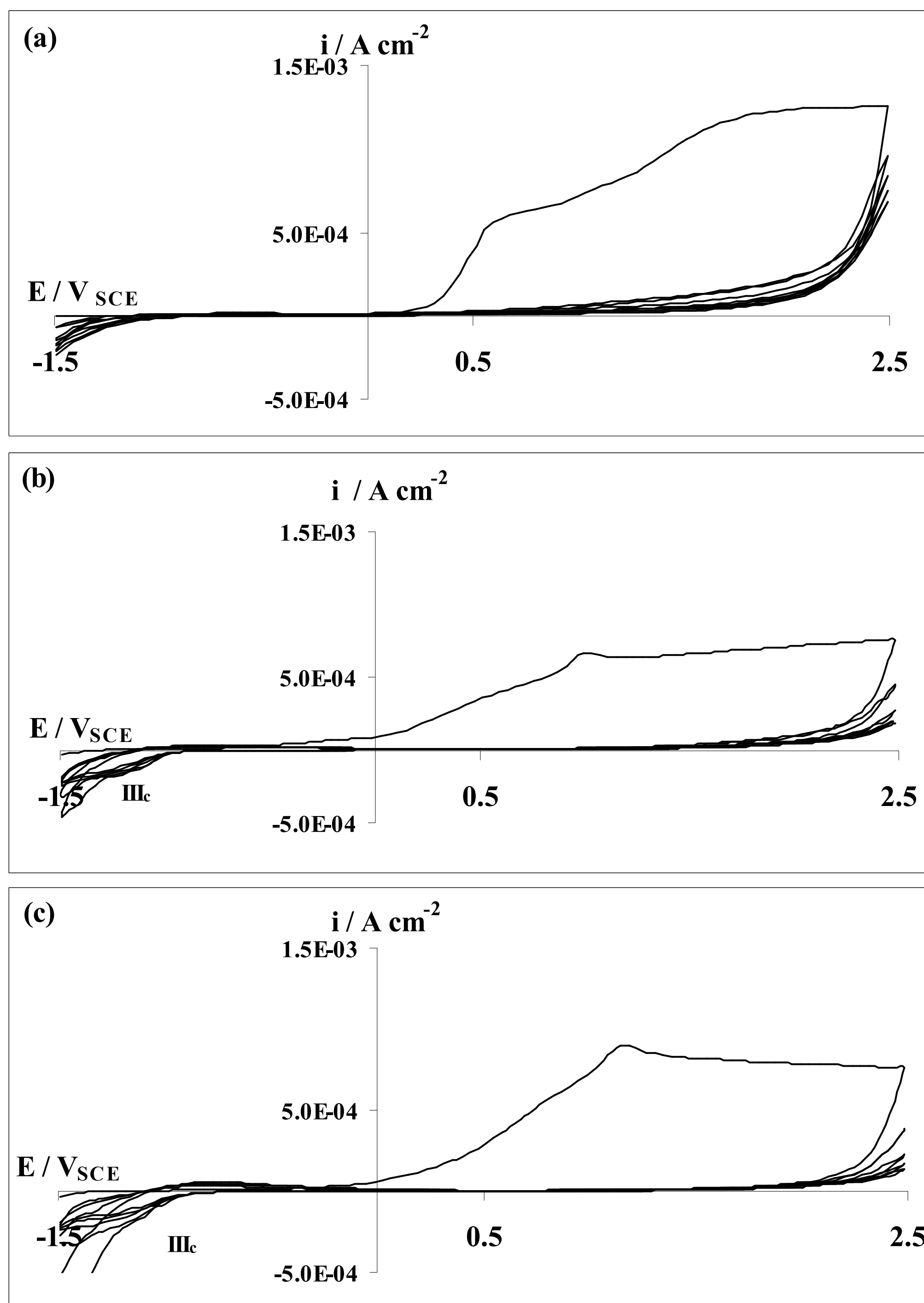

Figure 4.18 Voltammograms with multi-sweeps obtained at 0.2 V s^{-1}, from -1.5 V to + 2.5 V_{SCE} in 0.6 M Na_2SO_4 for the sputtered alloys: (a) Al-21 at.% Nb alloy; (b) Al-31 at.% Nb alloy; (c)Al-44 at.% Nb alloy.

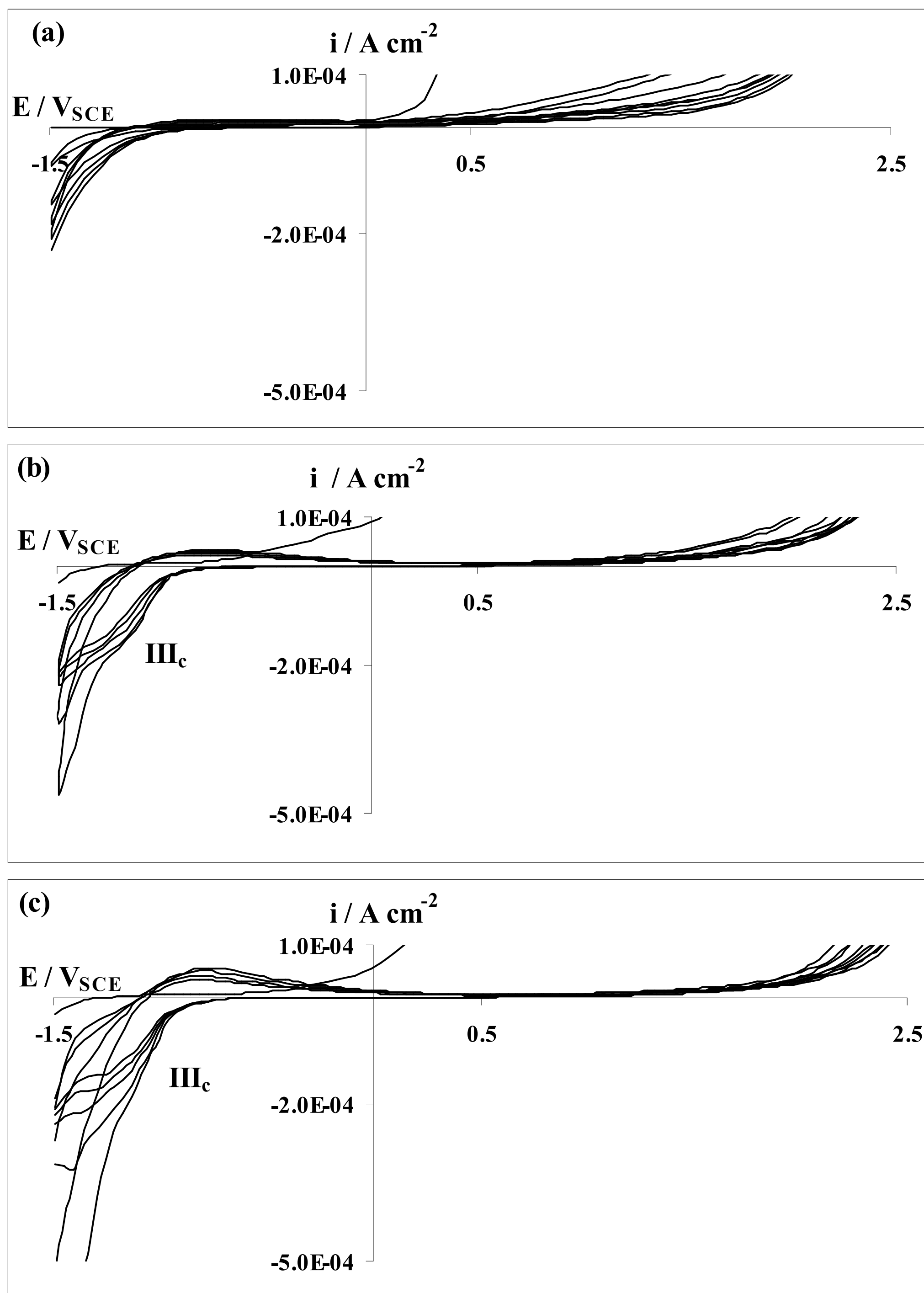

Figure 4.19 Cathodic side of the voltammograms with multi-sweeps obtained at 0.2 V s^{-1} from –1.5 V to + 2.5 V in 0.6 M Na_2SO_4 for the sputtered alloys: (a) Al-21 at.% Nb alloy; (b) Al-31 at.% Nb alloy; (c) Al-44 at.% Nb alloy.

4.8 Discussion

The experimental results obtained from the voltammetry studies, together with surface analysis of the electrodes by XPS and AES, suggest the following interpretation for the electrochemical processes observed at a the niobium surface:

Potential (V_{SCE})	Electrochemical Processes $I_a \rightarrow II_{st} \rightarrow III_c \rightarrow IV_a$
Anodic 1st sweep	adsorption of OH^-: (I_a) $NbO_x + OH^- \rightarrow NbO_x(OH^-)$ E= -0.75 V_{SCE} (related with the $[OH^-]$ and electrode surface condition) Formation and growing of Nb_2O_5: (II_{st}) $NbO_x / NbO_x(OH^-) + mH_2O \rightarrow Nb_2O_5 + ne + nH^+$ $E \geq -0.18$ V
Anodic 2nd and forward sweeps	Oxide discharge process (hydrogen ions removal): (IV_a) $H_xNb_2O_5 \rightarrow Nb_2O_5 + xH^+ + xe$ (observed after the formation of Nb_2O_5 and after cathodic polarization at ≤ -1.17 V_{SCE})
Cathodic 1st and forward sweeps	Oxide charge process (hydrogen ions insertion): (III_c) $Nb_2O_5 + xH^+ + xe \rightarrow H_xNb_2O_5$ (E= -1.17 V observed after the formation of Nb_2O_5)

The interpretation corresponds to experimental results of niobium electrodes with mechanical surface treatment. Sputtered niobium electrodes were also tested and the same electrochemical processes were identified, although the metal surface is relatively clean and flat, which improved peak definition, and the initial air-formed oxide layer is thicker (due to storage).

The first anodic peak (Ia) is associated with the surface treatment and with the initial air-formed oxide layer. XPS analysis, performed immediately after grinding, revealed not only the peaks associated with the species Nb_2O_5 but, it also revealed small peaks, associated with lower valence species (Table 4.1). Thus, it is considered that this initial oxide layer is a mixed layer of Nb_2O_5 and NbO_x. Finally it is considered that NbO_x provides preferential sites for adsorption of hydroxyl ions before oxidation to the more stable Nb_2O_5. The strong dependence of pH in alkaline range of the peak (I_a) reinforces this interpretation.

The AES profile, suggests that the anodic oxide layer formed potentiodynamically to 2.5 V is not an uniform layer of Nb_2O_5, even though the results were not conclusive since argon ion sputtering can change the stoichiometry of niobium species. Grundner and Halbriter analysed the composition of the initial air-formed oxide layer on pure niobium samples after different surface treatments, including electropolishing, using XPS and AES techniques. All the surfaces revealed that the initial oxide comprised two layers. The first, close to the metal, is an inhomogeneous layer of Nb_2O/NbO oxides of 1 nm thickness; the second, above the first one, is mainly Nb_2O_5 and has a thickness of 2 nm. The Nb_2O_5 film tends to thicken and stabilize at a thickness of 6 nm after storage [156]. The potential-time behaviour for anodising of pure niobium at constant current density becomes linear at 3-4 V (Chapter 5). These values, converted to thickness using the 2.32 nmV^{-1} formation ratio (determined by TEM in Chapter 5), correspond to a thickness range of 7-9 nm, which is very close to the values of Grundner et al. Such thicknesses appear to correspond to the stabilization value, which is reached after exposure to air. This value is thicker that the usual value obtained for pure aluminium anodised under similar experimental conditions of: 2V x 1.2 nm/V= 2.4 nm. Thus, this initial oxide layer has a thickness that is related to the electrical characteristics of the oxide, indicating that a less insulating oxide thickens during exposure to air.

The interpretation of the other peaks is in agreement with the processes proposed by several authors. The anodic oxide formed is Nb_2O_5. The variation log ip with log s, where ip is the peak current density and s is the sweep rate, shows a slope close to one which is in agreement with the theory of an oxide that grows according to the high field conduction model (Chapter 1). Further, as expected, the oxide has high

chemical stability, since the oxide is formed over the pH range tested (2.6 to 11), with a similar efficiency (constant charge).

The cathodic peak is associated with the hydrogen insertion reaction; this peak is only revealed after Nb_2O_5 has been formed on the electrode surface. The specimens prepared by sputtering show improved peak definition as a consequence of the improved surface condition, e.g. flatness and reduced contaminant species. Flatness contributes to better defined concentration profiles and homogeneous energy of the electrode surface; on the other hand, contaminant species can block local sites for redox-processes. The hydrogen insertion process is considered quasi-reversible. This statement is based on the diagnosis of an adsorption process, i.e, a reverse peak is observed, but both peaks are asymmetric and the peak potentials are not coincident [140]. The potential values of this process, around $-1V_{SCE}$, are out of the anodic potential range achieved during anodising at constant current; thus, it is not possible for hydrogen (due to this process) to interfere on the electrical properties of the anodic oxide layer.

The voltammograms obtained for the Al-Nb alloys show only one anodic peak, which is assumed to be the simultaneous oxidation of Nb and Al atoms. The peak shape on the voltamogram obtained for the alloy Al-21 at.% Nb suggests that there may be a slight difference at very commenment of the oxide formation, but as it is shown on Chapter 5, no enriched alloying element layer was observed by TEM or identified in the RBS spectrum.

The alloys with niobium content higher than 31 at.% show the cathodic peak related to the hydrogen insertion process. In a similar way as to that shown on niobium there is a “discharge” (peak IV_a) which is out of the potential range achieved during the anodising process at constant current density (Chapter V).

The voltammogram of the alloy Al-21 at.% Nb shows that the anodic current starts to raise at a higher than usual anodic potential, suggesting that the initial oxide layer is more resistive than that of the alloys Al-31 at.% Nb or Al-44 at.% Nb, as a consequence of the higher concentration of Al_2O_3.

4.9 Conclusions

The following conclusions are drawn from the results of this Chapter:

- The species formed by anodic polarization is Nb_2O_5. The anodic oxide starts to grow at potentials ≥ –0.18 V_{SCE} for the experimental conditions used in this work. From pH values of 2.6 to 12, the anodic oxide layer is chemically stable, forming a passive layer.

- The variation of the logarithm of the peak current density with sweep rate formation for Nb_2O_5 is linear with a slope close to one; this is in agreement with the equation deduced for a potentiodynamic growth of an anodic oxide according the high field conduction mechanism.

- The applied potential when Nb_2O_5 is formed at the sweep rate of 0.2 Vs^{-1} is not sufficient to produce a homogenous layer of Nb_2O_5, even though the species is identified at the oxide/electrolyte interface.

- After cathodic polarization at potentials less than –1.2 $V_{SCE,}$ protons are inserted in the oxide.

The results obtained by cyclic voltammetry of the Al-Nb of 21 to 44 at.% Nb alloys provide the following conclusions:

- The Al-Nb alloys with niobium contents of 21 to 44 at.% show only one peak corresponding to oxidation of niobium and aluminium.

- After cathodic polarization, the Al-31 at.% Nb and Al-44 at.% Nb alloys show peaks related to the insertion of hydrogen ions in the anodic oxide.

CHAPTER 5

ANODIC OXIDATION ON Al-Nb ALLOYS AND NIOBIUM

5.1 Introduction

This Chapter presents the results for anodising the Al-Nb alloys and niobium, prepared by magnetron sputtering, under the experimental conditions provided in Chapter 3. The anodic behaviour of the Al-Nb alloy system is examined in the concentration range of 21 to 89 at.% Nb. The results are compared with the behaviour reported in the literature for aluminium and niobium as well as for studies of niobium undertaken in this thesis.

Selected sputtered specimens were observed by SEM and TEM in order to characterize the surfaces and the associated anodic films. The compositions of the metallic and oxide layers were determined by RBS.

Specimens of Al-21, 31 and 44 at.% Nb alloys, and of niobium, after having been anodised to 10 V, were implanted with xenon atoms and then re-anodised to 200 V. This procedure enabled the determination of the oxide fraction thickness formed at the metal/oxide and film/electrolyte interfaces. With these values, the total anion and cation transport numbers were calculated, as well as the migration rates of Nb^{5+} ions relative to Al^{3+} ions.

5.2 SEM of the metallic surfaces

Selected sputtered specimens were analysed by SEM (Figures 5.1 to 5.3). The images show relatively uniform surfaces with relatively few surface defects. The defects appear to be associated with locally thinner regions of the sputtered material.

5.3 Voltage-time response

5.3.1 Al-Nb alloys

The voltage-time responses of the Al-Nb alloys, anodised to 150 V, are linear suggesting a constant growth rate of the anodic oxide films (Figure 5.4). The behaviour shows an initial surge between 1 and 4 V at the commencement of anodising, which is related to the pre-existing air-formed film.

Aluminium alloys, of 21 to 74 at.% Nb, show a linear decrease of slopes with increase of niobium content. This is related to a reduction of the field strength for ionic migration due to the presence of increasing contents of niobium cations in the anodic film with increase of niobium content in the alloy. The slope of the response for alloys with high niobium contents, from Al-74 at.% Nb to 100 at.% Nb show an increase from 1.3 to 1.5-1.6 V s^{-1} (Table 5.1 and Figure 5.6). The value of slope for the voltage-time response reported in the literature for sputtered niobium during anodising under similar experimental conditions is 1.4 V s^{-1} [131].

After anodising, selected specimens were observed by SEM; a uniform surface is generally observed, as revealed for the Al-81 at.% Nb alloy (Figure 5.6).

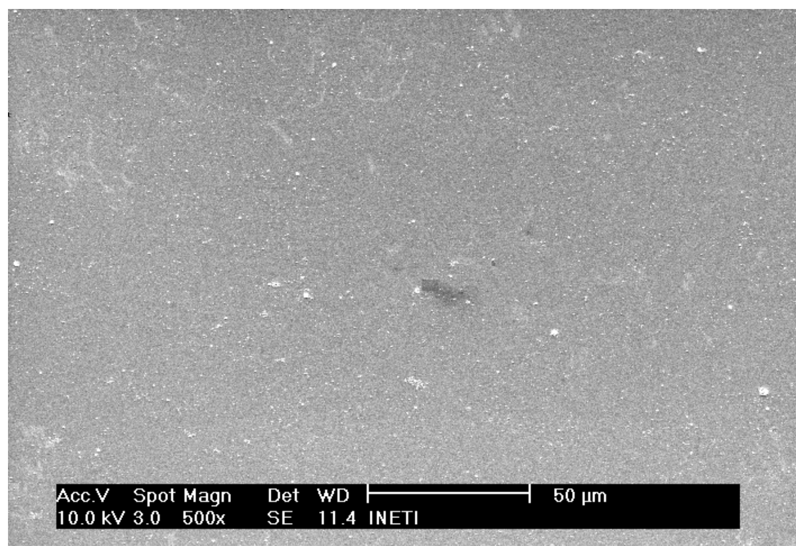

Figure 5.1 Scanning electron micrograph of the surface of a sputtered 100 at.% niobium specimen (set of specimens sputtered at 0.2 Pa).

Figure 5.2 Scanning electron micrograph of the surface of a sputtered Al-21 at.% Nb alloy specimen.

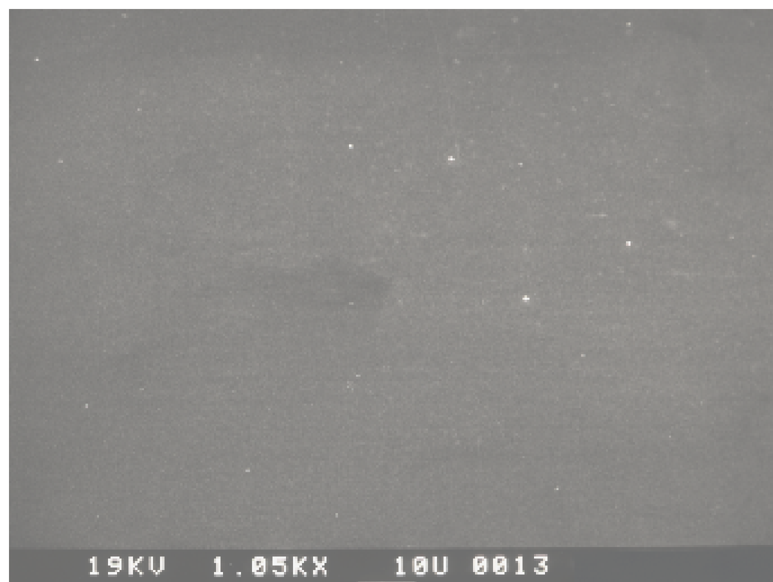

Figure 5.3 Scanning electron micrograph of the surface of a sputtered Al-31 at.% Nb alloy specimen.

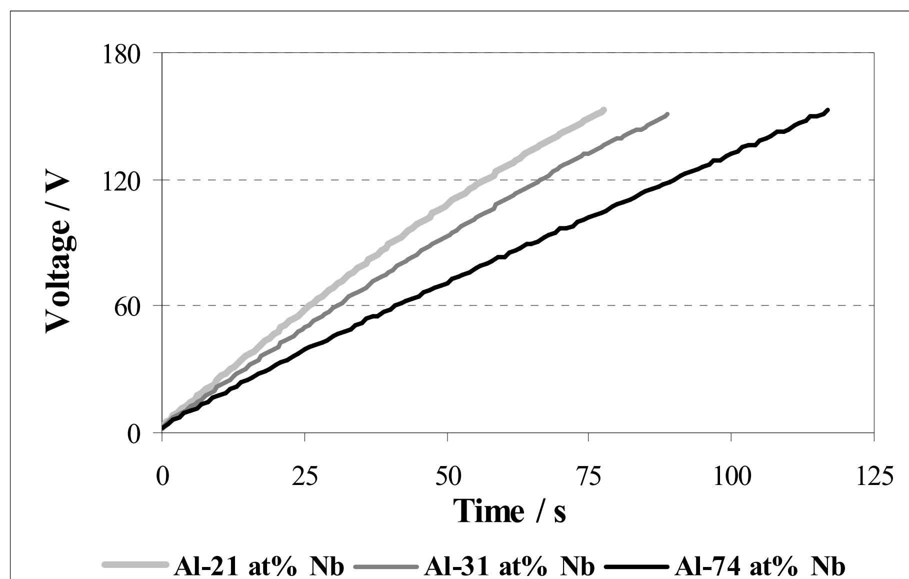

Figure 5.4 Voltage-time response of the Al-Nb alloys during anodising at 5 mA cm^{-2} in 0.1 M ammonium pentaborate.

Table 5.1 Slopes of the voltage-time responses of the sputtered 100 at.% niobium and Al-Nb alloys during anodising at 5 mA cm^{-2} in 0.1 M ammonium pentaborate to 150 V.

Metal/Alloy	dV/dt ($V\ s^{-1}$)
100 at.% Al*	2.3
Al-21 at.% Nb	1.95
Al-31 at.% Nb	1.68
Al-44 at.% Nb	1.50
Al-74 at.% Nb	1.26
Al-81 at.% Nb	1.43
Al- 89 at.% Nb	1.53
100 at.% Nb (set 1)	1.57
100 at.% Nb (set 2)	1.53
(*reported value)	

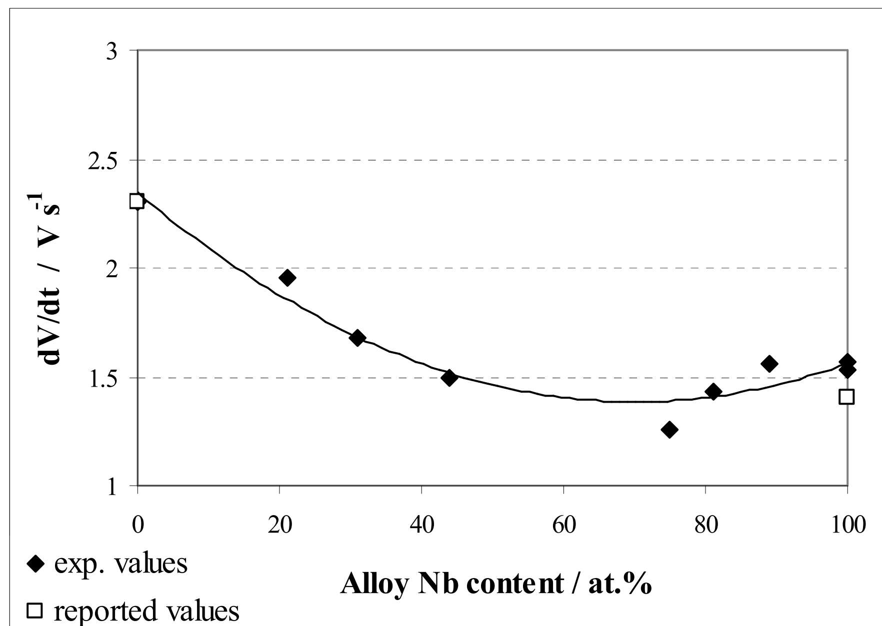

Figure 5.5 Variation of the slope of the voltage-time behaviour of the sputtered Al-Nb alloys (21 to 89 at.% Nb) and of the sputtered niobium during anodising at 5 mA cm^{-2} in 0.1 M ammonium pentaborate to 150 V with niobium content in the alloy.

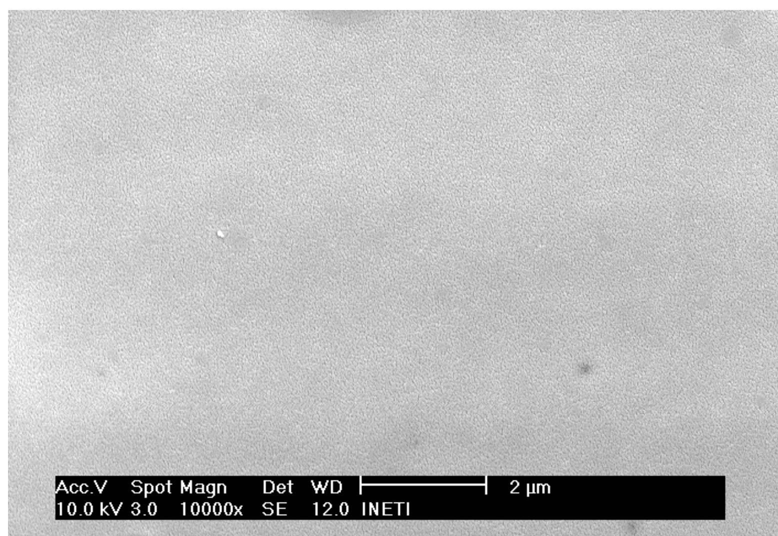

Figure 5.6 Scanning electron micrograph of the surface of a sputtered Al-81 at.% Nb alloy specimen after anodising at 5 mA cm^{-2} in 0.1 M ammonium pentaborate to 150 V.

5.3.2 Niobium

Two different sets of niobium specimens were deposited, with the argon pressure for sputter differing, i.e. 0.5 Pa for the first set and 0.2 Pa for the second one. During anodising, the niobium specimens of the first set show an initial region of reduced slope, observed over the first 8-10 s of anodising (Figure 5.7), meaning that the oxide is growing at a reduced rate. This feature was only observed when the specimens were anodised after a short time from sputtering. Specimens anodised after a month, or longer periods of time, showed that this feature had become vanishingly small (Figure 5.8).

A similar feature was found on anodising a sputtered Ta-0.3 at.% Fe alloy to 100 V [16]. The anodising behaviour showed two linear regions of different slopes, i.e. a reduced of slope of 0.5 V s^{-1} over the first 10 s of anodising, and a second slope, of 4.2 V s^{-1} evident to the end of the run. Transmission electron micrographs of ultramicrotomed sections revealed the existence of pores, of widths 16 nm to 30 nm, to be the possible cause of the observed low and high slopes [16]. The ultramicrotomed section of the sputtered niobium specimen (first set) prepared in this work, after anodising, did not_reveal pores (Figure 5.17). The results suggest that if pores or similar features were present on the metal surface, they are probably shallow and consequently not detected after anodising. The surfaces of the anodised specimens of the two sets were examined by SEM (Figure 5.9) and, it is evident that specimens generated under a lower pressure of argon display a less rough surface.

The anodising responses were also compared with the voltage-time response obtained on anodising a niobium rod electrode (99.9 %), after mechanical grinding followed by chemical polishing under the same experimental conditions. The voltage-time response is linear with a slope of 1.46 V s^{-1} (Figure 5.10). The electrode, after the chemical treatment reveals individual grains, probably through different dissolution rates of grains of particular orientation (Figure 5.11). Further, the relatively rough surface reveals a linear anodising response with a slope close to the expected value.

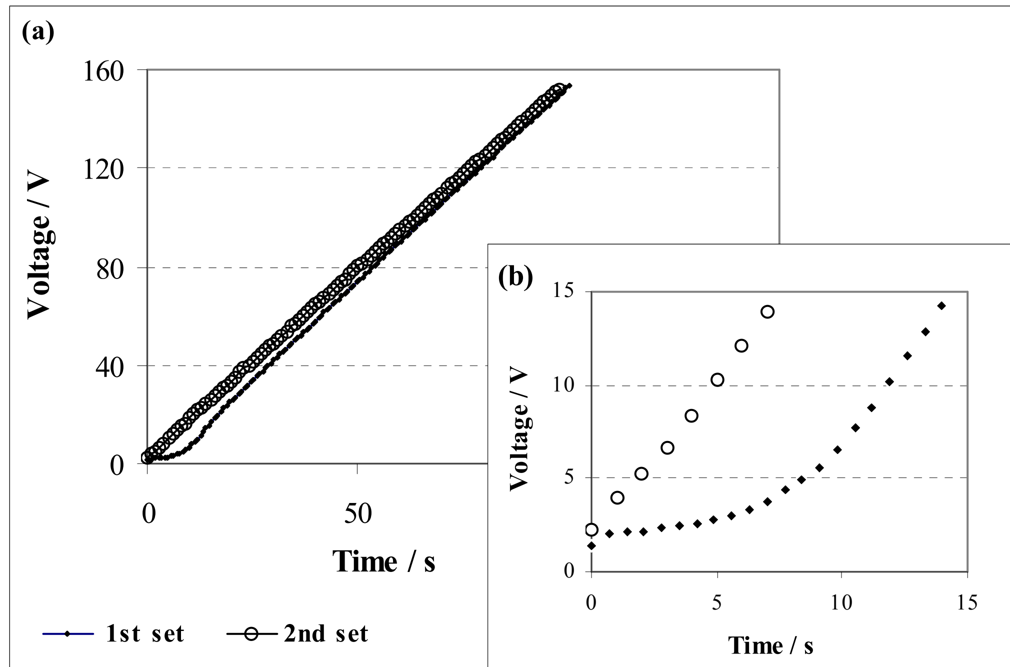

Figure 5.7 Voltage-time response of the sputtered niobium during anodising at 5 mA cm^{-2} in 0.1 M ammonium pentaborate to 150 V (a). Enlarged area of the previous plot (b).

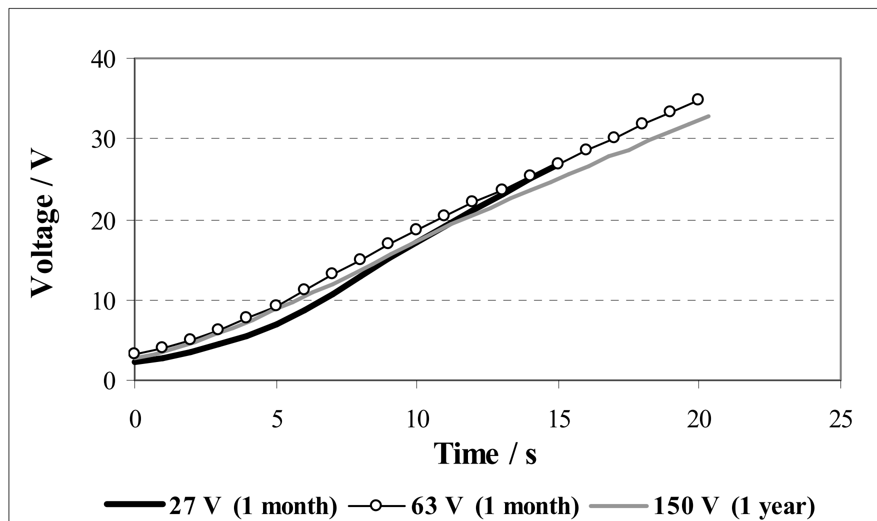

Figure 5.8 Initial 20 seconds period of the voltage-time response of the sputtered niobium (set of specimens sputtered at 0.5 Pa) after storage for different periods during anodising at 5 mA cm^{-2} in 0.1 M ammonium pentaborate.

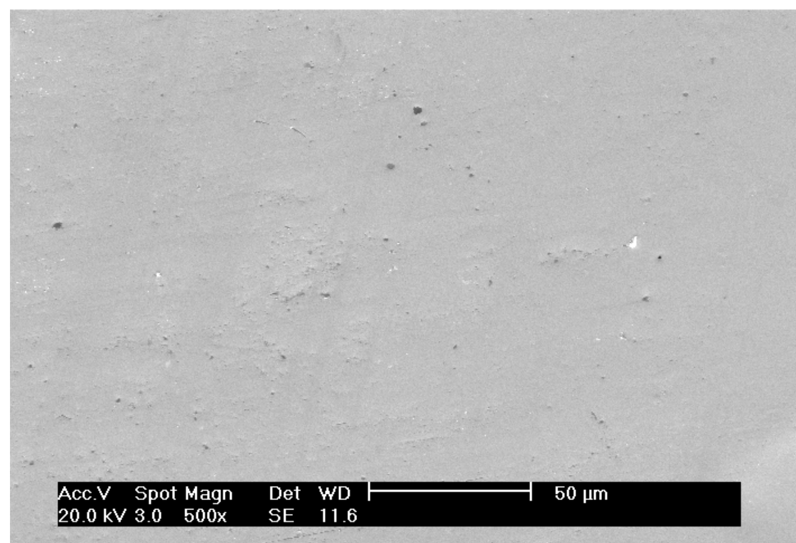

(a)

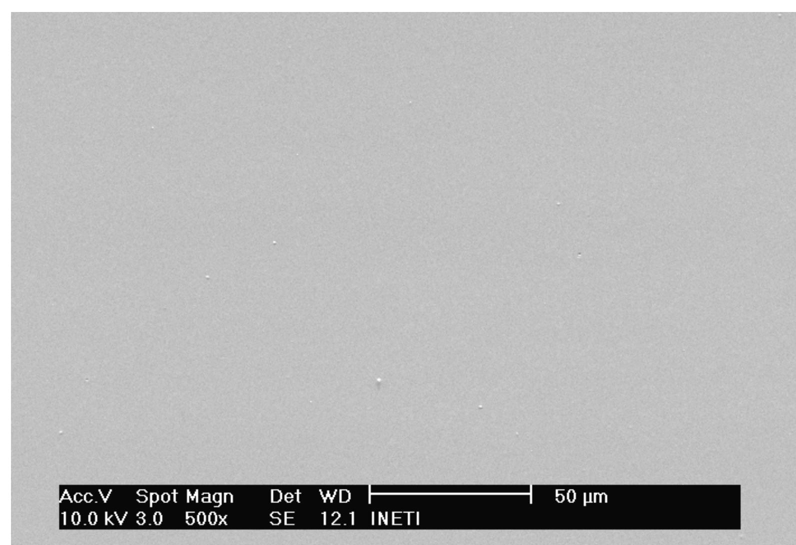

(b)

Figure 5.9 Scanning electron micrographs of the sputtered 100 at.% niobium after anodising to 150 V at 5 mA cm^{-2} in 0.1 M ammonium pentaborate: (a) set of specimens sputtered at 0.5 Pa argon; (b) set of specimens sputtered at 0.2 Pa argon.

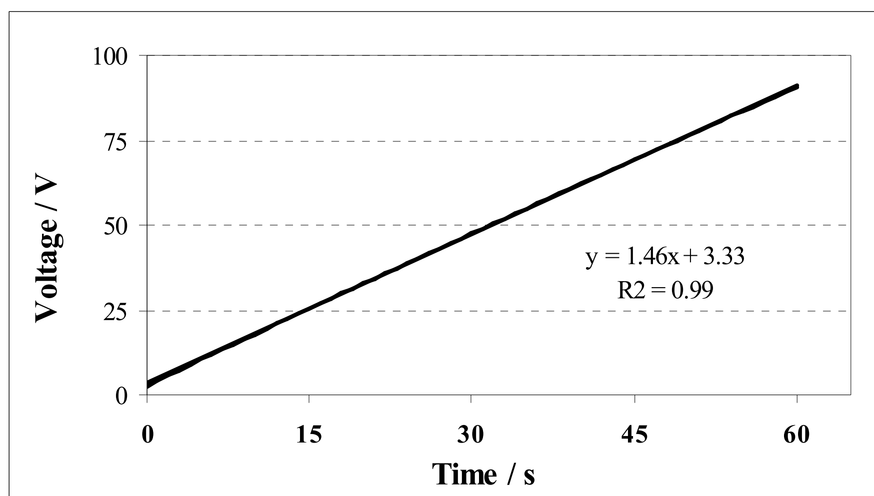

Figure 5.10 Voltage-time response of the niobium rod after mechanical grinding followed by chemical polishing, during anodising at 5 mA cm^{-2} in 0.1 M ammonium pentaborate to150 V.

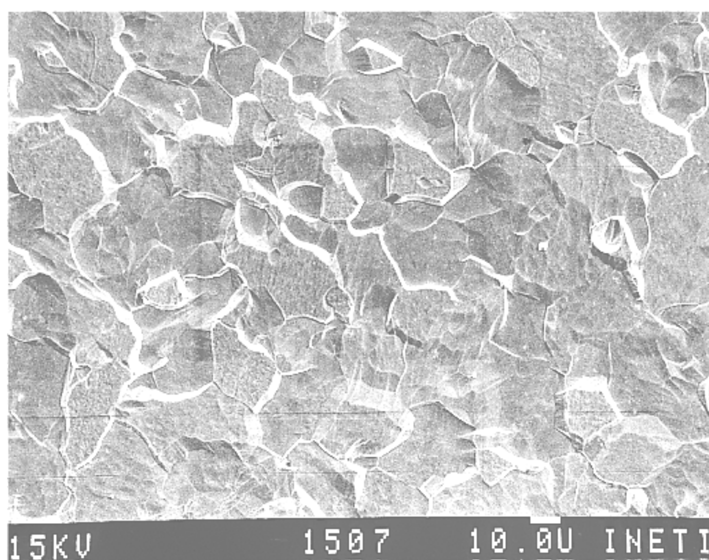

Figure 5.11 Scanning electron micrograph of the niobium rod surface after mechanical grinding followed by chemical polishing.

Thus, the initial feature, which is only evident on anodising fresh sputtered specimens, which were sputtered at 0.2 Pa argon, appears to be related with the surface roughness induced during sputtering. After storage, the air-formed oxide thickens and hinders the roughness effect; consequently, the oxide grows at an uniform rate and only one slope is observed in the voltage-time response. Nevertheless, the slope is higher (1.5-1.6 V s^{-1}) than expected (1.4 V s^{-1}). This initial "transient" behaviour, does not appear to affect the anodic oxide composition or morphology, since the oxide composition (determined by RBS) and oxide morphology (examined by TEM) reveal a relatively uniform Nb_2O_5 film with a density of 4.25 g cm^{-3}. The previous is considered reasonably close to the expected value (4.74 g cm^{-3}).

5.4 Oxide composition

Experimental and simulated RBS spectra of specimens anodised to high voltages (100/150 V) were determined for the sputtered niobium and for the Al-Nb alloys. The specimen compositions were determined by comparing measured and simulated spectra using the RUMP [138] or the NDF [139] programs. The results for the alloys with 21, 31, 44 and 100 at.% of niobium, anodised to 150 V, are shown in Figure 5.12 and Table 5.2.

The results show that the fitted spectra agree well with the experimental ones. The fit assumes that the oxides of the alloys contain units of Nb_2O_5 and Al_2O_3. Boron species are usually present in the oxide thickness developed at the oxide/electrolyte interface but, because of the low extent of incorporation, usually less than 1 at.%, they are neglected on this case. For anodising aluminium, boron species are present in the film formed at the oxide/electrolyte interface, since they are present as immobile species (Chapter 1). For anodic niobium oxides, boron species are only present in a thin layer close to the oxide/electrolyte interface. This feature is interpreted as a consequence of the change of boron species to B^{3+}, which move outward with higher migration rate than Nb^{5+} ions, under the electrical field [131].

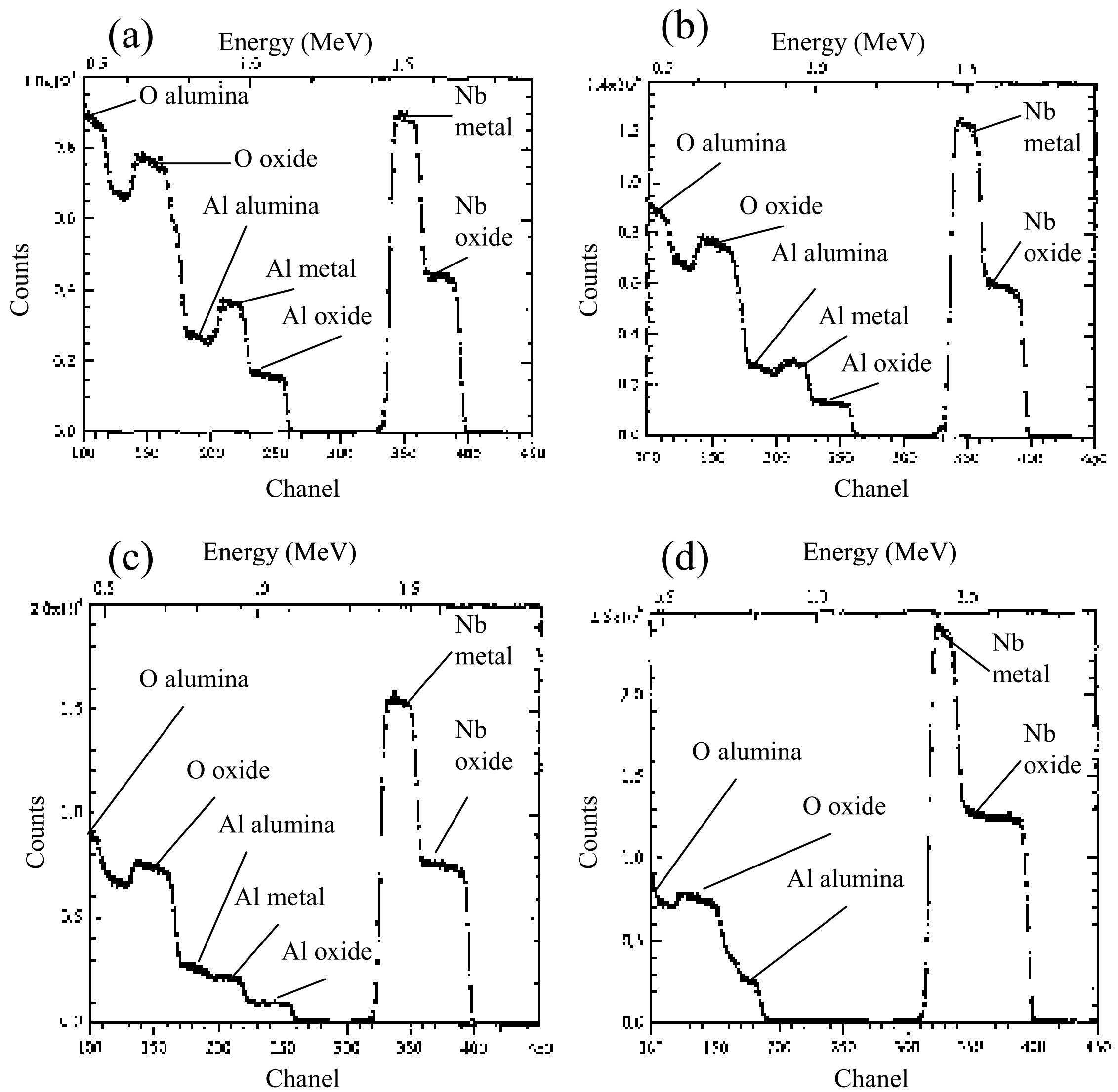

Figure5.12 Experimental and simulated RBS spectra (RUMP program) for the Al-Nb alloys and the sputtered niobium after anodising to 150 V at 5 mA cm^{-2} in 0.1 M ammonium pentaborate: (a) Al-21 at.% Nb alloy; (b) Al-31 at.% Nb alloy; (c) Al-44 at.% Nb alloy; (d) 100 at.% Nb.

Table 5.2 Results of RBS analyses of the Al-Nb alloys with 21 to 44 at.% Nb and the sputtered niobium after anodising at 5 mA cm^{-2} in 0.1 M ammonium pentaborate to 150V.

Nb alloy (%at)	Nb oxide (%at)	Nb x 10^{-17} (oxide) (atoms cm^{-2})	Al x 10^{-17} (inner oxide layer) (atoms cm^{-2})	Al x 10^{-17} (outer alumina layer) (atoms cm^{-2})	O x 10^{-18} (atoms cm^{-2})
21	21	1.38	4.84	4.4	1.14
31	31	2.06	4.54	1.8	1.22
44	45	3.11	3.81	-----	1.35
100	100	6.72	-----	-----	1.68

Thus, the boron species on anodic oxide layers on the Al-Nb alloys should be present in the anodic oxide layer formed at the oxide/electrolyte interface. However the fraction of the oxide thickness containing incorporated boron species will depend on transport number and effective field strength.

The niobium content of the anodic films is similar to that of the alloy to an accuracy of 1 %, indicating that the films were developed near 100 % of growing efficiency, with oxidation and ingress of aluminium and niobium species in the film close to the corresponding alloy percentages. The total amount of oxygen associated with the anodic film is less precise, since the oxygen peak overlaps with that of aluminium corresponding to alumina from the substrate. The Al-21 at.% Nb alloy shows a thin layer of reduced niobium content close to the oxide/electrolyte interface. This feature is indicated by a fine shift in the leading edge of the niobium peak. The shift can be accommodated in fitting the data by incorporating about 12 nm of anodic alumina of 3.17 g cm^{-3} density at the outer film surface. The fitting of the Al-31 at.% Nb spectrum was also improved when a thin alumina layer, of 5 nm thickness was included in the analysis, although this is at the margin of resolution (Table 5.2).

The results obtained on the alloys of high niobium content are shown on Figure 5.13 and Table 5.3. In this increased range of niobium concentration in the alloy, the oxide and the alloy results show a difference in niobium content of 5 % for the alloys of 74 and 81 at.%, which is acceptable as experimental error. The oxygen was calculated from the spectra but, due to overlap of the oxygen peak with the peak of aluminium from the alumina layer, the precision is less accurate than for niobium or aluminium.

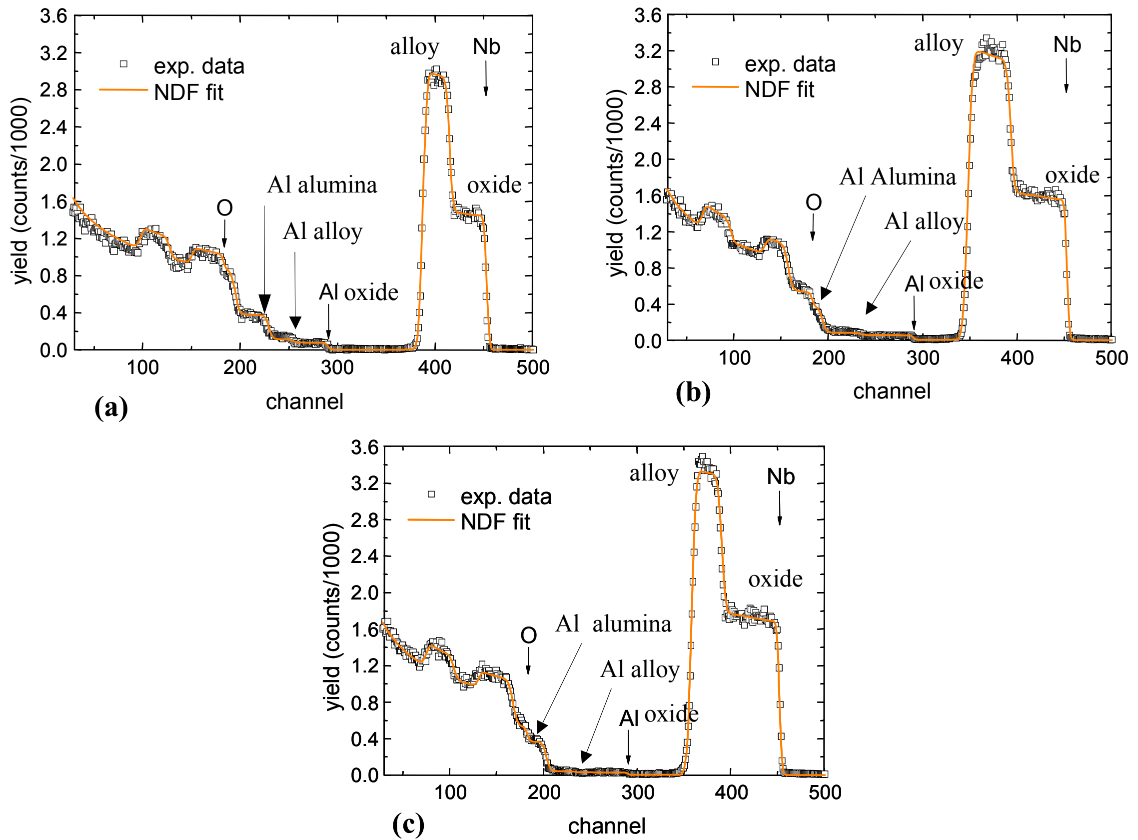

Figure 5.13 Experimental and simulated RBS spectra (NDF program) for the Al-Nb alloys after anodising to different voltages at 5 mA cm^{-2} in 0.1 M ammonium pentaborate: (a) Al-74 at.% Nb alloy (100 V); (b) Al-81 at.% Nb alloy (150 V); (c) Al-89 at.% Nb alloy (150 V).

Table 5.3 Results of RBS analyses of the Al-74 at.% Nb alloy after anodising to 100 V and of the Al-81 and 89 at.% Nb alloys after anodising to 150 V at 5 mA cm^{-2} in 0.1 M ammonium pentaborate.

Nb alloy (at.%)	Nb oxide (at.%)	Nb x 10^{-17} oxide (atoms cm^{-2})	Al x 10^{-17} oxide (atoms cm^{-2})	O x 10^{-18} oxide (atoms cm^{-2})
74	69	3.27	1.47	-- 0.91
81	76	5.51	1.70	1.40
89	88	6.21	0.86	1.43

5.5 Oxide Morphology

Transmission electron micrographs of ultramicrotomed sections of the alloys of 21 to 44 at.% Nb and of pure niobium, after anodising to 200 V, are now in Figures 5.14 to 5.17. Anodic films of uniform thickness are generally revealed. For the Al-21 at.% Nb alloy, the outer 13 % of the film disclosed fingers of darker oxide, of contrast similar to that of the underlying film and orientated approximately normal to the film surface, penetrating a lighter oxide (Figure 5.14). The width and separation of the fingers are up to about 10 nm. No distinct regions could be resolved in films formed on the Al-31 at.% Nb and Al-44 at.% Nb alloys, suggesting that any surface layers, if present, have thicknesses of less than a few nanometres (Figures 5.15 and 5.16). These specimens were implanted with xenon atoms before anodising to the final voltage, enabling the anodic oxide developed above and below the marker to be determined (Table 5.4). The oxide thicknesses formed at each interface were measured from the transmission electron micrographs, and the cation transport number calculated from the ratio of the oxide thickness formed at the oxide/electrolyte interface to the total oxide thickness. The results show that the total cation transport number decreases with increase of niobium in the alloy.

The sputtered niobium specimen also reveals an uniform anodic oxide and metal layers with relatively flat and parallel metal/oxide and oxide/electrolyte interfaces (Figure 5.17). Thus, that initial transient behaviour observed during anodising and previously reported, does not affect the subsequent film composition and morphology.

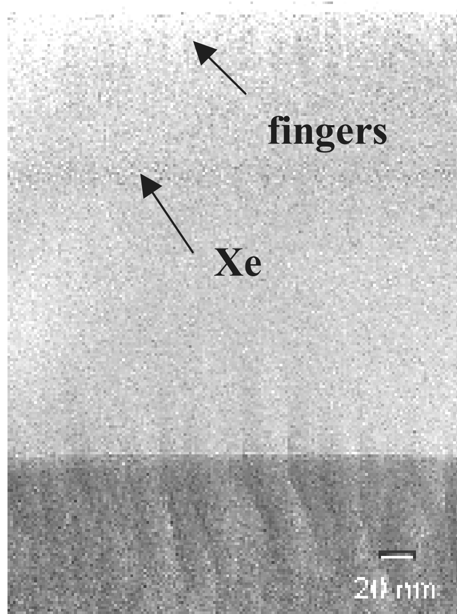

Figure 5.14 Transmission electron micrograph of an ultramicrotomed section of the Al-21 at.% Nb alloy, after anodising to 200 V at 5 mA cm^{-2} in 0.1 M ammonium pentaborate.

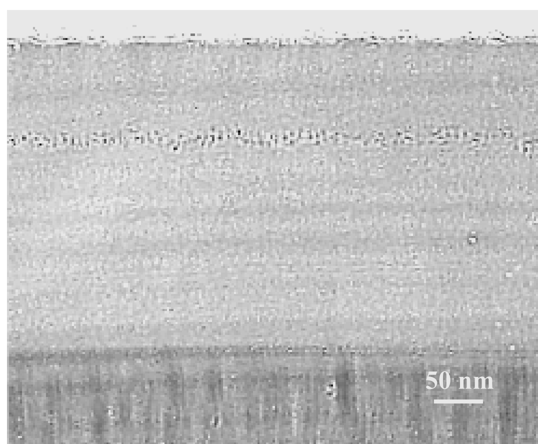

Figure 5.15 Transmission electron micrograph of an ultramicrotomed section of the Al-31 at.% Nb alloy after anodising to 200 V at 5 mA cm^{-2} in 0.1 M ammonium pentaborate.

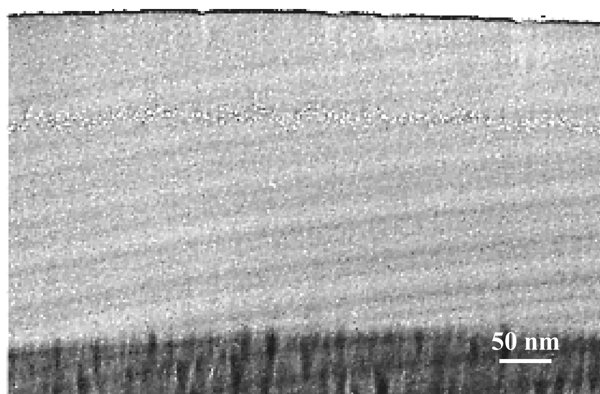

Figure 5.16 Transmission electron micrograph of an ultramicrotomed section of the Al-44 at.% Nb alloy after anodising to 200 V at 5 mA cm^{-2} in 0.1 M ammonium pentaborate.

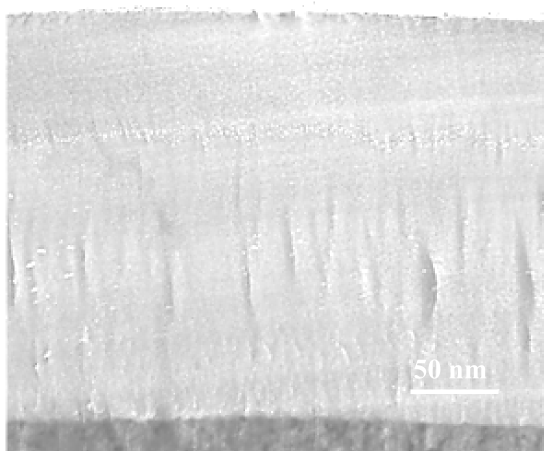

Figure 5.17 Transmission electron micrograph of an ultramicrotomed section of the sputtered niobium (set of specimens sputterd at 0.5 Pa argon) after anodising to 200 V at 5 mA cm^{-2} in 0.1 M ammonium pentaborate.

Table 5.4 Total cation transport numbers and formation ratios (nm/V) calculated for the Al-Nb alloys and the sputtered niobium after anodising to 200 V at 5 mA cm^{-2} in 0.1 M ammonium pentaborate. Oxide thicknesses measured from ultramicrotomed sections.

Al-Nb alloys	Oxide inner layer (nm) Al_2O_3 + Nb_2O_5	Oxide outer layer (nm)		Formation ratio (nm/V)	t^+
		Al_2O_3 + Nb_2O_5	Al_2O_3		
Al-21 at.% Nb	175	95	≈35	1.35	0.35
Al-31 at.% Nb	209	99	----	1.54	0.32
Al-44 at.% Nb	226	102	----	1.64	0.31
Niobium	Nb_2O_5 inner layer (nm)	Nb_2O_5 outer layer (nm)		Formation ratio (nmV^{-1})	t^+
100 at.% Nb	329.2	135.4	----	2.32	0.29

5.6 Oxide density

The densities of the oxides formed on alloys of niobium contents of 21 to 44 at.% and on niobium were calculated using the formation ratio, nmV^{-1}, determined by TEM (Table 5.4), together with the amounts of Al_2O_3 and Nb_2O_5 from the RBS analyses of specimens anodised to 150 V. The values were then compared with the densities obtained by assuming an average value weighted by the oxide composition (Table 5.5).The densities for amorphous alumina and amorphous niobia are respectively 3.17 g cm^{-3} and 4.74 g cm^{-3}. [27]. The results obtained show an accuracy ≤ 7 % for the mixed oxides, whereas the experimental value obtained for the niobia is 10 % less than the reported value (Table 5.6).

5.7 Efficiency of the anodising process

The efficiency of film growth during anodising was evaluated by comparing the charge passed and the corresponding amounts of niobium and aluminium cations within the film from RBS analyses (Table 5.7). The results show some dispersion between 2 and 17 %. An anodising efficiency close to 100 % was expected, with no losses of species to the electrolyte. For example, a sputtered Ta-35 at.% Al alloy specimen, anodised under similar experimental conditions, show similar charge values, differing by less than 5% [123]. A variation of 5 %, maximum 10 %, may be acceptable as experimental error. However, the differences in the corresponding charge values for the Al-31 at.% Nb and Al-74 at.% Nb alloys are, respectively 13 % and 17 %. These values suggest that, for these particular specimens, other oxidation processes had occurred giving an efficiency of less than 100 %.

Table 5.5 Anodic oxide densities formed on the Al-Nb alloys obtained from the values of pure oxides by assuming an average value weighted by the oxide composition.

Al (at.%)	Nb (at.%)	Oxide molecular weight (g)	n (number of electrons)	V_{Molar} (cm^{-3})	Oxide density (g cm^{-3})	Growth rate at 5 mA cm^{-2} (nm/s) (100% efficiency)
100	0	101.96	6.00	32.16	3.17*	2.78
79	21	136.37	6.84	37.18	3.67	2.82
69	31	152.75	7.24	39.58	3.86	2.84
56	44	174.05	7.76	42.68	4.08	2.85
26	74	223.20	8.96	49.86	4.47	2.88
19	81	234.67	9.24	51.54	4.55	2.89
11	89	247.78	9.56	53.45	4.64	2.90
0	100	265.80	10.00	56.08	4.74*	2.91
					* reported values	

Table 5.6 Oxide densities calculated from RBS and TEM data and from the values of pure oxides.

Oxide	ρ (g cm^{-3}) (TEM+RBS)	ρ (g cm^{-3}) $Q_{weighted\ comp.}$	$\frac{\rho_{RBS+TEM}}{\rho_{weighted\ comp.}}$ x 100%
Al-21 %at Nb	3.41	3.67	93
Al-31 %at Nb	3.73	3.86	97
Al-44 %at Nb	4.04	4.08	99
100 %at Nb	4.25	4.74 *	90
		* reportevalue	

Table 5.7 Anodising efficiency evaluated by comparing the charge passed during anodising and number of oxidised cations determined by RBS for the Al-Nb alloys and the sputtered niobium after anodising at 5 mA cm^{-2} in 0.1 M ammonium pentaborate to 150 V.

Alloy /metal	$Charge_{Anod.}$ ($C\ cm^{-2}$)	$Charge_{RBS}$ ($C\ cm^{-2}$)	$\frac{Charge_{Anod.}}{Charge_{RBS}}$
Al-21 at.% Nb	0.389	0.364	1.07
Al-31 at.% Nb	0.445	0.392	1.13
Al-44 at.% Nb	0.459	0.432	1.06
Al- 74 at.% Nb(1)	0.390	0.333	1.17
Al-81 at.% Nb	0.510	0.539	0.95
Al-89 at.% Nb	0.515	0.523	0.98
100 at.% Nb	0.490	0.538	0.91
(1) anodised only to 100V			

5.8 Discussion

5.8.1 Al-Nb alloys (21-44 at.% Nb)

For this range of alloy compositions, the formation rate, the oxide composition and the transport numbers show a linear behaviour proportional to the alloy compositions. (Figure 5.18). The anodic layer, considered as a mixed oxide, contains units of Al_2O_3 and Nb_2O_5 with a cation composition close to the corresponding alloy as determined by RBS analyses. The formation ratio (nm/V) of films increases with niobium content, indicating a reduction of the electric field for ionic transport with the incorporation of units of Nb_2O_5 into the amorphous alumina structure. The calculated oxide densities, as well as the transport number, show intermediate values between the values for anodic alumina and niobia, due to the equivalent cation composition of oxides and corresponding alloys.

The Al-21 at.% Nb alloy did not show enrichment of niobium at the metal/oxide interface when analysed by RBS or observed by TEM, although the Gibbs free energy per equivalent of niobium oxide is less negative than that for alumina (Chapter 2). Generally, the enriched layer is only observed on dilute aluminium alloys and, at this concentration, if there is any enrichment, it can be neglected. Consequently, the outward alumina layer formed on the oxide/electrolyte interface is related to the higher migration rate of Al^{3+} ions relative to Nb^{5+} ions. For many binary aluminium alloys, a two-layered oxide is formed because the cations have different mobilities under the electric field; the faster migrating cation forms an outer layer enriched in its own oxide, above an inner layer containing units of oxide of both types of cations [157]. The ion mobility, under the electric field, is directly related to the single metal-oxygen bond energy, i.e., elements with higher bond energy than the corresponding aluminium bond energy usually show a migration rate relative to aluminium ions less than 1 (Chapter 2).

Such a layered structure can be disturbed because the ionic resistivity of the inner oxide is lower than that of the outer oxide. Fingers of inner oxide can then penetrate the outer oxide. Such behaviour is particularly apparent in anodising superimposed

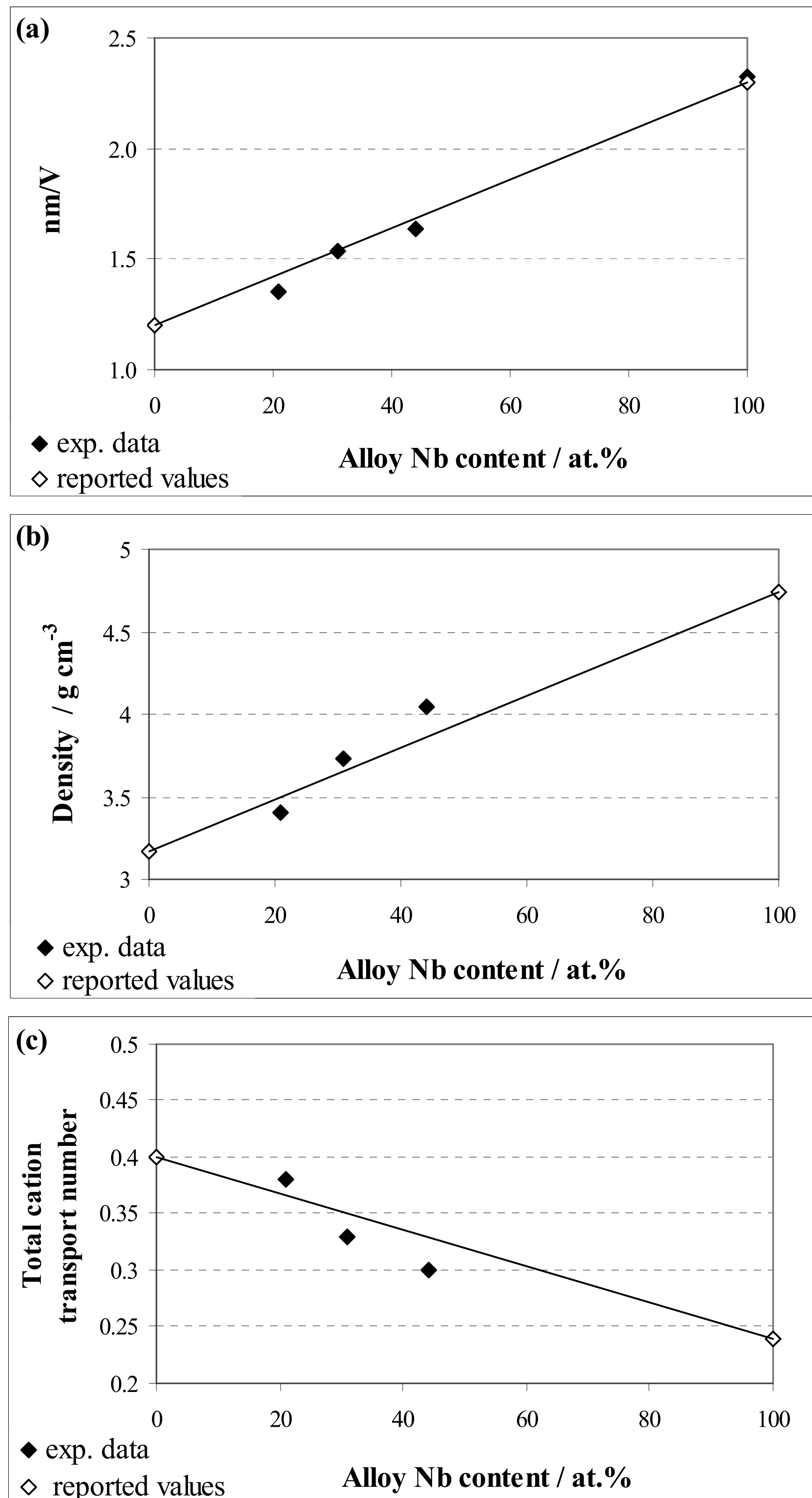

Figure 5.18 Variation of anodic film parameters with niobium content in alloy: (a) formation ratio (nm/V); (b) anodic oxide density; (c) total cation transport number.

layers of different metals; for instance, a layer of aluminium deposited on tantalum show the finger penetration [158]. A similar process proceeds for niobium; the ionic resistivity of anodic niobia is lower than that of anodic alumina [26], and incorporation of units of Nb_2O_5 into anodic alumina reduces the oxide resistivity, as evident from the increased formation ratios (Table 5.4). Consequently, fingers of the inner oxide, composed of units of Nb_2O_5 and Al_2O_3, may eventually penetrate the outer alumina layer. Such penetration has been observed by transmission electron microscopy for Al-Ta alloys formed to sufficiently high voltages [123], and is also evident here for the Al-21 at.% Nb alloy (Figure 5.15). Fingers had probably already penetrated any alumina layers on the Al-31 at.% Nb and Al-44 at.% Nb alloys, associated with the increased niobium content of the inner oxide, hindering their revelation by TEM. In addition, from the behaviour of Al-Ta alloys [123], the migration rate of Nb^{5+} ions relative to Al^{3+} ions is expected to increase with the increased presence of niobium species in the anodic oxide, thus reducing the thickness of any alumina layer. In agreement with this expectation, the relative migration rates of Nb^{5+} ions with respect to Al^{3+} ions are approximately 0.75 and 0.88 for the Al-21 at.% Nb and Al-31 at.% Nb alloys respectively (Figure 5.19), determined from the compositions of the above oxide layers, above the marker layer using data from RBS (Table 5.2). A decreasing relative mobility of Al^{3+} ions with increasing niobium content of the oxide, accompanied by a decreased ionic resistivity of the oxide, a reduced cation transport number and a reduced aluminium content of the alloy are consistent with the essential absence of a second layer in the oxide on the Al-44 at.% Nb alloy.

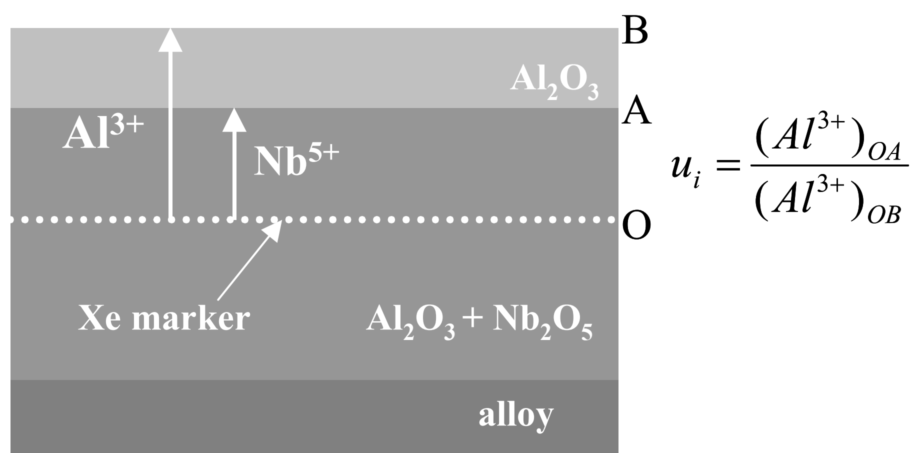

Figure 5.19 Schematic diagram showing the migration rate (u_i) of the Nb^{5+} ions relative to the Al^{3+} ions for the Al-21 at.% Nb and Al-31 at.% Nb alloys.

5.8.2 Al-Nb alloys (74-89 at.% Nb)

The anodic oxides formed on Al-Nb of high niobium contents, from 74 to 89 at.% Nb, show a composition close to the corresponding alloy as determined by RBS analyses. A variation between 1-5 at.% is considered to be within the experimental error expected for this technique. The voltage-time behaviour show a linear response to 100/150 V, indicating that the anodic oxide layers are relatively uniform, as determined by the RBS analyses.

Voltage-time responses of the Al-81 at.% Nb and Al-89 at.% Nb alloys show a progressive increase in the slope with niobium contents, ranging between 1.4 to 1.5 V s^{-1} (Table 5.1). This variation was not expected since increasing niobium contents in the film should decrease the electrical field necessary for oxide growth. The slopes from the voltage-time response for sputtered niobium are also higher than the values reported for anodising sputtered niobium under similar experimental conditions [129]. This feature could be associated with the vacuum pressure in the sputter chamber. Habazaky et al reported a linear voltage-time response, with a slope of 1.4 V s^{-1} [129]. In that work, the vacuum pressure was 1 x 10^{-5} Pa, whereas the pressure in this work was 5 x 10^{-5} Pa. It has also been reported that niobium sputtered in different mixtures of argon and oxygen at a pressure of $\approx$ 0.1 Pa, and then anodised at constant current density of 5 mA cm^{-2} in 0.1 M phosphoric acid electrolyte, showed voltage-time responses with slopes that increase with the oxygen content [159]. Thus, those results suggest that if the vacuum pressure is not sufficiently low, some co-deposition of oxygen within the metal layer can occur and, consequently, the presence of oxygen is a possible reason for the increase of slopes of the voltage-time behaviour observed in this alloy composition range (81 to 100 at.% Nb). In this case, it is assumed that aluminium hinders the oxygen deposition. Finallly, the anodising charges for this composition range (81 to 100 at.% Nb) are less than the corresponding charges of the oxidised cations determined by RBS analyses, which_reinforces this explanation.

5.8.3 Niobium

Voltage rises with time for anodising sputtered niobium under the selected conditions. As discussed for Al-Nb alloys of high niobium content (81-89 at.% Nb), the slopes of the voltage-time response for anodising niobium are in the range of 1.5-1.6 V s^{-1}, which are higher than the values reported in the literature for anodising under similar experimental conditions. This feature has been previously suggested to be related to the vacuum conditions of the sputter chamber (5.8.2). Nevertheless, the anodic niobia layer is uniform and formed at a constant rate of 2.32 nm V^{-1} with a density of 4.25 g cm^{-3}.

Two different sets of niobium specimens were deposited, at differing argon pressures; i.e. 0.5 Pa for the first set and 0.2 Pa for the second one. The surface observation by scanning electron microscopy of both sets of specimens, shows a rough surface on specimens of the first set. Tsukada et al. studied the influence of argon gas pressure on stress in sputtered niobium films; it was evident that the stress state changes from compressive to tensile as the argon pressure was increased [160]. The transition pressure was about 0.67 Pa. The same authors also found that the surface roughness depended on the stress condition of the film, showing the least value of roughness for the stress-free films [160]. The erosion of the target, the distance and angle target/substrate are parameters that influence the structure and stress condition [161, 162]. Thus, it is possible that individual factors or their combination, may influence the structure or density and they are consequently reflected on the anodising process. However the results obtained in this work suggest that roughness had only some influence at the initial instant of the anodising.

The transport number determined for pure niobium, 0.29, is higher than expected, but it is within the range reported in the Literature (0.24-0.33) [14, 26]. The transport number obtained for tantalum under similar experimental conditions is 0.24, so an equivalent value was expected for niobium, as these elements usually have similar chemical behaviour. The anodising curves obtained on niobium specimen after being

implanted with xenon show a slope of 1.8 V s^{-1} which is even higher than the experimental values found (1.5/1.6 V s^{-1}). This feature suggests that the implanted xenon is interfering with anodising and probably affects the cation transport number due to an increase of resistance to ionic migration. This change of slope is not observed, for instance, on re-anodising of the Al-21 at.% Nb alloy, after xenon implantion (Figure 5.20).

5.9 Conclusions

The conclusions of this Chapter for the oxides developed on alloys of niobium contents of 21 to 44 at.% are as follows:

- The alloys reveal an anodising response related to the alloy composition, with the amorphous oxides being mainly composed of units of Al_2O_3 and Nb_2O_5 in approximate proportions to the alloy composition.

- Al^{3+} ions migrate outward at a slightly faster rate than that of Nb^{5+} ions, which correlates with the relative energies of the Al^{3+}-O and Nb^{5+}-O bonds. However, formation of an outer alumina layer is countered by fingers of inner layer oxide, of reduced ionic resistivity, which penetrate any outer alumina layer.

- The oxides on the Al-Nb alloys grow by co-operative transport of cations and anions, with a cation transport number that increases with reducing amounts of niobium in the oxide. The values are intermediate between those of anodic alumina and anodic niobia. Similarly, formation ratios lie between those of anodic alumina, about 1.2 nm V^{-1}, and anodic niobia, about 2.3 nm V^{-1}, increasing from 1.35 to 1.64 nm V^{-1} for niobium content in the alloy from 21 to 44 at.%.

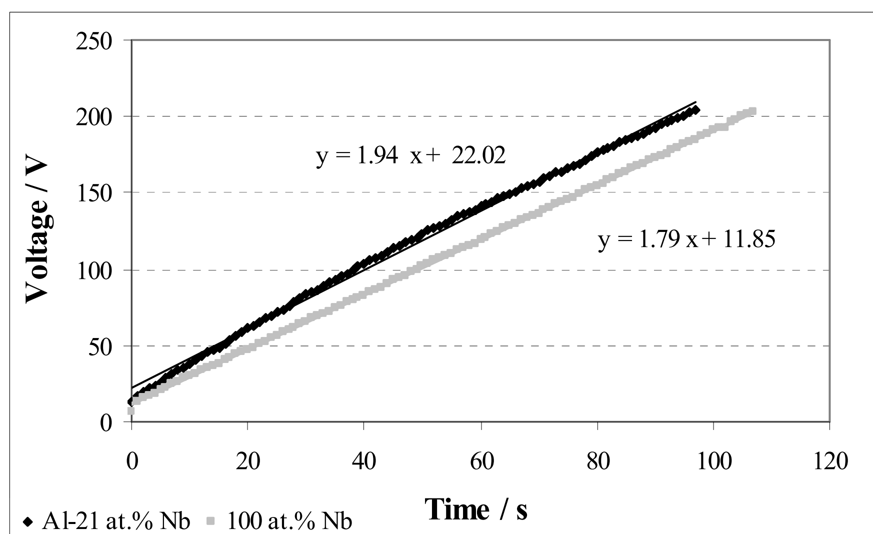

Figure 5.20 Voltage-time response of the sputtered niobium and the Al-21 at.% Nb alloy during anodising at 5 mA cm^{-2} in 0.1 M ammonium pentaborate to 200 V after implanting with xenon.

For alloys of increased niobium contents (74-89 at.% Nb), the following conclusions arise:

- The alloys reveal an anodising behaviour related to the alloy composition, with the amorphous oxides being mainly composed of units of Al_2O_3 and Nb_2O_5 in approximate proportion to the alloy composition.

- For this range of composition, the anodic films have higher niobia contents than alumina; no alumina layer was evident close to the oxide/electrolyte interface.

For pure niobium, the following may be concluded:

- The anodic niobia oxide is found with a formation ratio of 2.3 mn V^{-1} and a density of 4.25 g cm^{-3}, which are close to the values found on literature for anodic niobia.

- The cationic transport number (0.29) is within the range reported on literature (0.24-0.30), although the niobium specimen after xenon implantation shows a voltage-time response of slope higher than the values reported for the experimental conditions used in this work.

CHAPTER 6

DIELECTRIC PROPERTIES OF ANODIC OXIDES ON Al-Nb ALLOYS AND NIOBIUM

6.1 Introduction

In this Chapter the dielectric constant and the capacitive behaviour of the anodic oxides of Al-Nb alloys and niobium are examined from the oxide capacitances measured by EIS (Electrochemical Impedance Spectroscopy). Sputtered specimens of niobium and Al-Nb alloys were anodised under the usual experimental conditions to different final voltages, from 10 to 100 V. A specimen of the Al-21 at.% Nb alloy was anodised to 150 V to determine if the alumina layer formed at the oxide/electrolyte interface can be identified in the EIS spectrum. The anodic oxide thicknesses were calculated using the nm/V ratio determined from transmission electron micrographs, or calculated from the anodising curve, assuming 100% current efficiency of film growth and a density proportional to the film composition.

The EIS spectra were measured with a metal-oxide-metal system to eliminate interference effects at the oxide/electrolyte interface. The measuring system in which the second metal is a droplet of mercury was described in Chapter 3. Several EIS spectra were measured for each anodised specimen.

The EIS spectra were analysed by “Zview software”. The results were adjusted to an equivalent circuit formed by a CPE (Constant Phase Element) connected in parallel with a resistance, representing the capacitance and the resistance of the anodic oxide

layer (Figure 6.1). These elements are then connected in series with a resistance (R_S), which corresponds to the resistance of the measuring system (connecting wires and mercury drop).

The impedance of the CPE element is given by:

$$Z_{CPE} = \frac{1}{j(\omega)^n C} \qquad (6.1)$$

where C is the capacitance, ω is the frequency and from the exponent, n, the deviation from pure capacitive behaviour is calculated, according to:

$$\text{deviation} = (1\text{-n}) \times 100\% \qquad (6.2)$$

The best fit of an experimental spectrum is obtained by a nonlinear least square fitting method (NLLS-fit) which optimizes the values of the parameters of the applied electrical equivalent circuit: The quality of the fitting is judged by a percentage error determined to each parameter.

The fittings of the spectra showed a percentage error in the CPE and n elements of less than 1-2 %. The film resistances show a percentage error of 10-20 %. Some spectra were only adjusted at higher frequencies than 100 Hz because some dispersion was observed beyond that frequency. These spectra were only adjusted to a circuit of a CPE connected in series with a resistance to improve the fitting. The resistance, R_S, also shows a high relative error, but as this resistance is close to 1Ω, it does not affect the general fitting.

6.2 Anodic oxides on Al-Nb alloys of 21 to 44 at.% Nb

6.2.1 Dielectric constant and capacitive behaviour

On this range of alloy concentration, the EIS spectra (Figure 6.2) show a phase angle close to 90º and a decrease of the capacitance values with the increase of the oxide thickness and aluminium content (Table 6.1).

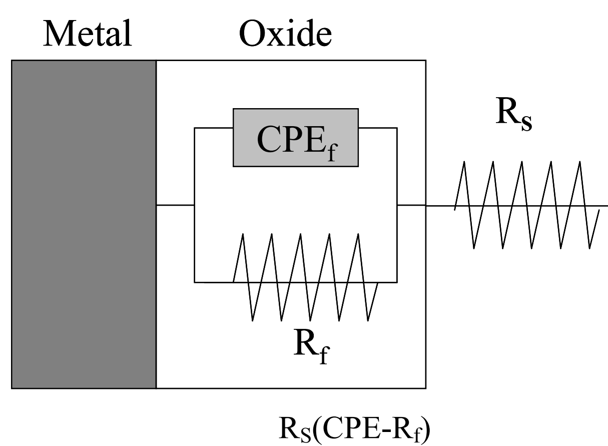

$R_S(CPE\text{-}R_f)$

Figure 6.1 Equivalent circuit used to characterize the alloy/ anodic oxide/mercury drop system.

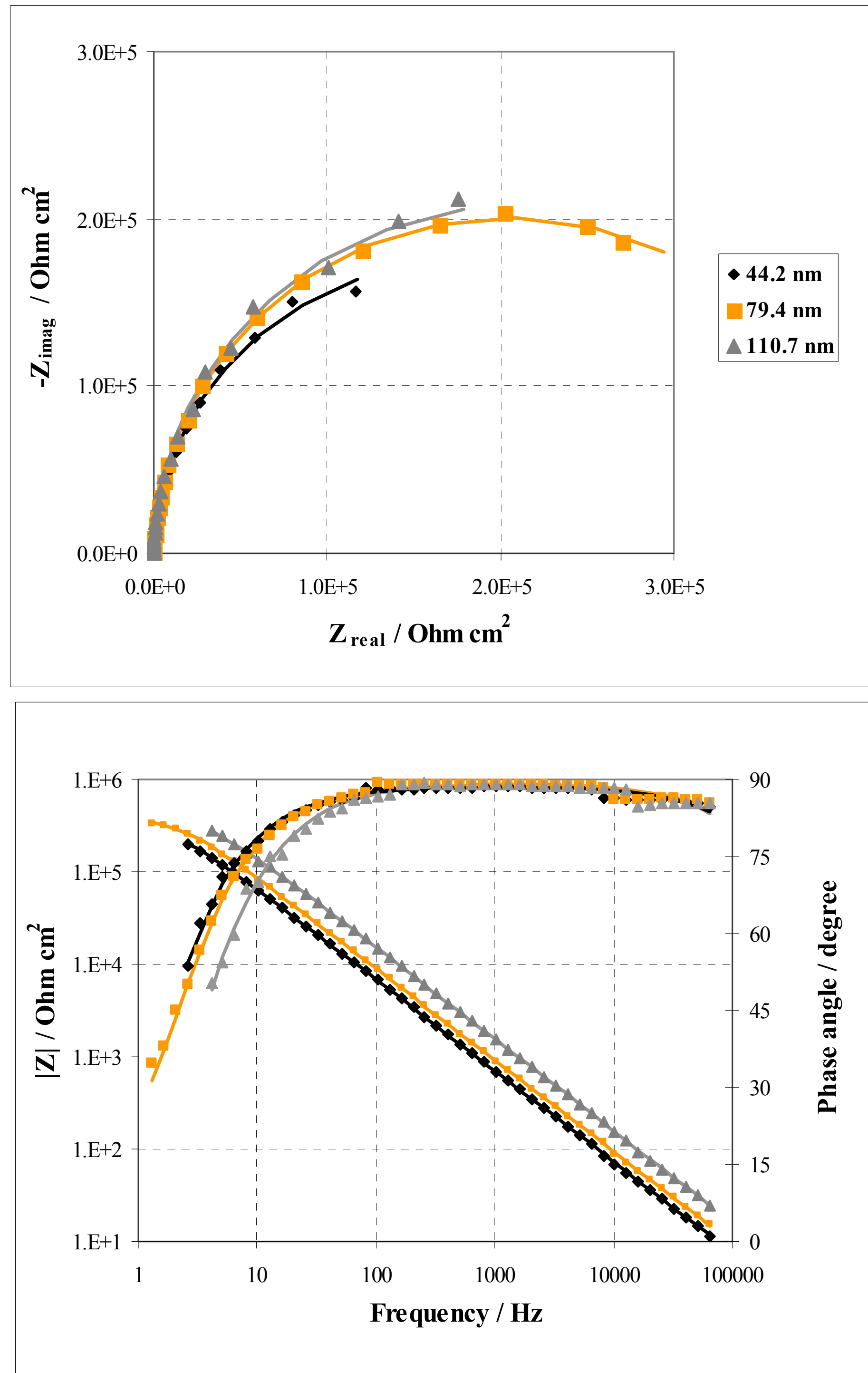

Figure 6.2 Experimental and simulated (line) EIS spectra obtained for the Al-21 at.% Nb alloy after anodising to different voltages at 5 mA cm^{-2} in 0.1 M ammonium pentaborate (oxide thicknesses of 44.2, 79.4 and 110.7 nm respectively).

Table 6.1 Values obtained with the fitting $R_S(CPE_f\text{-}R_f)$ on the EIS spectra measured on the Al-Nb alloys (21 to 44 at.% Nb) after anodising to different voltages at 5 mA cm^{-2} in 0.1 M ammonium pentaborate . Oxide thicknesses calculated from anodising charge.

Anodic Oxide Composition	Number of spectra	δ (nm)	R_f x 10^{-5} (Ohm cm^2)	C_f (μF cm^{-2})	n	(1-n) (%)
$Al_20_30.29Nb_2O_5$ (Al-21 at.% Nb)	3	44.2	3.86	0.24	0.983	1.7
	1	79.4	4.09	0.19	0.989	1.1
	3	110.7	3.91	0.11	0.990	1.0
	2	205.6	1.83	0.04	0.992	0.8
$Al_20_30.45Nb_2O_5$ (Al-31 at.% Nb)	3	15.7	0.41	0.76	0.976	2.4
	3	78.9	0.94	0.20	0.991	0.9
	3	141.3	2.57	0.08	0.983	1.7
$Al_20_30.82Nb_2O_5$ (Al-44 at.% Nb)	3	39.9	---	0.48	0.975	2.5
	2	75.4	1.60	0.26	0.986	1.4
	3	105.1	1.16	0.20	0.986	1.4
	3	136.3	---	0.13	0.991	0.9

The dielectric behaviour was checked, by plotting the reciprocal of the oxide capacitance (C^{-1}) with the factor $\delta\varepsilon^{-1}$ to verify if the plane-plate capacitor equation is obeyed (Figure 6.3). From the corresponding slopes, the relative dielectric constants found are 11, 14 and 22, for the films formed of the Al-21 at.% Nb, Al-31at.% Nb and Al-41 at.% Nb alloys respectively.

6.2.2 Simulation of an EIS spectrum of a two layered oxide

The anodic oxide formed on Al-21 at.% Nb alloy revealed an alumina layer close to the oxide/electrolyte interface (Chapter 5). According to the RBS spectrum, this layer achieved a 12 nm thickness at an the anodising voltage of 150 V. The experimental EIS spectrum of a specimen of the Al-21 at.% Nb alloy anodised to 150 V, did not reveal any feature related to a two layered oxide morphology (Figure 6.4). In order to consider this film, the EIS spectrum of a double layer oxide was simulated by utilising the equivalent circuit formed from two modules connected in series; each module comprises a capacitor connected in parallel with a resistance (Figure 6.5).The first module simulates the mixed alumina-niobia oxide and the second one corresponds to the thin alumina layer. The dielectric constant and the resistivity of anodic alumina are required to simulate the circuit. These values were obtained by anodising an aluminium specimen (99.99%) to 50 V under the usual experimental conditions. The EIS spectrum was measured using a mercury drop on the second metal electrode and fitted to the equivalent circuit Rs(CPE-Rf); finally, the dielectric constant and the electrical resistivity of alumina were calculated from the CPE and R values. The thickness of the alumina was calculated assuming a formation ratio of 1.2 nmV^{-1}. For the mixed oxide layer (Nb_2O_5 +Al_2O_3), the dielectric constant and resistivity of the oxide were calculated from the EIS results obtained already (Table 6.2).

The simulated spectra for the two circuits are almost coincident (Figure 6.6), thus, it is impossible for the values of resistance and capacitance involved, in which the corresponding time constants are also very close (Table 6.2) to distinguish the alumina layer by a simple EIS measurement.

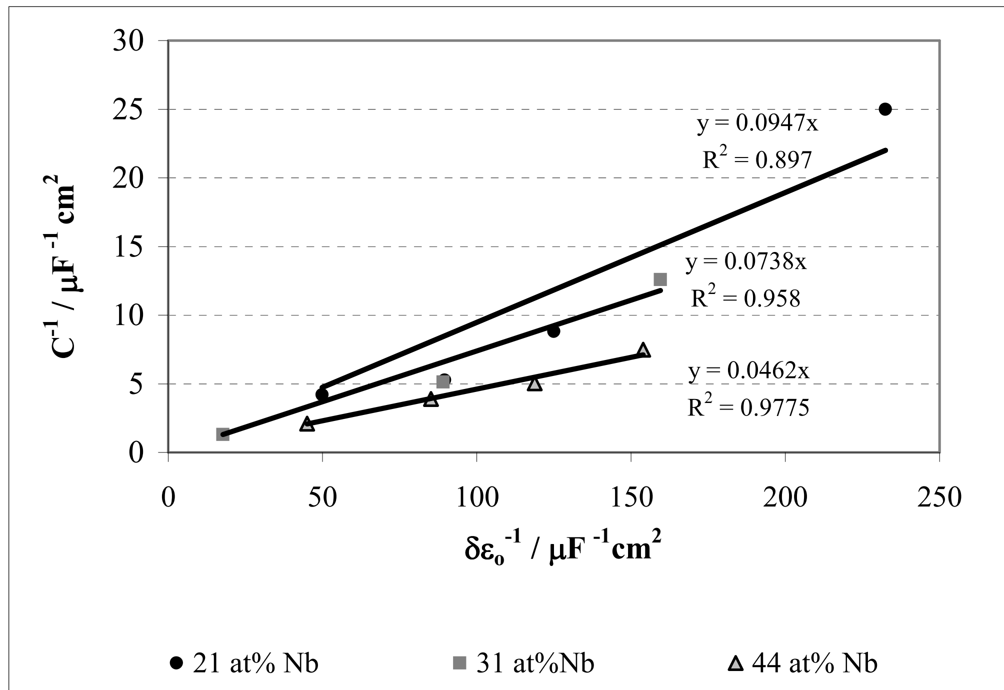

Figure 6.3 Variation of reciprocal capacitance with $\delta\varepsilon_o^{-1}$ for the Al-Nb alloys with niobium content of 21 at.% to 44 at.% Nb after anodising to different voltages at 5 mA cm^{-2} in 0.1 M ammonium pentaborate.

.

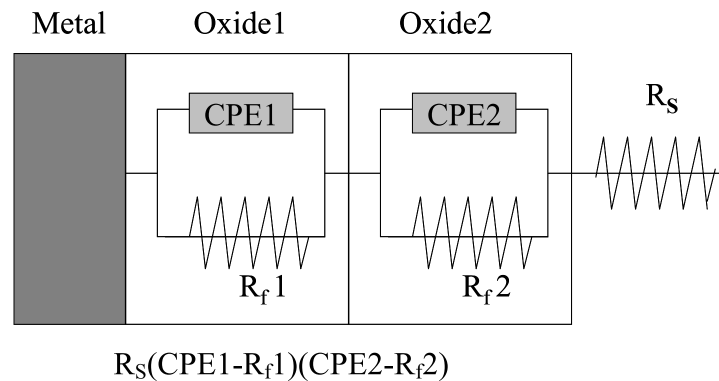

Figure 6.4 Equivalent circuit model for a two layered oxide.

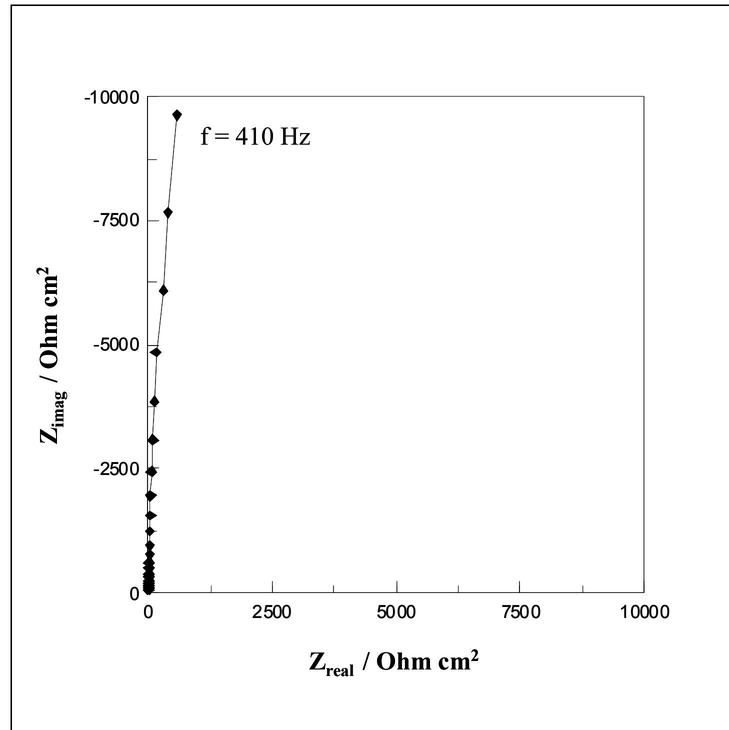

Figure 6.5 Experimental EIS spectrum obtained for the Al-21 at.% Nb alloy after anodising to 150 V at 5 mA cm^{-2} in 0.1 M ammonium pentaborate.

Table 6.2 Dielectric constants, oxide resistivities and corresponding time constants for pure anodic alumina and for the mixed oxide $(Al_2O_3)0.29(Nb_2O_5)$.

Equivalent circuit	Oxide layer	Oxide Composition	δ (nm)	ε_r	ρ (Ohm cm)	(RC) (s)
R_S (C-R_f) (C-R_f)	1st layer	(Al_2O_3) $0.29(Nb_2O_5)$	197	11	4.8 x 10^{10}	4.67 x 10^{-2}
	2nd layer	Al_2O_3	12	9	7.5 x 10^{10}	5.97 x10^{-2}
R_S (C-R_f)		(Al_2O_3) $0.29(Nb_2O_5)$	209	11	4.8 x 10^{10}	4.67 x 10^{-2}

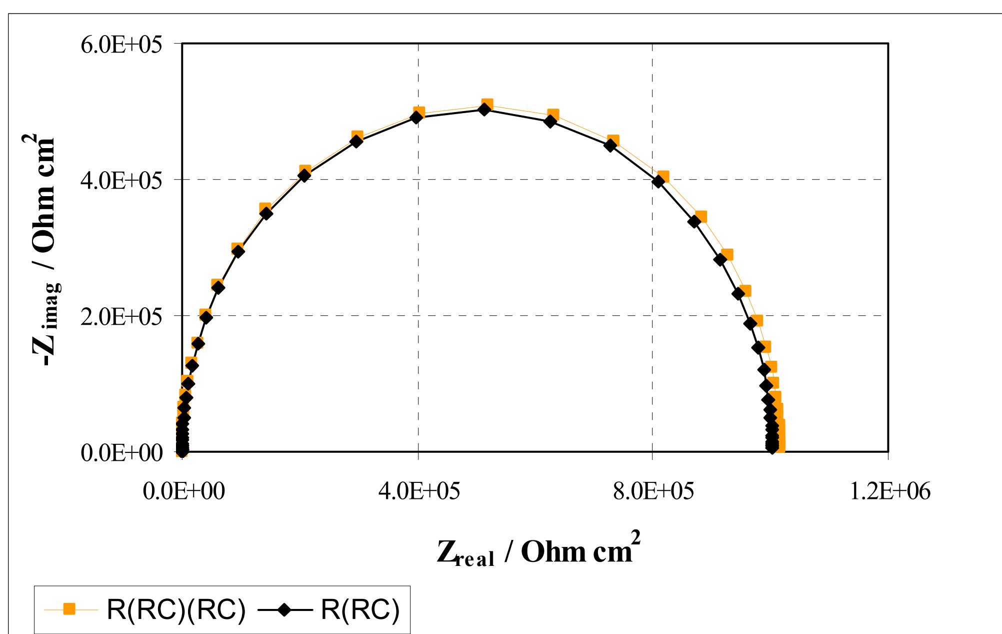

Figure 6.6 Simulated EIS spectra for the equivalent circuits Rs(RC) and Rs(RC)(RC) for the oxide layers according to Table 6.2.

6.3 Anodic oxides on Al-Nb alloys of high niobium content (≥ 74 at.% Nb) and niobium

6.3.1 Dielectric constant and capacitive behaviour

The EIS spectra obtained on the Al-74 at.% Nb and Al-81 at.% Nb alloys also show a phase angle close to 90º and a decrease of the capacitance values with increase of oxide thickness and aluminium ion content (Figure 6.8 and Table 6.3). The dielectric behaviour was confirmed, by plotting the reciprocal capacitance (C^{-1}) against the factor $\delta\varepsilon^{-1}$, to verify if the plane-plate capacitor equation is obeyed (Figure. 6.9). From the corresponding slopes, the relative dielectric constants found are 29 and 40 for the films formed on the Al-74 at.% Nb and Al-81at.% Nb alloys respectively.

The EIS spectra obtained for the anodic oxides of the Al-89 at.% Nb alloys and niobium are more complex and can not be represented by the simple R_s(CPE-R_f) circuit used for the previous anodic oxides formed on alloys of reduced niobium content (Figure 6.10). The variation of the phase angle with frequency suggests two semicircles or time constants (R x C), meaning that more than one process (or layers) respond to the perturbation imposed. The results suggest that a space-charge region, which is associated with the semiconductor characteristics of the oxide layers, could be formed at the oxide/liquid metal interface and, due to this new layer, the spectra show two time constants. The space-charge layers are formed due to the flow of charge across the interface, before reaching equilibrium and they can extend deep inside the oxide layers (Chapter 1). These layers show a variation of the capacitance with applied potential; thus, this feature was checked by measuring a series of EIS spectra for a niobium specimen anodised to 153 V at different applied voltages, between +1 and –1 V (figure 6.10). The results show that there is a continuous variation of the oxide capacitance from +1 V to –0.5 V (Figure 6.11). After this voltage, the capacitive component is reduced and, at –1 V, there is almost only a resistance (phase angle less than –25 º). The capacitance on Figure 6.11 was calculated with a R_s(CPE-R_f) circuit in the frequency range of 32577 to 13 Hz. The semiconductive properties of the anodic oxides formed on niobium and Al-Nb alloys are examined in the next Chapter (7).

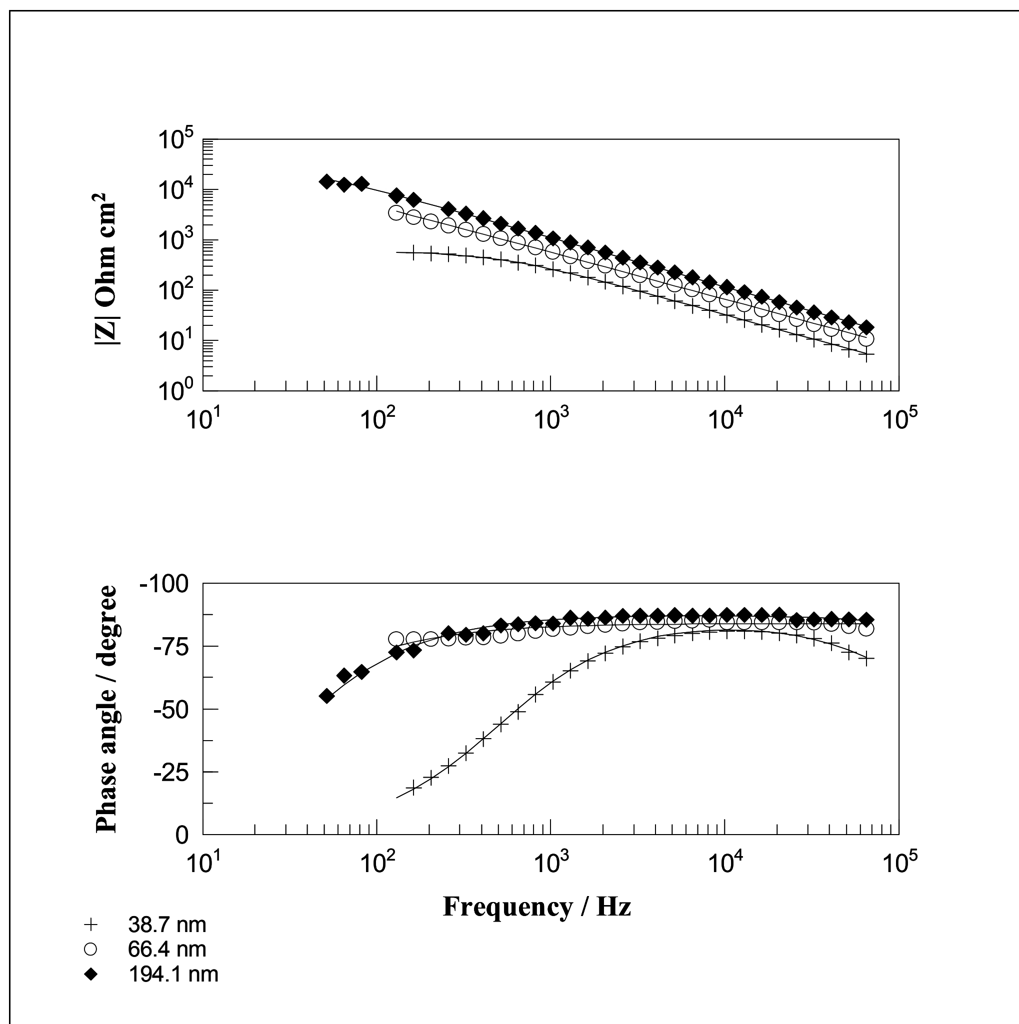

Figure 6.7 Experimental and simulated (line) EIS spectra obtained for the Al-81 at.% Nb alloy after anodising to different voltages at 5 mA cm^{-2} in 0.1 M ammonium pentaborate (oxide thicknesses of 38.7, 66.4 and 194.1 nm respectively).

Table 6.3 Values obtained with the fitting $R_S(CPE_f-R_f)$ on the EIS spectra for different anodic oxide thicknesses on the Al-74 at.% Nb and Al- 81 at.% Nb alloys. Oxide thicknesses calculated from anodising charge.

Anodic oxide composition	Number of spectra	δ (nm)	R_f x 10^{-5} (Ohm cm^2)	C_f (μF cm^{-2})	n	(1-n) (%)
$Al_20_32.84Nb_2O_5$ (Al-74 at.% Nb)	3	33.5	0.23	0.96	0.967	3.3
	3	63.3	0.01	0.38	0.976	2.4
	1	99.3	0.54	0.30	0.975	2.5
	3	129.6	20	0.28	0.973	2.7
	4	159.3	11	0.13	0.989	1.1
$Al_20_34.26Nb_2O_5$ (Al-81 at.% Nb)	3	38.7	0.01	0.705	0.966	3.4
	3	66.4	25.6	0.553	0.932	6.8
	3	123.5	0.11	0.277	0.982	1.8
	3	194.5	0.13	0.188	0.976	2.4

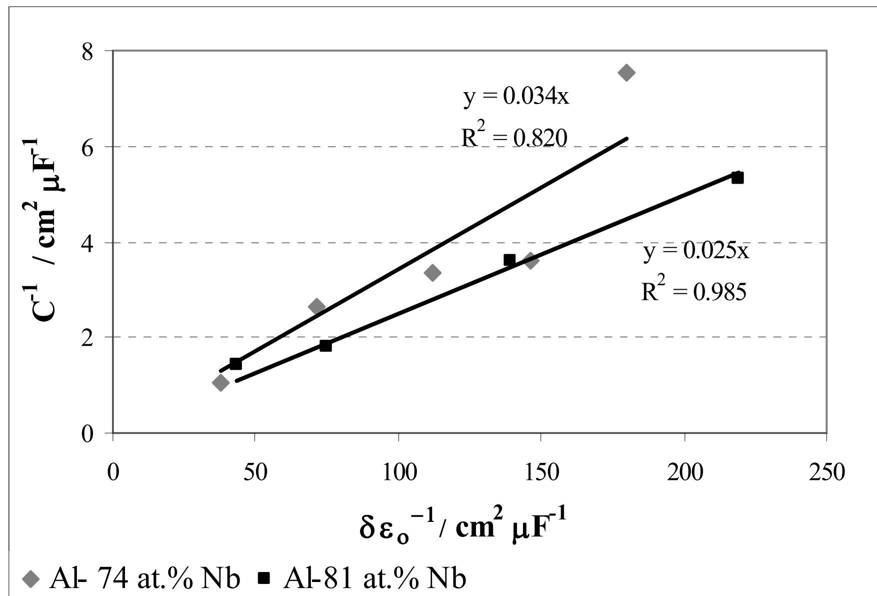

Figure 6.8 Variation of reciprocal capacitance with $\delta\varepsilon_o^{-1}$ for Al-74 at.% Nb and Al-81 at.% Nb alloys after anodising to selected voltages at 5 mA cm^{-2} in 0.1 M ammonium pentaborate.

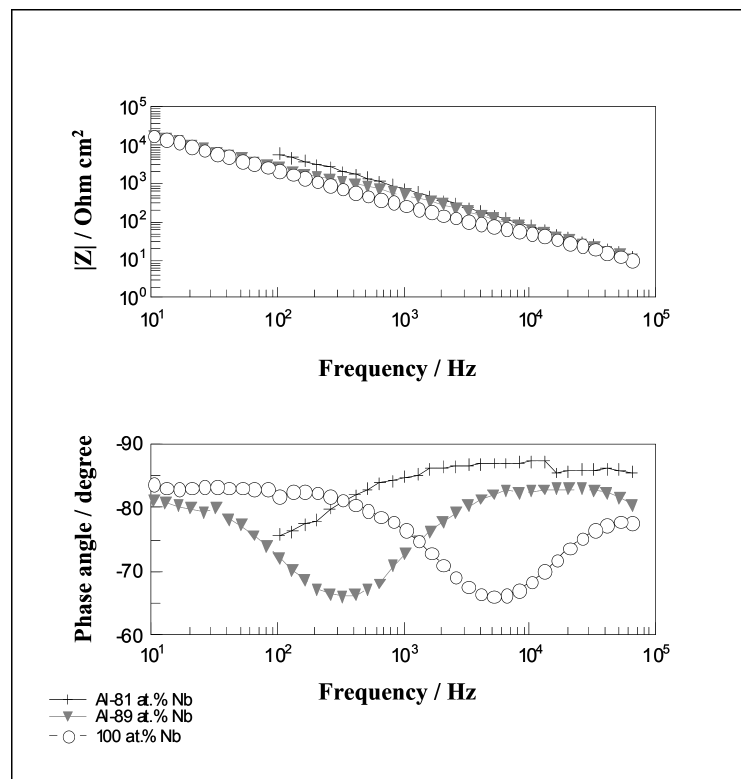

Figure 6.9 EIS spectra obtained for the Al-81 at.% Nb and Al-89 at.% Nb alloys and the sputtered niobium, after anodising to 60 V at 5 mA cm^{-2} in 0.1 M ammonium pentaborate.

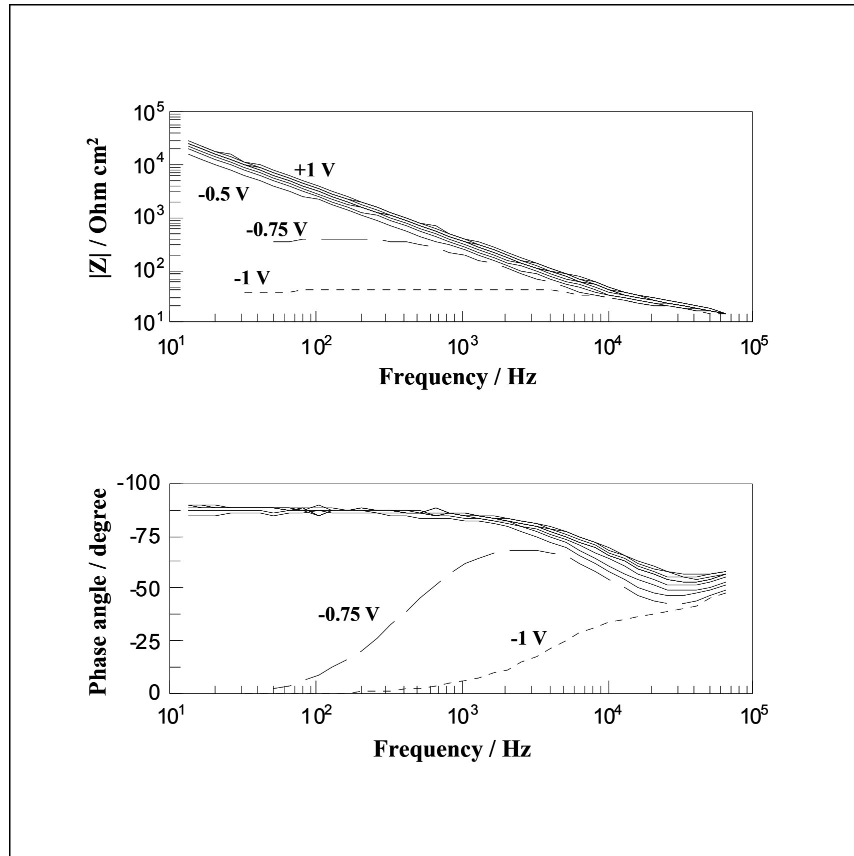

Figure 6.10 EIS spectra obtained at different applied voltages, from +1 to –1 V for the sputtered niobium after anodising to 153 V.

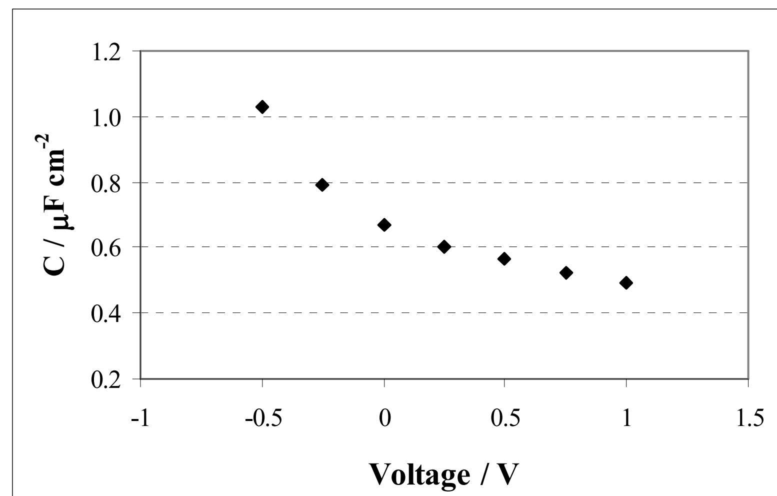

Figure 6.11 Variation of capacitance with voltage for the sputtered niobium after anodising to 153 V at 5 mA cm^{-2} in 0.1 M ammonium pentaborate.

6.4 Discussion

The dielectric constants were calculated from the slope of the linear trend of the reciprocal capacitance with $\delta\varepsilon_o^{-1}$. The results show a linear increase of the dielectric constants with the niobium content in the alloy in the range of 21-81 at.% Nb, where the limits are those of the dielectric constant of anodic oxides in the individual metals (Figure 6.12).

Other mixed oxides, not anodic, but containing units of niobia and prepared by different techniques, also have shown an increase of the dielectric constant with niobium content. For instance, Fujikawa and Taga have studied the system Ta_2O_5+Nb_2O_5, prepared by rf magnetron sputtering in which the niobium content was increased to 30 at.% Nb. They found that the dielectric constant and the inverse of the breakdown field strength were a direct function of the niobium content [163]. Kukli et al. also studied the Al/Nb system, using nanolaminate oxides by atomic layer chemical vapour deposition. They found that the resultant oxide layers were amorphous regardless of their composition and that the dielectric constants increased from 9 to 15-20 for a niobium cation concentration increase from 9 to 70 at.% [164].

The deviation from pure capacitive behaviour, calculated as a mean for all the thicknesses at each oxide composition, increases with niobium content due to the lower electronic resistivity of niobia. The niobium target, used in sputtering, was only of 99.9% purity, thus oxides formed on the alloys of increased niobium contents have also an increased impurity grade. The impurities are probably affecting the dielectric properties. The main impurities of the niobium target are tantalum (500 ppm) and tungsten (100 ppm), which are also valve-metals with insulating oxides. Other impurities in the target include iron (30 ppm), which can contribute to an increase of the loss factor by promoting electrons to the conduction band and consequently increasing electronic conductivity. Despite the low concentration, these impurities can affect the dielectric behaviour, in a similar way as that evident for a doped semiconductor in which a concentration of 100 ppm to 1000 ppm is sufficient to change the electrical behaviour [35].

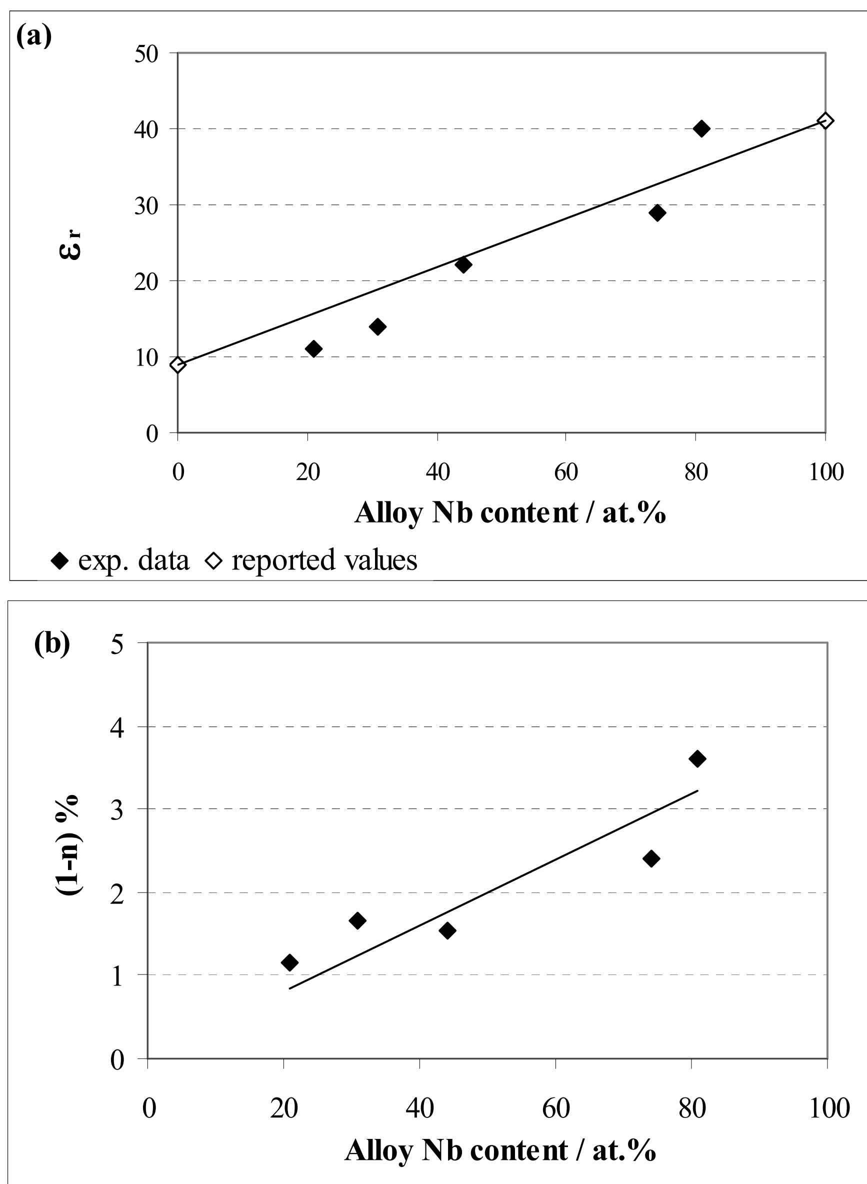

Figure 6.12 Variation of relative dielectric constant (a) and deviation from pure capacitive behaviour (b) with niobium content for the Al-Nb system.

The values obtained for the resistances of the oxides are highly dispersed. However, the associated capacitance values followed the trend of a dielectric behaviour. The explanation for this feature is probably associated with microdefects of the oxide layer that hinder the capacitive behaviour, especially in the range of low frequencies (10-100 Hz). This implies that the charge is not sustained and the leakage is enhanced and, consequently the resistance of the anodic oxide layer is reduced.

The EIS spectra obtained for the anodised Al-89 at.% alloys and niobium show more complex behaviour than that of a simple dielectric layer. The equivalent circuit with more than one time constant is an indication that more than one process is occurring. These results, together with the variation of the capacitance with the applied potential, suggest that such anodic oxides behave as a semiconductor due to the formation of space-charge regions despite the measurements being undertaken with a mercury drop electrode. It has been reported that semiconductor oxide/liquid-metal interfaces show similarities with oxide/electrolyte interfaces; for instance, surface charges have been reported for Al_2O_3 and NiO or Cr_2O_3 oxides [165]. Since anodic niobia usually shows semiconductive properties (Chapter 1), it is not surprising that this character is revealed at this type of interface (oxide/liquid metal). The semiconductive properties of the oxides are examined further in the next chapter.

It was assumed that the oxides are composed of Nb_2O_5 or Nb_2O_5 and Al_2O_3 units; however, electrolyte species are usually incorporated in the anodic oxide and, consequently, some influence on dielectric constant and loss factor may be anticipated. Ono et al, after determining the capacitances of anodic oxides formed at 10 mA cm^{-2} to 60 V with a subsequent voltage holding for 30 min in different electrolytes, including ammonium tetraborate, found that the oxide capacitances are almost constant for acid electrolytes. However, the capacitances change significantly in alkaline electrolytes; furthermore, the highest capacitance was obtained for the film formed in $(NH_4)_2B_4O_7$. They also found that films formed in acid electrolyte, but analysed in different alkaline electrolytes show a strong variation of the oxide capacitance [166, 167]. The literature results, as well as the results obtained in this work, suggest that despite any variation introduced by incorporated electrolyte

species, the capacitance can be strongly dependent of the oxide/electrolyte interface and this is related to the formation of surface charge layers.

6.5 Conclusions

The following conclusions result from this Chapter:

- The anodic layers on the sputtered Al-Nb alloys with 21 to 81 at.% Nb show dielectric behaviour, with the capacitance decreasing linearly with oxide thickness according to the plane-plate capacitor equation. The dielectric constants increase linearly with niobium content where the limits of the dielectric constant are those of the anodic oxides on the individual metals.

- The oxides formed on alloys of increased niobium content, i.e. 89 at.% Nb and of niobium, show a complex behaviour compared with that of a single dielectric layer when measured using the metal/oxide/liquid metal system . These results are associated with the existence of space-charge effects and consequently with semiconductive behaviour.

CHAPTER 7

SEMICONDUCTING PROPERTIES OF ANODIC OXIDES ON NIOBIUM AND Al-Nb ALLOYS

7.1 Introduction

In this Chapter the semiconducting properties of the anodic oxides formed on niobium and Al-Nb alloys have been examined by measuring the dependence of capacitance, C, with the applied potential, E. The results are plotted as C^{-2} versus E (Mott-Schottky plots) and if there is any semiconducting character, the type (n or p), the donor (n-type) or acceptor (p-type) concentration and the flat–band potential can be determined (Chapter 1). The capacitances were measured by EIS (electrochemical impedance spectroscopy) on sputtered specimens of niobium and Al-Nb alloys anodised to different final voltages at 5 mA cm^{-2} in 0.1 M ammonium pentaborate. The EIS experiments were measured in a three-electrode cell over a range of frequency from 65000 to 10 Hz in a borate buffer solution of pH 8.8. The reference was a saturated silver/silver chloride reference electrode. The results were analysed by "Zview software". The percentage errors of the adjusted parameters are less than 10%. The simulated spectra obtained at potentials where the equivalent circuit changes from one to two time constants show increased error percentage (≤ 30%). This increase is possibly related to the partial overlap of the two time constants, meaning that the physical processes related to the time constants are not completely separated in the frequency range tested.

The first results presented are from anodic niobia because, as expected, the anodic film on niobium reveals semiconducting characteristics; and hence this provides the

basis for comparison with the results obtained for the anodic films on the Al-Nb alloys.

Specimens, anodised to 10-12 V, were tested over a range of potential from +5 V to -1.35 V, whereas specimens anodised to increased voltages were tested from 12.5 V to –1.35 V. The applied potential was extended to high positive values with the aim of achieving a complete charge depleted oxide layer, but not so high that new oxide layers were formed at the metal/film and film/electrolyte interfaces. When a complete charge-depleted region is formed, all electrons are removed from the conduction band and then the effect observed is the polarization of ions within the oxide layer, which then behaves as a dielectric layer.

7.2 Anodic niobia

The EIS spectra obtained on the anodic niobia (Figures 7.1 and 7.2) were simulated by a simple equivalent circuit with a resistance, R_S, connected in series with a constant phase element (CPE). The parameters were optimised with the Zview software. This circuit was simulated to the spectra obtained over a range of potential of +12.5 to –1.35 V and frequency range of 20-65 KHz to 10 Hz. The dielectric constant was calculated from the capacitance obtained at the highest positive potential to determine if the value was close to 41. Such a value implies that the oxide layer behaves as a dielectric layer since the capacitance is only the result of the polarization of the anodic oxide and, consequently, the layer behaves as a plane-plate capacitor. The oxide thicknesses were calculated from the anodising charge, assuming an efficiency of 100 %. The results are given in Table 7.1.

The values calculated for the dielectric constant, are markedly greater than the value reported on literature for niobia (41-46); this suggests that the anodic oxide does not behave as a dielectric layer under the selected experimental conditions. Thus, the measured capacitances are related to the polarization of the anodic oxide layers (dieletric behaviour) but, simultaneously, space charge regions are formed at the oxide/electrolyte interface, which increase the capacitance values. The ratio, $E_{applied}/E_{anod}$, for the anodic oxides formed to 12 and 33 V is close to 40 % and the

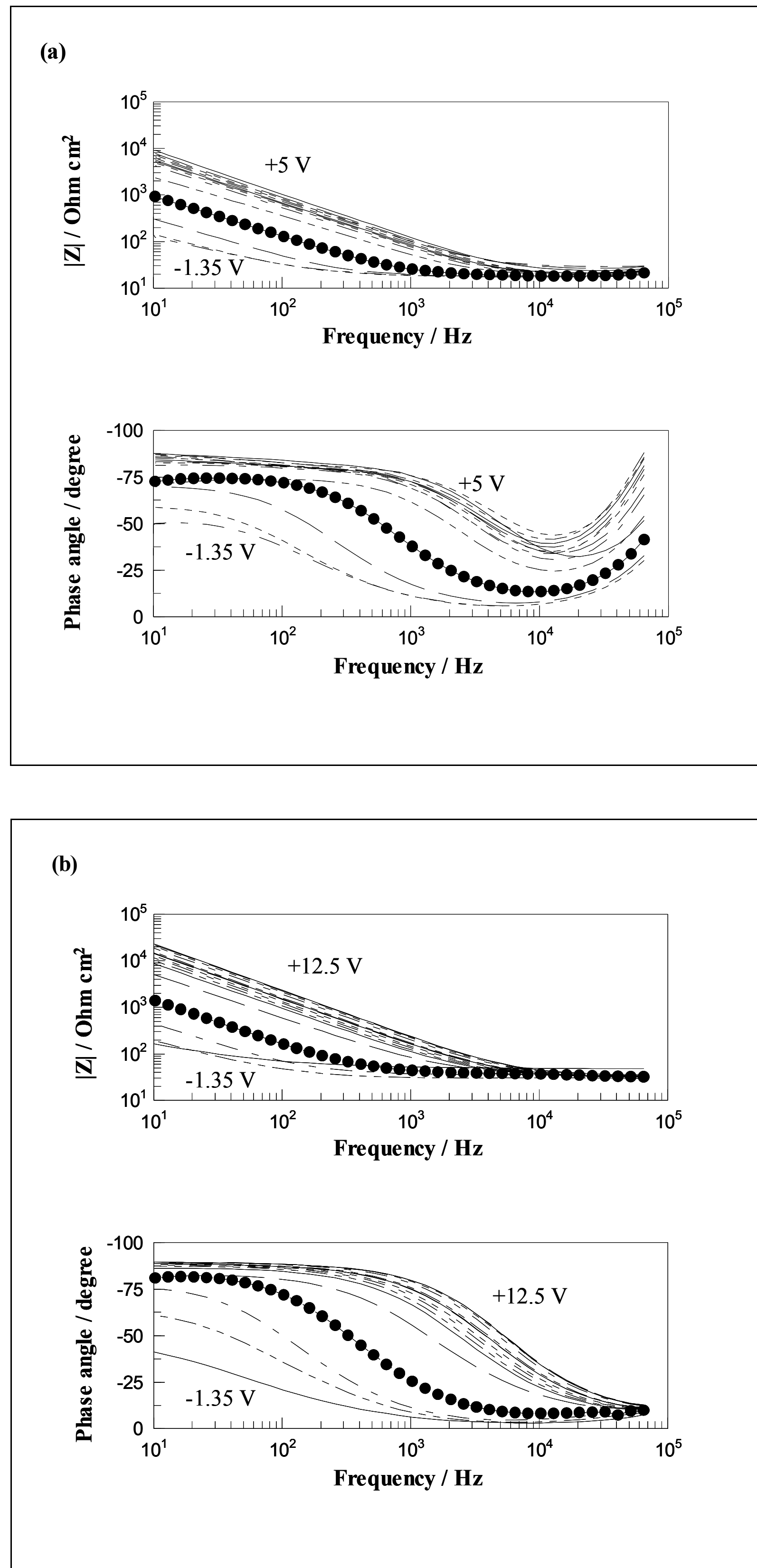

Figure 7.1 Bode plots obtained for the sputtered niobium after anodising to 12 V (a) and to 33 V (b) at 5 mA cm^{-2} in 0.1 M ammonium pentaborate. EIS spectra measured at different potentials in a borate buffer solution (filled circle = spectra at –0.75 V).

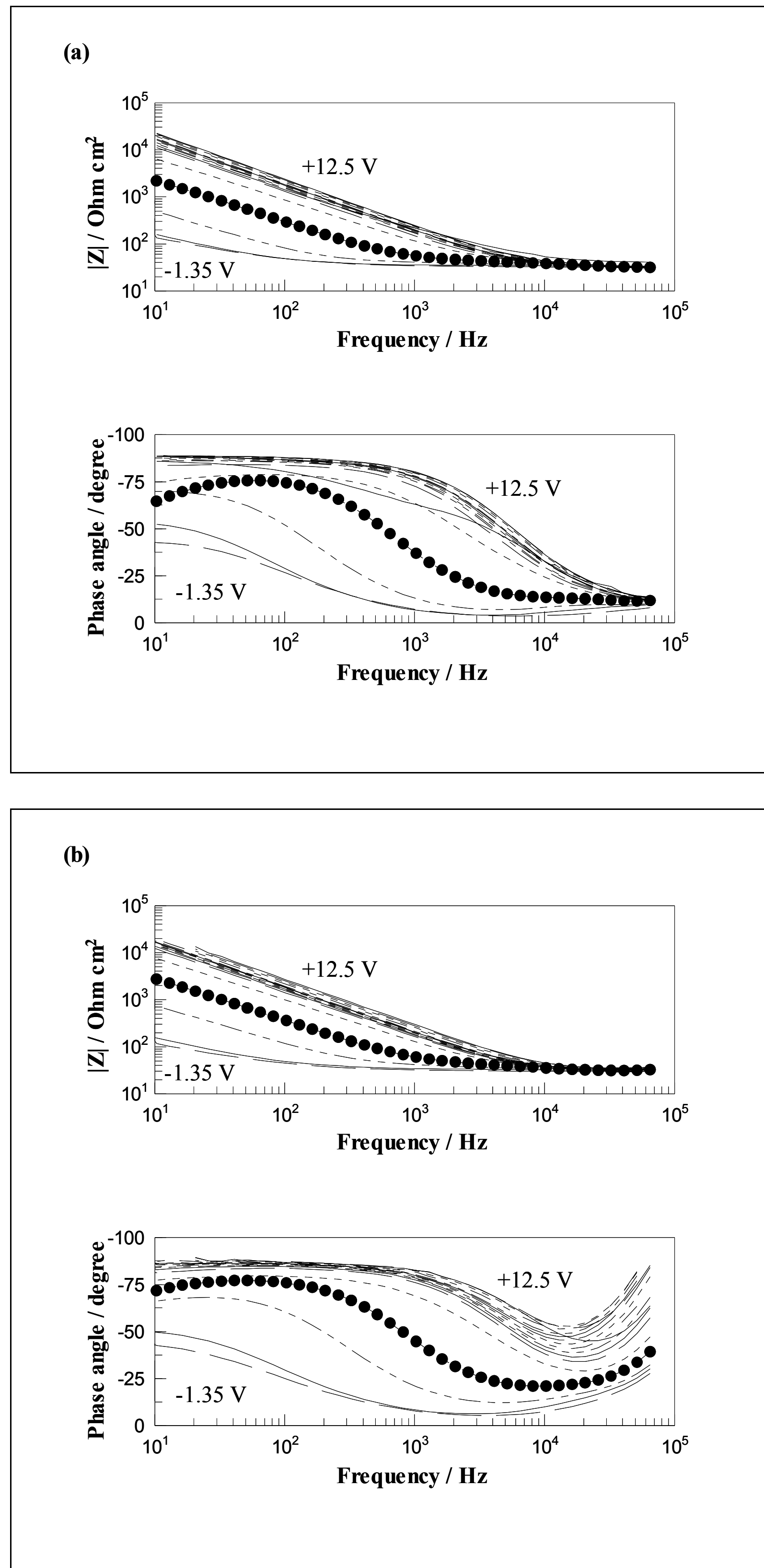

Figure 7.2 Bode plots obtained for the sputtered niobium after anodising to 54 V (a) and to 101 V (b) at 5 mA cm^{-2} in 0.1 M ammonium pentaborate. EIS spectra measured at different potentials in a borate buffer solution (filled circle = spectra at –0.75 V).

Table 7.1 Dielectric constants calculated for the sputtered niobium after anodising to selected voltages at 5 mA cm^{-2} in 0.1 M ammonium pentaborate. Capacitances were determined from EIS spectra measured in a borate buffer solution and oxide thicknesses calculated from anodising charge.

$E_{applied}$ / $E_{anod.}$	Anodising Voltage (V)	Oxide Thickness (nm)	Capacitance (μF cm^{-2}) at 5 V* or 12.5 V	Dielectric Constant ε_r
0.42	12	24	2.11*	57
0.38	33	71	0.74	60
0.23	54	100	0.77	86
0.12	101	192	0.68	146

dielectric constants are 57 and 60 respectively, suggesting that for applied potentials close to the anodising potential, the anodic oxide layer is depleted of electronic carriers and, consequently, behaves as a dielectric.

The Mott-Schottky plots obtained on anodic niobia suggest the formation of a space-charge layer associated with an n-type semiconductor (Figure 7.3). The carrier densities are in the range of 10^{18}- 10^{19} cm^{-3} (Table 7.2), which are in agreement with the values in the literature for such anodic oxides [14]. The values are also in the same range as results obtained in previously reported work, where the anodic oxides were analysed at fixed frequencies by sweeping the potential from +2.5 to –1 V at 5 mV s^{-1} [168]. The flat band potentials, U_{FB}, show some dispersion in the range of -0.418 to -0.496 V_{SHE} but are shifted to more positive values than those previously reported [-0.566, -0.610 V_{SHE}]. The variation is probably associated with the different techniques used for determining the semiconductor characteristics, since the anodic oxides are similar. Thus, it is possible that during potential sweeping, the equilibrium at the oxide/electrolyte interface is not completely achieved, and a shift of the flat band potential to more negative values results.

The values of the exponent, n, of the CPE of the fitted EIS spectra obtained at more positive potentials are between 0.95 and 0.99, showing good capacitive behaviour (Table 7.3). A constant decrease is evident, with values maintained above 0.90, until potentials of –0.35/–0.5 V. From the potential of –0.65 to –1 V, the exponent values are mainly in the range of 0.89-0.84 and, subsequently, the values decrease to 0.6/0.7. This range of potential is after the flat-band potential, U_{FB}, thus the anodic oxide should be associated with charge accumulation if no other process occurs.

The values of the exponent n of less than 1 indicate that the interface is in the no blocking condition, meaning that there is some charge passing through the oxide/electrolyte interface, and the strong increase of the capacitance values are associated with the initial step of proton insertion in the oxide. The capacitances from the EIS spectra obtained at –1.25 and –1.35 V are extremely high and are associated with the low values of n; low values of n, close to 0.5, are indicative of a contribution from a diffusion process [142] confirming the previous suggestion.

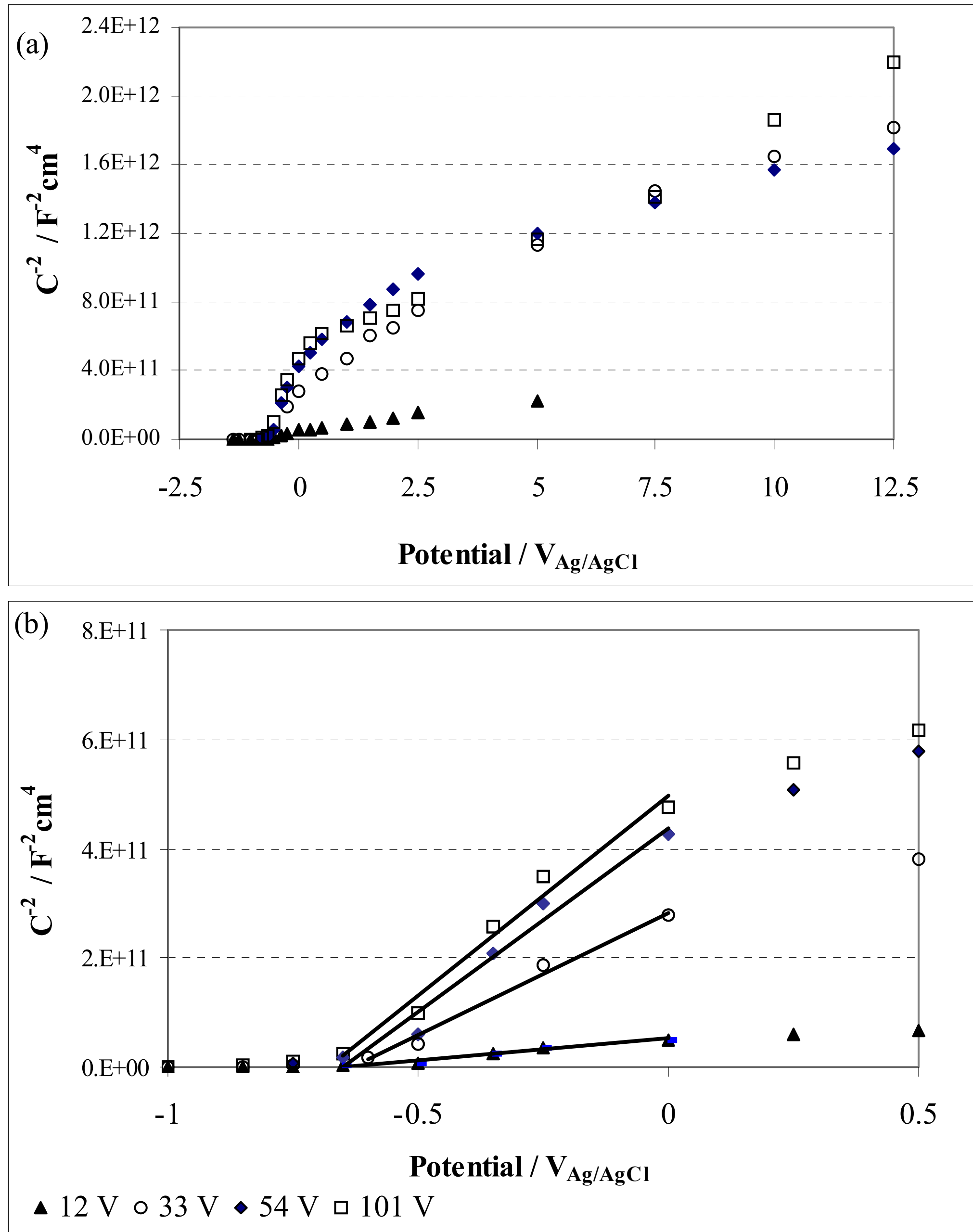

Figure 7.3 Mott-Schottky plots obtained for the sputtered niobium after anodising to 12, 33, 54 and 101 V at 5 mA cm^{-2} in 0.1 M ammonium pentaborate (a). Enlarged plot of figure 7.3a (b). Capacitance was determined from EIS spectra measured in a borate buffer solution.

Table 7.2 Donor concentrations (N_D) and flat band potentials (U_{FB}) for the sputtered niobium after anodising to selected potentials at 5 mA cm^{-2} in 0.1 M ammonium pentaborate and analysed in a borate buffer solution.

Anodising Voltage (V)	Oxide Thickness (nm)	N_D (cm^{-3})	U_{FB} (V_{SHE})
12	24	4.28 x 10^{19}	-0.473
33	72	7.62 x 10^{18}	-0.418
54	100	5.11 x 10^{18}	-0.468
101	192	4.71 x 10^{18}	-0.496

Table 7.3 Capacitance (C) and exponent (n) of the CPE elements of the R_s(CPE) circuit adjusted to the EIS spectra obtained on sputtered niobium after anodising to selected voltages at 5 mA cm^{-2} in 0.1 M ammonium pentaborate.

Anodising Voltage →	12 V		33 V		54 V		101 V	
Applied potential ↓	C (μF cm^{-2})	n	C (μF cm^{-2})	n	C (μF cm^{-2})	n	C (μF cm^{-2})	n
12.5	---		0.74	0.99	0.77	0.98	0.68	0.97
10	---		0.78	0.98	0.80	0.98	0.73	0.97
7.5	---		0.83	0.98	0.85	0.98	0.84	0.96
5	2.11	0.95	0.94	0.98	0.91	0.97	0.92	0.96
2.5	2.57	0.94	1.15	0.97	1.02	0.97	1.11	0.95
2	2.82	0.94	1.24	0.97	1.07	0.97	1.15	0.95
1.5	3.17	0.93	1.28	0.97	1.13	0.97	1.19	0.95
1	3.42	0.93	1.45	0.97	1.21	0.96	1.23	0.95
0.5	3.83	0.92	1.62	0.97	1.31	0.96	1.27	0.95
0.25	4.10	0.92	---	--	1.40	0.96	1.34	0.95
0	4.43	0.92	1.9	0.96	1.53	0.95	1.45	0.95
-0.25	5.21	0.91	2.32	0.95	1.83	0.94	1.70	0.95
-0.35	6.26	0.90	--	--	2.19	0.93	1.98	0.94
-0.5	12.26	0.86	4.78	0.91	4.04	0.88	3.20	0.92
-0.65	18.38	0.86	7.34	0.92	7.42	0.88	6.21	0.89
-0.75	29.04	0.87	15.75	0.93	12.86	0.87	9.47	0.88
-0.85	48.47	0.87	26.74	0.92	21.06	0.87	19.27	0.88
-1	101.54	0.84	59.63	0.88	58.53	0.86	42.44	0.84
-1.25	315.85	0.76	202.93	0.79	323.68	0.74	404.51	0.70
-1.35	490.17	0.70	564.77	0.63	591.20	0.65	754.10	0.63

Furthermore, the EIS spectrum at an applied potential of –1.35 V was extended to a frequency of 0.05 Hz and behaviour consistent with a diffusion process was evident (Figure 7.4). The complex diagram of an element of finite diffusion length is characterized by a straight line with the real part equal to the imaginary part on the high frequency range, which then evolves to a depressed semicircle [142]. The insertion of protons into an oxide or metallic layer is usually associated with an adsorption process step, followed by a charge transfer process and finally a diffusion process [169-171]. Thus, the complete diffusion process is simulated by an equivalent circuit with different elements (Appendix 1). The preliminary analysis of such results reported on Appendix 1 confirms a diffusion process.

7.3 Anodic oxides on Al-Nb alloys

7.3.1 Anodic oxides formed on Al-31 at.% Nb and Al-44 at.% Nb alloys

A similar experimental procedure was undertaken to determine the semiconducting properties of the anodic oxides on the alloys of niobium content of 31 at.% and 44 at.% formed to 51 and 31 V respectively (Figure 7.5). The EIS spectra obtained over the entire range of frequency (65000 –10 Hz) were adjusted to the same equivalent circuit used for the anodic niobium oxide; i.e., a resistance, R_s, connected in series with a CPE. The EIS spectra for the anodic oxide on the Al-44 at.% Nb alloy, from –0.85 to –1.35 V, were better simulated by a circuit represented by a resistance connected in series to a module of a CPE connected in parallel with a second resistance, R_s(CPE-R). For this negative range of potential, the change is associated with a decrease of anodic oxide resistance due to the cathodic polarisation, probably associated with some proton insertion. The capacitance is almost constant for the anodic oxide on Al-31 at.% Nb alloy over the entire range of applied potential, and there is a slight variation in the cathodic branch for the anodic oxide on the Al- 44 at.% Nb alloy, from 0.43 $\mu F\ cm^{-2}$ at 0 V to 0.48 $\mu F\ cm^{-2}$ at –1.35 V (Figure 7.6). The dielectric constants, calculated from the capacitance measured at +12.5 V, correspond to 13.3 for the anodic oxide on the Al-31 at.% Nb alloy and 26.6 for the anodic oxide on the Al-44 at.% Nb alloy. The values, obtained by measuring the capacitance with a mercury drop, are 16 and 20 respectively.

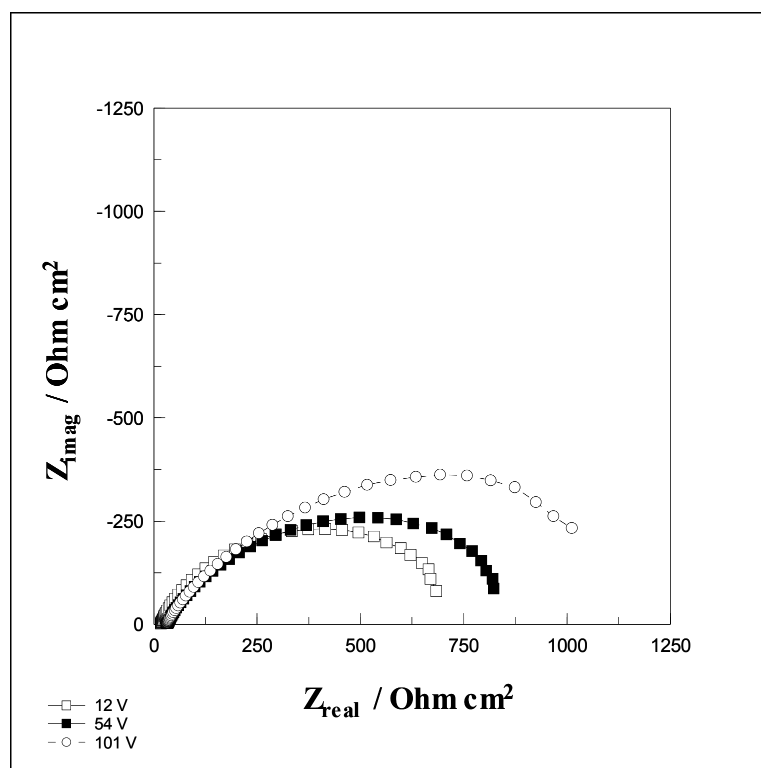

Figure 7.4 Complex plots obtained for the sputtered niobium after anodising to 12, 54 and 101 V at 5 mA cm^{-2} in 0.1 M ammonium. EIS spectra measured at –1.35 V in a borate buffer solution.

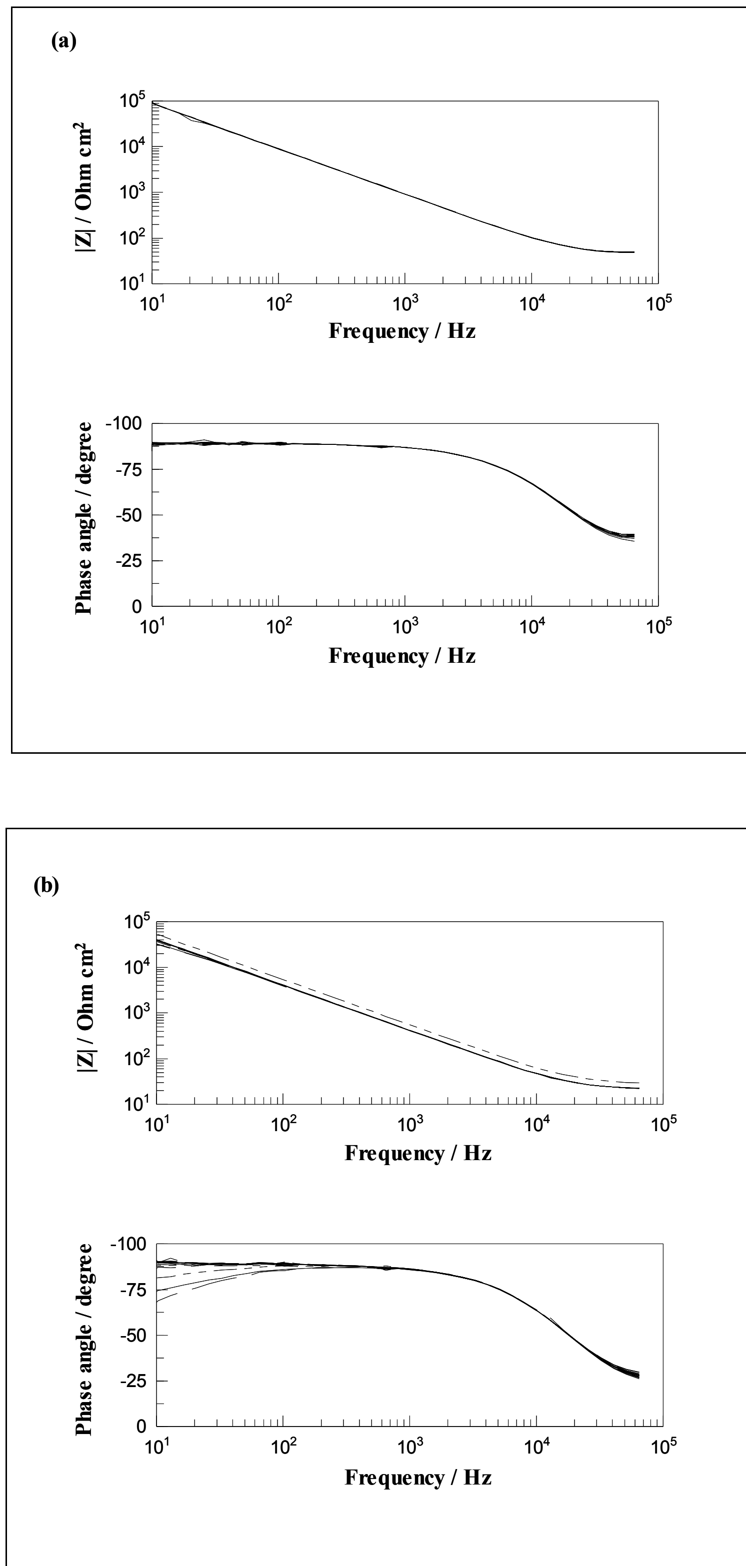

Figure 7.5 Bode plots obtained for the Al-31 at.% Nb alloy after anodising to 52 V (a) and for the Al-44 at.% Nb alloy after anodising to 31 V (b) at 5 mA cm^{-2} in 0.1 M ammonium pentaborate. EIS spectra measured in a borate buffer solution.

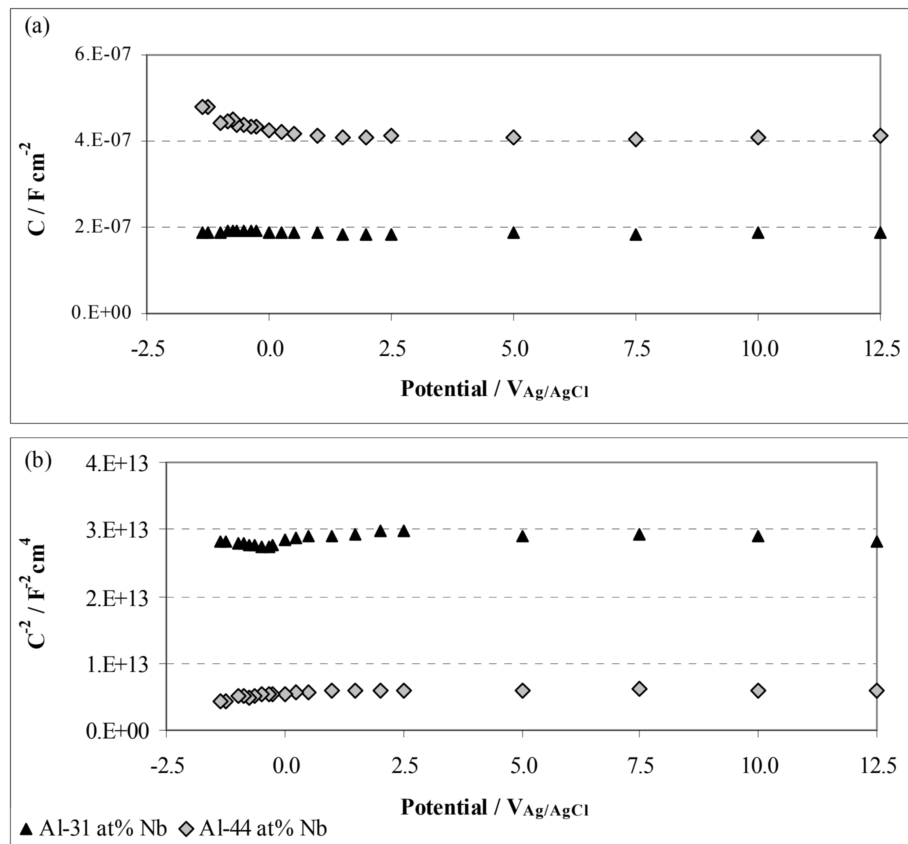

Figure 7.6 Variation of capacitance with potential (a) and Mott-Schottky plot (b) for the Al-31 at.% Nb alloy after anodising to 52 V and for the Al-44 at.% Nb alloy after anodising to 31 V at 5 mA cm^{-2} in 0.1 M ammonium pentaborate. Capacitance was determined from EIS spectra in a borate buffer solution.

7.3.2 Anodic oxides on Al-Nb alloys of high niobium content (≥ 74 at.% Nb)

Following the same experimental procedure, the semiconducting properties of the anodic oxides on the Al-Nb alloys of high niobium (≥ 74 at.%) content were also determined. Anodic films were formed to 51 V on the Al-74 at.% Nb alloy, and were formed to 11 and 31 V on the Al-at.% 81 Nb and Al-89 at.% Nb alloys.

The EIS spectra were measured from 5 to –1.35 V for the Al-81 at % Nb and 89 at.% Nb alloys anodised to 11 V (Figure 7.7). The spectra are similar to those obtained for anodised sputtered niobium and were simulated by a R_S(CPE) circuit. The Mott-Schottky plots show a linear trend and the corresponding calculated carrier density and flat band potentials were calculated (Figure 7.8 and Table 7.4). The values were 9.5×10^{18} and -0.489 V_{SHE} for the anodic oxide on the Al-81 at.% Nb alloy and 1.57×10^{19} and –0.488 V_{SHE} for the anodic oxide on the Al-89 at.% Nb alloy.

The anodic oxide thicknesses, calculated from the anodising charge, assuming an efficiency of 100 %, correspond to 20 and 21 nm respectively. The relative dielectric constants, calculated from the capacitances obtained at 5 V, are 37 for the anodic oxide on the Al-81 at.% Nb alloy and 42 for the anodic oxide on the Al-89 at.% Nb alloy. These values suggest that the amount of alumina within the oxide for this particular thickness is sufficient to induce a full charge depleted oxide and the anodic oxide behaves as an insulating layer at 40 % of $E_{applied}/E_{anod}$ when the capacitance is measured in 0.1 M ammonium pentaborate. Thus, the potential is sufficient to remove the electrons from the conduction band of the anodic oxide layer and, consequently, the only process detected is the polarization of atoms or ions, and the anodic oxide behaves as a dielectric layer.

The spectrum of the Al-74 at.% Nb alloy anodised to 51 V shows more than one time constant; similar behaviour is evident in the spectra obtained for the Al-81 at.% Nb and Al-89 at.% Nb alloys anodised to 31, since there is an inflection on the variation of phase angle with frequency, which suggests more than one process (Figures 7.9 and 7.10).

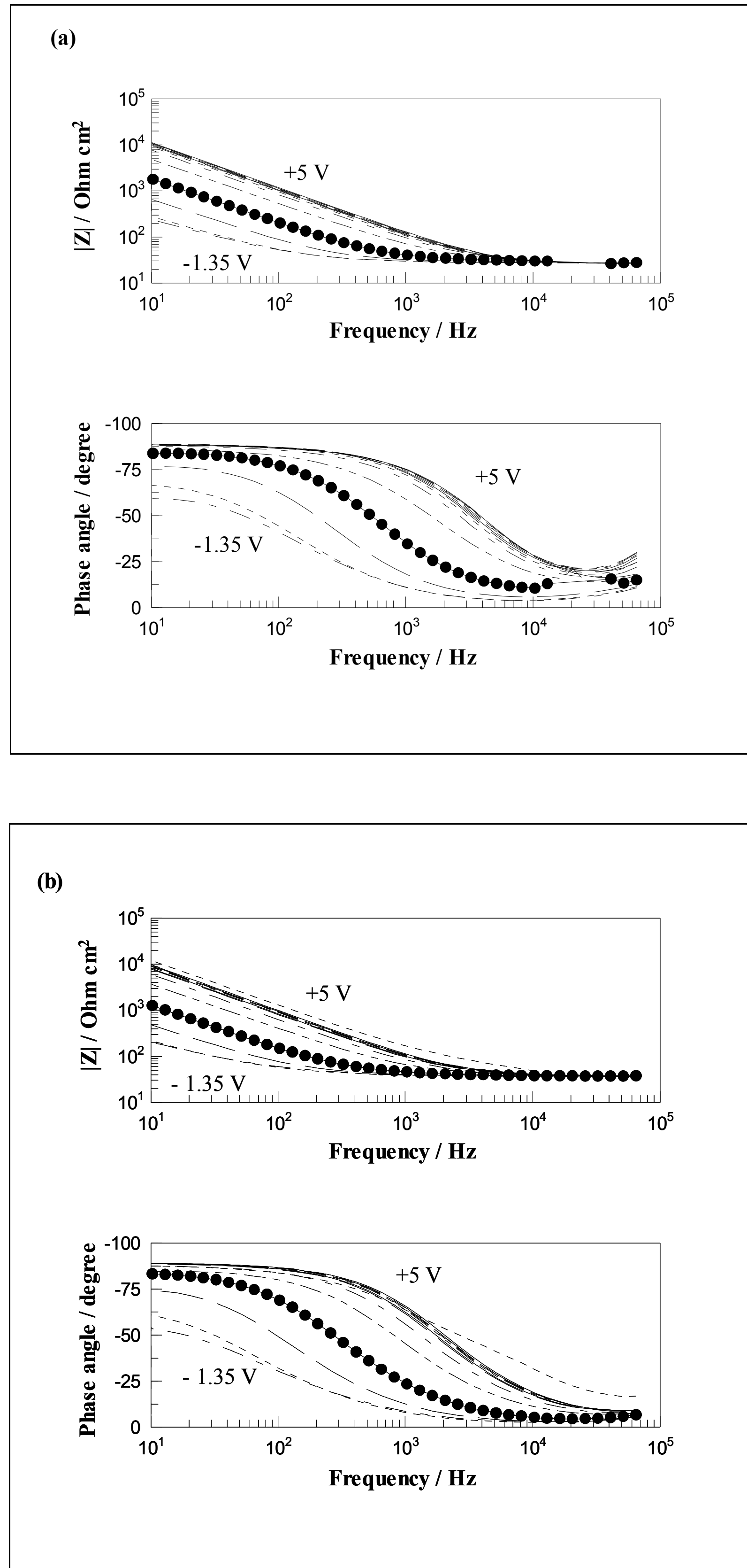

Figure 7.7 Bode plots obtained for the Al-81 at.% Nb alloy (a) and Al-89 at.% Nb alloy (b) after anodising to 11 V at 5 mA cm^{-2} in 0.1 M ammonium pentaborate. EIS spectra measured in a borate buffer solution (filled circle = spectrum at –0.75 V).

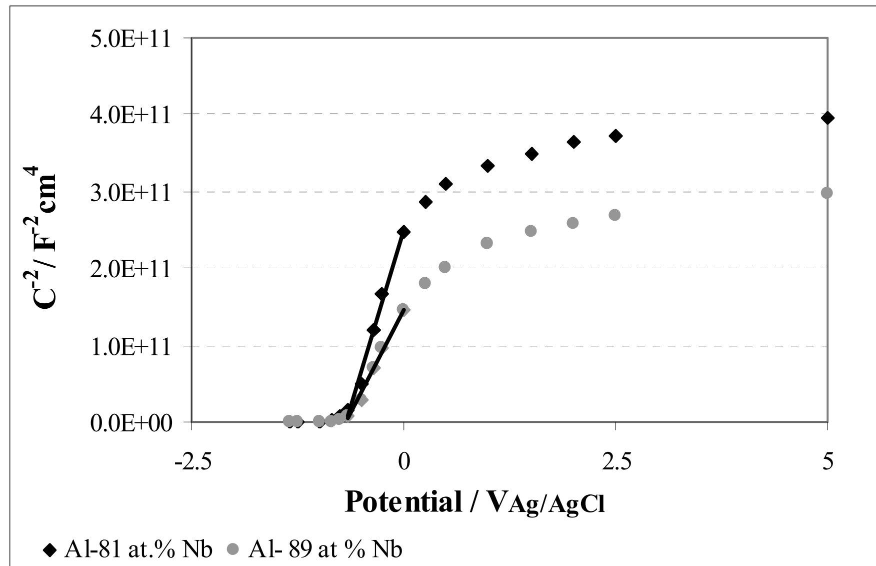

Figure 7.8 Mott-Schottky plots obtained for the Al-81 at.% Nb and Al-89 at.% Nb alloys after anodising to 11 V at 5 mA cm^{-2} in 0.1 M ammonium pentaborate. Capacitance was determined from EIS spectra measured in a borate buffer solution.

Table 7.4 Donor concentrations (N_D) and flat band potentials (U_{FB}) for the Al-81 and Al-89 at.% Nb alloys after anodising to 11 V at 5 mA cm^{-2} in 0.1 M ammonium pentaborate and analysed in a borate buffer solution.

Alloy	Anodising Voltage (V)	N_D (cm^{-3})	U_{FB} (V_{SHE})
Al-81 at.% Nb	11	9.50×10^{18}	-0.489
Al-89 at.% Nb	11	1.57×10^{19}	-0.488

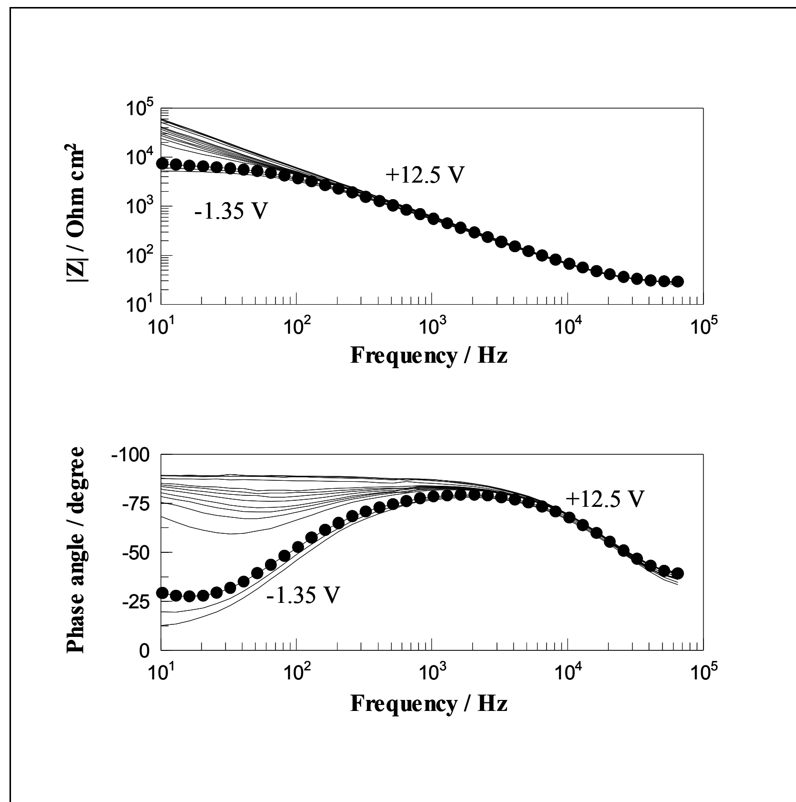

Figure 7.9 Bode plots obtained for the Al-74 at.% Nb alloy after anodising to 51 V at 5 mA cm^{-2} in 0.1 M ammonium pentaborate. EIS spectra measured in a borate buffer solution (filled circle = spectrum at –0.75 V).

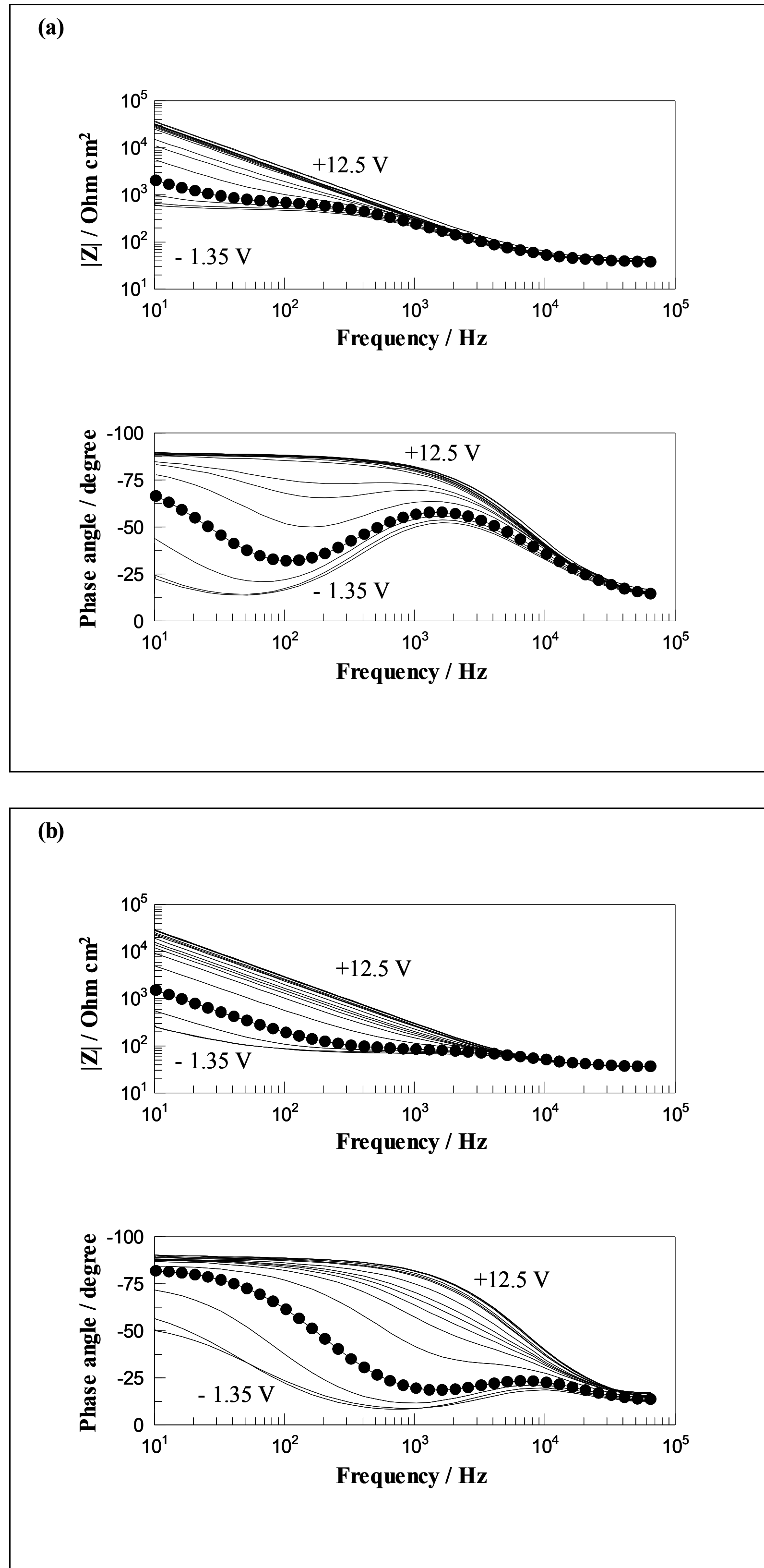

Figure 7.10 Bode plots obtained for the Al-81 at.% Nb and for the Al-89 at.% Nb alloy after anodising to 31 V at 5 mA cm^{-2} in 0.1 M ammonium pentaborate. EIS spectra measured in a borate buffer solution (filled circle = spectrum at –0.75 V).

The inflection point varies with alloy composition, since it was observed that for an increase of niobium content, the inflection point is shifted to high values of frequency and low values of potential (Table 7.5 and Figure 7.11). The spectra, after showing this inflection, were simulated to an equivalent circuit represented by $R_S(CPE_1\text{-}R_1)(CPE_2)$ (Figure 7.12), in which Rs is the usual system resistance, (CPE_1-R_1) is associated with the oxide layer, and the CPE_2 is associated with the space-charge region.

The capacitance obtained at +12.5 V was used to calculate the dielectric constant of the oxides as indicated on Table 7.6. The value obtained for the anodic oxide on the Al-74 at.% Nb alloys is in agreement with that measured previously with a mercury drop (29); the other values are close to the reported value for anodic niobia (41). Thus it is assumed that these anodic oxides at this potential form a complete charge depleted layer and behave as dielectric layers. The results are in agreement with those obtained on thin oxides, anodised to 11 V, showing that with this percentage of alumina within the anodic oxide layer, a ratio of $E_{applied}/E_{anod}$ of 40% is only necessary to achieve a depleted layer of electronic carriers.

The spectra of the anodised Al-74 at.% Nb alloy, were simulated by a simple R_S(CPE) circuit over the range of potential of 12.5 to 5 V. The capacitance of the CPE element changes from 0.27 μF cm^{-2} at 12.5 to 0.35 μF cm^{-2} at 5 V. Thus, it is considered that the anodic oxide is near complete charge depletion and, consequently, behaves as a dielectric layer. After the potential of 2.5 V, the spectra reveals two time constants and were adjusted to circuit represented on figure 7.12.The variation of the capacitance of CPE (before splitting), CPE1 and CPE2 , as well as of R1 with potential are shown in Figure 7.13.

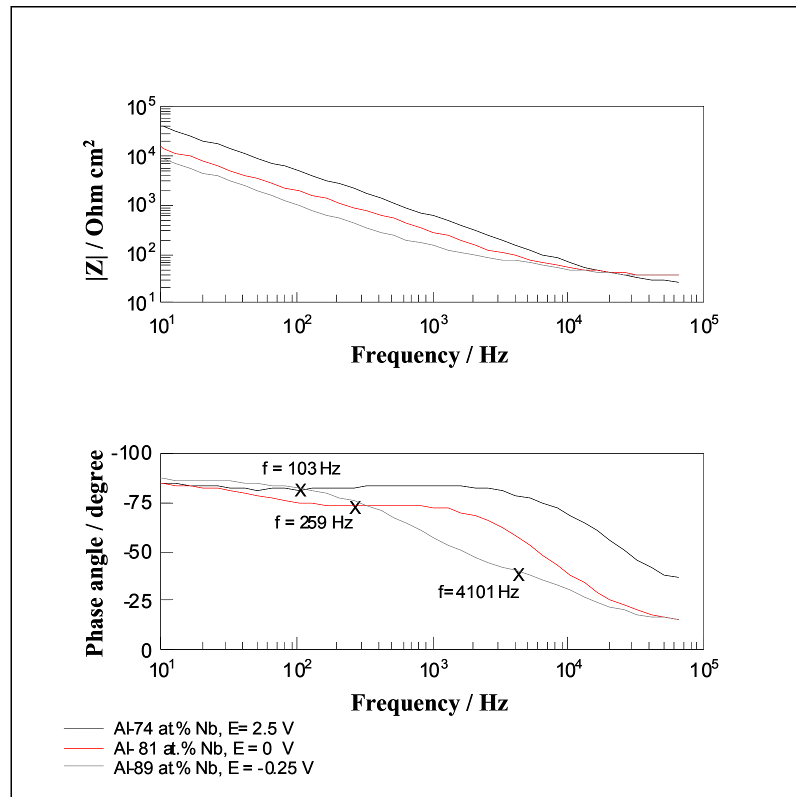

Figure 7.11 Bode Plots obtained for the Al-74 at.% Nb, Al-81 at.% Nb Al-and 89 at.% Nb alloys after anodising to 51, 31 and 31 V respectively at 5 mA cm^{-2} in 0.1 M ammonium pentaborate. EIS spectra measured in a borate buffer solution at the potential where it was observed an inflection point in the phase angle.

Table 7.5 Values of CPE (capacitance and n parameter) obtained from the fitting of the EIS spectra adjusted to a R_S(CPE) circuit for the Al-Nb alloys of high niobium content, after anodising to selected voltages at 5 mA cm^{-2} in 0.1 M ammonium pentaborate solution.

Anodic oxide →	Al- 74 At % Nb (51 V)		Al- 81 At % Nb (31 V)		Al- 89 At % Nb (31 V)	
Applied potential ↓	C (μF cm^{-2})	n	C (μF cm^{-2})	n	C (μF cm^{-2})	n
12.5	0.272	0.99	0.538	0.98	0.578	0.99
10	0.290	0.98	0.551	0.98	0.572	0.99
7.5	0.294	0.98	0.561	0.98	0.581	0.99
5	0.349	0.97	0.575	0.98	0.600	0.99
2.5			0.611	0.97	0.680	0.98
2			0.644	0.97	0.742	0.97
1.5			0.699	0.96	0.797	0.97
1			0.788	0.95	1.056	0.95
0.5			1.037	0.92	1.401	0.93
0.25			1.313	0.90	1.676	0.92
0					2.008	0.91

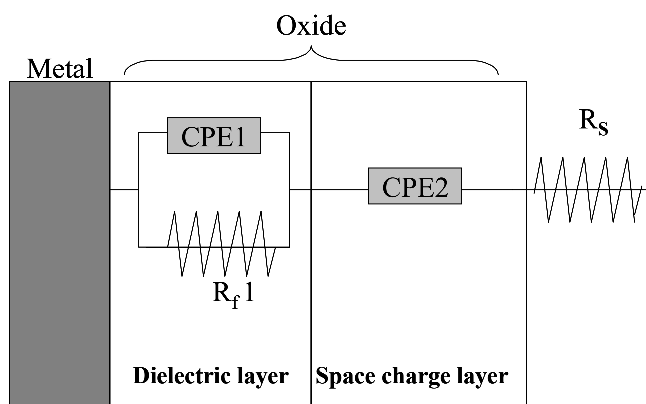

Figure 7.12 Equivalent circuit adjusted to the EIS spectra obtained for Al-Nb alloys after anodising to higher voltages than 31 V when two time constants were observed.

Table 7.6 Dielectric constants for the Al-74 at.% Nb, Al-81 at.% Nb and Al-89 at % Nb alloys after anodising to selected voltages at 5 mA cm^{-2} in 0.1 M ammonium pentaborate. Capacitances were determined from EIS spectra.

Anodic Oxide	Anodising Voltage (V)	Capacitance (μF cm^{-2})	Dielectric Constant (ε_r)
Al-74 at.% Nb	51	0.272	31
Al-81 at.% Nb	31	0.538	40
Al-89 at.% Nb	31	0.578	40

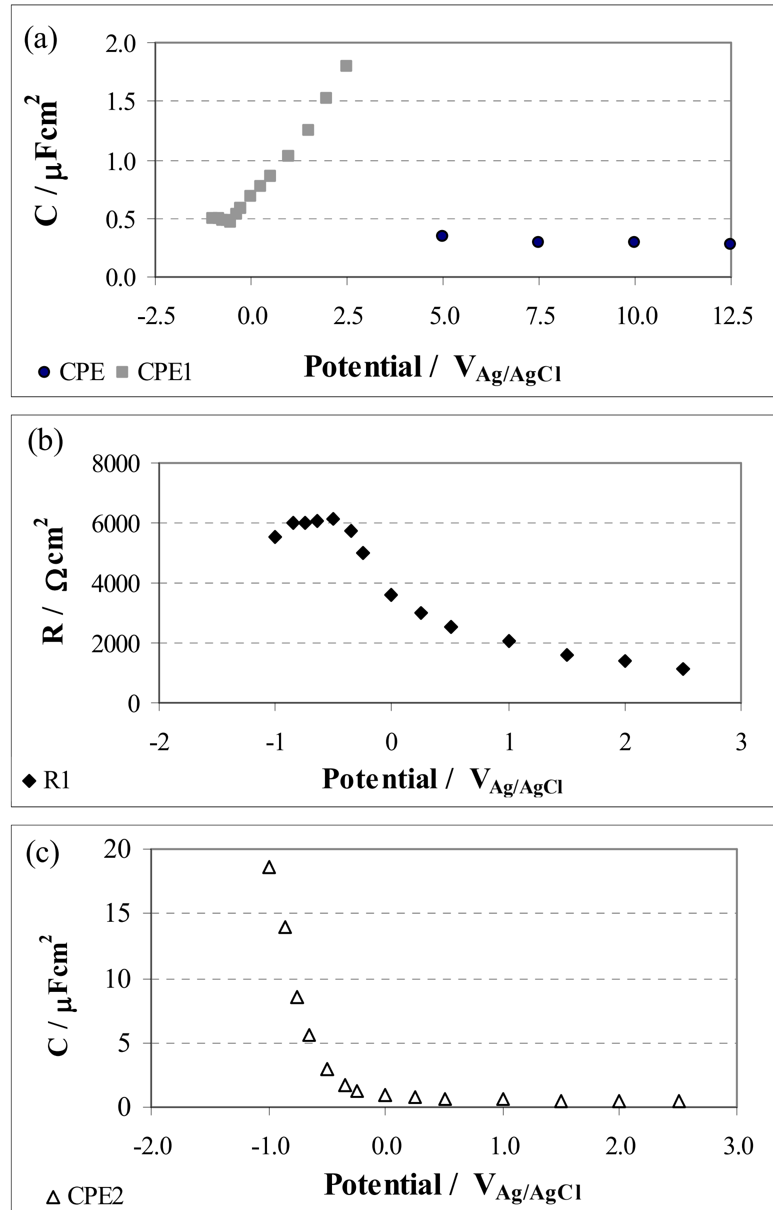

Figure 7.13 Variation of capacitance and resistance with potential for the different elements of the equivalent circuits adjusted to the EIS spectra obtained for the Al-74 at.% Nb alloy after anodising to 51 V: (a) CPE and CPE1; (b) R1; (c) CPE2.

The results suggest, by comparing with the spectra obtained on niobium oxide, that the capacitance associated with CPE2 corresponds to a space-charge formation. The variation of C^{-2} with potential shows two linear trends, from 2.5 to 0 V and from 0 to –0.5 V (Figure 7.14).

The straight line from 0 to –0.5 V is associated with space-charge formation. The elements CPE_1 and R_1 are associated with an anodic oxide layer close to the metal/oxide interface, behaving as dielectric, but of thickness less than the total oxide layer. This layer increases with decrease of potential, since the space-charge thickness decreases until the flat band condition is achieved (Chapter 1).

A similar analysis was performed for the spectra obtained for the anodic oxides formed on the Al-81 at.% Nb and Al-89 at.% Nb alloys (Figures 7.15 and 7.16). The spectra are also split but at reduced potentials, of 0 and –0.25 V respectively; prior to the split, there is a strong variation ob the capacitance associated with the CPE. After splitting, the spectra were adjusted to the circuit of Figure 7.11. Similar to the previous case, the capacitance of CPE2 is associated with the space-charge formation, and the variation of C^{-2} with potential also shows a linear region (Figure 7.17), allowing the carrier density and flat band potential to be calculated (table 7.7). The values of the resistance R_1 for both anodic oxides are much lower than the resistance obtained for the anodic oxide on the Al-74 at.% Nb alloy, due to the increased niobium content and also to the fact that the anodic oxides are thinner, due to the anodising potential of only 31 V.

Following the same experimental procedure, the spectra measured at –1.35 V were extended to a frequency of 0.05 Hz. The results reveal behaviour related to a diffusion controlled process associated with the proton insertion in the oxide layer, since a straight line, followed by a depressed circle, is evident (Figures 7.18 and 7.19). This effect is observed on all the anodic oxides on the Al-Nb alloys of niobium content greater than 74 at.% Nb. The spectra of the Al-74 at.% Nb alloy and Al-81 at.% Nb alloy anodised to 51 and 31 V respectively, show a well-defined semicircle in the range of high frequencies associated with dielectric behaviour of the anodic oxide layers.

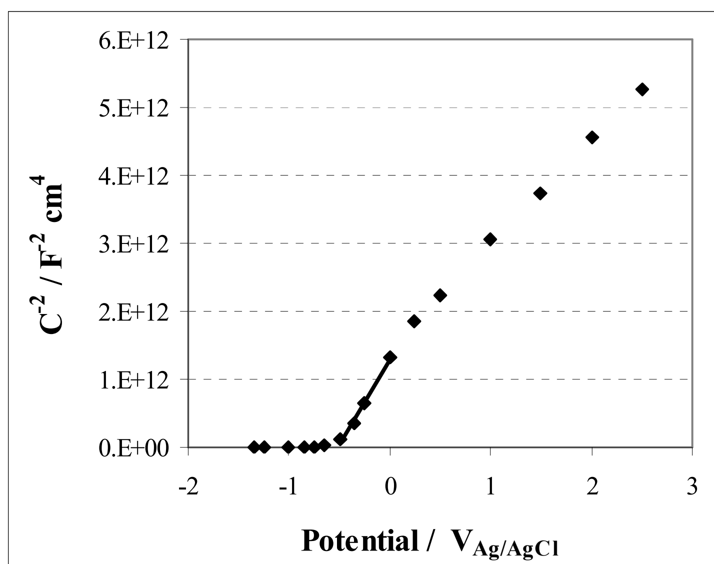

Figure 7.14 Mott-Schottky plot obtained for the Al- 74 at.% Nb alloy after anodising to 51 V at 5 mA cm^{-2} in 0.1 M ammonium pentaborate. Capacitance was determined from EIS spectra measured in a borate buffer solution.

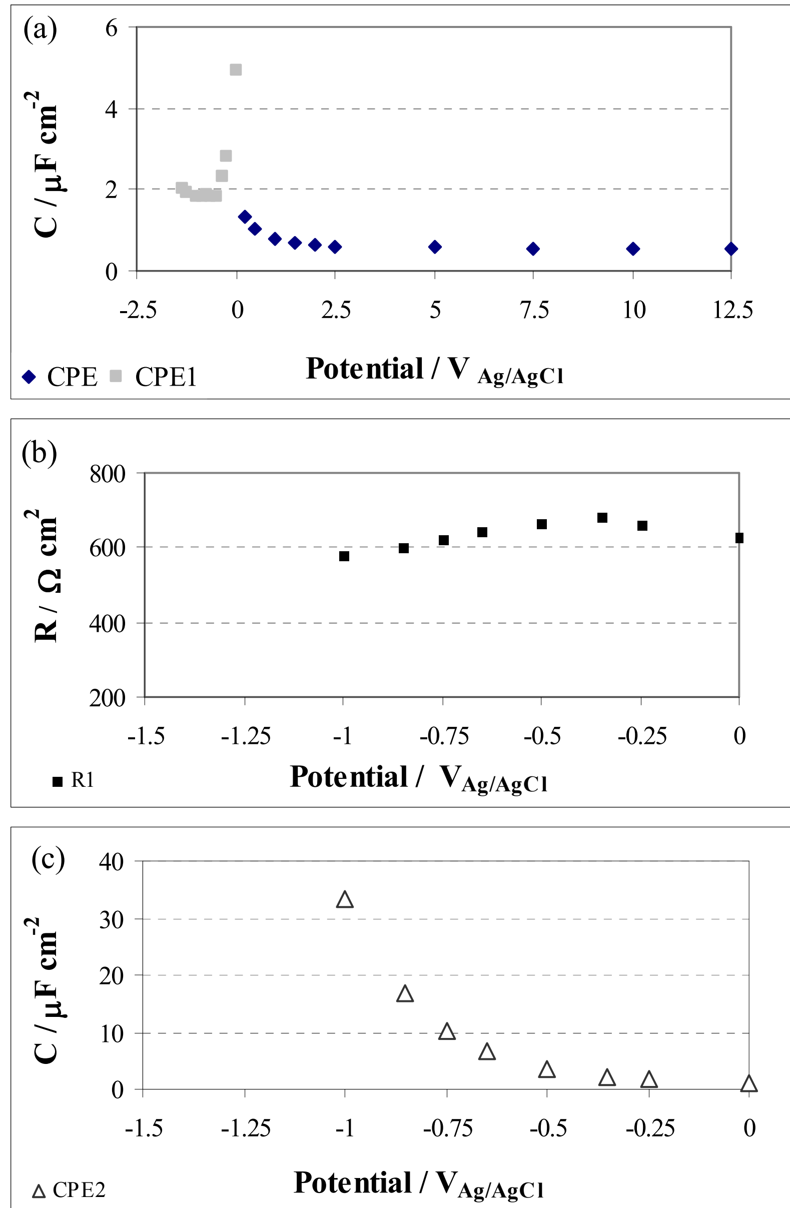

Figure 7.15 Variation of capacitance and resistance with potential for the different elements of the equivalent circuits adjusted to the EIS spectra obtained for the Al-81 at.% Nb alloy after anodising to 31 V: (a) CPE and CPE1; (b) R1, (c) CPE2.

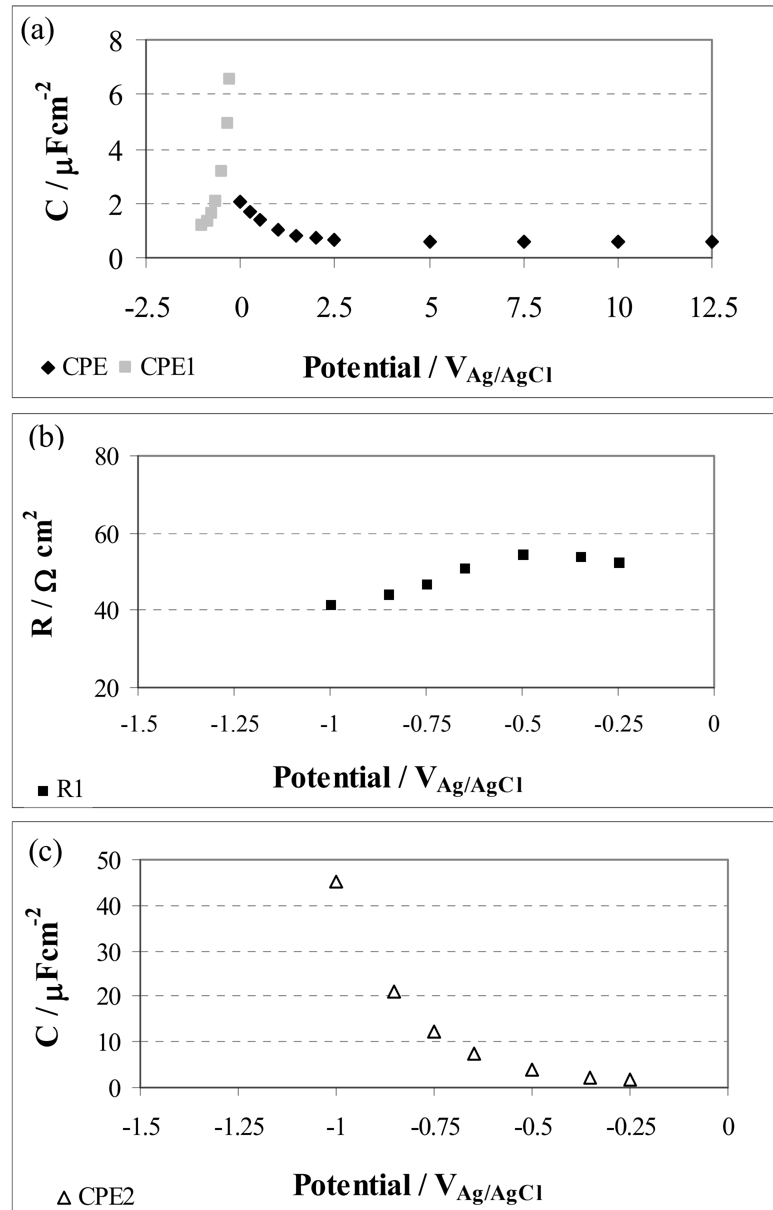

Figure 7.16 Variation of capacitance and resistance with potential for the different elements of the equivalent circuits adjusted to the EIS spectra obtained for the Al-89 at.% Nb alloy after anodising to 31 V: (a) CPE and CPE1; (b) R1; (c) CPE2.

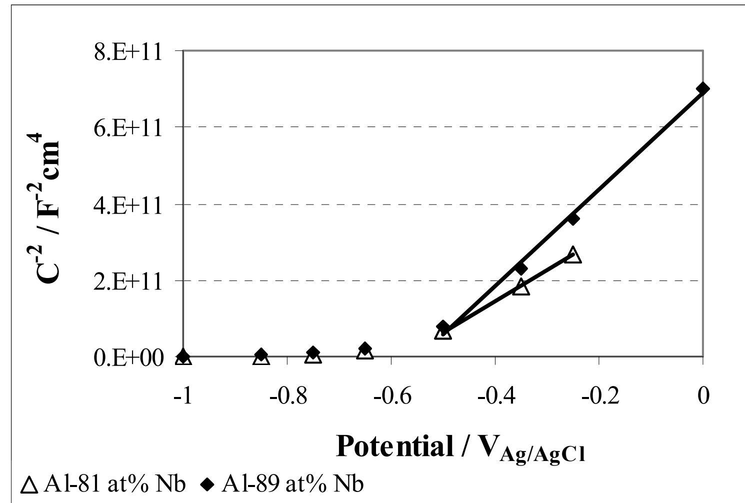

Figure 7.17 Mott-Schottky plots obtained for the Al- 81 at.% Nb and Al-89 at.% Nb alloys after anodising to 31 V at 5 mA cm^{-2} in 0.1 M ammonium pentaborate. Capacitance was determined from EIS spectra measured in a borate buffer solution.

Table 7.7 Donor concentration (N_D) and flat band potential (U_{FB}) of the Al-74 at.% Nb, Al-81 at.% Nb and Al-89 at % Nb alloys after anodising to selected potentials at 5 mA cm^{-2} in 0.1 M ammonium pentaborate and analysed in a borate buffer solution.

Alloy/ oxide	Anod. voltage (V)	Oxide thickness (nm)	N_D (cm^{-3})	U_{FB} (V_{SHE})
Al-74 at.% Nb	51	101	1.91 x10^{18}	-0.342
Al-81 at.% Nb	31	65	2.72 x 10^{18}	-0.364
Al-89 at.% Nb	31	61	4.28 x 10^{18}	-0.397

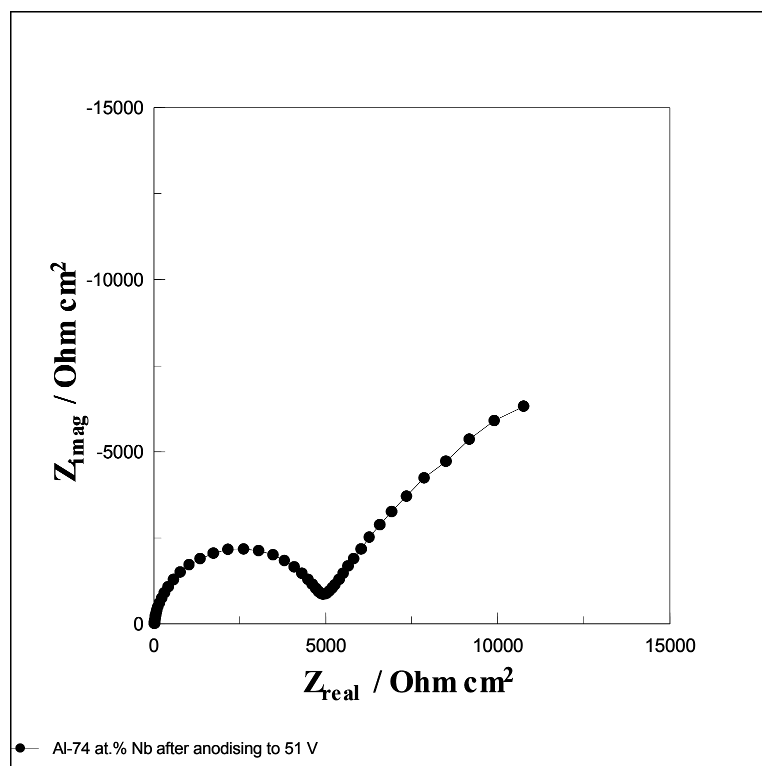

Figure 7.18 Complex plot obtained for the Al-74 at.% Nb alloy after anodising to 51 V at 5 mA cm^{-2} in 0.1 M ammonium pentaborate. EIS spectrum measured at –1.35 V in a borate buffer solution.

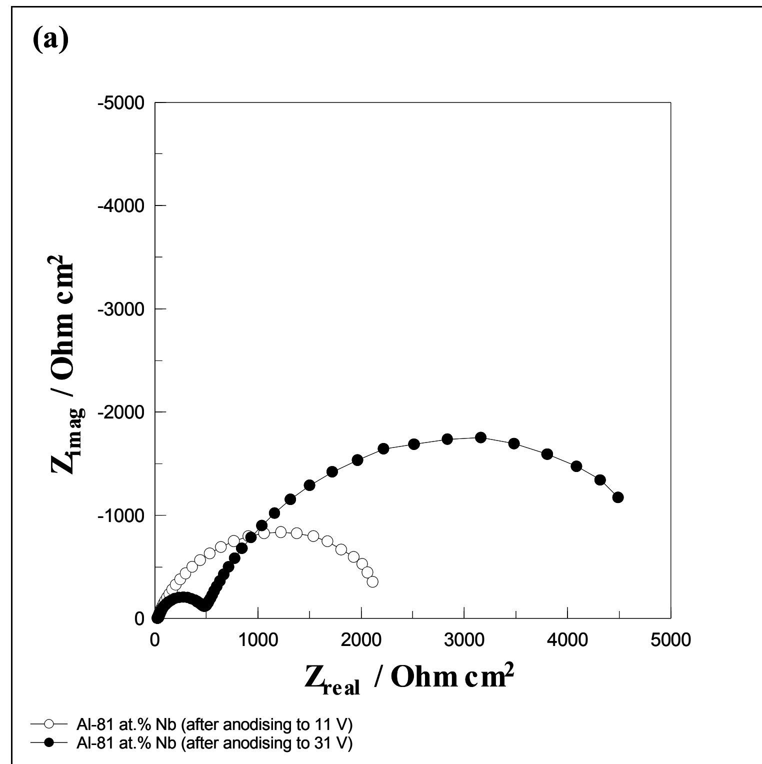

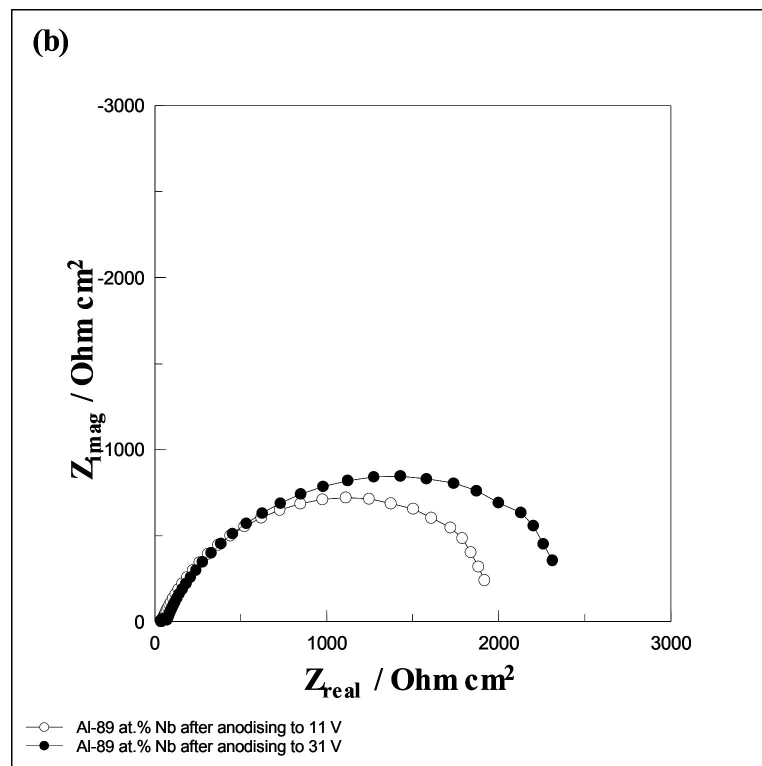

Figure 7.19 Complex plots obtained for the Al-81 at.% Nb alloy (a) and Al-89 at.% Nb alloy (b) after anodising to different voltages alloy after anodising at 5 mA cm^{-2} in 0.1 M ammonium pentaborate. EIS spectra measured at –1.35 V in a borate buffer solution.

7.4 Discussion

The analysis of the semiconducting properties of anodic oxides by EIS has the advantage of separating the space charge capacitance from others capacitances as a result of the frequency dependence of the behaviour. The EIS analysis is based on the adjustment of an equivalent circuit to the spectra; however, this can introduce some ambiguity if there is more than one possible circuit. Nevertheless, the technique is useful and it has been used in studies of semiconducting properties of different oxides like passive films [172], porous oxides [173, 174], mixed anodic films [175, 176] or relatively new semiconductors as $Ga_{(1-x)}Al_xAs$ and $GaInP_2$ [177].

The anodic oxides on niobium and Al-Nb alloys with niobium content ≥ 74 at.%, formed in 0.1 ammonium pentaborate and analysed in a borate buffer solution, show the formation of a space-charge layer in the range of potential of 0 to –0.5 $V_{Ag/AgCl}$. The values of carrier density and the flat band potential are given in Table 7.8.

The results show that both anodic oxide thickness and aluminium content decrease the carrier density. The variation of the carrier density with the anodising voltage (Figure 7.20) suggests an inverse power relation of the carrier density with the anodisingpotential for the anodic niobia as well as for anodic Al-Nb oxides. A similar trend has been reported for other anodic oxides like WO_3 [178, 179], TiO_2 [180] as well as for niobia [181]. A possible explanation is that, for relatively thin anodic oxides, the space charge layer extends over entire anodic oxide thickness, including the metal/oxide interface. It is also possible that, at this interface, some non-stoichiometric oxide species contribute to the increase of donor concentration.

The donor concentration in anodic niobia is usually associated with a deficit of oxygen, though the presence of oxygen vacancies [181]. Thus, the results suggest that the number of oxygen vacancies decreases with increase of thickness, which is reasonable since oxygen is incorporated within the oxide at the oxide/electrolyte interface.

Table 7.8 Donor concentrations (N_D) and flat band potentials (U_{FB}) of the sputtered niobium and Al-Nb alloys of high niobium content, after anodising to selected potentials at 5 mA cm^{-2} in 0.1 M ammonium pentaborate and analysed in a borate buffer solution.

Alloy/oxide	Anodising Voltage (V)	Oxide Thickness (nm)	N_D (cm^{-3})	U_{FB} (V_{SHE})
100 at.% Nb	12	24	42.8 x 10^{18}	-0.473
	33	**72**	**7.62 x 10^{18}**	**-0.418**
	54	100	5.11 x 10^{18}	-0.468
	101	*192*	*4.71 x 10^{18}*	*-0.496*
Al-89 at.% Nb	11	20	15.7 x 10^{18}	-0.488
	31	**61**	**4.28 x 10^{18}**	**-0.397**
Al-81 at.% Nb	11	21	9.50 x 10^{18}	-0.489
	31	**65**	**2.72 x 10^{18}**	**-0.364**
Al-74at.% Nb	51	101	1.91 x10^{18}	-0.342

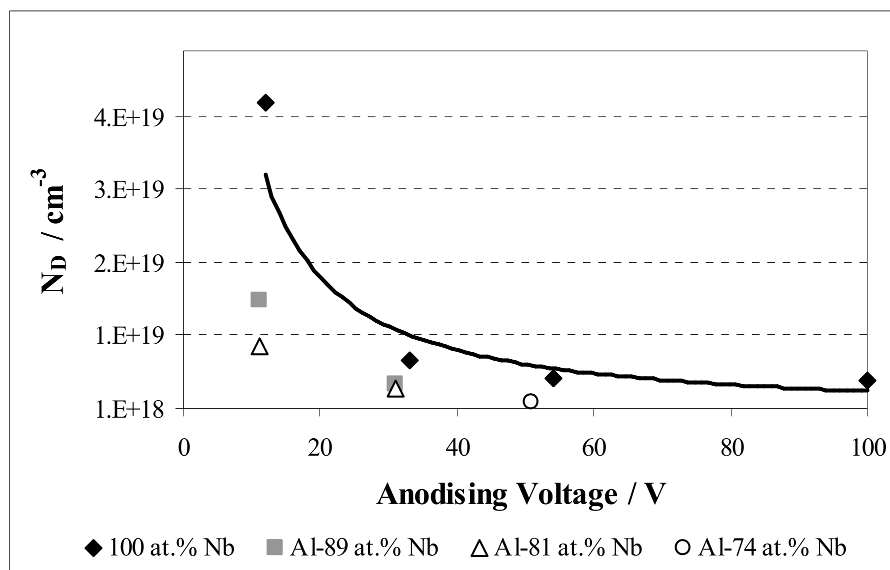

Figure 7.20 Dependence of the donor concentration on the anodising voltage for the sputtered niobium and Al-Nb alloys after anodising to selected voltages at 5 mA cm^{-2} in 0.1 M ammonium pentaborate.

Electrolyte species incorporated into the oxide during anodizing can also contribute to the variation of the carrier concentration. The anodic oxides were formed in 0.1 M ammonium pentaborate and it has been shown that borate species are immobile in alumina and move outward relatively fast in niobia, meaning that a fraction of the mixed anodic oxide formed at the oxide/electrolyte interface, should be contaminated with borate species. Thus, it is possible that borate species hinder the formation of oxygen vacancies. However, the decrease of N_D with thickness is also observed in anodic niobia per se; thus, the results sugest that thickness is the dominant factor on decreasing the carrier concentration.

The Mott-Schottky plots for pure niobia (formed to ≥ 30 V) show a second linear region in the range of potential from 2.5 / +12.5 V, suggesting two levels of electron donors. This feature has been reported in the study of other anodic oxides; for example, Metikos et al found two regions on the Mott-Schottky plots of passive films formed on tin electrodes which they attributed to the ionization of deep-state levels [182]. Features like interstitial cations or anions occupying cation positions can also induce donor sites [44]; thus, it is possible that such non-stoichiometric defects are related with the deep ionization levels, which are ionized only is the applied potential is sufficient high.

The EIS spectra obtained on the Al-74 at.% Nb alloy reveal two time constants when the applied potential is less than 2.5 V. The results suggest that from +12.5 to 5 V the anodic oxide is behaving as a dielectric, since the capacitance only varies slightly. After 2.5 V, a space charge is formed, also showing two linear regions, but a dielectric layer thickness less than the total oxide layer is still present close to the metal/oxide interface (Figure 7.21.a). From 2.5 to –0.5 V, the space charge thickness decreases until the flat band condition is achieved and, at the same time the thickness of the dielectric layer increases (Figure 7.21.b) This interpretation is consistent with the increase of the resistance of the oxide (R_{ox}) and decrease of the capacitance (C_{ox}) until –0.5 V which is a potential close to the flat band potential.

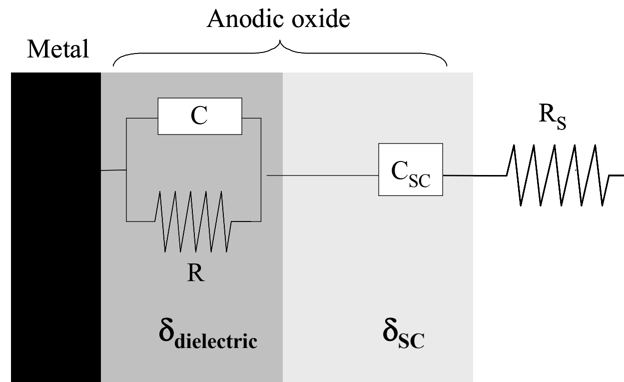

(a) $\mathbf{U_{FB} < U_1}$

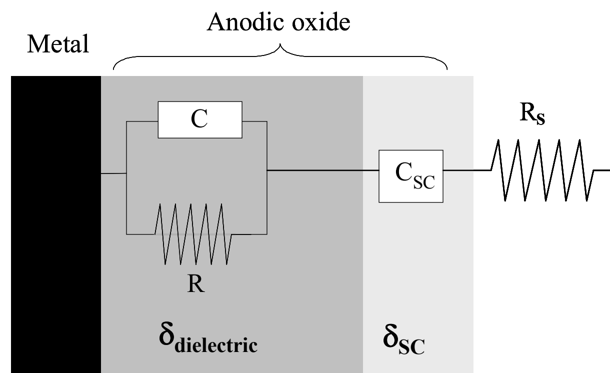

(b) $\mathbf{U_{FB} < U_2 < U_1}$

Figure 7.21 Schematic diagram showing the thickness variation of the dielectric and space-charge layers in the anodic oxide in film the range of potential: $U_{FB} < U << V_f$ (V_f = final voltage of oxide formation).

At more negative potentials, the capacitance of CPE2 is now associated with insertion of protons into the film. The capacitance of this element changes from 2.9 μF cm^{-2} at –0.5 V to 50 μF cm^{-2} at –1.35 V and the exponent n decreases from 0.9 to 0.8. Thus, it is possible that his element encloses a diffusion component (Appendix1).

The EIS spectra obtained for the Al-81 at.% Nb and 89 At.% Nb alloys anodised to 31 V also show two time constants. A similar interpretation can be made, even though the splitting is only observed after 0/–0.25 V and, previously to this behaviour, the capacitance of the CPE element increases from 2.5 to 0 V. These results suggest some limitation of the EIS technique to separate the dielectric and semiconducting responses or, due to the characteristics of the film and , identification is not possible.

The EIS spectra obtained for the specimens of Al-81 at.% Nb and Al-89 at.% Nb alloys anodised to 11 V only show one time constant. The interpretation is related to the space-charge layer embracing the entire anodic oxide layer thickness. The space charge thickness can be roughly estimated by $\delta_{SC}= C_{SC}/\varepsilon_r\varepsilon_o$. Using the capacitances obtained at 0 V, the space charge thicknesses are 18 and 14 nm which are very close to the total anodic oxide thicknesses obtained from the anodising charge (21 nm).

The decrease of donor concentration is more accentuated than that calculated by proportionally increasing alumina units in the oxide (Figure 7.22). This effect can be related to the influence of alumina on the band gap energy of the anodic oxide. In fact, the band gap energy of mixed oxides is related to the oxide composition.

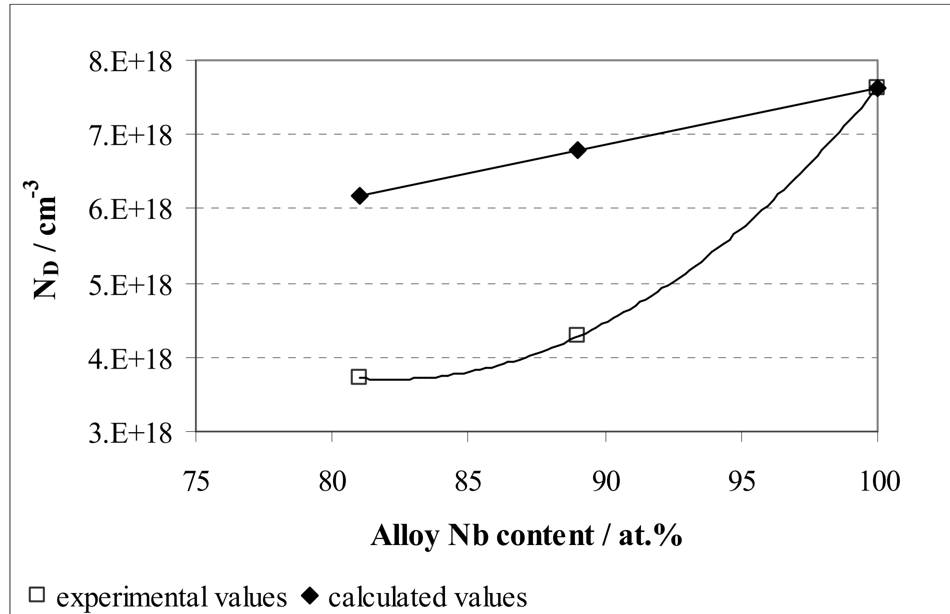

Figure 7.22 Dependence of the donor concentration on the amount of niobium (aluminium) for anodic oxides formed to 31/33 V.

Piazza et al have examined different mixed anodic oxides of transition metals (metals whose atoms have an incomplete d sub-shell), by photocurrent spectroscopy and found the following correlation [133]:

$$E_g^F\,(\text{eV}) = \Delta E_{am} + 1.35(\chi_M - \chi_O)^2 - 1.49 \qquad (7.1)$$

where, $E_g^F\,(\text{eV})$ is the optical bang gap energy of the oxide (amorphous), ΔE_{am} is the difference between E_g^F and E_g of amorphous and crystalline structure (usually varies from of 0.3 to 0.36 eV), and χ_M, χ_O are the electronegativity of the cation and of oxygen ion.

For a mixed oxide $A_aB_bO_o$, the cationic electronegativity is given by:

$$\chi_M = \frac{a\chi_A + b\chi_B}{a + b} \quad . \qquad (7.2)$$

The relation is also valid for mixed oxides of sp and d metals if the difference of the electronegativities of the metallic ions is less than 0.5 [183]. For example, the authors have studied mixed oxides of Al-W sputtered alloys formed at 5 mA cm^{-2} in 0.01 M ammonium pentaborate to different formation voltages. They found that the optical band gap energy decreases with increase of the amount of W in the range of 21 to 87 at.% W. The same authors also reported a value of 3.94 eV for the optical band gap for the mixed oxide obtained with a cast Al-25 at.% Nb alloy, mechanically polished and potentiodynamically polarized to 8 V in 0.1 M ammonium pentaborate. A value of 3.30-3.34 eV was also determined for a passive film on niobium [183]. Thus, the effect of alumina on the band gap energy of the mixed oxide of alumina and niobia may be the reason for the higher decrease of donor concentration.

The flat band potentials obtained for the anodic niobia show a dispersion of almost 100 mV (–0.496 to –0.418 V_{SHE}) despite the good definition of the linear region of the Mott-Schottky plots. Variation on flat band potentials has been attributed to a non-uniform distribution of charge carriers, dielectric relaxation, surface states or adsorption species. The exponent n of the constant phase elements near the flat band

potential is in the range of 0.86 to 0.9. This shows that there is some charge transfer at the oxide / electrolyte interface since only values of n close to 1 reveal a blocking interface. Flat band potentials are particularly sensitive to adsorption of H^+ and OH^- species at the oxide/electrolyte surface. If no other effects are present, like surfaces states, a Nernstian variation of U_{FB} with pH can be observed. For example, porous TiO_2 (crystalline) shows a negative shift of U_{FB} with pH increase [174]. At more negative potentials than U_{FB}, the process identified on anodic niobia is proton insertion in the film; thus, it is possible that some instability is created near the flat band potential due to the adsorption of protons.

The flat band potential obtained on the thicker films on the Al-Nb alloys show a shift to less negative values with increase of aluminum content. The variation observed is not in accordance with results reported on mixed oxides of Ta-Mo and Hf-W on sputtered alloys, where increase of the element with insulating characteristics shifts cathodically the flat band potentials [133, 134].

7.5 Conclusions

The EIS technique was used to determine the semiconducting properties on anodic oxides on sputtered niobium and Al-Nb alloys and the spectra obtained allow identification of the capacitances associated with space charge regions. The following conclusions are drawn from the present study:

- The results obtained on sputtered niobium, anodised to different final voltages (range of 10-100 V), in 0.1 M ammonium pentaborate and at constant current density of 5 mA cm^{-2}, show a donor concentration in the range of 10^{19} - 10^{18} cm^{-3} after analysis in a borate buffer solution (pH 9). The donor concentration of an oxide formed to 12 V is 4.3 x 10^{19} cm^{-3}, whereas films formed to higher voltages (30 to 100 V) have lower values in the range of 7.6 x 10^{18} to 4.7 x 10^{18} cm^{-3}. The variation suggests an inverse power relation with the anodisation voltage.

- For the same experimental conditions, the results obtained for anodic oxides on Al-Nb alloys show, that for niobium content ≥ 74 at.% Nb, the anodic oxides show n-type semiconductor behaviour when examined by Mott-Schottky analysis. The results show that both thickness and alumina content decrease the donor concentration.

- The EIS spectra show the formation of a complete charge depleted layer when the ratio $E_{applied}/E_{anod}$ is 40.%, which was not achieved for anodic oxides on niobium. Similar to the results obtained for anodic niobia, the donor concentration obtained on films formed at 11 V is higher than the values obtained at 31 V. The values are in the range 1.6×10^{19} and 9.5×10^{18} for anodic oxides of 89 and 81 at.% Nb content alloys formed to 11 V, whereas anodic oxides formed to higher voltages show values of 4.3×10^{18} and 2.7×10^{18} cm^{-3} respectively. The result obtained on the Al-74 at.% Nb alloy anodised to 51 V, is 1.9×10^{18} cm^{-3}.

- The flat band potentials obtained for the anodic niobia are in the range –0.496 to –0.418 V_{SHE}. The dispersion is probably associated with the instability promoted by the adsorption of protons at the oxide/electrolyte interface as this process was clearly identified at more negative potentials than U_{FB}. The flat band potentials obtained on mixed anodic oxides formed to 31 and 51 V, show a shift to less negative values in the range of -0.397 to-0.342 V_{SHE}.

- Al-Nb alloys with niobium contents of 31 and 44 at.%, anodised to 53 and 31 V respectively, show dielectric behaviour as the EIS spectra revealed an almost constant capacitance over the entire range of potential tested (+12.5 V to –1.35 V). The dielectric constants calculated are in agreement with the previous values obtained by measuring with a mercury drop.

GENERAL SUMMARY AND CONCLUSIONS

The aim of this work was to characterize the anodising process and the electrical properties of the anodic oxides developed on Al-Nb alloys; the results were compared with anodic films formed on aluminium and niobium, after anodising under the same experimental conditions. Results for aluminium prepared and anodised under the same experimental conditions are widely reported, but it was necessary to perform the same experimental procedure with niobium to obtain the values for comparison. The principal findings are summarized below.

The present work reveals that metastable Al-Nb alloys, prepared by magnetron sputtering with a niobium contents of 21 to 89 at.% Nb, anodised at high efficiency in 0.1 M ammonium pentaborate, develop uniform and featureless anodic oxide layers of similar cation composition to the corresponding alloy. The anodic oxides grow by counter migration of cations and anions under the high electrical field in a similar manner to that determined for alumina, niobia and other mixed valve-metal oxides.

The alloys of higher aluminium content than niobium (21- 44 at.% Nb) show an intermediate behaviour between alumina and niobia regarding the oxide density, the formation ratio and the total cation transport number. This is evidence of the linearity of the Al-Nb system in this range of composition. For the Al-21 at.% Nb alloy it was found that Al^{3+} ions migrate outward at a slightly faster rate than that of Nb^{5+} ions, which correlates with the relative energies of the Al^{3+}-O and Nb^{5+}-O single bond strength. The outer alumina layer, formed at the oxide/electrolyte interface, is penetrated by fingers of inner layer oxide, of reduced ionic resistivity. The layer is very thin, for instance, a specimen anodised to 150 V shows an alumina outer layer of 12 nm.

The results obtained on this work clearly show that alumina can be an effective additive to improve or stabilize the dielectric properties of anodic niobia. The linear increase of the dielectric constant with niobium content is the most significant evidence. Anodic oxides with up to 44 at.% of niobia show dielectric behaviour when analysed in a borate buffer solution (pH 8.8), whereas oxides of higher

niobium content than 74 at.% show n-type semiconductor characteristics with a donor concentration in the range of 2 x 10^{18}- 2 x 10^{19}. The anodic oxides of 74 to 89 at.% Nb achieve a fully depleted charge layer when the applied potential on measuring the capacitance is about 40% of the anodising voltage. This feature was not achieved on anodic niobia for similar experimental conditions, and shows that alumina decreases the number of electron donor levels within the anodic oxide and probably increases the band gap energy.

After cathodic polarization, the process of proton insertion in the oxide was detected even in mixed oxides of reduced niobium content (≥ 31 at.% Nb). This process was detected at potential of ≤ –1 V_{SCE} by voltammetry and EIS.

The results obtained on niobium, prepared by magnetron sputtering and anodised under the usual experimental conditions, show that niobium forms also a featureless oxide of composition represented by Nb_2O_5 as determined by RBS. The anodising process proceeds at high efficiency under the selected conditions and the anodic oxide grows at both interfaces as predicted for a typical valve-metal. The cation transport number is 0.29, which is in the range of values usually reported.

Some features related to the initial instance of the anodising process and corresponding anodising-slope suggest that the experimental sputtering conditions of niobium could be optimised further, i.e. the vacuum and argon pressure, since argon pressure has an influence on surface roughness and oxygen has an influence on the voltage-time response on anodising at constant current density. Nevertheless, the results show that anodic niobia shows n-type semiconductor behaviour with a donor concentration in the range of 5 x10^{18}- 4 x 10^{19}; the values are higher, as expected, than the values obtained for mixed Al-Nb anodic oxides of equivalent oxide thickness.

The voltametric studies have shown that the variation of the logarithm of the peak current density with sweep rate formation is linear with a slope close to one; this is in agreement with the high field equation for a potentiodynamic anodic oxide growth. Close to the oxide/metal interface, there is a non-stoichiometric layer of niobium oxide of reduced valence, as the XPS results suggest. This means that the electric

field during sweeping is not sufficiently strong to form an homogeneous Nb_2O_5 oxide layer. The oxide thickness is relatively constant, in the range of pH 3 to 11, as the charge corresponding to the oxide formation is constant and only depends on the maximum potential achieved on sweeping.

Proton insertion in the anodic niobia was detected by EIS or voltammetry at cathodic polarization $\leq -1\ V_{SCE}$. The results suggest that the process is semi-reversible and depends on oxide thickness.

SUGGESTIONS FOR FUTURE WORK

The findings of the present work have provided insight into the behaviour of anodic oxides on niobium and alloys with aluminium. However, interesting phenomena have also been revealed, which are the subject of further discussion. Further, additional studies are required to elucidate the processes proceeding.

Some anomalous features, observed on anodising the sputtered niobium specimens, e.g. the high values of anodising slopes, suggest that the experimental conditions for deposition can be optimised further. One possible reason is related to the vacuum pressure which if not sufficiently low, allows partial oxidation of the niobium (M-O) during sputtering. This oxygen can be one of the causes contributing for the higher anodising slopes than the usually reported, for the same anodising conditions. It is also possible that roughness and/or porosity are also related with the anomalous behaviour detected on the first seconds of time-voltage response of anodising at constant current. The roughness seems to be related with the argon pressure of sputtering; however, a more accurate surface observation by appropriate techniques like AFM should be carried out to determine that dependence.

The EIS technique was effective in determining the semiconducting properties of the anodic niobia and mixed Al-Nb oxides; however the analysis of the semiconductor properties can be completed with photocurrent spectroscopy, which allows the determination of the optical band gap energy of the anodic oxides. The technique is also more accurate in determining the flat band potentials, which have shown a strong dispersion when obtained by EIS.

The anodic niobia and mixed Al-Nb oxides of high niobium content (>74 at.% Nb) formed in 0.1 M ammonium pentaborate and analysed in a borate buffer solution show semiconducting characteristics, but the results should be expanded to other electrolytes. For instance, an acid electrolyte of phosphorus species should also be examined since phosphorus species are incorporated in anodic niobia [184] and it has been reported that reduced values of capacitance are obtained. Thus, it is possible that anodic films formed on these electrolytes show improved dielectric behaviour.

Anodising at constant current followed by current decay should also been investigated since it has been reported that those oxides show less potential dependence of the capacitance and also reduced leakage current [159, 185]. The explanation for this feature is not well understood, but it may be related to micro-variation on the oxide composition or structure, which decreases the donor concentration.

This work also suggests that other elements, or even a third element, should be examined in order to prove the possibility of stabilising the dielectric properties of niobia. For instance, an element of higher relative migration rate than Nb^{5+} will form a thin layer close to the oxide/electrolyte interface. This may offer the possibility of improving the dielectric behaviour of these oxides. For example, manganese species migrate faster than aluminium ions, and the same behaviour is expected with niobium. Furthermore MnO_2 is already used as a second electrode (the oxide is conducting) in the capacitor industry [186].

Finally, there are other features observed on niobium that should be examined in more detail, for example the electrochromic effect. The results obtained in this work suggest that the process is stable and reproducible. Furthermore, magnetron sputtering is highly appropriate to study this effect due the good quality of the metallic surfaces, e.g. flatness and cleanness, as well as to the possibility of adding other elements, e.g. tungsten or titanium, to enhance the effect, whilst maintaining a solid solution alloy.

APPENDIX 1 - Determination of the diffusion coefficient of H^+ in anodic niobia and anodic Al-Nb oxides

A1.1 Introduction

As already considered, the EIS spectra measured at –1.35 $V_{Ag/AgCl}$ on the anodic oxides of different thicknesses were extended to lower frequencies (0.1 Hz) in order to characterise the process associated with the proton insertion in the oxide. The equivalent circuit that simulates appropriately the experimental data includes a Warburg impedance element from which the chemical diffusion coefficient of H^+ was calculated, according to:

$$T = \frac{L^2}{D} \qquad \text{(A1.1)}$$

where D is the diffusion coefficient, L is the diffusion layer and T is one of the parameters of the element of finite length of diffusion calculated by the Zview analysis software (W_o-T) [187, 188].

A1.2 Anodic niobia

The spectra obtained on the niobium specimens after anodising to different voltages were adjusted to a simple Randles circuit with a Warburg element of finite length diffusion (Figure A1.1). The capacitance and the resistance are associated with the interfacing process where protons are initially adsorbed and then diffuse into the oxide.

The fitted spectra show good agreement with experimental data (Figure A1.2) with a relative error ≤ 12% for the diffusion element. The results show a decrease of the diffusion coefficient with increase of the anodic oxide thickness (Table A1.1) These low values of diffusion are consistent with a process that occurs in a solid phase [187].

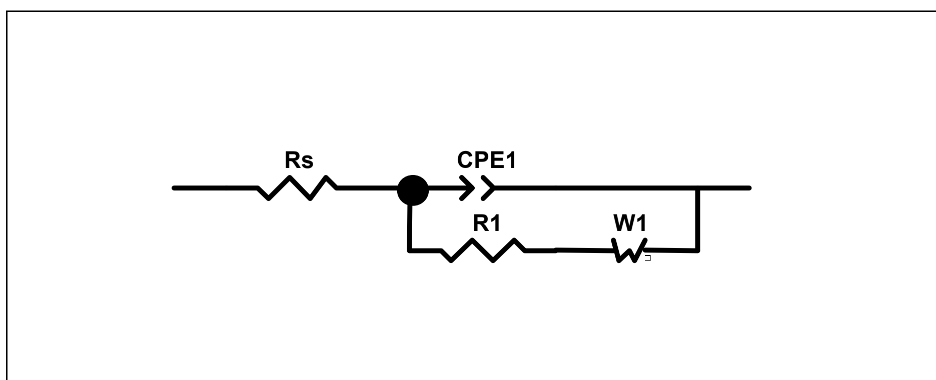

Figure A1.1 Equivalent circuit adjusted to the EIS spectra measured at –1.35 V for the sputtered niobium after anodising to selected voltages at 5 mA cm^{-2} in 0.1 M ammonium pentaborate.

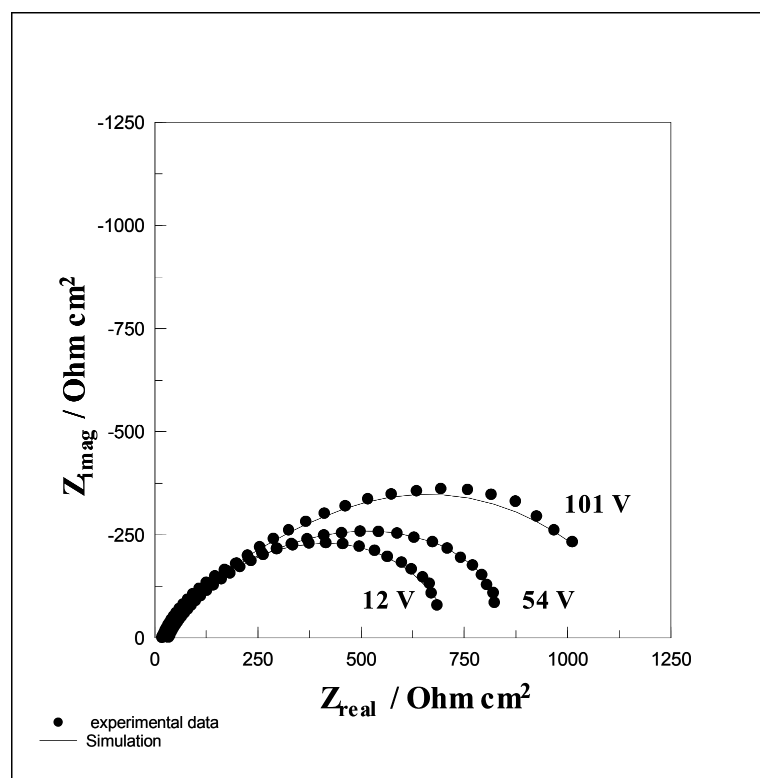

Figure A1.2 Complex plots obtained for the sputtered niobium after anodising to selected voltages at 5 mA cm^{-2} in 0.1 M ammonium pentaborate. EIS spectra measured at –1.35 V in a borate buffer solution.

Table A1.1 Coefficient of diffusion of H^+ in anodic niobia formed in 0.1 M ammonium pentaborate in contact with a borate buffer solution.

Anodising Voltage (V)	Oxide thickness (nm)	W_o- T (s)	Diffusion Coefficient ($cm^2\ s^{-1}$)
12	24	0.5	1.1×10^{-11}
54	100	0.8	1.3×10^{-10}
101	192	1.1	3.4×10^{-10}

A1.2 Al-Nb anodic oxides

The EIS spectra measured on the Al-Nb specimens with niobium contents of 74 at.% to 89 at.%, anodised to voltages of 30-50 V, were simulated by the equivalent circuit shown in Figure A1.3. The first semicircle is associated with the resistance and capacitance of the anodic oxide film and the second response is associated with the proton insertion in the film in a similar way as described for the niobia.

The spectra show good agreement with the experimental data (Figures A1.4 and A1.5).

The diffusion coefficient for each oxide was determined even though the relative errors are higher than the values obtained for niobia. One reason for this feature is related to the poor definition of the second semicircle, which, ideally, should had been extended to lower frequencies for completing. The results show an increase of resistance to proton diffusion with increase of aluminium species in the oxide.

A1.3 Conclusions

The experimental results allow the following conclusions:

- The EIS spectra identify clearly the process of hydrogen insertion in the anodic niobia and Al-Nb oxides containing 74 to 89 at.% Nb.
- Aluminium increases the resistance to proton diffusion in the oxide.

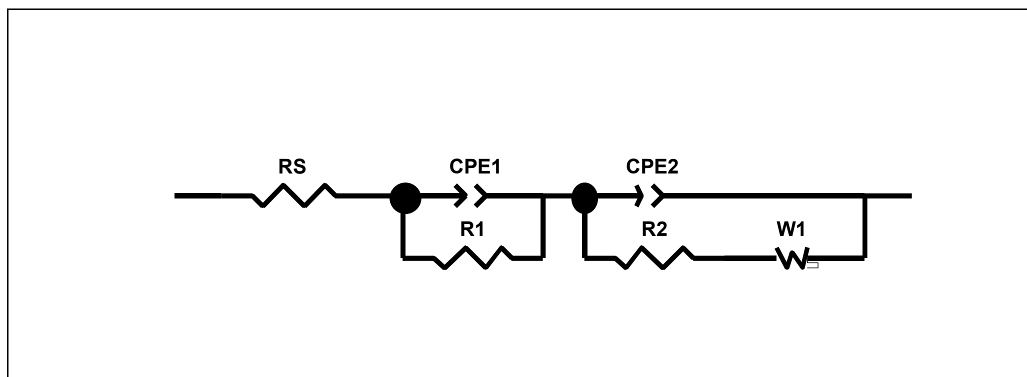

Figure A1.3 Equivalent circuit adjusted to the EIS spectra measured at –1.35 V for Al-Nb alloys after anodising to selected voltages at 5 mA cm^{-2} in 0.1 M ammonium pentaborate

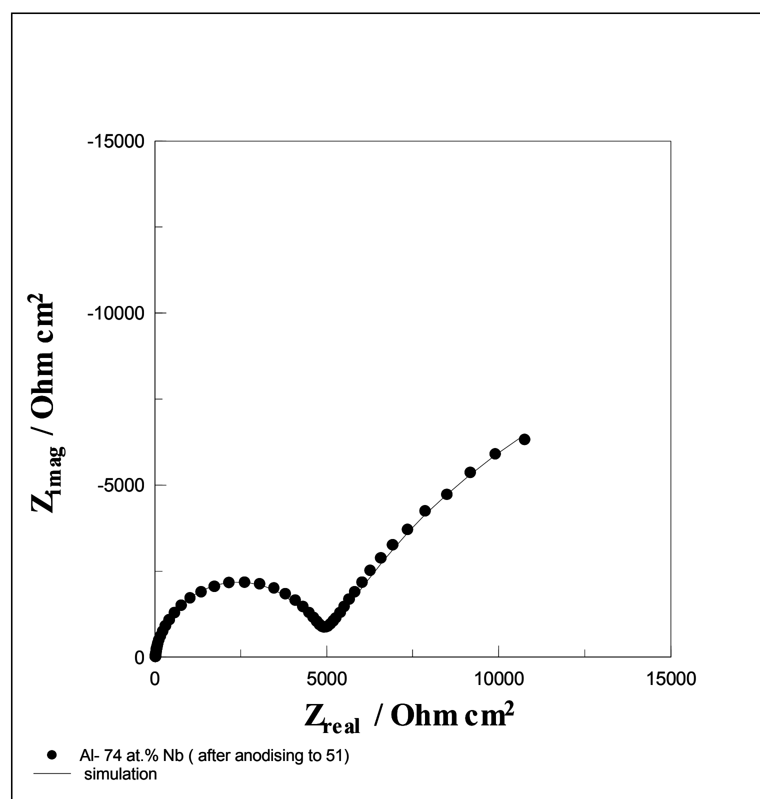

Figure A1.4 Complex plot obtained for the Al-74 at.% Nb after anodising to 51 V at 5 mA cm^{-2} in 0.1 M ammonium pentaborate. EIS spectrum measured at –1.35 V in a borate buffer solution.

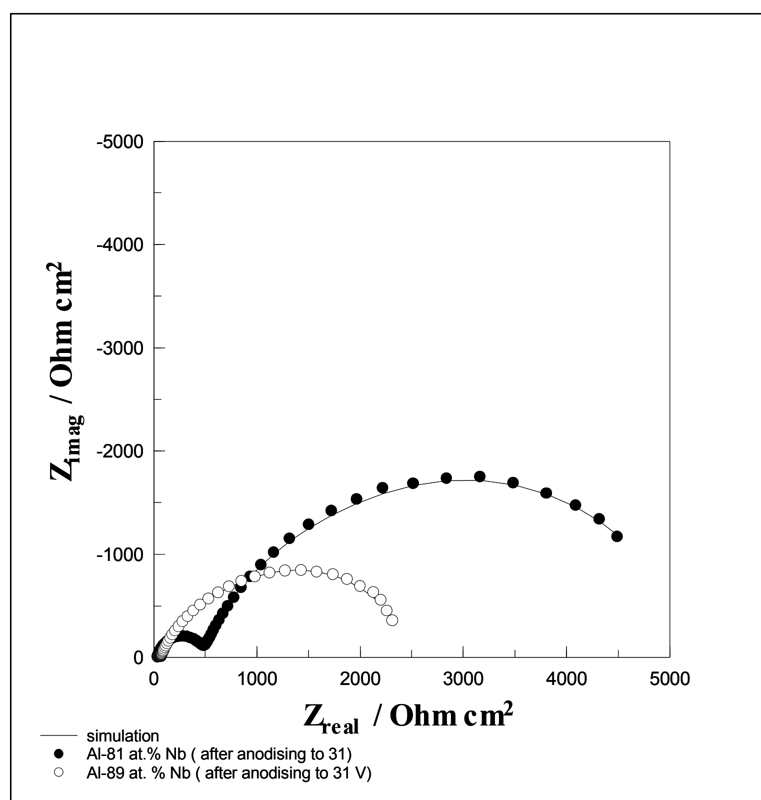

Figure A1.5 Complex plots of the Al-81 at.% Nb and Al-89 at.% Nb alloys after anodising to 31 V at 5 mA cm^{-2} in 0.1 M ammonium pentaborate. EIS measured at –1.35 V in a borate buffer solution.

Table A1.2 Coefficient of diffusion of H^+ in Al-Nb anodic oxides formed in 0.1 M ammonium pentaborate in contact with a borate buffer solution.

Alloy	Anodising Voltage (V)	Oxide thickness (nm)	W_o-T (s)	%error W_o-T	Diffusion Coefficient ($cm^2\ s^{-1}$)
Al-74 at.% Nb	51	101	2.5	75%	4.1×10^{-11}
Al-81 at.% Nb	31	65	1.4	19%	3.0×10^{-11}
Al-89 at.% Nb	31	61	0.8	8%	4.6×10^{-11}

REFERENCES

1. S. Wernick, R. Pinner, P.G. Sheashy, "The Surface Treatment and Finishing of Aluminium and its Alloys", 5th edition, ASM International, Ohio, USA (1987)

2. H. Fox, New Energy News, 5 (1997) 16

3. L. Young, "Anodic Oxide Films", Academic Press, London/New York (1961)

4. M.M. Lohrengel, Materials Sci. Eng., **R11** (1993) 243

5. G.E. Thompson, Thin Solid Films, **297** (1997) 192

6. M.L. Urmal, "Crescimento e Propriedades de Filmes de Óxidos Anódicos. Caracterização do Óxido de Zinco", LNETI/DER—0079, Lisbon (1990)

7. M.M. Lohrengel, Electrochim. Acta, **39** (1994) 1265

8. L. Young, F.G.R. Zobel, J. Electrochem Soc., **113** (1966) 277

9. Y.M. Li, L.Young, J. Electrochem. Soc., **147** (2000) 1344

10. C.J. Dell'Oca, L.Young, J. Electrochem. Soc., **117** (1970) 1545

11. C.J. Dell'Oca, L.Young, J. Electrochem. Soc., **117** (1970) 1548

12. M.H. Wang, K.R. Hebert, J. Electrochem. Soc., **146** (1999) 3741

13. M.J. Dignam in "Comprehensive Treatise of Electrochemistry", Vol. 4, edited by J.O´M. Bockris, B.E. Conway, E. Yeager, R.E. White, Plenum Press, New York and London (1980)

14. J.W. Schultze, M.M. Lohrengel, Electrochim. Acta, **45** (2000) 2499

15. H. Habazaki, K. Shimizu, P. Skeldon, G.E. Thompson, G.C. Wood, Thin Solid Films, **300** (1997) 131

16. Sonia Mato, PhD thesis, UMIST (2003)

17. K. Shimizu, S.Tajima, G.E. Thompson, G.C. Wood, Electrochim. Acta, **25** (1985) 1486

18. H. Uchi, T. Kanno, R.S. Alwitt, J. Electrochem. Soc., **148** (2001) B17

19. M.B.J.G. Freitas, L.O.S. Bulhões, J. Appl. Electrochem., **27** (1997) 612

20. "Handbook of Thin Film Technology, edited by I.I. Maissel, R. Gland, Mc. Graw-Hill. New York (1970)

21. A.C. Crossland, H. Habazaky, K. Shimizu, P. Skeldon, G.E. Thompson, G.C. Wood, X. Zhou, C.J.E. Smith, Corros. Sci., **41** (1999) 1945

22. J.A. Richardson, G.C. Wood, Corros. Sci., **10** (1970) 313

23. G.E. Thompson, P.E. Doherty, G.C. Wood, J. Electrochem. Soc., **129** (1982) 1515

24. G.C. Wood, P. Skeldon, G.E. Thompson, K. Shimizu, J. Electrochem. Soc., **143** (1996) 74

25. F. Brown, W.D. Mackintosh, J. Electrochem. Soc., **120** (1973) 1096

26. J.P.S. Pringle, Electrochim. Acta, **25** (1980) 1423

27. J.P.S. Pringle, J. Electrochem. Soc., **120** (1973) 398

28. J.P.S. Pringle, Electrochim. Acta, **25** (1980) 1403

29. Q. Lu, P. Skeldon, G.E. Thompson, D. Masheder, H. Habazaki, K. Shimizu, Corros. Sci., **46** (2004) 2817

30. P. Skeldon, K. Shimizu, G.E. Thompson, G.C. Wood, Thin Solid Films, **123** (1998) 127

31. K. Shimizu, K. Kobayashi, G.E. Thompson, P. Skeldon, G.C. Wood, J. Electrochem. Soc., **144** (1997) 418

32. K. Shimizu, G.M. Brown, K. Kobayashi, P. Skeldon, G.E. Thompson, G.C. Wood, Corros. Sci., **41** (1999) 1835

33. K. Shimizu, G.M. Brown, K. Kobayashi, P. Skeldon, G.E. Thompson, G.C. Wood, Corros. Sci., **41** (1999) 1971

34. A.R. West, "Basic Solid State chemistry", John Wiley & Sons, New York (1984)

35. W.F. Smith, " Principles of Materials Science and Engineering", Mc Graw –Hill, 3rd edition, New York (1996)

36. R.M. Hill, J.M. Alison, "Wiley Encyclopedia of Electrical and Electronics Engineering on-line", http:\\www.interscience.wiley.com:83/eeee

37. "Industrial Electronics Handbook", edited by W. D. Cockrell, McGrawHill, New York (1958)

38. R. Kötz, M. Carlen, Electrochim. Acta, **45** (2000) 2483

39. O. Kerrec, D. Devilliers, H. Groult, M. Chemla, Electrochim. Acta, **40** (1995) 719

40. R.A.B. Devine, A.G. Revesz, J. Applied Physics, **90** (2001) 389

41. A.K. Vijh, in "Oxides and Oxides Films", edited by Marcel Dekker, New York (1973)

42. A.K. Vijh, J. Electrochem. Soc., **116** (1969) 353

43. W.P. Gomes, D. Vanmaekelbergh, Electrochim. Acta, **41** (1996) 967

44. M. Cunha Belo, Corrosão e Protecção de Materiais, **12** (1993) 7

45. H. Gerisher, Electrochim. Acta, **35** (1990) 1677

46. A.J. Nozik, R. Memming , J. Phys. Chem., **100** (1996) 13061

47. L. Micaroni, C.N.P. Fonseca, F. Decker, M.A. Paoli, Solar Energy Materials & Solar Cells, **60** (2000) 27

48. S.R. Morrison,"Electrochemistry at Semiconductor and Oxidised Metal Electrodes", Plenum Press, New York (1980)

49. A.J. Bard, L.R. Faulkner,"Electrochemical Methods", John Wiley & Sons, New York (1980)

50. N.E. Hakiki, M.C. Belo, A.M. P. Simões, M.G.S. Ferreira, J.Electrochem. Soc., **145** (1998) 3821

51. "http://www.ebnews.com/digest/story/OEG20010721S0002"

52. "http://www.globalsources.com/MAGAZINE/EC/0111W4/tuniobium.htm"

53. J.W. Shultze, L. Elfenthal, J. Electroanal. Chem., **204** (1986) 153

54. G.E. Cavigliasso, M.J. Esplandiu, V.A. Macagno, J. Appl. Electrochem., **28** (1998) 1213

55. F.M. Al-Kharafi, W.A. Badawy, Electrochim. Acta, **40** (1995) 2623

56. A.D. Modestov, A.D. Dadydov, J. Electroanal. Chemistry, **460** (1999) 214

57. F. Di Quarto, S. Piazza, C. Sunseri, Electrochim. Acta, **35** (1990) 99

58. F. Di Quarto, F. La Mantia, M. Santamaria , Electrochim. Acta, **50** (2006) 5090

59. S.L. Albuquerque Maranhão, R.M. Torresi, Electrochim. Acta, **43** (1998) 257

60. B. Reichman, A.J. Bard, J. Electrochem. Soc., **127** (1980) 241

61. B. Othani, K. Iwai, S. Nishimoto, T. Inui, J. Electrochem. Soc., **141** (1994) 2439

62. M. Gomes, L. Bulhões, S. Castro, A. Damião, J. Electrochem. Soc., **137** (1990) 3067

63. B. Reichmam, A.J. Bard, J. Electrochem., **128** (1981) 344

64. P.R. Bueno, C.O. Avellaneda, R.C. Faria, L.O.S. Bulhões, Electrochim. Acta, **46** (2001) 2113

65. M. Schmitt, M.A. Aegerter, Electrochim. Acta, **46** (2001) 2105

66. N. Ozer, M.D. Rubin, C.M. Lampert, Solar Energy Materials and Solar Cells, **40** (1996) 285

67. M.A.B. Gomes, L.O.S. Bulhões, Electrochim. Acta, **35** (1990) 765

68. N. Kumagay, K. Tanno, T. Nakajima, N. Watanabe, Electrochim. Acta, **28** (1983) 17

69. R. Cabanel, J. Chaussy, J. Mazuer, G. Delabouglise, J.C. Jourbert, G. Barral, C. Montella, J. Electrochem. Soc., **137** (1990) 1444

70. C.K. Dyer, J.S.L. Leach, Electrochim. Acta, **20** (1975) 151

71. A. Vaskevich, M. Rosenblum, E. Gileadi, J. Electrochem. Soc., **142** (1995) 1501

72. T. Maruyama, T. Kanagawa, J. Electrochem. Soc., **141** (1994) 2868

73. R. Cabanel, G. Barral, J.P. Diard, B. Le Gorrec, C. Montella, J. Applied Electrochem., **23** (1993) 93

74. H. Habazaki, P. Skeldon, G.E. Thompson, G.C. Wood, Philos. Mag B, **73** (1996) 297

75. H. Habazaki, K. Shimizu, P. Skeldon, G.E. Thompson, G.C. Wood, Philos. Mag. B, **73** (1996) 445

76. H. Habazaki, K. Shimizu, P. Skeldon, G.E. Thompson, G.C. Wood, J. Electrochem. Soc., **143** (1996) 2465

77. L.Iglesias-Rubianes, P.Skeldon, G.E. Thompson, K. Shimizu, H. Habazaki, Corros. Sci., **43** (2001) 2217

78. L. Iglesias-Rubianes, P. Skeldon, G.E. Thompson, H. Habazaki, K. Shimizu, J. Electrochem. Soc., **149** (2002) B23

79. L. Iglesias-Rubianes, P. Skeldon, G.E. Thompson, H. Habazaki, K. Shimizu, Corros. Sci., **44** (2002) 751

80. J. De Laet, X. Zhou, P. Skeldon, G.E. Thompson, G.C. Wood, H. Habazaki, K. Takahiro, S. Yamaguchi, K. Shimizu, Corros. Sci., **41** (1999) 213

81. Y. Kihm, G.E. Thompson, G. Galaup, P. Skeldon, X. Zhou, K. Shimizu, H. Habazaki, Corros. Sci., **42** (2000) 533

82. H. Habazaki, P. Skeldon, K. Shimizu, G.E. Thompson, G.C. Wood, Corros. Sci., **37** (1995) 1509

83. Y. Liu, P. Skeldon, G.E. Thompson, H. Habazaky, K. Shimizu, Corros. Sci., **44** (2002) 1133

84. X. Zhou, H. Habazaki, K. Shimizu, P. Skeldon, G.E. Thompson, G.C. Wood, Corros. Sci., **38** (1996) 1563

85. A.C. Crossland, G.E. Thompson, C.J.E. Smith, H. Habazaki, K. Shimizu, P. Skeldon, Corros. Sci., **41** (1999) 2053

86. A.C. Crossland, G.E. Thompson, P. Skeldon, G.C. Wood, C.J.E. Smith, H. Habazaki, K. Shimizu, Corros. Sci., **40** (1998) 871

87. A.E. Herrera-Erazo, H. Habazaki, K. Shimizu, P. Skeldon, G.E. Thompson, Corros. Sci., **42** (2000) 1823

88. H. Habazaki, X. Zhou, K. Shimizu, P. Skeldon, G.E. Thompson, G.C. Wood, Electrochim. Acta, **42** (1997) 2627

89. H. Habazaki, K. Shimizu, P. Skeldon, G.E. Thompson, G.C. Wood, Corros. Sci., **43** (2001) 1393

90. H. Habazaki, K. Takahiro, S. Yamaguchi, K. Shimizu, P. Skeldon, G.E. Thompson, G.C. Wood, J. Electrochem. Soc., **146** (1999) 2507

91. I. Felhosi, H. Habazaki, K. Shimizu, P. Skeldon, G.E. Thompson, G.C. Wood, X. Zhou, Corros. Sci., **40** (1998) 2125

92. G.S. Frankel, R.C. Newman, C.V. Jahnes, M.A. Russak, J. Electrochem. Soc., **140** (1993) 2192

93. H. Yoshioka, Q. Yan, H. Habazaki, A. Kawashima, K. Asami, K. Hashimoto, Corros. Sci., **31** (1990) 349

94. Z. Grzesik, K. Takahiro, S. Yamaguchi, K. Hashimoto, S. Mrowec, Corros. Sci., **37** (1995) 801

95. Z. Grzesik, H. Habazaki, K. Hashimoto, S. Mrowec, Corros. Sci., **36** (1994) 1499

96. K. Hashimoto, P.Y. Park, J.H. Kim, H. Yoshioka, H. Mitsui, E. Akiyama, H. Habazaki, A. Kawashima, K. Asami, Z. Grzesik, S. Mrowec, Materials Sci. Eng., **A198** (1995) 1

97. F.A. Bonilla, A. Berkani, P. Skeldon, G.E. Thonpson, H. Habazaki, K. Shimizu, C. John, K. Stevens, Corros. Sci., **44** (2002) 1941

98. S. Mato, P. Skeldon, G.E. Thompson, D. Masheder, G.I. Sproule, M.J. Graham, H. Habazaki, K. Shimizu, Surf. Interface Analysis, **29** (2000) 895

99. S. Mato, G.E. Thompson, P. Skeldon, K. Shimizu, H. Habazaki, D. Masheder, Corros. Sci., **43** (2001) 993

100. H. Habazaki, M. Uozumi, H. Konno, K. Shimizu, S. Nagata, K. Asami, P. Skeldon, G.E. Thompson, Electrochim. Acta, **47** (2002) 3837

101. "Handbook of Deposition Technologies for Films and Coatings", Edited by R. F. Bunshah, William Andrew Publishing / Noyes, 2nd edition, New York (1987)

102. H. Habazaki, K. Shimizu, P. Skeldon, G.E. Thompson, G.C. Wood, X. Zhou, Corros. Sci., **39** (1997) 731

103. Loreto Iglesias-Rubianes, PhD thesis, UMIST (2002)

104. L. Iglesias-Rubianes, P. Skeldon, G.E. Thompson, P. Bailey, T.C.Q. Noakes, H. Habazaki, K. Shimizu, Corros. Sci., **45** (2003) 2915

105. L. Iglesias-Rubianes, P. Skeldon, G.E. Thompson, H. Habazaki, K. Shimizu, Corros. Sci., **45** (2003) 2905

106. K. Shimizu, G.M. Brown, H. Habazaki, K. Kobayashi, P. Skeldon, G.E. Thompson, G.C. Wood, Corros. Sci., **42** (2000) 831

107. H. Habazaki, M.A. Paez, K. Shimizu, P. Skeldon, G.E. Thompson, G.C. Wood, X. Zhou, Corros. Sci., **38** (1996) 1033

108. K. Tzoganakou, P. Skeldon, G.E. Thompson, X. Zhou, U. Kreissig, E. Wieser, H. Habazaki, K. Shimizu, Corros. Sci., **42** (2000) 1083

109. X. Zhou, G.E. Thompson, P. Skeldon, G. Wood, K. Shimizu, H. Habazaki, Corros. Sci., **41** (1999) 1599

110. N. Margadant, P. Skeldon, M. Textor, G.E. Thompson, J. Wan, H. Habazaki, K. Shimizu, N.D. Spencer, G.C. Wood, Corros. Sci., **42** (2000) 405

111. K. Shimizu, K. Kobayashi, J. Surf. Finishing Soc. Japan, **46** (1995) 402 (referred to16)

112. G. Alcalá, P. Skeldon, G.E. Thompson, X. Zhou, H. Habazaki, K. Shimizu, Workshop "Surface Treatments for Aluminium Structural Alloys", INETI, Lisbon (2001)

113. H. Habazaki, K. Shimizu, P. Skeldon, G.E. Thompson, G.C. Wood, X. Zhou, J. Phys. D, Appl. Phys., **30** (1997) 1833

114. X. Zhou, G.E. Thompson, H. Habazaki, M.A. Paez, K. Shimizu, P. Skeldon, G.C. Wood, J. Electrochem. Soc., **147** (2000) 1747

115. E. Zhuravlyova, L. Iglesias-Rubianes, A. Pakes, P. Skeldon, G.E. Thompson, X. Zhou, T. Quance, M.J. Graham, H. Habazaki, K. Simizu, Corros. Sci., **44** (2002) 2153

116. K. Shimizu, H. Habazaki, P. Skeldon, G.E. Thompson, G.C. Wood, Electrochim. Acta, **47** (2002) 1225

117. H. Habazaki, H. Konno, K. Shimizu, S. Nagata, P. Skeldon, G.E. Thompson, Corros. Sci., **46** (2004) 2041

118. X. Zhou, H. Habazaki, K. Shimizu, P. Skeldon, G.E. Thompson, G.C. Wood, Proc. R. Soc. London, **A 455** (1999) 385

119. L. Iglesias-Rubianes, P. Skeldon, G.E. Thompson, U. Kreissig, D. Grambole, H. Habazaki, K. Shimizu, Thin Solid Films, **424** (2003) 201

120. H. Habazaki, K. Shimizu, P. Skeldon, G.E. Thompson, G.C. Wood, Proc. R. Soc. London, **A 453** (1997) 1593

121. Y. Liu, M.A. Arenas, P. Skeldon, G.E. Thompson, P. Bailey, T.C.Q. Noakes, H. Habazaky, K. Shimizu, Corros. Sci., **48** (2006) 1225

122. Y. Liu, M.A. Arenas, P. Skeldon, G.E. Thompson, H. Habazaky, K. Shimizu, P. Bailey, T.C.Q. Noakes, Corros. Sci., 48 (2006) 1874

123. G. Alcalá, S. Mato, P. Skeldon, G.E. Thompson, P. Bailey, T.C.Q. Noakes, H. Habazaki, K. Shimizu, Corros. Sci., **45** (2003) 1803

124. S. Mato, G. Alcalá, G.E. Thompson, P. Skeldon, K. Shimizu, H. Habazaki, T. Quance, M. J. Graham, D. Masheder, Corros. Sci., **45** (2003) 2881

125. S. Mato, G. Alcalá, P. Skeldon, G.E. Thompson, D. Masheder, H. Habazaki, K. Shimizu, J. Electrochem. Soc., **150** (2003) B439

126. S. Mato, G. Alcalá, P. Skeldon, G.E. Thompson, D. Masheder, H. Habazaki, K. Shimizu , Corros. Sci., **45** (2003) 1779

127. H. Habazaki, T. Ogasawara, H. Konno, K. Shimizu, S. Nagata, P. Skeldon, G.E. Thompson, Corros. Sci., **49** (2007) 580

128. H. Habazaki, T. Ogasawara, H. Konno, K. Shimizu, S. Nagata, K. Asami, K. Takayama, P. Skeldon, G.E. Thompson, J. Electrochem. Soc., **153** (2006) B173

129. H. Habazaki, T. Matsuo, H. Konno, K. Shimizu, S. Nagata, K. Matsumoto, K. Takayama, Y. Oda, P. Skeldon, G.E. Thompson, Electrochim. Acta, **48** (2003) 3519

130. H. Habazaki, T. Matsuo, H. Konno, K. Shimizu, K. Matsumoto, K. Takayama, Y. Oda, P. Skeldon, G.E. Thompson, Surf. Interface Anal., **35** (2003) 618

131. H. Habazaki, T. Matsuo, H. Konno, K. Shimizu, S. Nagata, K. Takayama, Y. Oda, P. Skeldon, G.E. Thompson, Thin Solid Films, **429** (2003) 159

132. S. Mato, G. Alcalá, P. Skeldon, G.E. Thompson, A.B. Mann, D. Masheder, H. Habazaki, K. Shimizu, Surf. Interface Anal., **35** (2003) 477

133. M. Santamaria, D. Huerta, S Piazza, C. Sunseri, F. Di Quarto, J. Electrochem. Soc., **147** (2000) 1366

134. F. Di Quarto, M. Santamaria, P. Skeldon, G.E. Thompson, Electrochim. Acta **48** (2003) 1143

135. I. W.J.McG. Tegart, "The Electrolytic and Chemical Polishing of Metals in Research and Industry", Pergamom Press (1956)

136. German Álcala, PhD Thesis, UMIST (1992)

137. E.V. Koroleva, V.I. Ovcharenko, A.N. Fedorova, R.A. Machesvkaya, Protection of Metals, **30** (1994) 116

138. L.R. Doolittle, Nucl. Instrum. Methods, **B9** (1985) 344

139. N.P. Barradas, C. Jeynes, R.P. Webb, Appl. Phys. Lett., **71** (1997) 291

140. R. Grief, R. Peat, L.M. Peter, D. Pletcher, J. Robinson, "Instrumental Methods in Electrochemical", Ellis Horwood, Chichester U.K. (1985)

141. Gamry http:\\ ww.gamry.com\refence\EISTeory

142. A.M.O. Brett, C.M.A. Brett, "Electroquímica, Princípios, Métodos e Aplicações" Almedina, Coimbra, Portugal (1996)

143. B.A. Boukamp, "Equivalent Circuit Users Manual", University of Twente, Department of Chemical Tecnology, Canada (1989)

144. R. Macdonald, L. Potter, Solid States Ionics, **23** (1987) 61

145. "Impedance Spectroscopy, Emphasizing Solid Materials and Systems", edited by J.R. Macdonald, J. Willey and Sons, New York (1987)

146. R. Kukla, Surface and Coatings Technology, **93** (1997) 1

147. J.L. Vossen, W. Kern, "Thin Solid Processes", Academic Press, USA (1978)

148. “Surface Modification Technologies an Engineer’s Guide”, edited by T.S. Sudarshan, Marcel Dekker Inc., New York (1989)

149. C.M.G.S. Nunes, “Pulverização Catódica em Magnetrão Poste Obtenção de Películas Reflectoras”, tese de mestrado, FCL, INETI, Lisbon (1992)

150. “Metals Handbook”, vol. 10, “Materials Characterization”, ASM, 9th edition, Ohio, USA

151. J. Perrière, Vacuum, **37** (1987) 429

152. L.G. Earwaker, Vacuum, **45** (1994) 783

153. C.M.P Sá,” Caracterização Morfológica, Microestrutural e Microanalítica de Materiais por Microscopia Electrónica de Varrimento e Microanálise por Raios-X”, CEMUP, Porto (2001)

154. J.F. Watts, Vacuum, **45** (1994) 653

155. C. Linsmeier, Vacuum, **45** (1994) 673

156. M. Grundner, J. Halbritter, J. Appl. Phys., **51** (1980) 397

157. H. Habazaki, K. Shimizu, P. Skeldon, G.E. Thompson, G.C. Wood, X. Zhou, Trans. Inst. Met. Finishing, **75** (1997) 18

158. P. Skeldon, K. Shimizu, G.E. Thompson, G.C. Wood, Phil. Mag. B, **61** (1990) 927

159. H. Habasaki, T. Ogasawara, H. Konno, K. Shimizu, K. Asami, K. Saito, S. Nagata, P. Skeldon, G.E. Thompson, Electrochim. Acta, **50** (2005) 5334

160. K. Tsukada, J. Kawai, G. Uehara, H. Kado, IEEE Trans. Appl. Supercon., **3** (1993) 2944

161. S. Cattarin, M. Musiani, V. Palmieri, D. Tonini, Electrochim.Acta, **51** (2006) 1745

162. R.S. Amos, P.E. Breyer, H.H. Huang, A.W. Lichtenberger, IEEE Trans. Appl. Supercon., **5** (1995) 2326

163. H. Fujikawa, Y. Ttaga, J. Appl. Phys., **75** (1994) 2539

164. K. Kukli, M. Ritala, M. Lesleka, J. Electrochem.Soc., **148** (2001) F35

165. Y.H. Paik, W.J. Yoon, H.C. Shin, Journal of Colloid and Interface Science, **269** (2004) 354

166. H. Itaya, H. Asoh, S. Ono, ECS 201th Meeting, abstract **63**, (2006)

167. K. Kuramochi, H. Asoh, T. Mochizuki, S. Ono, J. Surf. Finish. Soc. Jpn., **55** (2004) 218

168. A.I. de Sá, C.M. Rangel, P. Skeldon, G.E. Thompson , Portugaliae Electrochim. Acta , **24** (2006) 305

169. J. Bisquert, G. Garcia-Belmonte, P. Bueno, E. Longo, L.O.S. Bulhões, J. Electroanal. Chem., **452** (1998) 229

170. S. Omanovic, M. Metikos-Hukovic, Thin Solid Films, **266** (1995) 31

171. R. Zanoni, F. Decker, C. Coluzza, F. Artuso, N. Cimino, G. Di Santo, E. Masetti, Surface and Interface Analysis, **33** (2002) 815

172. K. Darowicki, S. Krakowiak, P. Slepski, Electrochim. Acta, **51** (2006) 2204

173. J.C.S. Fernandes, R. Picciochi, M. da Cunha Belo, T. Moura e Silva, M.G.S Ferreira, I.T.E Fonseca, Electrochim. Acta, **49** (2004) 4701

174. B.P. Nelson, R. Candal, R.M. Corn, M.A. Anderson, Langmuir, **16** (2000) 6094

175. N.T.C. Oliveira, S.R. Biaggio, S. Piazza, C. Sunseri, F.Di Quarto, Electrochim. Acta, **49** (2004) 4563

176. N.T.C. Oliveira, S.R. Biaggio, P.A.P. Nascente, S. Piazza, C. Sunseri, F. Di Quarto, Electrochim. Acta, **51** (2006) 3506

177. S.S. Kocha, B.E. Liebert, Electrochim. Acta, **38** (1993) 1993

178. F. Di Quarto, A. Di Paola, C. Sunseri, Electrochim. Acta, **26** (1981) 1177

179. S.R. Biaggio, R.C. Rocha-Filho, J.R. Vilche, F.E. Varela, L.M. Gassa, Electrochim. Acta, **42** (1997) 1751

180. N. Ibris, Russian Journal of Electrochemistry, **39** (2003) 476

181. K.E. Heusler, M. Shulze, Electrochim. Acta, **20** (1975) 237

182. M. Metikos-Hukovic, S. Omanovic, A. Jukic, Electrochim. Acta, **45** (1999) 977

183. S. Piazza, M. Santamaria, C. Asunseri, F. Di Quarto, Electrochim. Acta, **48** (2003) 1105

184. S. Ono, J. Surf. Finish Soc. Jpn, **5**4 (2003) 447

185. H. Asoh, H. Odate, S. Ono, J. Surf. Finish. Soc. Jpn, **55** (2004) 202

186. V. Fischer, H. Stormer, D. Gerthsen, M. Stenzel, H. Zillgen, E. Ivers-Tiffée, Proccedings of 7th International Conference on Properties and Applications of Dielectric Materials, Nagoya, Japan (2003)

187. A. Hassanzadeh, M.H. Habibi, A. Zeini-Isfahani, Acta Chim. Slov., **51** (2004) 507

188. “Zview: Impedance /Gain Phase Graphics and Analysis software”, Scribner Associates, Southern Pines, N.C., USA (1993)